Development of a monolithic near-field optomechanical system

THÈSE N^{O} 8492 (2018)

PRÉSENTÉE LE 1ER JUIN 2018
À LA FACULTÉ DES SCIENCES DE BASE
LABORATOIRE DE PHOTONIQUE ET MESURES QUANTIQUES (SB/STI)
PROGRAMME DOCTORAL EN GÉNIE ÉLECTRIQUE

ÉCOLE POLYTECHNIQUE FÉDÉRALE DE LAUSANNE

POUR L'OBTENTION DU GRADE DE DOCTEUR ÈS SCIENCES

PAR

Ryan Daniel SCHILLING

acceptée sur proposition du jury:

Prof. H. Shea, président du jury
Prof. T. Kippenberg, directeur de thèse
Prof. E. Weig, rapporteuse
Prof. G. Steele, rapporteur
Prof. G. Villanueva, rapporteur

ÉCOLE POLYTECHNIQUE
FÉDÉRALE DE LAUSANNE
Suisse
2018

To my parents…

How can we escape the cold and heat?

Why not go where there is no cold and heat?

Is there such a place?

When cold, be thoroughly cold. When hot, be hot through and through

- Dongshan Liangjie (807–869)

Acknowledgements

This thesis work began when Professor Tobias Kippenberg took a chance with me, and provided an opportunity for which I am very grateful. As a supervisor, his persistent nature and relentless optimism fostered an environment where we felt undaunted in tackling complex and difficult experiments. Through his leadership I learned a great deal about how to approach these kind of challenges. Tobias instilled in me the idea that excellence is not something to be achieved but constantly perused - an endlessly receding goal. I've benefited from many enlightening conversations with Tobias over the years and am thankful that he would always find time in his busy schedule for discussion.

I joined the lab at the same time as Dr. Dalziel Wilson, who was a supervising post doc throughout my thesis work. During the first year of my thesis, while developing the initial devices, Dal was my go to for any assistance I needed in theory or experiment. In particular, he introduced me to precision optical experiments and high vacuum systems. I greatly benefited from his depth of knowledge in the lab. Moreover, I think all of us who have worked with him in the optomechanics team benefited from his patience and pragmatism.

Upon completing my first devices I joined the ^{3}He team, consisting at that time of Dal, Vivishek Sudhir, Nicolas Piro, and Hendrik Schütz. With their expertise, we made haste to capitalize on the new parameter regime these devices put us in. I appreciated discussions both philosophical and scientific with Nico, as well asb his broad perspective on the life of a scientist. Vivishek's quantitative rigor always served as a check on our more impetuous tendencies. I spent many hours in the lab working with Hendrik, making measurements and developing our vacuum system. I've always appreciated his convivial attitude, both in the lab and outside of it.

I want to also thank the broader optomechanics team with whom I worked, including Sergey Fedorov, Nils Engelsen, Amir Ghadimi, Ehsan Mansouri, and Mohammad Bereyhi. Sergey's intrepid spirit has been invaluable both in the work observing quantum correlations at room temperature and in developing low-dissipation *soft-clamped* nanobeams. Although, I have not had much chance to work with Nils I've enjoyed his good humor and collegiality in the office.

I'm grateful to have had the opportunity to collaborate with Dr. Hajime Okamoto on developing an electro-optomechanical system, during his one year sabbatical from NTT Japan. I learned many things from him and enjoyed our time working together very much. Moreover,

we succeeded in our goal and it was exciting to see that our system could be further extended as a practical charge sensor.

Throughout my thesis work my partner, Lina Carlini, has been a constant source of love and support. It's been wonderful sharing our lives together in Switzerland and I wouldn't want to imagine things any other way. I'm always inspired by her, not just as a thoughtful and gracious person, but also as a disciplined and impassioned scientist.

Finally, I would like to thank my parents, John and Barbara, and my siblings, Jeremy, Matthew, Joanna, and Bethany. You have to been there to support and guide me throughout my life. There is no greater gift than a family you can depend on.

Lausanne, 10 Fevrier 2018

Abstract

In the same year as Einstein's annus mirabilis, English engineer and physicist John Flemming patented the first rectifying diode, which he called the "Flemming valve". Einstein's work on the photoelectric effect would change our understanding of the nature of light - a pivotal moment in the development of quantum theory. Flemming's diode would transform our world as well, often pointed to as the beginning of modern electronics. These ideas, born in the same moment, have remained entwined. Quantum theory has been fundamental to transistor development, and that, in turn, led to the computer revolution and accompanying development of silicon manufacturing.

The theoretical and technological gifts these ideas have accumulated over the past hundred years are now laid to bare in the field of cavity optomechanics. The silicon technology that owes its very existence to quantum theory is now leveraged to test the limitations of theory and perhaps to exploit quantum resources for a new class of sensors. Micro-, and even nano-scale, optical cavities are coupled to commensurately miniaturized mechanical oscillators, where strong radiation pressure mediated interactions between their corresponding modes can be realized. The fluctuating position of a mechanical element is imprinted on the phase of light circulating within the cavity, while the varying amplitude of the light alters its momentum. Quantum fluctuations are imprinted on the mechanical element by light within the cavity, establishing correlations between its phase and amplitude. Utilizing the optomechanical system developed in this thesis work we are able to observe the signature of these induced correlations, even in the presence of thermal noise at room-temperature. Moreover, we demonstrate the principle by which correlations can be used to cancel measurement back-action, producing a quantum-enhanced sensitivity to external forces. The system in question is also demonstrated to achieve an imprecision more than three orders of magnitude below that at the standard quantum, at room-temperature, which is unprecedented.

A strong radiation pressure interaction between a micron-scale mechanical element and an optical cavity has been achieved by taking advantage of many of the powerful tools developed in the context of building modern computers. Using transistor technology in this new context we engineer an optomechanical system that exhibits an exceptionally large contribution of back-action relative to thermal noise. In addition to observing this back-action signature at ambient temperatures, the large interaction strength is applied to the task of laser cooling with a measurement-based feedback scheme. In this framework, we demonstrate the ability to reduce the thermal occupation of a cryogenically cooled mechanical mode by an additional

three orders of magnitude, to a mean occupancy of just 5.3 phonons.

Keywords: quantum measurement, room temperature cavity optomechanics, measurement back-action, quantum correlations

Résumé

Dans la même année que le célèbre annus mirabilis d'Einstein, l'ingénieur et physicien anglais John Flemming a breveté la première diode de redressement, qu'il a appelée la "valve Flemming". Le travail d'Einstein sur l'effet photoélectrique changerait notre compréhension de la nature de la lumière - un moment charnière dans le développement de la théorie quantique. La diode de Flemming transformerait aussi notre monde, souvent désigné comme le début de l'électronique moderne. Ces idées, nées au même moment, sont restées enlacées. La théorie quantique a été fondamentale pour le développement des transistors, ce qui a conduit à son tour à la révolution informatique et au développement de la fabrication du silicium.

Les dons théoriques et technologiques que ces idées ont accumulés au cours des cent dernières années sont maintenant mis à nu dans le domaine de l'optomécanique des cavités. La technologie du silicium qui doit son existence même à la théorie quantique est maintenant utilisée pour tester les limites de la théorie et peut-être pour exploiter les ressources quantiques pour une nouvelle classe de capteurs. Des cavités optiques à micro- et même à l'échelle nanométrique sont couplées à des oscillateurs mécaniques miniaturisés de manière communautaire, où de fortes interactions à médiation par pression de radiation entre leurs modes correspondants peuvent être réalisées. La position fluctuante d'un élément mécanique est imprimée sur la phase de lumière circulant dans la cavité, tandis que l'amplitude variable de la lumière modifie son moment. Les fluctuations quantiques sont imprimées sur l'élément mécanique par la lumière à l'intérieur de la cavité, établissant des corrélations entre sa phase et son amplitude. En utilisant le système optomécanique développé dans ce travail de thèse, nous sommes en mesure d'observer la signature de ces corrélations induites, même en présence de bruit thermique à température ambiante. De plus, nous démontrons le principe selon lequel les corrélations peuvent être utilisées pour annuler la backaction de mesure, produisant une sensibilité quantique accrue aux forces externes. On a également démontré que le système en question produisait une imprécision de plus de trois ordres de grandeur inférieure à celle du quantum standard, à la température ambiante, qui est sans précédent.

Une forte interaction de pression de radiation entre un élément mécanique à l'échelle micronique et une cavité optique a été obtenue en tirant parti de nombreux outils puissants développés dans le contexte de la construction d'ordinateurs modernes. En utilisant la technologie des transistors dans ce nouveau contexte, nous développons un système optomécanique qui présente une contribution exceptionnellement importante de la réaction au bruit thermique. En plus d'observer cette signature de backaction à des températures ambiantes, la grande force d'interaction est appliquée à la tâche de refroidissement laser avec un système de retour basé sur la mesure. Dans ce cadre, nous démontrons la capacité de réduire l'occupation thermique d'un mode mécanique refroidi cryogéniquement de trois ordres de grandeur supplémentaires, pour une occupation moyenne de seulement 5,3 phonons.

Mots clefs : Mesure quantique, optomécanique de cavité à température ambiante, backaction de mesure, corrélations quantiques

Contents

List of Figures

Symbols

Symbol	Meaning
C	Multi-photon cooperativity, $C = C_0 n_\mathrm{c}$
C_0	Single-photon cooperativity, $C_0 = 4g_0^2/(\kappa\Gamma_\mathrm{m})$
G	Optical frequency shift per displacement, $D = \partial\omega_\mathrm{c}/\partial x$
g_0	Single-photon optomechanical coupling strength, $g_0 = G \cdot x_\mathrm{ZPF}$
m_eff	Effective mass of the mechanical oscillation
n_imp	Imprecision noise expressed in phonon-equivalent units, $n_\mathrm{imp} = (16\eta_\mathrm{c} C_0 n_\mathrm{c})^{-1}$
n_qba	Quantum back-action noise expressed in phonon-equivalent units, $n_\mathrm{qba} = C_0 n_\mathrm{c}$
n_c	Intracavity photon number
n_th	Phonon occupation in thermal equilibrium, $n_\mathrm{th} = (e^{\hbar\Omega_\mathrm{m}/(k_\mathrm{B}T)} - 1)^{-1} \approx k_\mathrm{B}T/(\hbar\Omega_\mathrm{m})$
Q_m	Mechanical quality factor, $Q_\mathrm{m} = \Omega_\mathrm{m}/\Gamma_\mathrm{m}$
S_a	Single-sided spectral density only evaluated for $\Omega > 0$, $S_a(\Omega) = 2 \cdot \bar{S}_{aa}(\Omega)$
$S_{aa}(\Omega)$	Double-sided spectral density, $S_{aa}(\Omega) = \int_{-\infty}^{\infty} \mathrm{d}\tau \, \langle a(t)a(t+\tau)\rangle \, e^{i\Omega\tau}$
$\bar{S}_{aa}$	Symmetrized spectral density, $\bar{S}_{aa} \equiv (S_{aa}(\Omega) + S_{aa}(-\Omega))/2$
x_ZPF	Zero-point fluctuations of the mechanical resonator, $x_\mathrm{ZPF} = \sqrt{\hbar/(2m_\mathrm{eff}\Omega_\mathrm{m})}$
Γ_eff	Effective damping rate in the case of dynamical back-action (DBA)
Γ_m	Mechanical damping rate
Δ	Laser detuning, $\Delta = \omega_\mathrm{l} - \omega_\mathrm{c}$
η_c	Optical coupling efficiency, $\eta_\mathrm{c} = \kappa_\mathrm{ex}/\kappa$
κ	Total cavity decay rate, $\kappa = \kappa_0 + \kappa_\mathrm{ex}$
κ_0	Intrinsic loss rate of the cavity
κ_ex	Loss rate of the cavity from external coupling
$\chi_x(\Omega)$	Mechanical susceptibility, $\chi_x(\Omega) = \left(m_\mathrm{eff}(\Omega_\mathrm{m}^2 - \Omega^2 - i\Omega\Gamma_\mathrm{m})\right)^{-1}$
Ω_eff	Dynamical back-action spring shift
Ω_m	Mechanical resonance frequency
ω_c	Cavity resonance frequency
ω_L	Laser frequency

1 Introduction

Figure 1.1 – **Comet Hale-Bopp:** Ionized gas tail is seen in blue and dust tail in white. The gas component is acted up by solar wind (plasma), while the neutral dust tail only experiences the radiation pressure force [1].

The field of optomechanics, in which the work described here is grounded, centers around a rather subtle and yet profoundly powerful aspect about the way electromagnetic radiation interacts with matter. This is the fact that electromagnetic waves carry momentum and this momentum is transferred to matter upon reflection or absorption. The resulting force, known as radiation pressure, is so subtle that if one could survive standing in front on a light source with an intensity equivalent to that at the surface of the sun they could scarcely claim to feel the force, which would amount to the weight of about four sheets of paper. This force is so inconspicuous that its signature was first recognized just 400 years ago by the astronomer Johannes Kepler, in observing that the tails of comets consistently point away from the sun. He speculated that light from the sun must be exerting pressure on these comet tails. He was right, although it would be 243 years later when James Clerk Maxwell, upon publishing the famous equations that bear his name, provided a theoretical framework for this observation. It would be yet another 38 years before this effect could be proven experimentally, by physicist Pyotr Lebedev. His proof came in the observation that a large light weight mirror attached to a low friction spindle rotates when illuminated with a high intensity light. The experimental device, called a radiometer, had been invented almost thirty years earlier but radiation pressure had remained elusive.

It would not be until the advent of the laser in 1960 that radiation pressure would become a force to contend with - both as an experimental resource and a limitation to precision measurements. High intensity coherent light sources would become a very important tool in coaxing this force from obscurity. In parallel, an understanding of the frictional force that an electromagnetic field exerts within a resonator would be critical to the development of optomechanics. Physicist Vladimir Braginsky realized that the finite build up time of the field within such a resonator allows it to perform mechanical work. This principle could be used to reduce or amplify motion via the radiation pressure interaction. One very powerful use of this principle was to diminish the thermally driven motion of an oscillator – a technique known as *laser cooling*.

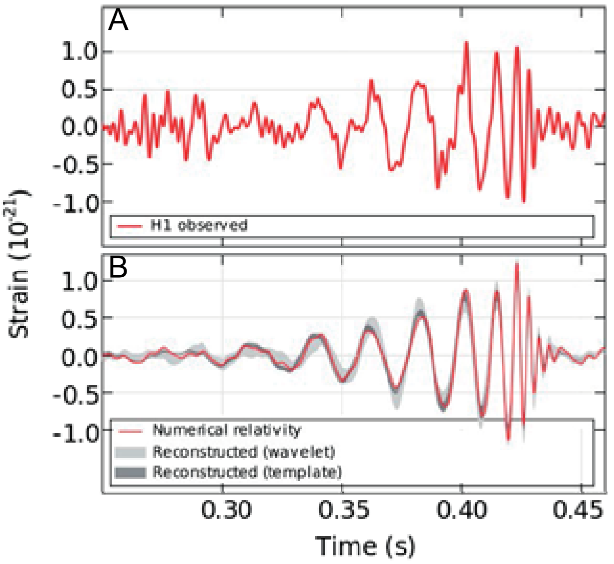

Figure 1.2 – **LIGO measurement of gravitational waves (Hanford):** September 14, 2015. The first detection of gravitational waves, resulting from the merger of two black holes with masses ~30 times that of the sun, ~1.4 billion light years from earth. Measurement data in (A) and numerical model in (B) [2].

Braginsky also the realized that radiation pressure set a fundamental limit on precision optical measurements. His work in this direction was fundamental to the development of gravitational wave interferometers. These large-scale precision measurement systems are essentially very large Fabry-Pérot cavities (section 1.1.2), composed of two mirrors several kilometers apart with a high intensity optical field circulating between them. Photons make hundreds of round trips between the mirrors before exiting the cavity and this makes them extremely sensitive to a change its length. Such systems have been specifically developed to search for gravitational waves, which very slightly alter the length of the cavity. However, in this context radiation pressure has a counterproductive effect in that it imparts a random force on the end mirrors due to quantum fluctuates of the light field. Through careful study of this effect and painstaking development of the mechanical systems that support the end mirrors a system was developed with sufficient sensitivity to detect the first gravitational waves in 2016 [3]. This wave resulted from the merging of two black holes, ~1.4 billion light years away, which caused a change in length to the 4 km Laser Interferometer Gravitational-Wave Observatory (LIGO) interferometer by approximately one billionth of a nanometer. This exquisitely precise measurement apparatus provides a completely new way of observing the universe, and the implications it will have for astronomy can only be guessed at.

In contrast to LIGO, the field of optomechanics generally has the goal of using radiation pressure as a resource to laser cool microscopic objects and to study quantum effects. To this end laser cooling of cryogenically pre-cooled optomechanical systems into the ground state (here defined as an average phonon occupancy less than unity) has been achieved in a number of different system configurations. This goal, however, remains outstanding at room-temperature. The generation of squeezed light in optomechanical systems, which results when radiation pressure induced fluctuations resulting from quantum noise dominate over thermal fluctuations, has also been observed in cryogenically pre-cooled devices (including the one developed in this thesis). This effect also remains to be demonstrated at room-temperature.

Another goal which applies to optomechanics as a practical sensing technology is that of making a (near) ideal measurement. That is to say one that approaches Heisenberg's uncertainty limit, which states the minimum achievable product of measurement force noise and read out noise. To this author's knowledge the system in this thesis has been demonstrated to come closest to this limit, both at cryogenic-temperature (chapter 5) and room-temperature (chapter 2). This result, in addition to the ability to functionalize the mechanical resonator in order to couple to external forces (see chapter 6) makes this system compelling as a practical high precision, micro-scale transducer.

The remainder of this chapter lays out the conceptual framework with which to understand the basis of optomechanics and the dynamical back-action that arises in such systems. Chapter 2 describes the specific implementation of a near-field optomechanical device, as developed in this thesis. In this chapter the relevant properties of the system are explored conceptually as well as experimentally. Chapter 3 details the fabrication process used to realize the system described in chapter 2 and provides a conceptual background to the processes used in fabrication. Observation for the first time at room-temperature, of correlations between the quadratures of light, driven by quantum fluctuations, is described in chapter 4. In chapter 5, an experiment performed at cryogenic temperatures (4K) to exploit the high coupling efficiency of this system to implement measurement based feedback cooling (cooling via an external feedback loop) to an unprecedented occupancy with such a technique, of ~5 phonons, is detailed. Finally, chapter 6 describes recent advances in engineering of low dissipation nanobeams that can be exploited to significantly improve the current system, as well as a fabrication method developed to utilize the existing system as an electrometer. In addition, some concepts for improving the optomechanical coupling rate are discussed.

1.1 Cavity optomechanics

The following sections provide a conceptual overview of an optomechanical system composed of a mechanical oscillator coupled to an optical resonator by radiation pressure. First the salient attributes of a damped harmonic oscillator are explored, and its equation of motion is transformed to a power spectral representation of displacement. Consideration is given to the role of thermal fluctuations in driving the oscillator's motion and the limitations this implies to its use as a practical sensor are briefly discussed. A waveguide coupled optical cavity is described next and input-output formalism is used to quantify the output power from this coupled system, in terms of the cavity parameters. Brief discussion is given to how coupling is achieved experimentally as well as the various accessible coupling regimes. In the last section we describe the situation where a mechanical resonator is dispersively coupled to an optical cavity. We explore the dynamics that arise as a result of the finite response of radiation pressure within the cavity to mechanical fluctuations and briefly discuss the practical implications of these dynamics.

1.1.1 Damped mechanical oscillators

Consider a simple harmonic oscillator, with a single resonance frequency at Ω_m, an effective mass m_eff, and a non-zero dissipation given by the rate Γ_m. The equation describing its motion along the coordinate x, written in terms of a time-dependent force, $F(t)$,is

$$\frac{\mathrm{d}^2 x(t)}{\mathrm{d}t^2} + \Gamma_\mathrm{m}\frac{\mathrm{d}x(t)}{dt} + \Omega_\mathrm{m}^2 x(t) = \frac{F(t)}{m_\mathrm{eff}} \tag{1.1.1}$$

where $\Omega_\mathrm{m} = \sqrt{k/m_\mathrm{eff}}$ is strictly speaking the undamped resonance frequency in angular units. The dissipation rate multiplied by the resonator mass, $\Gamma_\mathrm{m} m_\mathrm{eff}$, can be understood as a coefficient of friction opposing the oscillator's motion. This produces an exponential decay in the oscillators amplitude of motion, with decay constant $\lambda = \Gamma_\mathrm{m}/2$. Damping also causes a modification of the resonance frequency $\Omega_{\mathrm{m},\Gamma_\mathrm{m}} = \Omega_\mathrm{m}\sqrt{1-\zeta^2}$, with $\zeta = \lambda/\Omega_\mathrm{m}$ known as the damping coefficient. For practical oscillators that we are interested in, with very weak damping $\zeta \ll 1$, we can ignore this modification. However, the damping factor is of great relevance in defining how close the system approximates an ideal undamped oscillator ($\zeta = 0$), and this is normally expressed as a *quality factor* (Q). The Q defines the ratio of energy stored in the oscillator to energy lost per cycle

$$Q \equiv \frac{1}{2\zeta} = \frac{\Omega_\mathrm{m}}{\Gamma_\mathrm{m}} \tag{1.1.2}$$

where the stored energy is multiplied by a factor of 2π to allow for the simple expression in terms of oscillation frequency. The dissipation rate represents the sum total of dissipation channels, such as coupling to the point(s) at which it is anchored (radiation loss), interaction with the surrounding gas, and intrinsic material losses (e.g. thermoelastic damping). As will be explored in section 2.1.1, in the case of silicon nitride nanobeams used in this thesis the latter is the dominant loss mechanism.

In eq. (1.1.1) effective mass is used for convenience as we would like to model the mechanical devices we work with in terms of a simple harmonic oscillator and this description applies to point-like masses. In this thesis a range of physical oscillators with varying geometry and non-trivial displacement profiles are used. The effective mass allows an arbitrary mode of an arbitrarily shaped mechanical system to be treated as a point-like oscillator. A mechanical system with uniform density, ρ, can be reduced to a point-like oscillator at point p by calculating the energy stored in the displacement profile, $u(x,y,z)$, normalized to the displacement at p, $u(p)$

$$m_{\mathrm{eff}} = \frac{\int_V \rho |u(x,y,z)|^2 dxdydz}{|u(p)|^2} \tag{1.1.3}$$

Clearly it is advantageous to choose a point of interaction where the displacement is maximum, as is rather intuitive. Near nodes the effective mass will tend towards infinity as is explored in section 2.2.6. In section 2.2.6 the normalization factor is weighted over the region of optical coupling, but the same behavior emerges for modes with antisymmetric displacement centered in the coupling region.

Returning to equation eq. (1.1.1), we would like to transform to the frequency domain which provides a convenient algebraic representation for the differential equation and corresponds to quantities dealt with in experiment. Thus we apply the Fourier transformation, $x(\Omega) = \int_{-\infty}^{\infty} \mathrm{d}t x(t) e^{i\Omega t}$, to eq. (1.1.1), finding the solution

$$x(\Omega) = \chi_x(\Omega) F(\Omega) \tag{1.1.4}$$

Which relates displacement, $x(\Omega)$, to an applied force, $F(\Omega)$, by a transfer function known as the mechanical susceptibility,

$$\chi_x(\Omega) = \frac{1}{m_{\mathrm{eff}}(\Omega_{\mathrm{m}}^2 - \Omega^2 - i\Omega\Gamma_{\mathrm{m}})} \tag{1.1.5}$$

It is useful to transform eq. (1.1.4) into the experimentally relevant units of power spectral density (from here on referred to as the power spectrum or just spectrum where it is clearly understood), which represents the average signal power distributed in frequency space. Here we will apply a convenient transformation known as Wiener–Khinchin theorem [4], which states that the autocorrelation of a function describing a stochastic process with a constant mean (weak-sense stationary) is simply given by the Fourier transform of the absolute square of that function in frequency space. Since we would like to take the Fourier transform of the autocorrelation function, in order to arrive at units of power spectrum, we can use the simple (Wiener–Khinchin) relation that

$$S_{aa}(\Omega) = \int_{-\infty}^{\infty} (a(t) \star a(t)) e^{i\Omega\tau} \mathrm{d}\tau = |(a(\Omega)|^2 \tag{1.1.6}$$

with $\star$ denoting the cross-correlation. Making use of this convenient representation eq. (1.1.4) can be written as a power spectrum, with the resulting expression

$$\begin{align} S_{xx}(\Omega) &= \left|\chi_x(\Omega)\right|^2 S_{FF}(\Omega) \tag{1.1.7} \\ &= \frac{1}{m_{\mathrm{eff}}^2 \left[(\Omega_{\mathrm{m}}^2 - \Omega^2)^2 + \Gamma_{\mathrm{m}}^2 \Omega^2\right]} S_{FF}(\Omega) \tag{1.1.8} \end{align}$$

In optomechanics, as well as in sensing applications in general, we are interested in the thermal force acting on the oscillator. This can be analyzed using fluctuation dissipation theorem, where the fluctuations arise from Brownian motion and the dissipation results from losses in the oscillator, Γ_{m}. Such analysis was carried out by Saulson [5] applied to low dissipation oscillators, finding the resulting thermal force power spectrum

$$S_{FF}^{\mathrm{th}}(\Omega) = -\frac{2k_{\mathrm{B}}T}{\Omega} \mathrm{Im}\left(\frac{1}{\chi_x(\Omega)}\right) \tag{1.1.9}$$

Substituting eq. (1.1.5) into eq. (1.1.9), we end up with a rather simple expression for the thermal driving force

$$S_{FF}^{\mathrm{th}} = 2 m_{\mathrm{eff}} \Gamma_{\mathrm{m}} k_{\mathrm{B}} T \tag{1.1.10}$$

Now we can write an expression for the thermally driven amplitude fluctuations of a damped harmonic oscillator in terms of a power spectrum, using eq. (1.1.7)

$$S_{xx}^{\mathrm{th}}(\Omega) = \frac{2\Gamma_{\mathrm{m}} k_{\mathrm{B}} T}{m_{\mathrm{eff}} \left[(\Omega_{\mathrm{m}}^2 - \Omega^2)^2 + \Gamma_{\mathrm{m}}^2 \Omega^2\right]} \tag{1.1.11}$$

In optomechanics we are generally interested in a high sensitivity to the thermal forces (which correspondingly implies a high sensitivity to radiation pressure). In other words, we would like to maximize the thermally generated displacement spectrum S_{xx}^{th}. Let us consider the displacement on resonance,

$$S_{xx}^{\mathrm{th}}(\Omega_\mathrm{m}) = \frac{2k_\mathrm{B}T}{m_\mathrm{eff}\Gamma_\mathrm{m}\Omega_\mathrm{m}^2} \tag{1.1.12}$$

It immediately becomes clear why there is a large degree of interest in working with oscillators that minimize both the dissipation rate and effective mass.

Sensing applications in the presence of thermal noise

When considering the ultimate sensitivity of a damped mechanical oscillator to external force, it is instructive to consider the scaling of the displacement spectrum generated by the force, S_{xx}^{ext}, relative to that driven by thermal fluctuations, S_{xx}^{th}. In this context we consider a scheme where optomechanical coupling is used to read out the displacement of an oscillator (as described in chapter 2) to which a force of interest has been coupled. An example of such a system in described in section 6.3. In that specific implementation a dielectrophoretic force is applied to an oscillator, by means of placing electrodes on either side of a nanobeam such that an electric field gradient can be generated across it. A similar example would involve placing one plate of a capacitor on the nanobeam, with the other fixed above or below. An electrostatic force generated between the plates would lead to a displacement of the beam. In a context such as this we are interested in the ratio

$$\frac{S_{xx}^{\mathrm{ext}}(\Omega)}{S_{xx}^{\mathrm{th}}(\Omega)} = \frac{1}{2k_\mathrm{B}Tm_\mathrm{eff}\Gamma_\mathrm{m}}S_{FF}^{\mathrm{ext}}(\Omega) = \frac{Q}{2k_\mathrm{B}Tm_\mathrm{eff}\Omega_\mathrm{m}}S_{FF}^{\mathrm{ext}}(\Omega) \tag{1.1.13}$$

Clearly lower temperatures increase sensitivity but in practical situations we can assume this is not a free parameter. Let's assume, for example, that the device in section 6.3 is intended to be operated at ambient temperatures. Lower resonant frequencies apparently increase the relative sensitivity to an external forces, but one must consider that effective mass tends to scale inversely proportional with resonant frequency. In the case of the high-stress nanobeams, described in section 2.1.1, since $\Omega_\mathrm{m} \propto L^{-1}$ and $m_\mathrm{eff} \propto L$, if we assume a fixed thickness and width, then the ratio $m_\mathrm{eff}\Omega_\mathrm{m}$ is constant. When ignoring the effect on optomechnical coupling (section 2.2) or external force coupling, it's clear that minimizing the width and thickness is advantageous. However, these parameters will be largely defined in terms of optimizing coupling coefficients and can also assumed to be fixed in this context. This leaves the Q parameter, which can be understood to represent the degree to which the oscillator is decoupled from the thermal environment.

From the above considerations, it seems that one would like to simply maximize the Q in order to maximize sensitivity, which would imply going to arbitrarily low frequencies. However, for a practical sensor the frequency is generally set by the desired bandwidth. Note that the ratio in eq. (1.1.15) applies irrespective of the external force frequency, Ω. However, if we consider the condition that the external force is at $\Omega \gg \Omega_\mathrm{m}$, then the mapping of force spectrum to the displacement spectrum scales as

$$S_{xx}^{\mathrm{ext}}(\Omega \gg \Omega_\mathrm{m}) \approx \frac{1}{m_{\mathrm{eff}}^2 \Omega^4} S_{FF}^{\mathrm{ext}}(\Omega \gg \Omega_\mathrm{m}) \tag{1.1.14}$$

The transduction drops off rapidly above the resonance frequency and so it is not reasonable to operate a sensor above resonance. On the other hand for $\Omega \ll \Omega_\mathrm{m}$ the transduction is independent of frequency but is reduced relative to that on resonance by

$$\frac{S_{xx}^{\mathrm{ext}}(\Omega \ll \Omega_\mathrm{m})}{S_{xx}^{\mathrm{ext}}(\Omega = \Omega_\mathrm{m})} \approx \frac{\Gamma_\mathrm{m}^2}{\Omega_\mathrm{m}^2} = \frac{1}{Q^2} \tag{1.1.15}$$

So for broadband sensing at the thermal limit, it is required that the thermal displacement spectrum can resolved at a level of $1/Q^2$ below that on resonance. Moreover, to minimize the thermal noise floor, Q should be made as high as possible. This implies that working to minimize imprecision in the displacement readout is a highly productive endeavor. This concept is explored at the end of chapter 2.

1.1.2 Optical cavities

Here the idea of an optical cavity is introduced. In analogy to the mechanical resonators discussed in the previous section, an optical cavity causes photons to circulate along a fixed path, much as a mass element retraces its path in the mechanical counterpart. Likewise, the rate at which a round trip on the path is completed defines the resonance frequency, ω (in this work ω for the optical case and Ω for the mechanical case). Further, the amplitude of the resonant mode is dissipated at κ (Γ for mechanics). When an optical cavity resonance is modulated by a mechanical oscillator (see section 1.1.3), the coupled resonator arrangement known as an optomechanical system is formed.

Optical cavities come in many different forms, but probably the most elementary example is that of a Fabry-Pérot cavity. This arrangement, illustrated in fig. 1.3, consists of two highly reflective mirrors facing each other. A photon traveling within the cavity on a path normal to the mirror will undergo multiple reflections before either being transmitted through the mirror or undergoing dissipation (e.g. by absorption in the mirror coating). When the path length between the mirrors, L, is an integer multiple of the optical frequency, constructive interference will cause power to build up in the cavity. For a Fabry-Pérot cavity in vacuum its resonant frequencies are thus defined by

$$\omega_\mathrm{m} \approx m\pi \frac{c}{L} \tag{1.1.16}$$

with m being an integer and c the speed of light.

The type of optical cavity used in this thesis is known as a whispering gallery mode (WGM) resonator. This obscure sounding name originates from Lord Rayleigh's description of the uncanny ability to hear the whispers of someone far away in the circular gallery of St Paul's Cathedral, in London (this type of gallery also exists in many other places, e.g. the Temple of Heaven in Beijing). This phenomenon is equivalent to that described above for Fabry-Pérot cavities. In this case acoustic waves are reflected along the wall of the gallery and those frequencies that undergo an integer number of oscillations while traveling the perimeter are amplified. In the case of St Paul's Cathedral resonant modes occur in acoustic band. A WGM optical cavity, such as the microdisk shown in fig. 2.3(A), is exactly analogous to this with photons being guided around the perimeter by total internal reflection. In the case of an optical WGM cavity the resonant modes are given by

$$\omega_\mathrm{m} \approx m\frac{c}{nR} \tag{1.1.17}$$

with R being the resonator's radius and n the index of refraction for the resonator material. To describe the resonant modes of St Paul's Cathedral, n would be set to 1 and c becomes the speed of sound.

Optical cavities coupled to a waveguide

Here we introduce the analytical description of an optical cavity (resonator) coupled to waveguide at a rate, κ_ext. The resonator is pumped via the waveguide, with the mode amplitude in the waveguide given by the time varying complex scalar value, $\tilde{s}_\mathrm{in}(t)$. This amplitude is normalized such that $|\tilde{s}_\mathrm{in}(t)|^2$ has units of power. The amplitude of the mode in the resonator, also represented by a complex scalar value $\tilde{a}(t)$, is normalized such that $|\tilde{a}(t)|^2$ has units of energy. This stored energy decays at a rate given by κ, which combines intrinsic loss within the resonator, κ_0, and loss to the waveguide, κ_ex. Thus the total resonator loss rate is $\kappa = \kappa_0 + \kappa_\mathrm{ex}$.

The coupled-mode representation used here exactly describes the time evolution of this coupled system, assuming the input state is quantum white noise [6, 7]. This description is derived from the Hamiltonian description of a system interacting with a thermal bath, from which the quantum Langevin equations are developed. Time reversal symmetry is applied to describe the time evolution of the coupled-mode system, in terms of the resonant mode of the cavity, ω_c,

$$\frac{\mathrm{d}\tilde{a}(t)}{\mathrm{d}t} = -\left(i\omega_\mathrm{c} + \frac{\kappa}{2}\right)\tilde{a}(t) + \sqrt{\kappa_\mathrm{ex}}\tilde{s}_\mathrm{in}(t) \tag{1.1.18}$$

We note that the mode energy, $|\tilde{a}(t)|^2$, when rescaled by the per photon energy, $\hbar\omega$, expresses the photon number in the cavity. Likewise, rescaling the input power, $|\tilde{s}_\mathrm{in}(t)|^2$, gives units of photon flux. The input amplitude is assumed to be composed of slowly and rapidly varying components. The rapidly varying component oscillates at the laser frequency, ω_{L}, and the slowly varying component arises from factors such as adjustment of the laser power, with $\tilde{s}_{\mathrm{in}}(t) \equiv s_{\mathrm{in}}(t)e^{-i\omega_{\mathrm{L}}t}$. Assuming the second component varies much more slowly than ω_{L}, a convenient transform known as the *rotating wave approximation* can be used. Here the cavity amplitude is described in a frame rotating at the laser drive frequency, $\tilde{a}(t) \equiv a(t)e^{-i\omega_{\mathrm{L}}t}$, and as such the cavity time evolution can be described in this frame as

$$\frac{\mathrm{d}a(t)}{\mathrm{d}t} = \left(i\Delta - \frac{\kappa}{2}\right) a(t) + \sqrt{\kappa_{\mathrm{ex}}} s_{\mathrm{in}}(t) \tag{1.1.19}$$

with the difference in frequency between the driving field and the cavity resonance captured by the detuning,

$$\Delta = \omega_{\mathrm{L}} - \omega_{\mathrm{c}} \tag{1.1.20}$$

A positive value of Δ is typically referred to as *blue detuning*, indicating a higher relative energy for the drive, and conversely a negative value is referred to as *red detuning*. Note that the subscript L indicates that the driving field is normally supplied by a laser.

For a constant driving amplitude, $s_{\mathrm{in}}(t) \equiv \bar{s}_{\mathrm{in}}$, the cavity amplitude settles to the steady state with a decay constant $\tau = 2/\kappa$. For $t \gg \tau$ the steady state amplitude, $\bar{a}$, is

$$\bar{a} = \frac{1}{-i\Delta + \kappa/2} \sqrt{\kappa_{\mathrm{ex}}} \bar{s}_{\mathrm{in}} \tag{1.1.21}$$

In the steady state we can easily solve for power in the cavity in terms of the time it takes for photons to make on round trip, τ_{rt}.

$$|\bar{s}_{\mathrm{cav}}|^2 = \frac{|\bar{a}|^2}{\tau_{\mathrm{rt}}} = \frac{1}{\tau_{\mathrm{rt}}(\Delta^2 + (\kappa/2)^2)} \kappa_{\mathrm{ex}} |\bar{s}_{\mathrm{in}}|^2 = \frac{4\eta_{\mathrm{c}}}{\tau_{\mathrm{rt}}\kappa(1 + 4\Delta^2/\kappa^2)} |\bar{s}_{\mathrm{in}}|^2 \tag{1.1.22}$$

In the form on the right hand side the quantity $\eta_{\mathrm{c}} \equiv \frac{\kappa_{\mathrm{ex}}}{\kappa}$ is introduced. This is the so-called coupling parameter, which is a convenient way to express the coupling regime in which the cavity is being operated. This will be returned to, but first we introduce another parameter to generalize the expression above. This parameter is the finesse and it defines the average number of rounds trips a photon in the cavity undergoes before being out-coupled to the waveguide or dissipated

$$\mathscr{F} = \frac{1}{\tau_{\mathrm{rt}}} \frac{2\pi}{\kappa} \tag{1.1.23}$$

Expressing eq. (1.1.22) in terms of finesse gives

$$|\bar{s}_{\text{cav}}|^2 = \mathscr{F}\frac{2\eta_\text{c}}{\pi(1+4\Delta^2/\kappa^2)}|\bar{s}_{\text{in}}|^2 \tag{1.1.24}$$

For a *critically coupled* cavity, $\eta_\text{c} = 1/2$ ($\kappa_{\text{ex}} = \kappa_0$), and input drive tuned to cavity resonance ($\Delta = 0$), $\mathscr{F}/\pi$ quantifies the enhancement of power circulating within the cavity relative to the input power.

To determine the transmitted field amplitude, $\bar{s}_{\text{out}}$, from the cavity-coupled waveguide, the input-output relation [6] is used, applied to the steady state amplitudes,

$$\bar{s}_{\text{out}} = \bar{s}_{\text{in}} - \kappa_{\text{ex}}\bar{a} = \frac{(1-2\eta_\text{c})\kappa/2 - i\Delta}{\kappa/2 - i\Delta}\bar{s}_{\text{in}} \tag{1.1.25}$$

and the transmitted power is found to be

$$|\bar{s}_{\text{out}}|^2 = \left(1 - \frac{\eta_\text{c}(1\eta_\text{c})\kappa^2}{\Delta^2+(\kappa/2)^2}\right)|\bar{s}_{\text{in}}|^2 \tag{1.1.26}$$

Which defines the characteristic Lorentzian lineshape, producing a reduction in transmission through the waveguide, with a full width at half maximum of κ.

Returning to the coupling parameter, η_c, we consider the effect of varying this parameter in the case of resonant coupling ($\Delta = 0$). In practice varying η_c is accomplished by varying the waveguide coupling rate, κ_{ext}. The way this is done in the experiments described in this thesis, is by means of an optical fiber that has been locally thinned by with a focused heat source (typically a small torch). The glass is melted locally and the ends of the fiber are pulled, causing it to thin. This *tapered fiber* is reduced to a diameter similar to the thickness of the microdisks to which it is coupled. Since both the fiber and microdisk are composed of SiO_2, this allows for synchronous coupling (i.e. the propagation constants are matched).

The fiber is positioned relative to the cavity using piezo actuators with nanometer-level precision. In this way κ_{ext}, which has an exponential dependence on the distance from the cavity, can be sensitively adjusted. In the case of critical coupling, where $\eta_\text{c} = 1/2$, we can see from eq. (1.1.26) that the transmitted power is zero. In this case the power being coupled out of the cavity is exactly equal to the pump power but with a π phase shift, leading to destructive interference. Operating with $0 < \eta_\text{c} < 1/2$ is known as *undercoupled* and results in power exiting the cavity being lower than the pump power. The *overcoupled* condition, $1/2 < \eta_\text{c} < 1$ leads to higher power exiting the cavity. Generally in optomechanics the operation point is near the critically coupled regime, achieving a balance between reduction in finesse and photon collection efficiency. In this case the transmitted light consists only of photons that have undergone an addition phase shift imparted by the mechanical element (of course

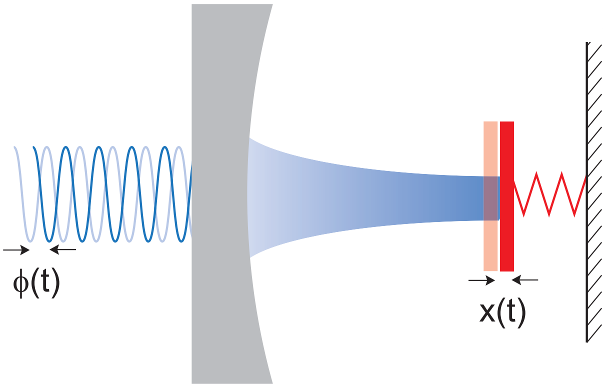

Figure 1.3 – **Cavity optomechanics:** the canonical picture, where the oscillating position, $x(t)$, of one end mirror in a Fabry-Pérot cavity imparts a phase shift, $\phi(t)$, on light that exits.

assuming perfectly ideal conditions). Of course, in this case half the photons will be lost to internal dissipation. In some scenarios overcoupling is desired in order to have a higher efficiency in recovering photons. However, this also implies a reduction to the cavity finesse.

1.1.3 Cavity optomechanics

Dispersive optomechanical coupling arises in the situation where the frequency of an optical cavity is modulated by the displacement of a mechanical object. Typically we consider the coupling between a single resonant mode of the cavity and the mechanical system. This is canonically described in terms of a Fabry-Pérot cavity with one fixed end mirror and one that is free to move along the cavity's axis, as illustrated in fig. 1.3. The mirror and spring form a simple harmonic oscillator with a time dependent displacement, $x(t)$. We assume the cavity frequency, $\omega(t)$, has a linear dependence on the mirror's position described by

$$\omega_{\mathrm{c}}(t) = \omega_{\mathrm{c}} + Gx(t) \tag{1.1.27}$$

where ω_{c} is the cavity frequency given for the equilibrium position of the end mirror, $x = 0$, and the optomechanical coupling constant is,

$$G = \frac{\partial \omega_{\mathrm{c}}}{\partial x} \tag{1.1.28}$$

defining the cavity frequency dependence on the end mirror's displacement. For a Fabry-Pérot cavity, with $\omega_c = \pi c/L$, this constant (often referred to as the *frequency pull parameter*) is $G = -\omega_{\mathrm{c}}/L$.

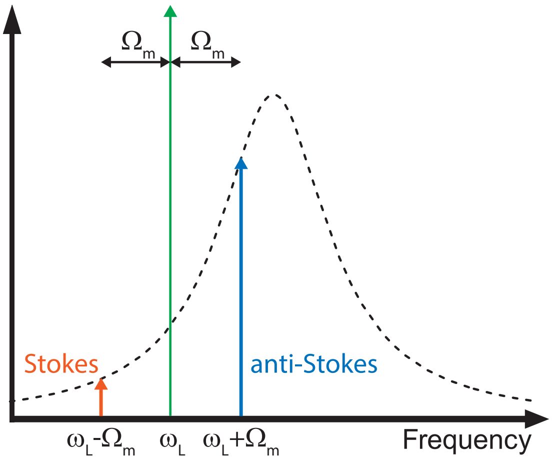

Figure 1.4 – **Optomechanical cavity response to a detuned drive:** A detuned drive laser, at ω_L, imparts mechanical mediated sidebands, weighted by the cavity response.

Dispersive coupling in the absence of radiation pressure

In the situation above photons circulating in the cavity carry a momentum $\hbar k$ (with $k = \omega_\mathrm{c}/c$), and clearly momentum transfer to the movable mirror will contribute to its displacement. However, to begin with we consider only the mechanical mode's effect on the optical cavity's amplitude. Assuming a monochromatic, constant amplitude drive at frequency ω_L and rewriting the cavity amplitude equation of motion from eq. (1.1.18), to include the frequency pulling parameter, we have

$$\frac{\mathrm{d}a(t)}{\mathrm{d}t} = \left(-i\left(\omega_\mathrm{c} + Gx(t)\right) - \frac{\kappa}{2}\right) a(t) + \sqrt{\kappa_\mathrm{ex}}\bar{s}e^{-i\omega_\mathrm{L}t} \tag{1.1.29}$$

with $\kappa = \kappa_0 + \kappa_\mathrm{ex}$, as before. We now consider that the mechanical displacement is described by a simple harmonic mode at Ω_m, with amplitude x_0, giving $x(t) = x_0 \sin(\Omega_\mathrm{m} t)$. In this case the differential equation can be solved in terms of Bessel functions of the first kind [8]. For small displacements the solution can be approximated by the first two terms

$$a(t) \approx a_0(t) + a_1(t) \tag{1.1.30}$$

$$a_0(t) = \frac{\sqrt{\kappa_\mathrm{ex}}\bar{s}}{-i\Delta + \kappa/2} e^{-i\omega_\mathrm{L}t} \tag{1.1.31}$$

$$a_1(t) = \frac{Gx_0}{2} \frac{\sqrt{\kappa_\mathrm{ex}}\bar{s}}{-i\Delta + \kappa/2} \left(\underbrace{\frac{e^{-i(\omega_\mathrm{L}+\Omega_\mathrm{m})t}}{-i(\Delta + \Omega_\mathrm{m}) + \kappa/2}}_{\text{anti-Stokes}} - \underbrace{\frac{e^{-i(\omega_\mathrm{L}-\Omega_\mathrm{m})t}}{-i(\Delta - \Omega_\mathrm{m}) + \kappa/2}}_{\text{Stokes}} \right) \tag{1.1.32}$$

with $\Delta = \omega_\mathrm{L} - \omega_\mathrm{c}$, also as before. Here the first term, $a_0(t)$, is simply the steady state cavity pumping term that was found in section 1.1.2. The second term, $a_1(t)$, gives the mechanically modulated amplitude that produces a pair of sidebands, offset from the pump frequency at $\omega_\mathrm{L} - \Omega_\mathrm{m}$ and $\omega_\mathrm{L} + \Omega_\mathrm{m}$. The relative contribution of these sidebands, typically referred to as Stokes and anti-Stokes, depends on the drive detuning, Δ, the mechanical frequency, Ω_m, and the cavity decay rate, κ. This picture of sideband generation is illustrated in fig. 1.4. Further insight into the role the sidebands play is gained when considering the modulation of cavity power

$$\begin{aligned}|a(t)|^2 \approx & |a_0(t)|^2 + a_0(t)a_1^*(t) + a_0^*(t)a_1(t)\\ = & \frac{\kappa_\mathrm{ex}|\bar{s}|^2}{\Delta^2 + (\kappa/2)^2}\Bigg(1+\\ & Gx_0\left(\frac{\Delta+\Omega_\mathrm{m}}{(\Delta+\Omega_\mathrm{m})^2+(\kappa/2)^2} + \frac{\Delta-\Omega_\mathrm{m}}{(\Delta-\Omega_\mathrm{m})^2+(\kappa/2)^2}\right)\sin(\Omega_\mathrm{m}t)+\\ & Gx_0\left(\frac{\kappa/2}{(\Delta+\Omega_\mathrm{m})^2+(\kappa/2)^2} - \frac{\kappa/2}{(\Delta-\Omega_\mathrm{m})^2+(\kappa/2)^2}\right)\cos(\Omega_\mathrm{m}t)\Bigg)\end{aligned} \tag{1.1.33}$$

We see that the cavity power is modulated at the mechanical frequency, with one component acting in phase and one in quadrature (orthogonal) with the mechanical oscillation. Clearly the relative contributions of these terms have a complicated dependence on the values of κ, Ω_m, and Δ. However, in the case that $\kappa << \Omega_\mathrm{m}$ and $\Delta = \pm\Omega_\mathrm{m}$ it is clear that the in quadrature term dominates. This is a condition of particular interest in optomechanics, with the condition that $\kappa << \Omega_\mathrm{m}$ known as the sideband resolved regime. The reason for this interest becomes clear when we consider the effect of radiation pressure.

Consideration of radiation-pressure

To understand the complete picture for an optomechanical system we consider not only that a moving boundary gives rise to fluctuation in cavity power, but that in turn this fluctuation in power leads to a change in the radiation pressure which acts back on the mechanical element. This radiation pressure force, arising from the momentum carried by photons, $\hbar k$, is appropriately referred to as "back-action" in this context. In the Fabry-Pérot example a reflected photon transfers momentum of $2\hbar k$ on the movable end mirror at a rate defined in terms of the cavity round trip time, $1/\tau_\mathrm{rt} = c/2L$. Thus a per photon force of $F_\mathrm{n} = \hbar k c/L = \hbar\omega_\mathrm{c}/L$ acts back on the mirror. Given a cavity power, $|a(t)|^2$, here normalized by photon number for convenience, the total back-action force is

$$F_\mathrm{rp}(t) = F_\mathrm{n}|a(t)|^2 = \hbar\frac{\omega_\mathrm{c}}{L}|a(t)|^2 = -\hbar G|a(t)|^2 \tag{1.1.34}$$

The above is described in terms of a Fabry-Pérot cavity, but use of the frequency pulling parameter in the expression, $F_{\mathrm{rp}}(t) = -\hbar G|a(t)|^2$, makes it generally valid for a wide range of optomechanical systems. In the current example, the interaction force is interpreted as momentum transfer by reflection, while for trapped dielectric particles [9], or the system described in this thesis (section 2.1.3), the interpretation is in terms of a gradient force. However, regardless of the interpretation of the force, when characterized in terms of a dispersive shift, G, eq. (1.1.34) is valid.

Clearly the mechanical and optical equations of motion are mutually coupled and we would like to understand the emergent behavior. First we'll rewrite the cavity amplitude equation of motion (eq. (1.1.29)) in the more convenient rotating frame for a laser drive given by ω_{L} (as for eq. (1.1.19))

$$\frac{\mathrm{d}a(t)}{\mathrm{d}t} = \left(i\left(\Delta - Gx(t)\right) - \frac{\kappa}{2}\right)a(t) + \sqrt{\kappa_{\mathrm{ex}}}s_{\mathrm{in}}(t) \tag{1.1.35}$$

Here the drive power, $|s_{\mathrm{in}}(t)|^2$, is also normalized by the photon number. Now the mechanical oscillator equation of motion (eq. (1.1.1)) is rewritten with the radiation pressure force, $F_{\mathrm{rp}}(t) = -\hbar G|a(t)|^2$, acting on it

$$\frac{\mathrm{d}^2x(t)}{\mathrm{d}t^2} + \Gamma_{\mathrm{m}}\frac{\mathrm{d}x(t)}{\mathrm{d}t} + \Omega_{\mathrm{m}}^2 x(t) = -\hbar G\frac{|a(t)|^2}{m_{\mathrm{eff}}} \tag{1.1.36}$$

To understand the dynamics of this system we consider the effect of a small force applied to the mechanics, $\delta F(t)$, in producing fluctuations of the cavity amplitude, $\delta a(t)$, and mechanical displacement, $\delta x(t)$. We assume a small perturbation and start from the equilibrium state in the presence of a constant drive $s_{\mathrm{in}}(t) = \bar{s}_{\mathrm{in}}$. When the system settles to a steady state, there is a static displacement of the boundary, $x(t) = \bar{x}$ and a constant cavity amplitude, $a(t) = \bar{a}$. Thus eq. (1.1.35) and eq. (1.1.36) become

$$\bar{a} = \frac{1}{-i(\Delta - G\bar{x}) + \kappa/2}\sqrt{\kappa_{\mathrm{ex}}}\bar{s}_{\mathrm{in}} \tag{1.1.37}$$

$$\bar{x} = -\frac{\hbar G|\bar{a}|^2}{m_{\mathrm{eff}}\Omega_{\mathrm{m}}^2} \tag{1.1.38}$$

Here the radiation-pressure induced displacement, $\bar{x}$, leads to a modified detuning

$$\bar{\Delta} \equiv \omega_{\mathrm{L}} - (\omega_{\mathrm{c}} + G\bar{x}) \tag{1.1.39}$$

To find the dynamical perturbation of this state we plug $x(t) = \bar{x} + \delta x(t)$, $a(t) = \bar{a} + \delta a(t)$ and $\bar{\Delta}$ into eqs. (1.1.35) and (1.1.36). Here also using the steady state solutions, eqs. (1.1.37) and (1.1.38), the resulting linearized equations are

$$\delta\dot{a}(t) = \left(i\bar{\Delta} - \frac{\kappa}{2}\right)\delta a(t) - iG\bar{a}\delta x(t) \tag{1.1.40}$$

$$m_{\text{eff}}\left(\delta\ddot{x}(t) + \Gamma_{\text{m}}\delta\dot{x}(t) + \Omega_{\text{m}}^2\delta x(t)\right) = -\hbar G\bar{a}\left(\delta a(t) + \delta a^*(t)\right) + \delta F(t) \tag{1.1.41}$$

As it is assumed that $\delta a \ll \bar{a}$, second order terms, $\propto \delta a(t)\delta x(t)$ and $\propto |\delta a(t)|^2$, are neglected. Moreover, here $\bar{a}$ is chosen to be real-valued, which is simply dependent on the appropriate choice of phase for the driving term, $\bar{s}_{\text{in}}$.

For ease of analysis the above equations are transformed to the Fourier domain, using $f(\Omega) = \int_{-\infty}^{+\infty} f(t)e^{i\Omega t}\,dt$. First the fluctuating amplitude of the cavity is considered, with the transform rendering

$$-i\Omega\delta a(\Omega) = \left(+i\bar{\Delta} - \frac{\kappa}{2}\right)\delta a(\Omega) - iG\bar{a}\delta x(\Omega) \tag{1.1.42}$$

$$-i\Omega\delta a^*(\Omega) = \left(-i\bar{\Delta} - \frac{\kappa}{2}\right)\delta a^*(\Omega) + iG\bar{a}\delta x(\Omega) \tag{1.1.43}$$

where conjugate symmetry, $\delta a^*(\Omega) = \delta a(-\Omega)$, is used given that $\bar{a}$ is real-valued. Rearranging the above, in terms of the cavity amplitude fluctuations, results in

$$\delta a(\Omega) = \frac{-iG\bar{a}}{-i(\bar{\Delta} + \Omega) + \kappa/2}\delta x(\Omega) \tag{1.1.44}$$

$$\delta a^*(\Omega) = \frac{iG\bar{a}}{i(\bar{\Delta} - \Omega) + \kappa/2}\delta x(\Omega) \tag{1.1.45}$$

Here, as in eq. (1.1.32), the anti-Stokes and Stokes sidebands appear in the cavity amplitude, now driven by the fluctuating mechanical oscillator position, $\delta x(\Omega)$. However, here we take into account the resulting for radiation-pressure force acting back on the mechanical element, substituting the fluctuating cavity amplitude into eq. (1.1.34)

$$\begin{aligned}\delta F_{\text{rp}}(\Omega) =& -\hbar G\bar{a}\left(\delta a(\Omega) + \delta a^*(\Omega)\right)\\ =& -\hbar G^2\bar{a}^2\left(\frac{\bar{\Delta}+\Omega}{(\bar{\Delta}+\Omega)^2 + (\kappa/2)^2} + \frac{\bar{\Delta}-\Omega}{(\bar{\Delta}-\Omega)^2 + (\kappa/2)^2}\right)\delta x(\Omega)\\ &+ i\hbar G^2\bar{a}^2\left(\frac{\kappa/2}{(\bar{\Delta}+\Omega)^2 + (\kappa/2)^2} - \frac{\kappa/2}{(\bar{\Delta}-\Omega)^2 + (\kappa/2)^2}\right)\delta x(\Omega)\end{aligned} \tag{1.1.46}$$

The resulting fluctuating force has real and imaginary components corresponding to the in phase and in quadrature fluctuations of cavity power. This complex force acting on the mechanical oscillator leads to a modification of its susceptibility to an external force. The radiation-pressure induced modification of its dynamics is referred to as *dynamical back-action.* The manifestation of this is seen by transforming eq. (1.1.41) to the frequency domain, as done for eq. (1.1.40),

$$m_{\text{eff}}\left(-\Omega^2 - i\Gamma_{\text{m}}\Omega + \Omega_{\text{m}}^2\right)\delta x(\Omega) = -\hbar G\bar{a}\left(\delta a(\Omega) + \delta a^*(\Omega)\right) + \delta F(\Omega) \tag{1.1.47}$$

and substituting $-\hbar G\bar{a}\left(\delta a(\Omega) + \delta a^*(\Omega)\right) = \delta F_{\text{rp}}(\Omega)$ into the above. This should be rearranged to the form of eq. (1.1.4)), with an effective susceptibility, modified by the back-action

$$\delta x(\Omega) = \chi_{\text{eff}}(\Omega)\delta F(\Omega) \tag{1.1.48}$$

Solving for the susceptibility, we have

$$\chi_{\text{eff}}^{-1}(\Omega) = m_{\text{eff}}\left(\left(\Omega_{\text{m}}^2 + \frac{k_{\text{dba}}(\Omega)}{m_{\text{eff}}}\right) - \Omega^2 - i\left(\Gamma_{\text{m}} + \Gamma_{\text{dba}}(\Omega)\right)\Omega\right) \tag{1.1.49}$$

with the dynamical back-action components of the damping, Γ_{dba}, and spring constant, k_{dba}, defined as

$$\Gamma_{\text{dba}} = \frac{\hbar G^2\bar{a}^2}{m_{\text{eff}}\Omega}\left(\frac{\kappa/2}{(\bar{\Delta}+\Omega)^2 + (\kappa/2)^2} - \frac{\kappa/2}{(\bar{\Delta}-\Omega)^2 + (\kappa/2)^2}\right) \tag{1.1.50}$$

$$k_{\text{dba}} = \frac{\hbar G^2\bar{a}^2}{m_{\text{eff}}}\left(\frac{\bar{\Delta}+\Omega}{(\bar{\Delta}+\Omega)^2 + (\kappa/2)^2} + \frac{\bar{\Delta}-\Omega}{(\bar{\Delta}-\Omega)^2 + (\kappa/2)^2}\right) \tag{1.1.51}$$

In the case of a small perturbation to the dynamics, the behavior can still be described by a damped harmonic oscillator [10], now with an effective damping rate, Γ_{eff}, and resonance frequency, Ω_{eff},

$$\Gamma_{\text{eff}} \approx \Gamma_{\text{m}} + \frac{\hbar G^2\bar{a}^2}{m_{\text{eff}}\Omega_{\text{m}}}\left(\frac{\kappa/2}{(\bar{\Delta}+\Omega_{\text{m}})^2 + (\kappa/2)^2} - \frac{\kappa/2}{(\bar{\Delta}-\Omega_{\text{m}})^2 + (\kappa/2)^2}\right) \tag{1.1.52}$$

$$\Omega_{\text{eff}} \approx \Omega_{\text{m}} + \frac{\hbar G^2\bar{a}^2}{2m_{\text{eff}}\Omega_{\text{m}}}\left(\frac{\bar{\Delta}+\Omega_{\text{m}}}{(\bar{\Delta}+\Omega_{\text{m}})^2 + (\kappa/2)^2} + \frac{\bar{\Delta}-\Omega_{\text{m}}}{(\bar{\Delta}-\Omega_{\text{m}})^2 + (\kappa/2)^2}\right) \tag{1.1.53}$$

It is insightful to recognize that the dynamical back-action contribution to the above expressions can take on either positive or negative values depending on the sign of the detuning.

A positive (blue) detuning leads to an apparent reduction in the mechanical damping rate, which corresponds to driving of the oscillator. Conversely, negative (red) detuning, leads to an increase in Γ_{eff}, as the optical field opposes the oscillator's motion. This optical damping is utilized in the process of laser cooling. The effect of detuning on the oscillator frequency is known as the *optical spring* effect and is demonstrated in section 2.2.3.

This concludes the illustrative description of optomechancial coupling. The reader should now appreciate how the dynamical coupling between the optical field and mechanical oscillator results in a modification of the oscillator's properties. In particular, the optical field may be used to damp the oscillator's motion and effectively reduce its thermal occupation. A quantum mechanical description of this behavior is developed in appendix F and the experimental results of feedback cooling are presented in chapter 5. Appendix E gives a quantum mechanical description of the optomechanically induced correlations between the amplitude and phase quadratures of light. These can be used to locally (in frequency space) reduce the oscillator's apparent motional noise, in a homodyne measurement scheme. Experimental results observing this characteristic modification of the oscillator's lineshape are presented in chapter 4 and serve as a signature of quantum back-action at room-temperature.

2 A monolithic near-field optomechanical system

Nano-scale mechanical oscillators [11] are particularly well suited to measuring small forces and exhibit large zero-point fluctuations, making them an attractive platform for both precision sensing technology [12–14] and basic quantum science [15]. The past decade has witnessed significant efforts toward development of nanomechanical transducers in the electrical domain, including single-electron transistors [16], atomic point contacts [17], and superconducting microwave cavities [18]. Despite impressive experimental achievement [19], these techniques are practically limited by the need for cryogenic operation. A particularly compelling approach is to parametrically couple a nanomechanical oscillator to an optical cavity. The field of a laser-driven cavity can be quantum-noise-limited at room temperature, and as such represents a practically ideal form of mechanical transducer, with read out enabled by standard interferometric techniques and actuation provided by radiation pressure. Moreover, the finite build-up time of the cavity field allows it to do work on the mechanical element, enabling low-noise optical cooling and amplification [20]. Investigation of these effects has led to two paradigmatic goals in the contemporary field of cavity optomechanics [21]: cooling of a solid-state mechanical oscillator to its ground state and, concomitantly, read-out of its zero-point motion with the minimal disturbance allowed by the Heisenberg uncertainty principle (due to radiation pressure shot noise (RPSN) [22]). The first challenge has been met by several cryogenic optomechanical [23, 24] and electromechanical systems [25] (via resolved-sideband cooling [26]). The latter, corresponding to a measurement at the standard quantum limit (SQL) [27], remains outstanding; however, readout noise far below the zero-point displacement has been reported [28, 29], as well as RPSN dominating the thermal force [30, 31]. Reaching the SQL ultimately requires a 'Heisenberg-limited' displacement sensor for which the product of the read out noise and the total force noise is the minimum allowed by the uncertainty principle. This regime has been approached to within an order of magnitude by several cryogenic systems [25, 28]; it also forms the basis for measurement-based quantum feedback protocols such as ground-state cooling [28, 32] and squeezing [33] of an oscillator.

Efficient cavity optomechanical transduction involves co-localization of optical and mechanical modes with high $Q/(\text{mode volume})$ and high optical power handling capacity. Moreover, it is desirable that the cavity support a mechanism for efficient input/output coupling. A diverse set of micro- and nanoscale cavity optomechanical systems (COMS) has risen to meet these challenges, ranging from cantilevers [34] and membranes [35] coupled to Fabry-Pérot cavities to mechanically-compliant whispering-gallery-mode (WGM) microcavities [36] and photonic crystals [37]. They generally employ two types of radiation pressure force coupling: traditional scattering-type coupling, in which the cavity field exchanges energy with the mechanical element via momentum transfer, and gradient force coupling [38], in which energy is exchanged via induced-dipole coupling to a field gradient. The net effect is a parametric coupling $G = \partial\omega_c/\partial x$ between the cavity resonance frequency ω_c and the mechanical degree of freedom x, which expresses the force applied per intracavity photon, $\hbar \cdot G$ [21].

A particularly promising platform for optomechanical transduction involves placing a (dielectric) mechanical substrate next to the surface of a WGM microcavity, so that it samples its evanescent field. Since the evanescent decay length is $\sim \lambda/10$, this topology offers the opportunity for strong gradient force coupling to *nanoscale* mechanical devices. It also has the virtue of naturally accommodating optical and mechanical substrates of dissimilar material and geometry, enabling separate optimization of $Q/(\text{mode volume})$. Moreover, WGMs can be input/output coupled with high ideality using tapered optical fibers [39], making them well-suited to interferometric displacement sensing. Recent work has focused on coupling of nano-beams [40], -cantilevers [41], and -membranes [40, 42] to the evanescence of WGM micro-toroids [40], -spheres [42, 43], and -disks [41, 44], with mechanical materials ranging from (ultra low loss) high-stress Si_3N_4 [40] to (ultra low mass) single-layer graphene [42], typically using SiO_2 as the optical material. Gradient force coupling as high as $G \sim 2\pi \cdot 100$ MHz/nm has been achieved [40]. Combined with the high power handling capacity of SiO_2 and low extraneous displacement noise (typically thermo-refractive noise (TRN) in the cavity substrate [45]), optimized systems have achieved room temperature displacement imprecisions as low as $10^{-16}\,\text{m}/\sqrt{\text{Hz}}$, sufficient to in principle resolve the zero-point motion in several cases [40, 45].

Despite these advances, the full potential of evanescent cavity optomechanics has been inhibited by the difficulty of positioning the nanomechanical element within $\lambda/10 \sim 100$ nm of the cavity substrate. This chapter describes a system where a high-stress Si_3N_4 thin film resonator and a SiO_2 microdisk cavity are integrated *within the evanescent near-field*, without deteriorating the intrinsic Q of either element. The following chapter details the fabrication process of devices in which the nanobeam is monolithically suspended as little as 25 nm above the SiO_2 microdisk — $\sim 3\times$ smaller than the evanescent decay length of its WGMs — while maintaining mechanical and optical mode qualities in excess of 10^5 and 10^6, respectively. The process is compatible with e-beam lithography, thus we are able to locally pattern the beam with sub-10 nm imprecision and laterally position it with sub-100 nm imprecision across a full 4" Si wafer.

A typical device is shown in fig. 2.1, corresponding to a $60 \times 1 \times 0.06\,\mu\text{m}^3$ beam positioned 25 nm above a 0.65-μm-thick, 25-μm-diameter microdisk. By carefully varying the dimensions of the beam, the disk, and their lateral offset with respect to this nominal geometry, we achieve optomechanical coupling rates (G) in excess of $2\pi \cdot 1$ GHz/nm while maintaining cavity decay rates (κ) as low as $2\pi \cdot 100$ MHz and radio frequency ($\Omega_\mathrm{m} = 2\pi \cdot (1-10)$ MHz) flexural beam modes with damping rates (Γ_m) as low as 10 Hz. In conjunction with the small mass ($m \sim 10$ pg) and large zero-point displacement ($x_\mathrm{zp} \equiv \sqrt{\hbar/2m\Omega_\mathrm{m}} \sim 10$ fm) of the beam modes, the combined low-loss, small gap and parralel-plane geometry result in a vacuum optomechanical coupling rates ($g_0 \equiv G \cdot x_\mathrm{zp}$) as high as $2\pi \cdot 100$ kHz and room temperature single-photon cooperativies as high as $C_0 \equiv 4g_0^2/\kappa\Gamma_\mathrm{m} = 2$. The latter is notably a factor of 10^5 times larger than in [44] and on par with the state-of-the-art for both room temperature and cryogenic COMS (fig. 2.1).

In conjunction with high C_0, several features of the system make it well-suited for quantum-limited operation. First, SiO_2 microcavities with the reported dimensions and internal loss readily support intracavity photon numbers of $n_\mathrm{c} \sim 10^6$. This enables quantum cooperativities ($C_0 n_\mathrm{c}/n_\mathrm{th}$) approaching unity — a basic requirement for performing a Heisenberg-limited displacement measurement — for a room temperature thermal occupation of $n_\mathrm{th} \approx k_\mathrm{B}T/\hbar\Omega_\mathrm{m} \sim 10^6$, corresponding to $\Omega_\mathrm{m} \sim 2\pi \cdot 5$ MHz. Another striking feature is the exceptionally large magnitude of the cavity frequency noise produced by zero-point motion of the mechanical oscillator, $S_\omega^{zp}(\Omega_\mathrm{m}) \equiv 4g_0^2/\Gamma_\mathrm{m} \sim 10\,\mathrm{kHz}/\sqrt{\mathrm{Hz}}$. This magnitude is many orders of magnitude larger than typical extraneous sources of noise due to laser frequency fluctuations or TRN [45]. In section 2.3, a measurement with an imprecision 32 dB below that at the SQL and an imprecision-back-action product of $60 \cdot \hbar$, using a moderate input power of 10 μW. Remarkably, the imprecision due to microdisk TRN [45] can be 20 dB lower.

2.1 System overview

The following sections detail the geometric and physical details of the optomechanical system that is used to observe correlations between the phase and amplitude of a coupled light field at room-temperature (chapter 4), and is also laser cooled to an average occupancy of just ≈ 5.3 phonon in a ^{3}He cryostat (chapter 5). The first two subsections detail the constituent components of this system - namely a high-stress Si_3N_4 nanobeam and the SiO_2 microdisk to which it is optomechanically coupled. We begin with a discussion of the physics behind the exceptionally high Q/mass that can be achieved in such nanobeams at room-temperature, before describing the specific geometries used for mechanical resonators in this thesis, as well as their measured properties (section 2.1.1). The following section describes the microdisk resonator that is integrated onto the same chip as the nanobeam and our specific choice of material and geometry is motivated (section 2.1.2). Finally, the mechanism of coupling a resonant mode of the microdisk to the out-of-plane motion of the nanobeam is presented in terms of a simplified analytical model, which is shown to be in close agreement with finite element models (FEM) (section 2.1.3). In sum we provide a compelling argument for the device developed in this thesis work and used to demonstrate the experimental results mentioned

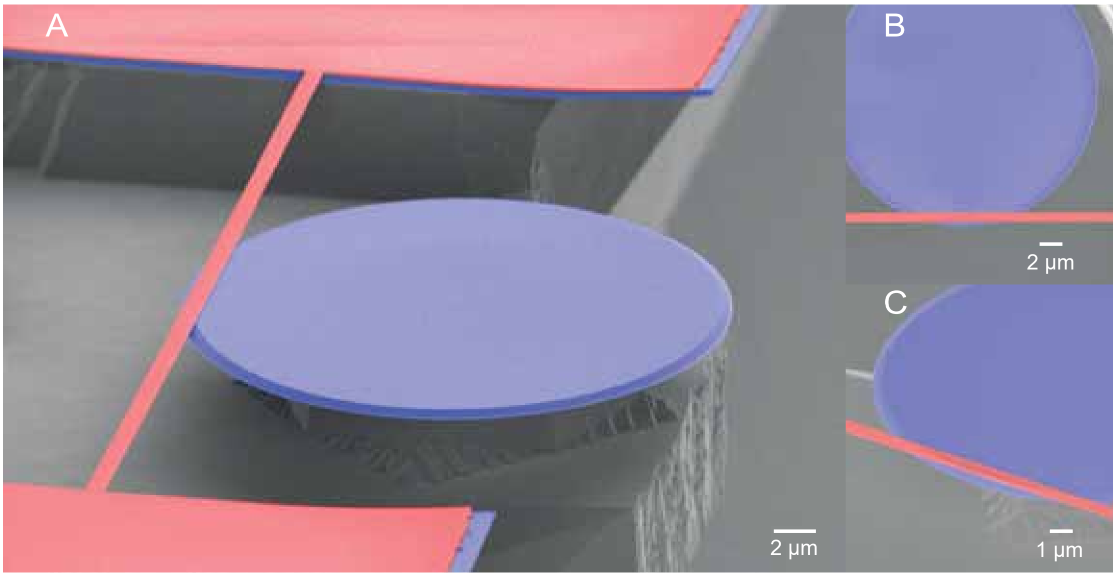

Figure 2.1 – **False-colored SEM of the monolithic optomechanical system:** consisting of a high-stress Si_3N_4 (red) nanobeam integrated into the evanescent near-field of a SiO_2 (blue) microdisk. The disk and beam are fabricated on a single Si (gray) wafer. Subpanels B and C highlight the lateral and vertical positioning of the beam.

above, as well as to observe sideband asymmetry and mechanically mediated squeezing of light at cryogenic temperatures [46].

2.1.1 Silicon nitride nanobeams

The mechanical resonators studied in this thesis, and featured throughout the experimental work herein, are composed of a doubly-clamped nitride nanobeam under high tensile stress. In their most simple form these resonators are rectangular in cross-section and axially invariant. In 2006, such devices were first demonstrated, and recognized to stand in a class of their own in terms of the product of Q and cross-sectional area, making them particularly well suited to mass sensing [47]. In the context of optomechanics this property can be understood as leading to large zero-point fluctuations as a consequence of high Q/m values. For typical devices formed of thin nitride film just tens to hundreds of nanometers thick, a large mechanical impedance mismatch to the anchoring substrate exists at the clamping points [48]. This can be understood as a highly reflective boundary, leading to a strongly localized standing wave, or low radiation loss to the substrate. This loss can be largely neglected for such nanobeams, meaning that the primary loss mechanism is internal material loss.

To understand the mechanism of internal loss and the role that stress plays in increasing Q, we consider potential energy for a given eigenmode. This can be represented as being composed of a two components: one resulting from bending, $U_E = \frac{1}{2}E_0\int_0^L I(x)[u''(x)]^2 dx$ and giving rise to losses, and another component that is conservative and due to elongation, $U_\sigma = \frac{1}{2}\int_0^L T(x)[u'(x)]^2 dx$. Here E_0 is Young's modulus, $I(x) = \frac{1}{12}w(x)h^3$ is the moment of inertia, $u(x)$ the eigenmode displacement profile, $T(x) = hw(x)\sigma(x)$ the tension, h is the nanobeam thickness, $w(x)$ is its width, and $\sigma(x)$ the axial stress. Note that here the nanobeam's width is not assumed to be axially invariant - this will be of relevance in 6.1. One may immediately recognize that while the conservative energy component increases proportionally to stress the dissipative component is invariant, implying that the lossy energy contribution may be diluted by increasing the axial stress. This effect is typically referred to as "dissipation dilution" for this reason. The dissipation dilution, or Q enhancement, factor is given by the participation ratio of conservative and lossy energy contributions [49–51]:

$$\frac{Q}{Q_0} = 1 + \frac{U_\sigma}{U_E} \approx \frac{12}{E_0 h^2} \cdot \frac{\int_0^L \sigma(x)[u'(x)]^2 dx}{\int_0^L [u''(x)]^2 dx}, \tag{2.1.1}$$

where Q_0 is the intrinsic quality factor of the unstressed material.

For the sake of illustration, eq. eq. (2.1.1) can be rewritten assuming a sinusoidal displacement profile, $u(x) \propto \sin(\pi n x/L)$, leading to:

$$\frac{Q}{Q_0} \approx \frac{3}{\pi^2} \frac{\sigma^2}{E_0 h^2 \rho f^2}, \tag{2.1.2}$$

where ρ is the material density and the modal frequency is $f = \frac{n}{L}\sqrt{\sigma/\rho}$, with n being the mode number and L the nanobeam's length. However, this turns out to be a very poor assumption with measured Qs being orders of magnitude lower than what would be predicted by eq. eq. (2.1.1). The reason for this is additional curvature near the nanobeam's boundaries - a consequence of the clamping condition which requires that $u'(x_0) = u(x_0) = 0$. Note that for a pure sinusoidal displacement the mode would meet the material plane at a 45° angle. The additional curvature required to meet the boundary conditions turns out to be the main source of loss for such resonators. Taking into account the true mode shape eq. eq. (2.1.1) can be expressed as [49, 52]:

$$\frac{Q}{Q_0} \approx (\underbrace{2\lambda}_{\text{boundaries}} + \underbrace{\pi^2 n^2 \lambda^2}_{\text{antinodes}})^{-1}, \tag{2.1.3}$$

where $\lambda = \frac{h}{L}\sqrt{E_0/12\sigma}$. Generally, nanobeams have a high aspect ratio where $h << L$ which implies $\lambda << 1$ and thus losses are dominated by the first term in eq. eq. (2.1.2). This holds at least for low order modes. Since n does appear in the second term sinusoidal bending eventually dominates for very high order modes.

Nanobeams that form the mechanical element of the hybrid structures studied in this work typically have geometry $\{\text{length}\,(l), \text{width}\,(w), \text{thickness}\,(t)\} \sim \{60, 0.5, 0.05\}$ μm, with corresponding effective masses $m_{\text{eff}} \sim 10$ pg for the fundamental modes. Figure 2.2 shows the Q and $Q\times$ frequency products for the out of plane, odd numbered flexural modes of nanobeam with these dimensions. Despite the complex integration process, they exhibit state of the art quality factors for high-stress nitride nanobeams of comparable dimensions, described by $Q_\text{m}\Omega_\text{m}/2\pi$ as high as 5×10^{12} Hz [52, 53]. The dashed red line in fig. XYZ shows a fit to eq.

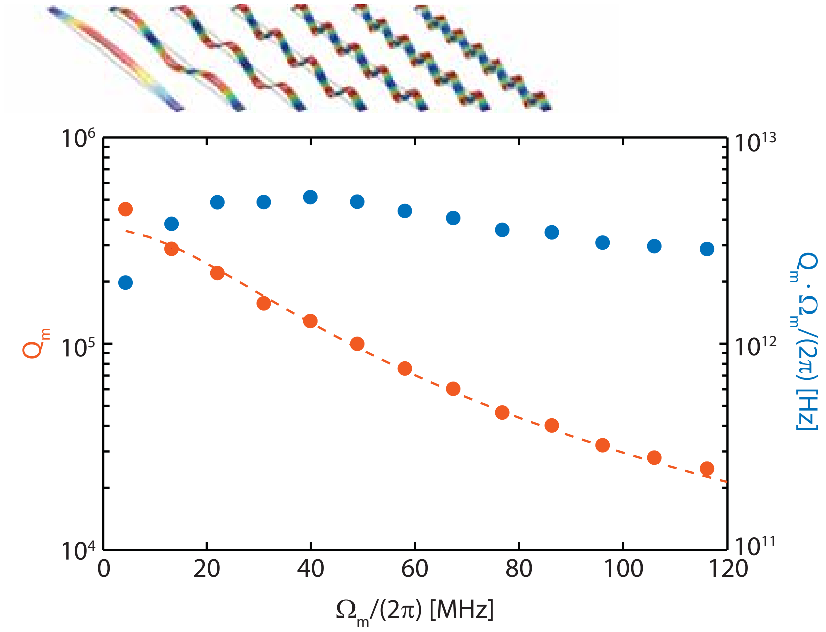

Figure 2.2 – **Measurement of odd numbered out-of-plane flexural modes for a representative nanobeam.** Q-factor (red) and $Q \cdot$frequency product (blue) for a nanobeam with dimensions $\{l, w, t\} = \{60, 0.6, 0.05\}$ μm (sample M2/CU/T/+1) are shown as a function of mode frequency. The dashed red curve is a fit to the dissipation dilution model in eq. eq. (2.1.3). Finite element simulations of corresponding displacement profiles are shown above the figure.

eq. (2.1.3) for Q of the harmonics, assuming $E_0 = 200$ GPa. The mechanical spectrum, which is close to linear with $\Omega_m^{(n)} \approx 2\pi n \cdot 4.3$ MHz, implies a tensile stress of $\sigma \approx (\rho l \Omega_m^{(0)}/\pi)^2 \approx 800$ MPa assuming a density of $\rho = 2700\ \mathrm{kg/m^3}$ [47]. The fit yields an intrinsic Q of $Q_0 \approx 6700$, which is approximately an order of magnitude below that of bulk nitride. However, assuming the material Q is surface loss limited, as has been compellingly argued, we find $Q_{\mathrm{int}}/t \approx 1.1 \cdot 10^5\ \mu\mathrm{m}^{-1}$ which agrees closely with literature [52]. When measured in a ^{3}He cryostat at 0.5 K, Q_0 is observed to increase to a value of $Q_0 > 10^4$ [54].

As mentioned, the nanobeams described here are an excellent choice for integration in an optomechanical system as they exhibit very large zero-point motion. When expressed as a single-sided spectral density, the fundamental mode for such beams exhibits peak zero-point noise density of $S_x^{\mathrm{zp}}(\Omega_m) = 2\hbar Q_m/m\Omega_m^2 \sim 10\ \mathrm{fm}/\sqrt{\mathrm{Hz}}$. Moreover, the frequency window for this mode at $Q_m \approx 4.3$ MHz, sits in a range where low noise electronics and laser sources are readily available. It is for this reason that nanobeams were the first solid-state mechanical resonators to be read out electrically [55] and optically [45] with an imprecision lower than $S_x^{\mathrm{zp}}(\Omega_m)$. In addition to the favorable mechanical properties, nitride is also attractive for its optical properties. It has a significantly larger index of refraction compared to the oxide that forms the optical resonator, with $n \approx 2$. It also has relatively low optical absorption at near infrared wavelengths, owing to its ~ 3 eV bandgap, characterized by an imaginary index of

$n_{\mathrm{im}} \sim 10^{-5} - 10^{-6}$ [56].

2.1.2 Silicon dioxide microdisks

The other fundamental component of the optomechancial system described in this chapter is a oxide microdisk that support circumferential WGMs. The microdisk senses displacement of the nanobeam via its evanescent field, and there are several reasons that oxide is an advantageous material to use in this system. First, oxide has a wide transparency window covering the near infrared as well as the ability to operate stably with high field intensities or large intracavity photon numbers (n_{c}). In the near infrared maximum n_{c} is practically limited by Kerr and Raman nonlinearity, and not by two photon absorption as is the case with Si. Another advantage is oxide can be used to fabricate WGM resonators with exceptionally high Q factors in the near infrared [57]. Although crystalline resonators hold the record for highest achieved Q-factors [58, 59], such devices cannot be produced using wafer-scale fabrication techniques. On the other hand, oxide microdisks fabricated using standard CMOS techniques have demonstrated Q-factors just shy 10^9, with an inferred material Q of 2.5×10^9 [60]. Such resonators are assumed to be scattering loss limited, and when produced by wet chemical etching the sidewall takes on a characteristic wedged shape that helps to minimize the WGM's interaction with the confining surfaces. A further advantage is the ability to evanescently couple such microdisks to a tapered optical fibers with high ideality [39]. The ability to critically couple by this technique is of fundamental importance to avoiding additional optical loss which would otherwise raise the shot-noise imprecision [36].

Microdisk resonators and corresponding optomechancial systems were designed for operation in the range of $\lambda \approx 750-850$ nm, to allow for smaller optical mode volumes. As discussed in section 2.1.3, reducing the disk radius (r_{d}) and thickness ($t_{\mathrm{d}} \sim \lambda/n$) results in smaller mode volumes with fractionally larger energy in the evanescent field, resulting in larger optomechanical coupling strength. For microdisks with thickness $t_{\mathrm{d}} > 300$ nm, numerical simulations [61] reveal that radiation loss remains insignificant for radii greater than 10 μm. Figure 2.3 shows measurements of optical Q as a function of radius for microdisk samples of thickness with oxide thickness of 700 nm. The data consists of two types of devices produced with differing lithographic processes. The set shown in blue was prepared with photolithography and those shown in red with electron-beam lithography. The sets differ by their corresponding wedge angle, which is 30 degrees for photolithography and 10 degrees for electron-beam lithography (see chapter 3 for details). For both disk preparation methods, intrinsic $Q > 10^6$ was measured for radii as low as 10 μm, corresponding to loss rates of $\kappa < \pi \cdot 100$ MHz. For electron-beam produced samples, Q as high as $4 \cdot 10^7$ ($\kappa \sim 2\pi \cdot 10$MHz) was obtained for radii of 50 μm Dotted red and blue lines in fig. 2.3 are guide-to-the-eye models for $Q \propto r_{\mathrm{d}}$, consistent with loss due to surface scattering [62], and corresponding to a fixed finesse of $\mathscr{F} \equiv \Delta\omega_{\mathrm{FSR}}/\kappa \approx c/(r_{\mathrm{d}}\kappa) = 0.6 \cdot 10^5$ and $1.2 \cdot 10^5$, respectively. Impressively, the highest measured quality factors, $Q \approx 4 \cdot 10^7$, are similar to those measured at telecommunication wavelengths, where scattering losses are significantly lower [60, 63]. As discussed in section 2.2.4, the intrinsic microdisk Q is ultimately

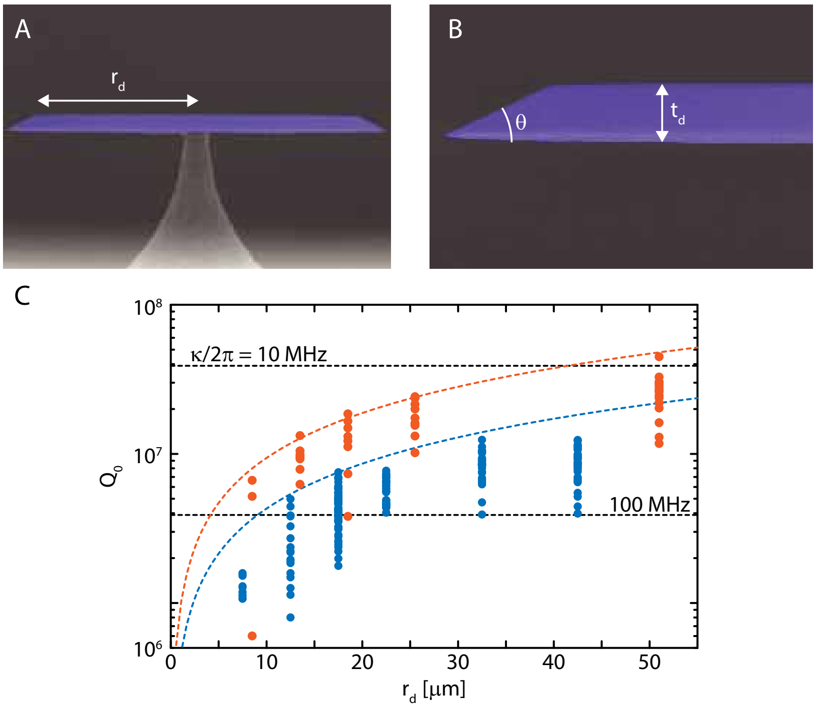

Figure 2.3 – **Characterization of oxide microdisk Q-factors.** (A,B) SEM side profile of a oxide (blue) microdisk on a Si (grey) pillar showing its characteristic wedged sidewall. (C) Intrinsic (under-coupled) Q-factors for a set of microdisks with oxide thickness of 700 nm and varying radii. TM and TE modes are not distinguished. The set shown in red is produced by e-beam lithography with sidewall angle $\theta \approx 10°$, and in blue by photolithography with $\theta \approx 10°$ (shown in the above SEM). Dashed grey lines indicate corresponding resonance linewidths, $\kappa = 2\pi c/(\lambda Q_o)$, at $\lambda = 780$ nm (the measurement wavelength). Blue and red dashed lines indicate $Q \propto r_\mathrm{d}$, corresponding to a fixed finesse of $\mathscr{F} = 0.6\,(1.2) \cdot 10^5$.

reduced by loss introduced by the nanobeam, in the case of vertical separations between the nanobeam and microdisk of less than 100 nm.

2.1.3 Near-field coupling

Displacement of the nanobeam is coupled the optical mode frequency of the microdisk by placing the nanobeam near the top surface of the microdisk, such that its mid-section occupies the evanescent volume of one of the microdisk WGMs. When the WGM is excited, the beam experiences a gradient force, F_opt. The magnitude of this force, as well as the frequency pulling factor $G = \partial\omega_\mathrm{c}/\partial x$, can be derived by calculating the work done on the WGM, $-\delta U_\mathrm{cav}$, by a small displacement of the beam, δx. The gradient force can be found in terms of the frequency pulling factor as $F_\mathrm{opt} = -\partial U_\mathrm{cav}/\partial x \approx -G U_\mathrm{cav}/\omega_\mathrm{c}$, where U_cav is the potential energy stored in the cavity field [38, 64]. To first order, G can be determined by the fractional change in the

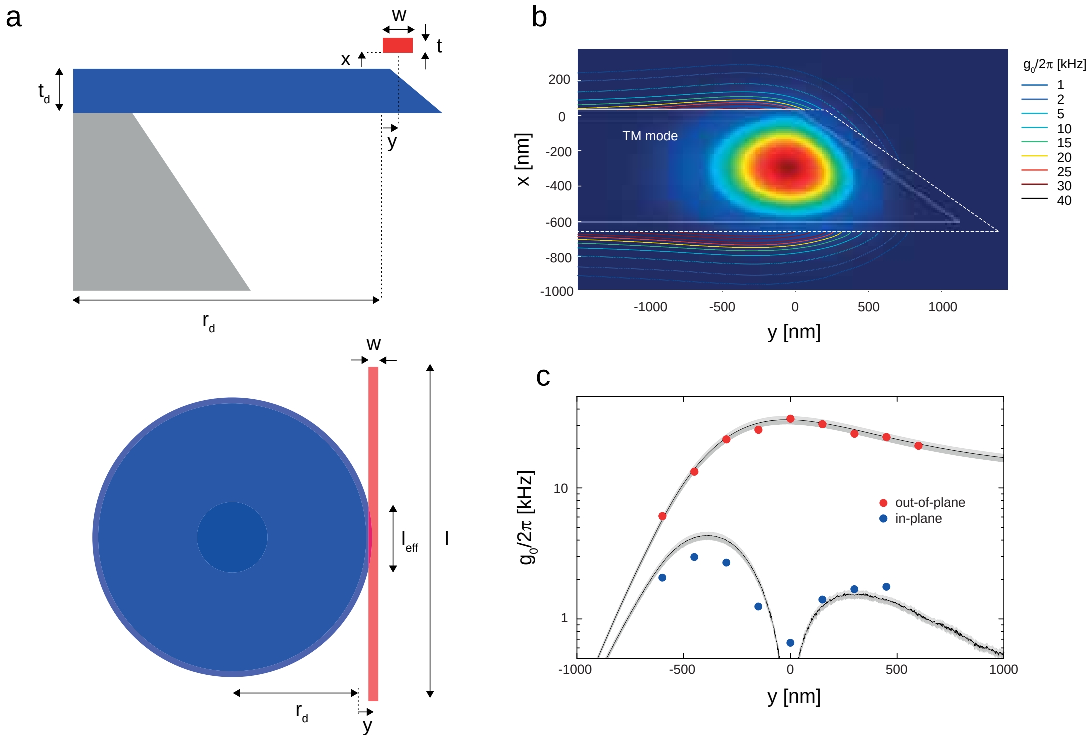

Figure 2.4 – **Simulation of the optomechanical coupling in monolithic system.** (A) Geometry of the nanobeam-microdisk system with x and y representing the vertical (out-of-plane) and lateral (in-plane) position of the beam, respectively. These positions are referenced with respect to the top rim of the disk (thickness t_d, radius r_d). (B) Simulated optomechanical coupling rates for varying beam position in the device shown in fig. 2.1. The intensity profile of a TM-like WGM (computed using FEM) is shown in the background. Solid white lines denote the disk surface and deshed white lines the boundary within which the beam touches the disk surface, for the coordinate system defined in (A). Contours indicate lines of constant g_0 for the 4.3 MHz fundamental out-of-plane mode. (C) Measured and simulated g_0 versus y for the beam shown in fig. 2.1 (samples on chip M2/BD/T). Black and blue data are for fundamental out-of-plane and in-plane vibrational modes, respectively (for details can be found in section 2.2.4). Black lines correspond to numerical solutions to eq. (2.1.4) with a vertical offset of $x = 25$ nm. Gray shading bounds the solution space for x =20 to 30 nm.

WGMs energy caused by displacement of the nanobeam [40]

$$G \approx \frac{\omega_\text{c}^{(0)}}{2}\frac{\partial}{\partial x}\left(\frac{\int_\text{beam}(\epsilon(\vec{r})-1)|\vec{E}^{(0)}(\vec{r})|^2 d^3r}{\int_\text{disk}\epsilon(\vec{r})|\vec{E}^{(0)}(\vec{r})|^2 d^3r}\right) \approx \frac{\omega_\text{c}^{(0)}}{2}\frac{\partial}{\partial x}\left(\frac{n_\text{SiN}^2-1}{n_{\text{SiO}_2}}\frac{|E_\text{max}^{(0,\text{beam})}|^2}{|E_\text{max}^{(0,\text{disk})}|^2}\frac{V_\text{beam}}{V_\text{disk}}\right) \tag{2.1.4a}$$

Here $\epsilon(\vec{r})$ is the local relative permittivity, $\vec{E}^{(0)}(\vec{r})$ is the unperturbed cavity field amplitude, and the integral terms are over the over the volume occupied by the beam and disk. The simplified expression in (2.1.4)b replaces ϵ with an index of refraction n and parameterizes each integral in terms of the intensity-weighted volume of the nanobeam or microdisk. Thus in the case of the nanobeam we have $V_\text{beam} \equiv \int_\text{beam}|E_0|^2 d^3r/|E_\text{max}^{(0,\text{beam})}|^2$, where $E_\text{max}^{(0,\text{beam})}$ is the maximum of the unperturbed field within the nanobeam.

Figure 2.4 illustrates the coupling geometry described above and defined by eq. (2.1.4). The beam is placed above the disk, so that its out-of-plane motion can localized along the maximum of the WGMs evanescent field gradient. Here we will assume that the width of the beam is much smaller than the transverse extents of the evanescent field. Specifically, $w \ll \sqrt{A_{\mathrm{WGM}}}$ and $t \ll x_{\mathrm{ev}}$, where A_{WGM} is the effective cross-sectional area of the WGM and x_{ev} is the exponential decay length of the evanescent field. In this case V_{beam} can be approximated as twl_{eff}, where l_{eff} is the intensity-weighted "sampling length" of the beam. Similarly V_{disk} can be parameterized as $V_{\mathrm{disk}} \approx 2\pi r_{\mathrm{d}} A_{\mathrm{WGM}}$, where r_{d} is the physical disk radius. Assuming the form $|E_{\mathrm{max}}^{(0,\mathrm{beam})}|/|E_{\mathrm{max}}^{(0,\mathrm{disk})}| = \xi e^{-\frac{x+t/2}{x_{\mathrm{ev}}}}$, neglecting the weak position dependence of V_{beam}, and assuming the effective mass of a point probe, $m = \rho twl/2$ (for the fundamental mechanical mode), the vacuum optomechanical coupling rate can be approximated as

$$g_0 \approx \frac{1}{2}\frac{\omega_{\mathrm{c}}^{(0)}}{x_{\mathrm{ev}}}\frac{n_{\mathrm{SiN}}^2-1}{n_{\mathrm{SiO_2}}}\frac{twl_{\mathrm{eff}}}{2\pi r_{\mathrm{d}} A_{\mathrm{WGM}}}\xi^2 e^{-\frac{x+t/2}{x_{\mathrm{ev}}}} \cdot \sqrt{\frac{\hbar}{\rho twl\Omega_{\mathrm{m}}}} \tag{2.1.5}$$

where ρ is the mass density of the beam. In practice x_{ev}, A_{WGM} and ξ must be determined numerically for a wedged microdisk. However, an estimate can be made by assuming the mode shape of a microtoroid WGM with a minor radius of $t_{\mathrm{d}}/2$, which can then be solved analytically [40]. In this case, using $n_{\mathrm{SiO_2}} \approx 1.4$, one has $x_{\mathrm{ev}} \approx \lambda/(2\pi\sqrt{n_{\mathrm{SiO_2}}^2 - 1}) \approx \lambda/12$, $A_{\mathrm{WGM}} \approx 0.15 r_{\mathrm{d}}^{7/12} t_{\mathrm{d}}^{1/4} \lambda^{7/6}$ and $\xi \approx 1.1(\lambda/r_d)^{1/3}$ [65]. Using these formulas, the device geometry in fig. 2.1 ($\{t, w, l\} = \{0.06, 0.4, 60\}$ μm, $x = 25$ nm, $r_{\mathrm{d}} = 14.2$ μm, $t = 0.65$ μm) and assuming $\lambda = 780$ nm, $n_{\mathrm{SiN}} = 2.0$, $\rho = 2700$ kg/m^3, $\Omega_{\mathrm{m}} = 2\pi \cdot 4.3$ MHz, and $l_{\mathrm{eff}} = 10$ μm (see section 2.2.6), eq. (2.1.5) predicts that $G \approx 2\pi \cdot 1.0$ GHz/nm, $x_{\mathrm{zp}} \approx 33$ fm, and $g_0 = 2\pi \cdot 33$ kHz. As shown in fig. 2.4c, this estimate agrees well with numerically and experimentally determined values. Notably, (2.1.5) implies that to achieve large g_0, it is necessary to reduce the vertical gap to $x < x_{\mathrm{ev}} \approx 100$ nm, and to maximize l_{eff} by laterally positioning the beam *above* the disk.

A numerical model for $g_0(x, y)$ is shown in fig. 2.4B and fig. 2.4C(grey bands). Unperturbed WGM mode, $\vec{E}^{0)}(\vec{r})$, were computed using an axially-symmetric finite element model (COMSOL FEM axial symmetric package [61]). The energy stored in the WGM is given by:

$$U_{\mathrm{cav}}^{(0)} \approx \tfrac{1}{2}\int_{\mathrm{disk}} \epsilon(\vec{r})|\vec{E}^{(0)}(\vec{r})|^2 d^3r \tag{2.1.6}$$

Similarly, the energy shift of the WGM caused by placing a nanobeam into the evanescent near-field is:

$$\Delta U_{\mathrm{cav}}(x, y) \approx \tfrac{1}{4}\int_{\mathrm{beam}} (\epsilon(\vec{r}) - 1)|\vec{E}^{(0)}(\vec{r})|^2 d^3r \tag{2.1.7}$$

Here ΔU_{cav} is found by expanding the Unperturbed WGM mode, $\vec{E}^{0)}(\vec{r})$, into the third dimension and integrating over the volume contained by the nanobeam. Differentiating the total

WGM energy with respect to a vertical displacement of the beam gives,

$$G(x, y) = \omega_c \frac{\partial}{\partial x}(\Delta U_{\text{cav}}(x, y)/U_{\text{cav}}^{(0)}) \tag{2.1.8}$$

for out-plane-motion (in this case numerical differentiation). The result of this calculation is shown in fig. 2.4b shows $g_0(x, y) = G(x, y) \cdot x_{\text{zp}}$ for varying position of a nanobeam and microdisk with the dimensions given above, in the case of a TM-like WGM mode. Contours represent lines of constant g_0 and indicate that the optimal position of the beam is above and inside the inner rim of the disk. It can also be observed that the magnitude of g_0 scales exponentially with vertical displacement from the disk surface, with a decay length of ∼ 100 nm. A horizontal cut through the contours for $x = 25$ nm is shown in fig. 2.4c. Upper and lower curves show models for fundamental in-plane (IP) and out-of-plane (OP) flexural modes. Significantly, maximizing $g_0^{(\text{OP})}$ also minimizes $g_0^{(\text{IP})}$. Thus optimal placement of the nanobeam opens a wide spectral window, $\Delta\Omega \sim \Omega_m$, for measurement of the out-of-plane mode without contamination from the neighboring in-plane mode. Experimental measurements (see section 2.2.2) of $g_0(25\,\text{nm}, y)$ are also shown in fig. 2.4c . The numerical and analytical models agree well with experiment assuming a vertical offset of 25 ± 5 nm.

2.2 Optomechanical characterization

2.2.1 Experimental setup

Samples are characterized using the experimental setup shown in fig. 2.5. Light from a 765−785 nm tunable diode laser (New Focus Velocity 6312) is coupled into the microdisk using a tapered optical fiber (780 HP) [39]. The forward-scattered (“transmitted") field is monitored using one of two techniques: direct detection with an avalanche photodiode (Thorlabs APD110) or balanced homodyne detection with a pair of fast Si photodiodes (FEMTO HCA-S-100). The photosignal is split into DC and AC filtered components which are sent to an oscilloscope (Tektronix DPO4034) and a spectrum analyzer (Tektronix RSA5106A), respectively. When operating the laser in swept mode (such as for measuring the optical cavity linewidth) the frequency range is calibrated by sending a fraction of the input field ithrough a 20-cm-long (FSR ∼ 350 MHz) fiber loop cavity with a known free spectral range. Optical decay rates are inferred from measurements of transmitted power versus laser detuning (fig. 2.5B). Mechanical properties, including the optomechanical coupling rates, are inferred from measurements of thermomechanical cavity frequency noise [66] (fig. 2.5C). This noise is calibrated by frequency modulating the input field using an electro-optic modulator (EOSpace) with a calibrated modulation depth. Residual amplitude modulation — an important source of calibration error — is actively suppressed using PID feedback to stabilize the phase of an out-of-loop heterodyne beat [67]. To avoid gas damping of the nanobeam, the sample chip and the fiber coupling setup (based on an Attocube stack) are embedded in a vacuum chamber operating below 10^{-6} mbar.

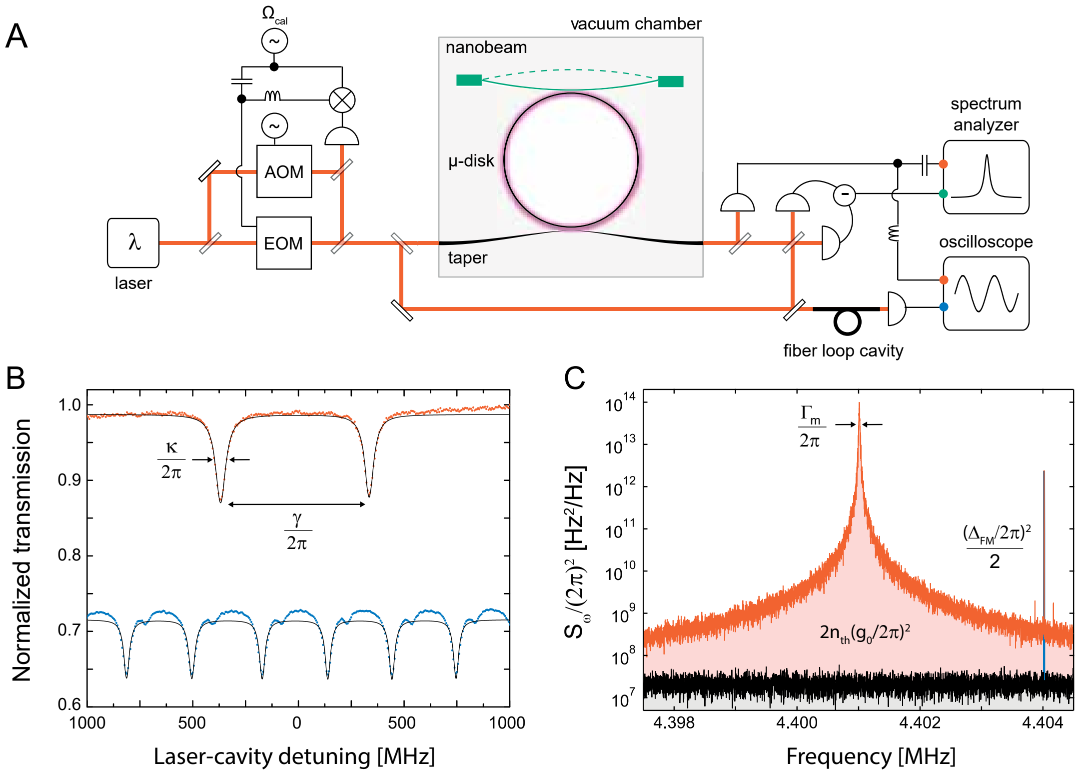

Figure 2.5 – **Characterization setup and methods.** (A) Overview of the experimental apparatus, described in section 2.2. (B) Representative optical Q measurement. WGM loss rates (κ) and mode splitting (γ) are fitted to the cavity transmission profile (red), which is generated by sweeping the diode laser frequency (typically 30 GHz range) while monitoring the transmitted power. Frequency is calibrated by simultaneously monitoring transmission through a fiber loop cavity with known free spectral range (blue). (C) Representative thermomechanical noise measurement. $\Omega_\text{m}, \Gamma_\text{th}$, and g_0 are inferred from the center frequency, linewidth, and area beneath the thermal noise peak (pink), respectively. The latter is calibrated by normalizing to the area beneath a FM tone (blue) generated by the EOM in (A).

2.2.2 Thermal noise measurement

Mechanical mode frequencies Ω_m, damping rates Γ_m, and optomechanical coupling rates g_0, were determined by analyzing the cavity resonance frequency noise produced by thermal motion of the nanobeam. A detailed description of this method is given in [66]. An overview of this calibration method is given below:

Thermal motion of the nanobeam $x(t)$, is written onto the cavity resonance frequency $\omega_c(t)$ via the frequency pulling factor, $G = d\omega_c/dx$. To measure $\omega_c(t)$, the power of the transmitted field is monitored while operating at a fixed detuning of $|\Delta| \approx \kappa/2$. Referred to the output voltage (V) of the photodetector transimpedance amplifier, the uncalibrated noise spectrum can be expressed as $S_V(\Omega) = |G_{V\omega}(\Omega)|^2 S_\omega(\Omega)$, where $G_{V\omega}(\Omega)$ is the frequency to voltage transfer function and $S_\omega(\Omega)$ is the apparent cavity frequency noise. $G_{V\omega}(\Omega)$ is calibrated by applying a phase modulation tone of known depth (β_cal) and frequency (Ω_cal) to the input, resulting in a narrow spectral peak with area $|G_{V\omega}(\Omega_\text{cal})|^2 \beta_\text{cal}^2 \Omega_\text{cal}^2/2$ [66].

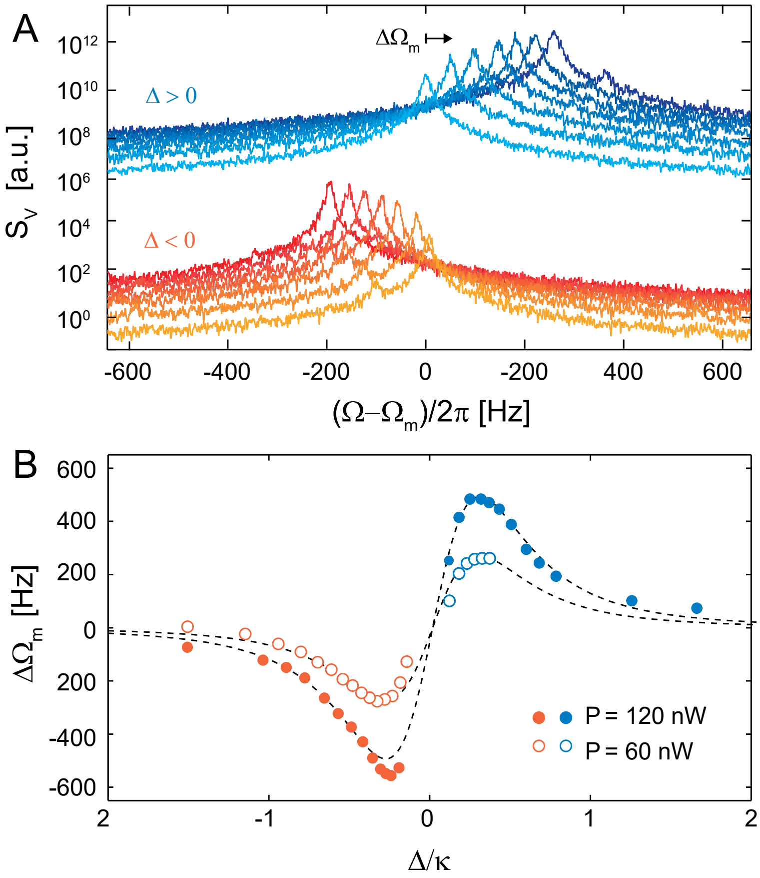

Figure 2.6 – **Characterization of optical spring:** (A) Thermal noise spectrum of the fundamental beam mode as a function of laser detuning. Blue and red spectra indicated blue ($\Delta > 0$) and red ($\Delta < 0$) detuning, respectively. Lighter shades indicate smaller detuning. Blue spectra are vertically offset. (B) Plot of optical spring shift, $\Delta\Omega_\mathrm{m}$, versus normalized detuning, Δ/κ. Dashed black lines are a fit to eq. (2.2.2) using g_0 as a free parameter.

A representative measurement is shown in fig. 2.5C. Red, blue, and grey components correspond to thermal noise, $S_\omega^\mathrm{th}(\Omega)$, the calibration tone, $S_\omega^\mathrm{cal}(\Omega)$, and measurement imprecision, $S_\omega^\mathrm{imp}(\Omega)$, respectively. The full signal can be modeled as

$$\begin{aligned} S_\omega(\Omega) &= S_\omega^\mathrm{th}(\Omega) + S_\omega^\mathrm{cal}(\Omega) + S_\omega^\mathrm{imp}(\Omega) \\ &\approx 2g_0^2 n_\mathrm{th} \cdot \mathscr{L}(\Omega - \Omega_\mathrm{m}) + \frac{\beta_\mathrm{cal}^2 \Omega_\mathrm{cal}^2}{2} \cdot \mathscr{G}(\Omega - \Omega_\mathrm{cal}) + S_\omega^\mathrm{imp}(\Omega), \end{aligned} \tag{2.2.1}$$

where $\mathscr{L}(\Omega) = 4\Gamma_\mathrm{m}/(\Gamma_\mathrm{m}^2 + 4\Omega^2)$ is a normalized Lorentzian (characterizing the mechanical susceptibility) and $\mathscr{G}(\Omega) = e^{-\Omega^2/(2B^2)}/\sqrt{2\pi B^2}$ is a normalized Gaussian (characterizing the window function of the spectrum analyzer, which is assumed to have a resolution bandwidth $B \ll \Gamma_\mathrm{m}$). To calibrate the vertical axis in fig. 2.5C, it is assumed that $|G_{V\omega}(\Omega_\mathrm{m})| \approx |G_{V\omega}(\Omega_\mathrm{cal})|$. Fitting the calibrated spectrum to (2.2.1) gives Ω_m, Γ_m, and g_0. Determination of g_0 requires that n_th is known. By using input powers low enough to neglect photothermal/radiation pressure damping ($\sim$ 10 nW), we assume that $n_{\mathrm{th}} \approx k_{\mathrm{B}} \cdot 295\,\mathrm{K}/(\hbar\Omega_{\mathrm{m}})$. Practically, a sufficiently low input power is determined by reducing the cavity power until the inferred g_0 saturates to a minimum value.

2.2.3 Optical spring characterization

As a cross-check of the thermal noise measurement, g_0 was independently estimated from the optical spring effect [21]. In the experimentally relevant bad cavity limit ($\Omega_{\mathrm{m}} \ll \kappa$), the mechanical frequency shift produced by a radiation pressure optical spring is

$$\Delta\Omega_{\mathrm{m}}(\Delta) \approx \frac{8g_0^2}{\kappa} \cdot n_{\mathrm{c}}(\Delta) \cdot \frac{\Delta/\kappa}{1+4(\Delta/\kappa)^2} \tag{2.2.2}$$

where Δ is the laser-cavity detuning, $n_{\mathrm{c}}(\Delta) = (4P/(\hbar\omega_0\kappa))(\kappa_{\mathrm{ex}}/\kappa)/(1+4(\Delta/\kappa)^2)$ is the intracavity photon number, and P is the power injected into the cavity. (We note that radiation pressure damping also occurs for a detuned input field; however, in the devices studied, for which $\Omega_{\mathrm{m}}/\kappa \sim 0.01$, this effect was found to be overwhelmed by photothermal damping [68]).

A measurement of the optical spring effect is shown in fig. 2.6, corresponding to the sample also characterized in fig. 2.5c. The injected powers used — $P = 60, 120$ nW — were chosen to avoid instabilities due to photothermal/radiation pressure damping. The cavity was critically coupled ($\kappa_{\mathrm{ex}} \approx \kappa/2 \approx 2\pi \cdot 550$ MHz) and laser detuning was estimated from the mean transmitted power. Overlaid models correspond to (2.2.2) with the value $g_0 = 2\pi \cdot 60$ kHz, inferred from a least-squared fit to the low power measurement. This value is within 10% of that inferred from thermal noise in fig. 2.5c.

2.2.4 Coupling dependence on nanobeam position

As discussed in section 2.1.3, g_0 depends sensitively on the lateral positioning of the nanobeam, and assumes a maximum (minimum) value for out-of-plane (in-plane) flexural modes when centered above the WGM. This behavior was studied by sweeping the lateral position of the beam within the lithography step where its geometry is defined (see chapter 3). Measurements of g_0 versus lateral beam position are shown in fig. 2.7A. Results shown here are for beam and disk dimensions of $\{l, w, t\} = \{60, 0.4, 0.06\}$ μm and $\{r, t_{\mathrm{d}}, \theta\} = \{15\,\mu\mathrm{m}, 0.60\,\mu\mathrm{m}, 30\,\mathrm{deg.}\}$, respectively, and for a vertical gap of 25 nm. In agreement with numerical modeling (dashed line), g_0 assumes a maximum of $2\pi \cdot 40$ kHz as the outer edge of the beam eclipses the rim of the disk.

Also shown in fig. 2.7b are measurements of κ versus lateral beam position (y). When the beam is displaced far from the disk, κ converges to the intrinsic value of $\sim 2\pi \cdot 100$ MHz observed in fig. 2.3, suggesting that the processing described in chapter 3 does not significantly affect microdisk surface quality. As the beam is brought within 100 nm of the disk, κ is observed to increase sharply. The observed exponential dependence κ on y is independent of mode

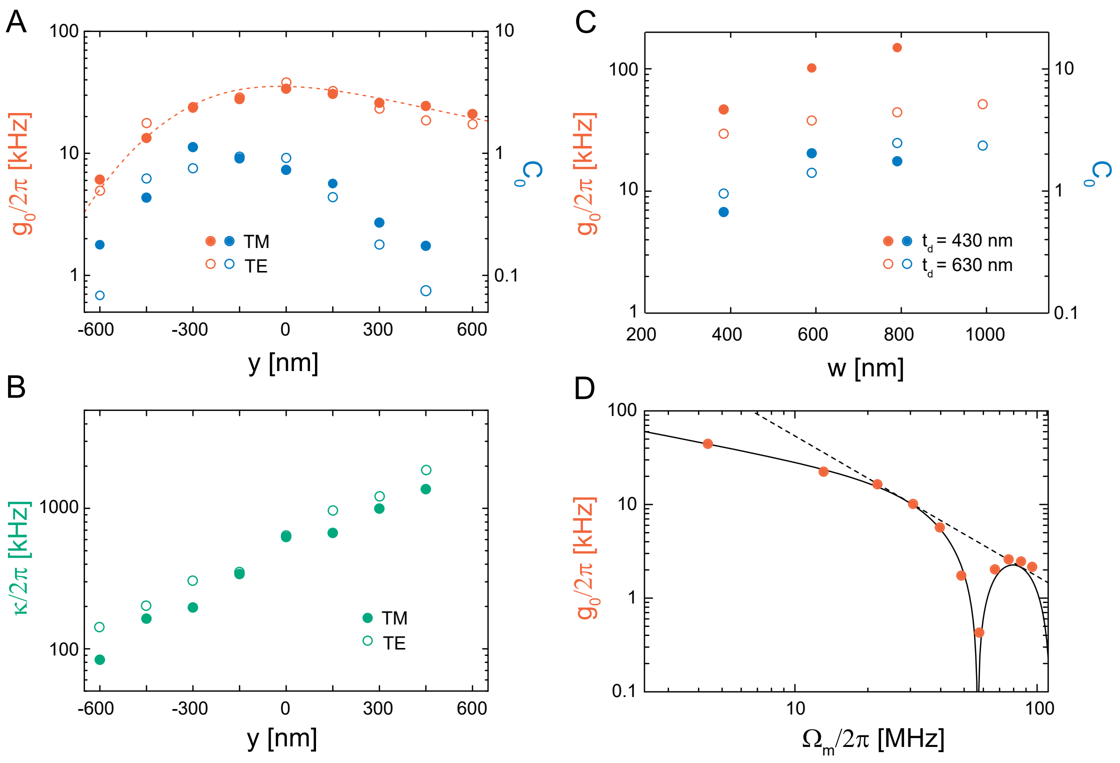

Figure 2.7 – **Optomechanical characterization of system:** (A) Measured vacuum optomechanical coupling rate (g_0) and cooperativity (C_0, assuming $\Gamma_\mathrm{m} = 2\pi \cdot 20$ Hz) versus lateral beam position (y) for TM (solid circles) and TE (open circles) cavity modes. (B) Corresponding intrinsic cavity decay rate (κ_0). (C) Measured g_0 versus beam width (w) for two disk thicknesses (t_d). (D) Measured g_0 versus mode frequency, $\Omega_\mathrm{m}^{(n)} \approx n\Omega_\mathrm{m}^{(0)}$. Red dots correspond to odd harmonics ($n = 1, 3, 5...$). Solid and dashed lines are model curves (Eq. 2.2.3b) for a sampling length of $l_\mathrm{eff} = 9.6$ and $l_\mathrm{eff} = 0$, respectively

polarization and similar to the scaling observed in [45] with a beam coupled to a microtoroid. The absolute magnitude of the loss is also inconsistent with bulk Si_3N_4 optical absorption — specifically, accounting for the relatively small fraction of energy stored in the beam, the observed loss would require an imaginary index of $\sim 10^{-4}$, which is 1-2 orders of magnitude larger than conventionally observed for Si_3N_4 at NIR wavelengths [56, 69]. We thus conjecture that this loss is due to scattering from and/or waveguide coupling into the beam.

Combining measurements of g_0 and κ with a typical room temperature mechanical damping rate of $\Gamma_\mathrm{m} = 2\pi \cdot 15$ Hz (we observed no change in Γ_m for small beam-disk separation, suggesting that squeeze-film gas damping [53] was not a factor), the single-photon cooperativity is observed to approach $C_0 \sim 1$. This value is limited by the unfavorable scaling of g_0^2/κ as g_0 begins to saturate. Despite this limitation, the inferred C_0 represents a nearly 50 dB increase over our prior chip-scale implementation [44], owing to the combined 100-fold increase of g_0 and 10-fold reduction in κ. Increase g_0 is due to the precise vertical and lateral positioning of the beam afforded by CMP and e-beam processing. Reduced κ is due to greater isolation of the disk during beam patterning, making use of the poly-Si sacrificial layer and Al_2O_3 etch-stop layer. Figure 2.7b suggests that κ is ultimately dominated by beam-induced scattering/absoption loss, rather than deterioration of intrinsic disk quality resulting from the fabrication steps taken to integrate the beam (fig. 2.3). This implies that an additional 10-fold reduction in κ may yet be realized with appropriate beam shaping or positioning.

2.2.5 Coupling dependence on microdisk and nanobeam thickness

Wider beams ($w \sim \lambda$) and thinner disks ($t_\mathrm{d} < \lambda$) were fabricated in an attempt to increase g_0 and C_0 by increasing the mode overlap and evanescent field energy, respectively (see eq. (2.1.5)). Measurements of $\{g_0, C_0\}$ vs w for two microdisk thicknesses, $t_\mathrm{d} \approx 0.43$ and $0.63\ \mu$m, are shown in fig. 2.7C. Fixed dimensions of the nanobeam and microdisk are $\{t, l\} \approx \{0.06, 60\}\ \mu$m and $\{r_\mathrm{d}, \theta\} \approx \{15\ \mu\mathrm{m}, 30\ \mathrm{deg.}\}$, respectively. The lateral beam position was chosen to maximize g_0 for the 0.4 μm-wide beam (see fig. 2.7). For the TE optical modes studied, a roughly $2\times$ increase in g_0 was observed for the 30% thinner disk. In both cases, g_0 scaled roughly linearly for widths $w \in [0.4, 1]\ \mu$m. C_0 also increased with w, roughly in proportion to g_0^2, for both t_d. This is due to the fact that κ (not shown) was roughly independent of w for both disk thicknesses and a factor of four larger for the thinner disk. The highest optomechanical coupling rate we have measured, $g_0 \approx 2\pi \cdot 150$ Hz, was for a 1 μm-wide beam coupled to a 0.43 μm-thick disk. The highest cooperativities observed, $C_0 > 2.5$, were for 1 μm-wide beams coupled to disks of both thicknesses.

2.2.6 Coupling dependence on mechanical mode number

g_0 was also studied for higher order mechanical modes. As shown in fig. 2.7D, g_0 decreases as the vibrational node spacing approaches the dimensions of the effective sampling length l_eff. In this case the model in section 2.1.3 — which assumes rigid displacement of a beam with effective mass $m = \rho t w l/2$ — breaks down. A simple extension of the model is shown as a red line in fig. 2.7D. Here m is computed with respect to optical-intensity-weighted displacement of the mechanical mode:

$$m = \frac{\int_\mathrm{beam} \rho |u(r)|^2 d^3 r}{|\int_\mathrm{beam} |E(r)|^2 u(r) d^3 r / \int_\mathrm{beam} |E(r)|^2 d^3 r|^2} \approx \frac{\rho t w l}{1-(-1)^n} \frac{1}{\mathrm{sinc}^2\left(\frac{n\pi}{2}\frac{l_\mathrm{eff}}{l}\right)} \tag{2.2.3}$$

where $\vec{u}(x, y, z) \approx \sin(n\pi x/l)\hat{z}$ is the displacement profile of the n^th-order out-of-plane flexural mode. The latter expression is appropriate when the transverse dimensions of the beam are much smaller than that of the WGM, and assumes that the intensity distribution sampled by the beam is uniform along the beam axis with an effective sampling length l_eff. Using $\Omega_\mathrm{m} \propto n$ gives $g_0^{(n)}/g_0^{(0)} \approx |\mathrm{sinc}\left(\frac{n\pi}{2}\frac{l_\mathrm{eff}}{l}\right)|/\sqrt{n}$ for odd n and 0 for even n. The model shown in fig. 2.7d agrees quantitatively with experiment assuming an effective length of $l_\mathrm{eff} = 9.6\ \mu$m as the only free parameter. A simple route to increasing g_0 would be to remove mass from the beam outside of the effective sampling length (see fig. 2.9).

2.3 Displacement sensitivity

As an illustration of device performance, we use the microdisk to perform a cavity-enhanced interferometric measurement of the beam's displacement. For this purpose, the fiber taper and microdisk are embedded in one arm of a length- and power-balanced homodyne interferometer (fig. 2.5). The cavity is driven on resonance using the Pound-Drever-Hall technique. A piezoelectric mirror is use to stabilize the interferometer path length difference so that the homodyne photocurrent is proportional to the phase of the transmitted cavity field.

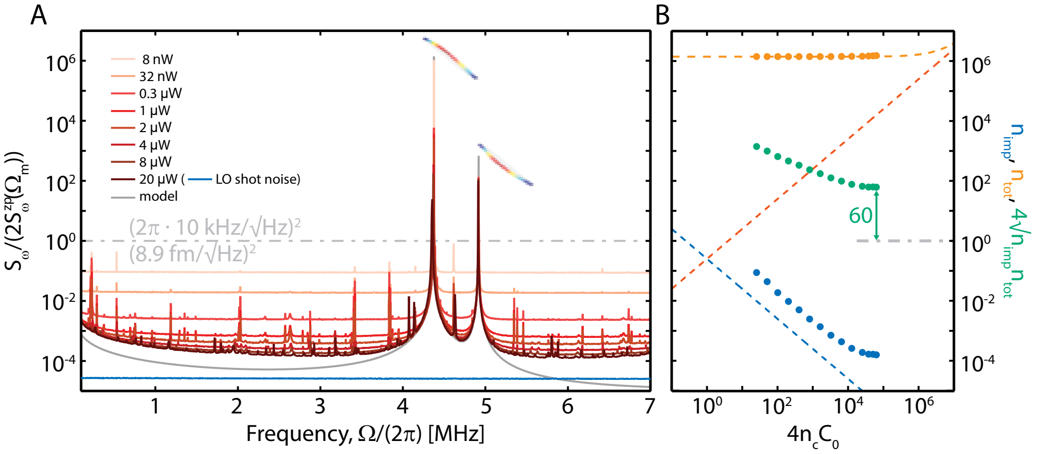

Figure 2.8 – **Nanobeam displacement noise:**(A) measured by balanced homodyne detection of the microdisk output field, for various input powers. Noise spectra are expressed in units relative to the cavity frequency noise produced by one phonon of fundamental out-of-plane vibration, $2S_\omega^{\mathrm{zp}}(\Omega_\mathrm{m}) = (2\pi\cdot 10\,\mathrm{kHz}/\sqrt{\mathrm{Hz}})^2$, where $\Omega_\mathrm{m} = 2\pi{\cdot}4.4$ MHz. At large powers, the fundamental noise peak is shifted and broadened by optical spring softening and damping, respectively. The peak at 4.9 MHz is due to thermal motion of the fundamental in-plane mode. The gray curve is a model for the intrinsic thermal motion of the fundamental out-of-plane and in-plane modes ((2.3.1)). (B) Measured phonon equivalent displacement, $n_\mathrm{tot} = S_\omega(\Omega_\mathrm{m})/2S_\omega^{\mathrm{zp}}(\Omega_\mathrm{m})$, displacement imprecision, $n_\mathrm{imp} \equiv S_\omega^{\mathrm{imp}}(\Omega_\mathrm{m})/2S_\omega^{\mathrm{zp}}(\Omega_\mathrm{m})$, and their geometric mean versus intracavity photon number n_c weighted by single-photon cooperativity C_0. Dashed lines denote ideal values for $n_\mathrm{tot} = n_\mathrm{th} + n_\mathrm{ba} + n_\mathrm{imp}$ (orange), $n_\mathrm{ba} = C_0 n_\mathrm{c}$ (red), and $n_\mathrm{imp} = 1/16C_0 n_\mathrm{c}$ (blue), using $n_\mathrm{th} \approx 1.4\cdot 10^6$ and $C_0 = 0.45$. Green arrow indicates proximity to the uncertainty limit, $4\sqrt{n_\mathrm{imp} n_\mathrm{tot}} \geq 1$.

Displacement noise spectra are shown in fig. 2.8A for a $\{l, w, t\} = \{60, 0.4, 0.06\}$ μm beam with a vertical beam-disk separation of approximately 35 nm and optomechanical parameters $\{\Omega_\mathrm{m}, \Gamma_\mathrm{m}, \kappa, g_0, C_0\} \approx \{2\pi\cdot 4.4\,\mathrm{MHz}, 2\pi\cdot 10\,\mathrm{Hz}, 2\pi\cdot 700\,\mathrm{MHz}, 2\pi\cdot 28\,\mathrm{kHz}, 0.45\}$. Here κ corresponds to the critically-coupled cavity linewidth and other parameters correspond to the fundamental out-of-plane mechanical mode. For the measurements shown, the cavity was critically coupled and the power of the input field was swept from $0.01-20$ μW. The homodyne photocurrent noise spectrum is plotted in units relative to the signal produced by a phonon of displacement $2S_\omega^{\mathrm{zp}}(\Omega_\mathrm{m}) \approx (2\pi\cdot 10\,\mathrm{kHz}/\sqrt{\mathrm{Hz}})^2$ (equivalent to $2S_x^{\mathrm{zp}}(\Omega_\mathrm{m}) \approx (2\pi\cdot 8.9\,\mathrm{fm}/\sqrt{\mathrm{Hz}})^2$ assuming $x_\mathrm{zp} = 25$ fm). In these units, the magnitude of the fundamental thermal noise peak (neglecting photothermal or dynamical back-action) is equal to the effective thermal occupation $n_\mathrm{tot} \equiv S_\omega(\Omega_\mathrm{m})/(2S_\omega^{\mathrm{zp}}(\Omega_\mathrm{m}) = n_\mathrm{th} + n_\mathrm{ba} + n_\mathrm{imp}$, where $n_\mathrm{th} \equiv S_\omega^{\mathrm{th}}(\Omega_\mathrm{m})/2S_\omega(\Omega_\mathrm{m})$ is the ambient bath occupation, n_ba is the effective thermal bath occupation associated with classical and quantum measurement back-action (radiation pressure shot noise), and

$n_{\mathrm{imp}} \equiv S_\omega^{\mathrm{imp}}(\Omega_{\mathrm{m}})/2S_\omega^{\mathrm{zp}}(\Omega_{\mathrm{m}})$ is the apparent thermal occupation associated with the measurement imprecision. The noise spectra are calibrated by bootstrapping a low power measurement to $n_{\mathrm{tot}} \approx n_{\mathrm{th}} \approx k_{\mathrm{B}}T/\hbar\Omega_{\mathrm{m}} \approx 1.4 \cdot 10^6$ (for larger optical powers, dynamic spring/-damping forces modify the peak value, $S_\omega(\Omega_{\mathrm{m}})$). At the highest optical powers, the displacement imprecision in the vicinity of Ω_{m} is estimated (from the saddle at 2.5 MHz) to be $n_{\mathrm{imp}} \approx 1.5 \cdot 10^{-4}$, while the shot-noise imprecision (blue curve, obtained by decoupling the fiber from the cavity) is $n_{\mathrm{imp}}^{(\mathrm{shot})} \approx 2.6 \cdot 10^{-5}$. These correspond to imprecisions 32 and 40 dB below that at the SQL ($n_{\mathrm{imp}} = 0.25$), respectively. The magnitude of the extraneous imprecision, $2S_\omega^{\mathrm{zp}}(\Omega_{\mathrm{m}}) \cdot (n_{\mathrm{imp}} - n_{\mathrm{imp}}^{(\mathrm{shot})}) \approx (2\pi \cdot 110\,\mathrm{Hz}/\sqrt{\mathrm{Hz}})^2$, is independent of optical power and gives rise to the saturation of the blue points in 2.8b. This extraneous noise is consistent with a mixture of diode laser frequency noise ($\sim 30\,\mathrm{Hz}/\sqrt{\mathrm{Hz}}$ [28]), thermorefractive noise ($\sim 10\,\mathrm{Hz}/\sqrt{\mathrm{Hz}}$ [40]), and off-resonant thermal noise ($\sim 70\,\mathrm{Hz}/\sqrt{\mathrm{Hz}}$). The latter is estimated using the 'structural damping' model of Saulson [5],

$$\frac{S_\omega(\Omega)}{2S_\omega^{\mathrm{zp}}(\Omega_{\mathrm{m}})} \approx n_{\mathrm{th}} \frac{\Omega_{\mathrm{m}}}{\Omega} \frac{\Gamma_{\mathrm{m}}^2 \Omega_{\mathrm{m}}^2}{(\Omega^2 - \Omega_{\mathrm{m}}^2)^2 + \Gamma_{\mathrm{m}}^2 \Omega_{\mathrm{m}}^2} \gtrsim \frac{7 n_{\mathrm{th}}}{Q_{\mathrm{m}}^2}, \tag{2.3.1}$$

shown in gray in fig. 2.8, for $Q_{\mathrm{m}} = \Omega_{\mathrm{m}}/\Gamma_{\mathrm{m}} = 4.4 \cdot 10^5$.

The total efficiency of the measurement is estimated by comparing the power dependence of the imprecision (n_{imp}), the effective thermal bath occupation (n_{tot}), and their geometric mean $\sqrt{n_{\mathrm{imp}} n_{\mathrm{tot}}}$ to the ideal values $1/(16 C_0 n_{\mathrm{c}})$, $C_0 n_{\mathrm{c}}$, and $1/4$, respectively, where the last case represents the Heisenberg uncertainty limit. As shown on the right hand side of fig. 2.8, the imprecision is a factor of 7.5 larger than ideal, due to a combination of cavity loss (50%, corresponding to critical coupling), taper loss (~ 10%), homodyne detector loss/misalignment, and optical mode splitting [28]. The effective thermal bath occupation is inferred by fitting to the off-resonant tail of the fundamental noise peak (to avoid the systematic error due to optical damping). From these fits we infer a heating of $C_0^{\mathrm{ext}} \equiv (n_{\mathrm{tot}} - n_{\mathrm{th}})/n_{\mathrm{c}} = 1.4$, two times larger than expected due to quantum measurement back-action. The imprecision-back-action product is constrained, at high powers, to $4\sqrt{n_{\mathrm{imp}} n_{\mathrm{tot}}} \approx 60$, due to the saturation of the measurement imprecision. To the best of our knowledge, this represents the closest approach to the uncertainty limit for a room temperature mechanical oscillator.

2.4 Conclusion

We have presented a method to heterogeneously integrate a high-stress, Si_3N_4 nanobeam within the evanescent near-field of a SiO_2 microdisk. Building on earlier strategies [40, 44], the principle advance is a fabrication technique which preserves the high Q/(mode volume) ratio of each resonator while enabling the beam and the disk to be separated by a vacuum gap of 10-100 nm — significantly smaller than the evanescent decay length of the optical mode. Samples of various dimensions were fabricated and characterized. Simultaneously low mechanical loss, $\Gamma_{\mathrm{m}} = 2\pi \cdot (10 - 100)$ Hz, low optical loss, $\kappa = 2\pi \cdot (100 - 1000)$ MHz, and

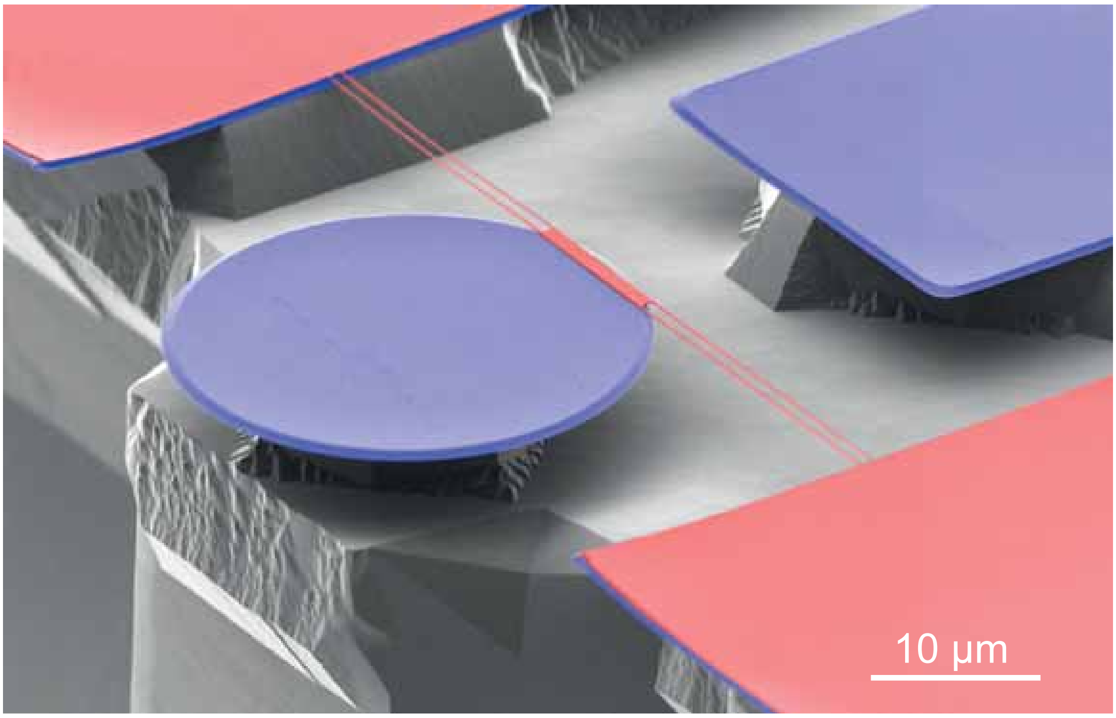

Figure 2.9 – **Tethered nanobeam integration:** suspending the nanobeam from tethers enables higher g_0 by reducing mass without changing optomechanical mode overlap. Here the central beam coincides with the effective sampling length of the optical mode.

large optomechanical coupling rates, $g_0 = 2\pi \cdot (10-100)$ kHz, were measured, corresponding to room temperature single-photon cooperativities as high as $C_0 \equiv 4g_0^2/\Gamma_m\kappa = 2$.

The reported system holds particular promise as a quantum-limited displacement sensor, owing to the large vacuum displacement of the nanobeam and the high power handling capacity of the microdisk. For a typical device, possessing $\{\Omega_m, \Gamma_m, \kappa_0, g_0\} \approx 2\pi \cdot \{4.5\,\text{MHz}, 15\,\text{Hz}, 500\,\text{MHz}, 50\,\text{kHz}\}$, the resonant vacuum displacement noise, $S_\omega^{zp}(\Omega_m) = 4g_0^2/\Gamma_m \approx (2\pi \cdot 26\ \text{kHz}/\sqrt{\text{Hz}})^2$, is orders of magnitude larger than major sources of imprecision — such as laser frequency and thermorefractive noise [45] — and commensurate with shot noise for an ultra-low intracavity photon number of $n_c = 1/(16C_0) = 0.05$ [28]. Operating a similar device at 4 K with $n_c \sim 10^5$ (corresponding to $P \sim 100\ \mu$W when critically coupled to the fiber waveguide), we were recently able to achieve a displacement imprecision n_{th} times (43 dB) below S_ω^{zp}, while maintaining an imprecision-back-action product within a factor of 5 of the uncertainty limit [28]. This regime of ‘efficient’ measurement — characterized by the ability to resolve a phonon-equivalent displacement in the thermal decoherence time — enabled us to feedback-cool the mechanical mode to near its ground state [28], and might be extended to other quantum control tasks, such as squeezed-state preparation [33].

An intriguing question is whether the reported device may be used to realize Heisenberg-limited displacement measurements at room temperature — namely, an apparent imprecision-back-action product $(n_{ba}+n_{th}) \cdot n_{imp} \to 1/4$ (see section 2.3). For the radio frequency oscillators under study ($n_{\mathrm{th}} \sim 10^6$), the main challenges are (1) pumping the cavity with $n_{\mathrm{c}} = n_{\mathrm{th}}/C_0 \sim 10^6$ photons in order to achieve the necessary measurement strength (characterized by a phonon-equivalent RPSN of $n_{\mathrm{ba}} = C_0 n_{\mathrm{c}} > n_{\mathrm{th}}$), (2) reducing extraneous sources of measurement imprecision to $S_\omega^{\mathrm{zp}}/n_{\mathrm{th}} < (2\pi \cdot 10\,\mathrm{Hz}/\sqrt{\mathrm{Hz}})^2$, and (3) reducing extraneous heating to ensure that n_{ba} is dominated by RPSN. Because of the (blue-stable) thermal self-locking effect in room temperature $\mathrm{SiO_2}$ microresonators [70], the first requirement is expected to be limited by parametric radiation pressure instabilities, requiring active feedback damping. The second requirement — for microdisks with dimensions studied here — is expected to be limited by thermorefractive noise at the level of $S_\omega^{\mathrm{trn}} \sim (2\pi \cdot 10\,\mathrm{Hz}/\sqrt{\mathrm{Hz}})^2$ [45], an impressive 60 dB lower than S_ω^{zp}. Reaching $S_\omega^{\mathrm{trn}} < S_\omega^{\mathrm{zp}}/n_{\mathrm{th}}$ would require a moderate increase in $g_0^2 \cdot Q_{\mathrm{m}}$ (for instance, by using lower-mass, “tethered" beams [29]; see fig. 2.9). The third requirement depends on the details of the nanoscale heat transfer process. At 4 K, we have observed photothermal heating consistent with an extraneous cooperativity of $C_0^{\mathrm{ext}} \equiv n_{\mathrm{ba}}^{\mathrm{ext}}/n_{\mathrm{c}} \sim 1$ [28]; we anticipate this heating to reduce to tenable levels ($C_0^{\mathrm{ext}} < C_0$) at room temperature, provided that the underlying process is related to the temperature-dependent thermal conductivity of amorphous glass [71]. Preliminary room temperature measurements, discussed in section 2.3, suggest that $C_0^{\mathrm{ext}} \sim C_0$ can be met for a moderate $C_0 \sim 0.8$.

In addition to high cooperativity, the evanescent sensing platform and reported fabrication method have as a compelling feature the ability to incorporate new materials and/or planar geometries above a high-Q microdisk with nanometric precision. This capability opens the door to a variety of “hybrid" sensing applications. For example, the system may be electrically functionalized by vertically integrating the beam into a parallel plate capacitor, or into the gradient field between two closely spaced electrodes [72]. This interface — which need not compromise the mechanical quality of the beam [73] — can form the basic building block of a high-efficiency electro-optic converter, with applications such as precision radio wave sensing [74]. Pushed to a different extreme, two dimensional materials such as graphene or $\mathrm{MoS_2}$ may be integrated with a microdisk by using the SiN film as a sacrificial substrate [75]. Another intriguing possibility, in conjunction with the preparation of low entropy mechanical states using measurement-based feedback, is to functionalize the beam with a two-level system, such as an NV center embedded in a diamond nanocrystal [76]. Nanobeams integrated with microdisks may also serve as a platform for remotely-coupled “atom-optomechanics" [77, 78], taking advantage of the low oscillator mass, high cavity finesse, and recent developments in fiber-based atom traps [79]. In addition, we note that the ability to perform broadband, thermal-noise-limited measurements of high-Q nanomechanical oscillators (c.f. fig. 2.8) may help shed light on the microscopic origin of intrinsic damping [80].

Finally, we remark that while our discussion has focused on quantum (imprecision and back-action) noise in the measurement of nanomechanical motion, nanomechanical sensors of mass/force/charge are in fact fundamentally limited by thermal motion. For such applications, the practical utility of the reported high-cooperativity evanescent sensing platform lies in the ability to resolve thermal motion with high signal-to-noise and large bandwidth for devices with widely-varying in-plane geometry. (By contrast, thermal motion in MEMS sensors is typically masked by Johnson noise.) [81]. This might enable, for instance, precision force sensors based on high-Q nanomechanical beam oscillators [44] or chip-scale accelerometers based on membrane-like micromechanical test masses [82]. For the nanobeam displacement measurements shown in fig. 2.8, thermal noise is resolved over a bandwidth of ~ MHz at the level of $4k_B T\Gamma_m m \sim (100\,\mathrm{aN}/\sqrt{\mathrm{Hz}})^2$ employing $\sim 10\,\mu\mathrm{W}$ of injected optical power. Notably, a moderate reduction in extraneous imprecision would enable thermal noise to be resolved over a full octave, a difficult challenge for high-Q resonators as it requires resolving the thermal peak with a signal-to-noise of $\sim Q^2$ ((2.3.1)).

3 System fabrication

This following chapter provides an overview of the fabrication process used to realize the monolithic optomechanical devices described in chapter 2. The first two sections introduce the film deposition techniques used to realize the materials that compose our device (section 3.1), and the dry etching methods used in many steps throughout process (section 3.2). These concepts are fundamental to understanding the processes and design choices employed in the work described in the remainder of the chapter, as well as in appendix B, appendix C and appendix D. These sections are intended to present the concepts as they pertain to the work herein, and a reader unfamiliar with them, who would like to understand remainder of the chapter is highly recommended to start here. It should also be mentioned that this presentation assumes the reader is familiar with the basic processes of microfabrication, such as pattern transfer by photolithography. Following this introduction, the fabrication process is described sequentially, starting with patterning of the microdisk (section 3.3.1), planarization of a sacrificial layer (section 3.3.2), construction of the nanobeam (section 3.3.5), and structural release of the device (section 3.3.6). Less common topics, such as chemical mechanical planarization (CMP) or atomic layer deposition (ALD) are described within the relevant sections.

All steps were carried out in the Center of Micronanotechnology (CMi) at École Polytechnique Fédérale de Lausanne. The facility is designed around 100 mm wafer processing and contains a wide array of processing equipment encompassing photolithography, electron-beam lithography (e-beam), dry and wet etching, chemical vapor and atomic layer deposition, mechanical planarization, metal evaporation, wafer bonding, and wire bonding. There are also a wide variety of metrology tools available, including optical microscopy, scanning electron microscopy (SEM), atomic force microscopy, profilometry, and ellipsometry.

3.1 Materials synthesis

The substrate used during the fabrication process described below is crystalline silicon, and in order to realize the final structure described herein several steps of film growth and deposition must take place. A high purity silicon dioxide is desired in order to form a microdisk with low losses and high linearity (see section 2.1.2). Since this film is grown by oxidation of the silicon substrate, it is critical that the substrate itself has a low level of impurities, as these impurities will end up being incorporated into the resulting silicon dioxide. The wafers we use to realize our devices are produced by a method known as float zone crystal growth.

3.1.1 Silicon crystal growth

Typically, crystalline silicon ingots (called *boules*) are produced by a method known as Czochralski (CZ) crystal pulling method. This method, originally developed by Polish chemist Jan Czochralski in 1915 [83] is to this day the most commonly used method of silicon crystallization. It consists of dipping a silicon crystal *seed* into a slowly rotating molten polysilicon bath and pulling it upwards, drawing out silicon from the bath. The molten silicon is contained in a quartz crucible and heated to ~1500 °C. As the silicon is drawn out and cools, it crystallizes around the seed, forming an extended single crystal. This process requires that the molten polysilicon be highly purified, as any contaminants will be included in the resulting boule. Moreover, the molten silicon reacts with the quartz crucible releasing oxygen and any contaminants which exist in the quartz.

Float zone growth

Float zone (FZ) crystal growth (or FZ refining) gets around the above contamination problem by avoiding contact with a crucible. This method was developed by chemical engineer Henry Theuerer at Bell Labs in the early 1950s [85]. Here a solid polysilicon rod is suspended vertically with a heating coil closely following its circumference, surrounding it locally as seen in fig. 3.1. The coil can be translated vertically along the rod creating a local hot zone. This allows for the silicon to be locally melted and then recrystallize, as the coil moves along the rod and the previously molten silicon cools. The equipment is housed in an inert gas environment to avoid inclusion of gas

Figure 3.1 – **Start of float zone crystal growth:** Heating coil locally melts the polysilicon, attached to a thin top seed crystal layer [84]

contaminants in the silicon. The process starts at one end of the rod where a seed crystal is placed (see fig. 3.1). As the silicon recrystallizes during the process impurities are pulled away towards the molten zone, as most impurities are more soluble in the molten silicon than than the crystal. This process can be repeated many times to realize extremely high purity crystal, in a method known as *zone refining*. For the devices described in this chapter we use 100 mm diameter <100> (indicating the wafer is cut along the <100> plane) FZ silicon wafers with a resistivity of 15 000 ohm-cm. The high resistivity is indicative of extremely high purity. As such this is an excellent substrate for growing a silicon dioxide film with very low optical absorption properties. This is the next step in the fabrication process. Before describing the oxidation process, we first introduce the furnace arrangement used for this growth, as well as for depositing films such as polysilicon and silicon nitride (deposited in the steps described in section 3.1.2 and section 3.1.2, respectively).

3.1.2 Low-pressure chemical vapor deposition

The thin films used to construct our device - namely silicon dioxide, polysilicon, and silicon nitride - are produced using a low-pressure chemical vapor deposition (LPCVD) system. Technically, the silicon dioxide used in our process is not deposited but rather grown (LPCVD deposition of silicon dioxide is also possible). Nonetheless, it is grown in an LPCVD system. A typical LPCVD arrangement, as illustrated in fig. 3.3, consists of a reaction chamber containing closely spaced wafers standing on edge, embedded in a resistance-heated *hot wall* tube furnace under vacuum. Hot wall indicates that the walls of the furnace are heated rather than the walls of the reaction chamber, resulting in better temperature uniformity within the reaction chamber as compared to *cold wall* furnaces (direct heating of the reaction chamber). Precursor gases are introduced to the heated reaction chamber, where they adsorb onto the wafer surface, undergoing thermal dissociation and reacting to form the desired non-volatile product. Low pressure, typically ranging from 10-1000 mTorr, results in large diffusion coefficients for the precursor gases

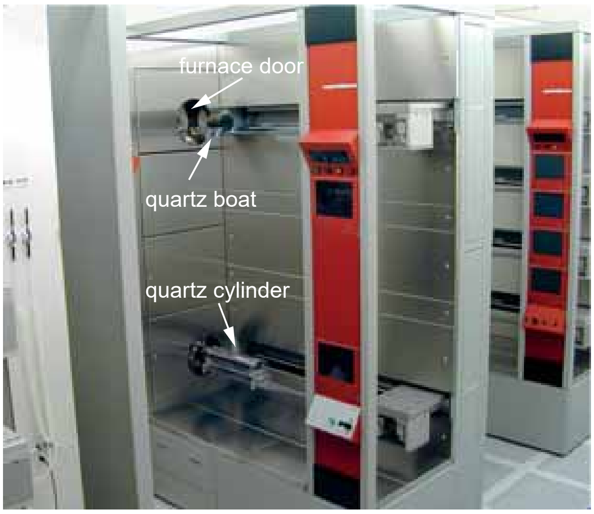

Figure 3.2 – **Centrotherm LPCVD system:** A loading arm containing wafers vertically placed on quartz boat, sits in front of LPCVD furnace door, with the reaction chamber recessed behind the wall

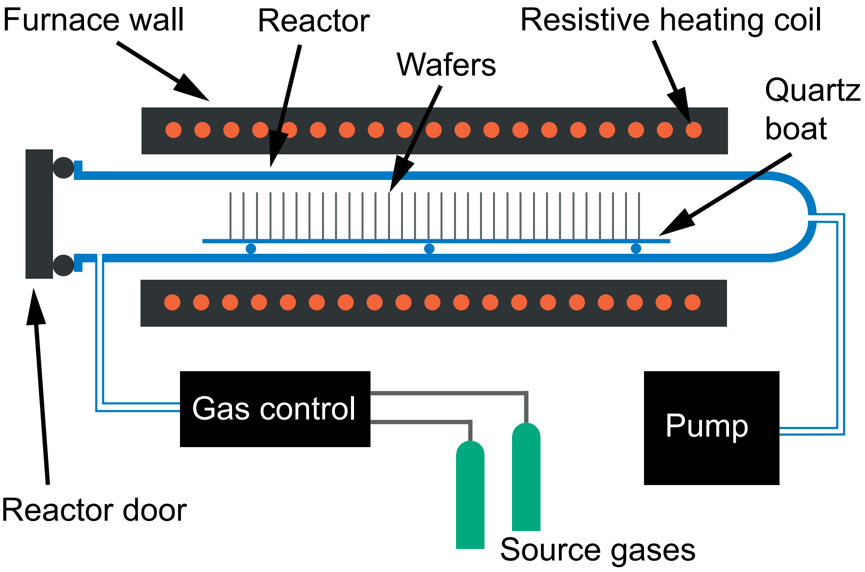

Figure 3.3 – **LPCVD reactor schematic:** consisting of a quartz reactor tube, containing wafers vertically stacked on a quartz carrier, embedded in a hot wall furnace. The furnace walls are resistively heated to a temperature range of 300-1100 °C. The reactor tube is kept under vacuum, ranging from 100-1000 mTorr. The reactant source gas flow rates are external controlled and fed into one end of the tube, while a vacuum pump attached to the other end maintains a stable pressure.

which is critical to operating in the regime where reaction rates are temperature-limited rather than being limited by mass transport. This regime, typically referred to as *surface-reaction limited* results in highly uniform films and the ability to stack wafers very densely. The hot wall furnace configuration is also key to high temperature uniformity, and thus uniform reaction rates, but requires frequent maintenance as films are also deposited on the reactor walls and can lead to particle contamination from flaking off. Deposited films typically have thickness variations of <5%. The reactor chamber (indicated in fig. 3.3) is normally made of quartz and operates in a range of 300-1100 °C. Typically operation pressure during film deposition is 100-1000 mTorr.

The LPCVD system used in the CMi is produced by Centrotherm and can hold up to 75 wafers. As can be seen in figs. 3.2 and 3.3 the wafers are stacked vertically on a quartz holder (typically called a *boat*), which is loaded into the furnace by a robotic arm. The wafers are sometimes enclosed in a quartz cylinder (bottom of fig. 3.2) to avoid particle contamination from the reactor walls. Once the wafers are loaded into the chamber and have thermalized, the reactant gases are introduced to one end of the furnace and evacuated from the other end (flowing perpendicular to the wafer surface). The Centrotherm chamber in the CMi is capable of a maximum temperature of 1050 °C.

Silicon nitride deposition

Silicon nitride is widely used in semiconductor manufacturing as an insulator, diffusion barrier, or an etch mask [86, 87]. In addition, the large tensile stress that can be achieved has been exploited to increase mobility in modern strained channel transistors [88]. Our devices also exploit this stress, but for the purpose of reducing mechanical dissipation (see section 2.1.1). It is by making use of the LPCVD nitride deposition process that we are able to achieve tensile stress of ~1 GPa.

In an LPCVD process silicon nitride is deposited by adsorbed gas phase reactions of silane (SiH_4) or dichlorosilane (SiH_2Cl_2) with ammonia (NH_3). Films grown in the CMi utilize dichlorosilane to produce silicon nitride by the following reaction mechanism:

$$3SiH_2Cl_2 + 4NH_3 \rightarrow Si_3N_4 + 6HCl + 6H_2 \tag{3.1.1}$$

Here SiH_2Cl_2 is preferred over SiH_4 as mass transport in the case of SiH_4 has a non-negligable effect on the deposition rate, leading to less uniform films [89]. In addition, SiH_4 more readily decomposes, leading to reactions in the gas bulk, and subsequent particle contamination. This reaction is carried out at a temperature of ~750 °C and ~200 mTorr pressure, where the kinetic product is favored [90], meaning that the deposition rate is highly dependent on temperature and reactant partial pressure. Thus, formation of the stoichiometric product in eq. (3.1.2) (Si_3N_4) requires the correct balance of reactants delivered to the wafer surface. In practice this means operating with an excess of NH_3, where the ratio NH_3:SiH_2Cl_2 > 10:1 [91]. At lower ratios a silicon rich product is formed, which is sometimes desired due to its lower intrinsic stress.

However, in our case the high stress that can achieved for LPCVD nitrides is of key interest. The total stress in the film is a function of stress induced by thermal relaxation, σ_{th}, and the intrinsic deposition stress, σ_{i}. Thus we have, $\sigma_{\mathrm{total}} = \sigma_{\mathrm{th}} + \sigma_{\mathrm{i}}$. The thermal stress can be easily estimated from the elastic modulus of silicon nitride as well as the thermal expansion coefficients of Si and silicon nitride. At a deposition temperature of ~750 °C this implies a thermal stress of σ_{th} ~75 MPa. From this it is clear that the ~1 GPa stress achieved is dominated by deposition stress. This stress is generated by desorption of hydrogen and chlorine from the precursor molecules following the initial Si–N bond forming reactions on the wafer surface [92]. Thermal dissociation of Si–H and N–H, and subsequent rearrangement of dangling bonds to form stable Si–N bonds, leads to shrinkage of the film. It is this shrinkage that is the fundamental mechanism behind the generated stress. This process is highly sensitive to temperature, on which the deposition rate depends exponentially (as described by the empirical Arrhenius equation), and it has been demonstrated that at higher deposition temperatures stress is reduced. This is a result of incomplete dissociation of S–H and N–H bonds before the next molecular layer is deposited and thus reduced shrinkage of the film [91]. Deposition at higher temperatures is often used when *low stress* (hydrogen-rich) silicon nitride is desired. In the case of the CMi, the near-stoichiometric we utilize is deposited at ~770 °C, achieving a residual stress of ~1 GPa, whereas the *low-stress* variant is deposited at ~830 °C resulting in a stress of ~200 MPa.

Polysilicon deposition

Polycrystalline silicon, typically referred to as just polysilicon, is a common structural material in MEMS applications [93–96]. It is also used to form electrical leads and gate electrodes in metal oxide semiconductor fabrication [97, 98]. In our process polysilicon is used as a sacrificial material (see section 3.3.2) due to its high temperature compatibility (during silicon nitride deposition), compatibility with CMP techniques (exhibiting a ~1:1 selectivity to silicon dioxide) and ability to be rapidly dissolved in KOH during the structural release step, as described in section 3.3.6.

Polysilicon is deposited with LPCVD by reduction of silane at ~600 °C, producing hydrogen gas:

$$\mathrm{SiH_4} \rightarrow \mathrm{Si} + 2\mathrm{H_2} \tag{3.1.2}$$

LPCVD polysilicon exhibits a thickness dependent residual compressive stress that ranges from -450 MPa for films of ~100 nm to -300 MPa for films of ~1000 nm [99]. This variation in the value of compressive stress is attributed to the columnar growth of the constituent silicon grains. Initially the grains grow in arbitrary directions, with those grains with growing normal to the wafer dominating in thicker films, all the columns extend [99, 100]. Thus in the initial growth stage grains grow both in and out of plane, resulting in compressive stress. As growth competition favors those growing out of plane, stress is reduced in thicker films. Interestingly, it has been demonstrated that this stress relaxes to -50 MPa after annealing for 2 hours at 1000 °C and to -20 MPa when annealed at 1100 °C [101]. This may be of interest for future process modification, as discussed at in appendix B.6. However, in the current process polysilicon is not annealed and the resulting film, after CMP (see section 3.3.2), is assumed to have compressive stress of -300 to -350 MPa.

Silicon dioxide growth

As mentioned above in our case silicon dioxide is grown rather than being deposited. Bare silicon oxidizes at room temperature in reaction with ambient H_2O, forming a native oxide of ~2 nm. Further oxidation is prevented but low diffusivity of H_2O at room temperature. However, thicker silicon dioxides can be easily grown at elevated temperatures (typically 600-1200 °C), using either by *wet* or *dry* processes. The reaction processes for two types of growth processes are, respectively:

$$\mathrm{Si} + 2\mathrm{H_2O} \rightarrow \mathrm{SiO_2} + 2\mathrm{H_2} \quad \text{(wet oxidation)} \tag{3.1.3}$$

$$\mathrm{Si} + \mathrm{O_2} \rightarrow \mathrm{SiO_2} \quad \text{(dry oxidation)} \tag{3.1.4}$$

In addition, typically HCl or Cl_2 gas is also added to remove any metal impurities that would otherwise be incorporated into the oxide during growth. Chlorine reacts with metals to form volatile products that are then evacuated from the growth chamber (e.g. $AuCl_3$). During wet oxidation, hydrogen atoms create defects in the growth layer forming Si-H and O-H, resulting in increased optical absorption at telecom wavelengths. Dry grown silicon dioxide on the other hand is relatively defect free due to lack of hydrogen in the reaction process (in this case Cl_2, and not HCl, should be used as a metal scavenger). However, the dry oxidation process also proceeds at a much slower rate as a result of the fact that O_2 has a much lower partial pressure in SiO_2 as compared to H_2O (and thus proportionally lower concentration in the silicon dioxide). This is of relevance as the reactants must diffuse through the oxide layer to react at the SiO_2/Si interface. This difference is partial pressure leads to very large differences in growth time for thick films [102]. A practical example of this is that when growing a 750 nm layer of SiO_2 at 1050 °C, as is our case, dry oxidation takes ~40 hours whereas wet oxidation takes only ~2 hours. Regardless of the greatly increased expense, we opt for dry oxidation to ensure that material absorption is kept to a minimum in the optical resonator.

3.2 Dry Etching

Dry etching refers to set of techniques used to engrave solid surfaces using atoms or molecules in the gas phase. This may occur physically by ion bombardment, chemically with a reactive species or by a combination of these processes - the latter being the case for dry etches considered in the processes described in this chapter. In general dry etching involves the creation of a plasma using a diode (glow discharge etching) or triode configuration (ion-beam etching (IBE)). In the triode type dry etching system plasma is generated in a separate part of the vacuum chamber from where the substrate to be etched is located. Ions are extracted from the plasma through a grid electrode and focused in a beam towards the substrate. A non-reactive ion species (most often argon) is used for this process and etching occurs purely by momentum transfer from the impinging ions, causing material to be sputtered from the surface. In a diode type configuration the substrate is itself located on the cathode and enveloped by the plasma. This type of system may be operated in a mode where purely chemical etching occurs as a result of highly reactive neutral radical species generated in the plasma. This type of operation is known as chemical plasma etching (PE). Radical species diffuse from the plasma and adsorb on the substrate surface where they react with the material to be etched, forming volatile products that are evacuated from the system. The most common type of dry etching method, referred to as reactive ion etching (RIE) operates in a mode that combines both IBE-type and PE-type processes. In this case momentum transfer from ion bombardment is used to induce surface damage, making the substrate more reactive by creating dislocations and dangling bonds. The *activated* surface is then etched by radical neutrals formed in the plasma, as in the PE process. In a more complex implementation of this method, ion bombardment is used to sputter away a passivating layer, as is the case for inhibitor-driven anisotropy and the *Bosch process* discussed below. To understand why RIE is the preferred etch method for IC fabrication, we will consider the etch profile formed by each type of process.

Figure 3.4 shows three types of dry etch profile, typically characteristic of IBE (A), PE (B), and RIE (C). As illustrated in fig. 3.4(A), IBE typically results in a sidewall that is not completely vertical (exaggerated for clarity), with the degree of the slope being a function of the aspect ratio of the etched feature (ratio of depth to width). As IBE is a purely physical sputtering process, the sputtered material is non-volatile and will be redeposited in part onto the feature sidewalls, with larger amounts of build up near the top of the feature opening. In addition, the sloping sidewalls typically lead to a secondary effect known as *trenching*, where the etch rate at the edges of the feature is increased due to a preferential concentration of ions there as a result of ions grazing off of the sidewalls. IBE also exhibits a poor selectivity (difference between the etch rate of masking layer (resist in fig. 3.4) and layer to be etched) as the etch rate is purely dependent on material hardness. For these reasons IBE is mostly reserved for applications where a practical etch chemistry does not exist. Figure 3.4(B) shows a typical etch profile for PE etching, which is isotropic in nature. As etching occurs purely by chemical means, there is no difference between vertical and lateral etch rates. PE exhibits a higher selectivity than IBE, but in most processes a high degree of anisotropy is also desired. RIE has the advantage of allowing a high degree of anisotropy, which can also be adjusted as required, as well as a high degree of selectivity. An idealized, perfectly anisotropic, RIE etch is illustrated in fig. 3.4(C). In reality, the sidewalls will have a

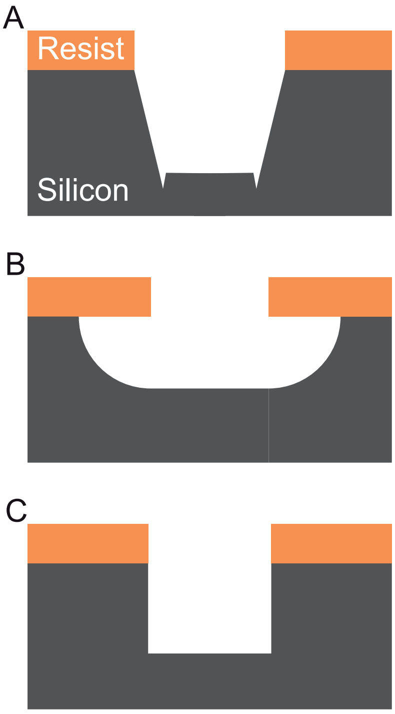

Figure 3.4 – **Characteristic dry etch profiles:** with a masking layer of resist shown in orange. (A) illustrates the etch profile resulting from ion beam (sputter) etching, with sloping sidewalls caused by partial redeposition of sputtered material as well as *trenching* at the sidewall edges (see text for details). (B) shows the isotropic etch profile that results from a purely chemical plasma etch. (C) is the idealized anisotropic etch profile generated by ion activated chemical etching, known as reactive ion etching. For the purpose of illustration silicon is indicated, but the same profiles apply to dry etching of other materials.

non-zero etch rate, but this can be kept relatively small by tuning of the process parameters, as described in the following sections.

3.2.1 Diode reactor configuration

A simple diode-type PE or RIE reactor configuration is shown in fig. 3.5. The substrate to be etched sits on the cathode and plasma is generated by an AC voltage. A DC plasma cannot be used in such reactors as charge accumulation on the dielectric substrate (e.g. silicon with an oxide layer) would cause the electric field to drop and stop the plasma generation. This is a result of the *cathode sheath* (also known as the *Debye sheath*) that has a net positive charge due to the excess of positive ions with respect to electrons that exists in the region close to the cathode. This effect can be understood to arise from the difference in positive ion and electron fluxes, as result of the large difference in their masses. Thus an AC voltage is used to alternate between bombardment of ions and electrons at rate that is faster than the charge up time of the dielectric. Typically the frequency 13.56 MHz is used as it is dedicated by the FCC for Industrial, Scientific and Medical (ISM) applications and is far above the charge up rate for typical substrates. Powers used are generally in the range of a few kilowatts.

The RF voltage source is capacitively coupled to the cathode, causing the cathode to build up a negative DC bias (V_{DC}), while the anode is grounded. This self-biasing (typically a few hundred volts) is a result of the high mobility of low mass electrons, relative to the (positive) ions that are weakly response to the high frequency field. Given a plasma potential, V_P (typically a few tens of volts), this negative biasing results in a large difference in average energy between ions bombarding the cathode, $E = e(V_P - V_{DC})$, and the anode, $E = eV_P$. This imbalance is important as it allows sputtering of the substrate while avoiding sputtering of the anode. In some configurations a variable resistor is added in parallel to the capacitor, allowing adjustment of V_{DC} and thus control over the energy of impinging ions. In more sophisticated systems, like the inductively-coupled RIE discussed below, the substrate bias is decoupled from the plasma generating field allowing complete control over ion momentum.

As shown in fig. 3.5, etching gases are introduced to the reactor over the anode and evacuated beneath the cathode. It is critical to have an even diffusion of (neutral reactive) gas particles over the substrate to ensure uniform etching. For this reason a *shower head* type anode with small, evenly distributed, perforations is typically used. Operating pressures are normally in the range of 10-1000 mTorr, with lower pressures resulting in an etch dominated by sputtering and higher pressures by chemical etching.

Ion bombardment raises the temperature of the substrate and, as heat transfer is low in the vacuum, a flow of helium gas over the backside of the substrate is normally used to thermalize the wafer to the cathode and maintain a stable temperature. The rate of helium flow may also be adjusted to effect the difference in etch rate between purely chemical attack and chemical attack assisted by ion mediated surface damage (purely chemical attack is more sensitive to temperature). Thus helium flow rate is another tool that can be used to adjust the anisotropy

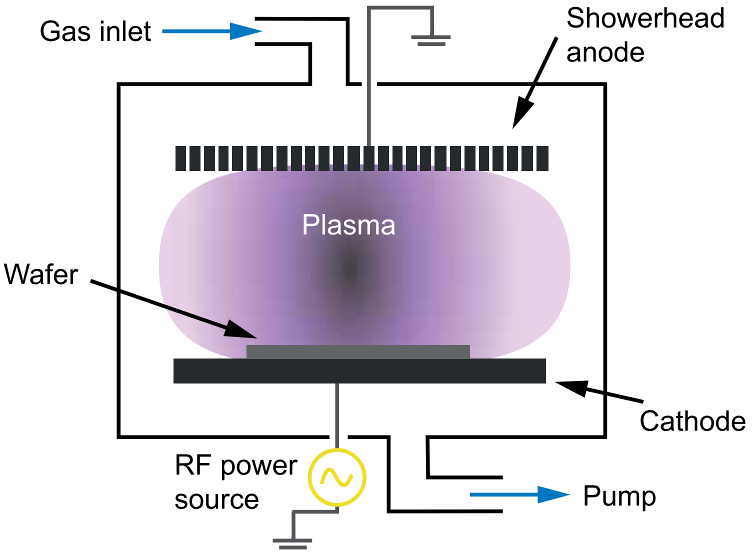

Figure 3.5 – **Diode-type RIE system:** A simple type of RIE system, with plasma generated by an RF power source (rather than DC), to avoid charge up of the substrate (wafer). The wafer is located on top of the cathode in the ion-rich *cathode sheath* region. Ions accelerated by DC self-biasing of the capacitively-coupled power source provide the physical etch component. Reactant gases are introduced to the plasma volume through perforations in the (showerhead) anode - designed to provide even diffusion of radicals generated in the plasma to the wafer surface.

of a given etch process.

3.2.2 Reactive Ion Etching

As mentioned, RIE systems operate in an intermediate range between purely physical etch by ion bombardment and purely chemical etch by free radicals generated in the plasma. In adjusting the relative ratios of physical and chemical contributions to the etch process, pressure is a key variable. Since ions responsible for physical etching are accelerated by the DC field and neutral reactive species are transported by diffusion alone, operating at low pressures results in a more physical etch and operating at higher pressures increases the chemical etching contribution. An increase in pressure results in a decreased mean free path of the ions and thus a decreased momentum, while at the same time an increased flux of neutral reactive species to the substrate, and vice versa. Typical pressures used in the RIE regime are in the range of 100 mTorr.

When setting the gas flow rate it is important to avoid *loading effects*, which result when the material etch rate is limited by the supply of reactant gas. In this regime areas of the substrate where a large degree of material is exposed for etching will etch more slowly than areas where a small degree of material is exposed. In order to avoid loading effects and achieve a high degree of uniformity the reactant gas should be oversupplied. Here a so-called *utilization factor* must be considered. This factor is the ratio of etch product formation to etch gas flow rate. As a general rule a utilization factor less than 0.1 should be maintained in order to achieve high

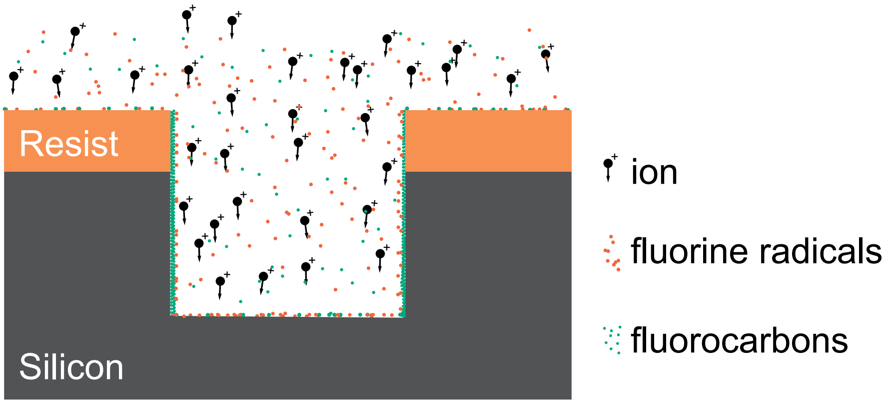

Figure 3.6 – **Inhibitor-driven anisotropy in RIE:** is a process that utilizers reactant gases that, in addition to forming radicals that drive chemical etching, deposit polymers that build up on vertical surfaces and increase the anisotropy of the etch. Here a fluorine etch process is illustrated, with fluorine radicals in red ($F^{\bullet}$), and polymeric species in green (e.g. C_2F_4). We note the buildup of polymers on vertical surfaces where relatively low levels of ion bombardment take place, thus blocking chemical attack. Horizontal surfaces are clear of polymer and thus exposed to $F^{\bullet}$.

uniformity.

Inhibitor-driven anisotropy

When etching silicon-based materials fluorine gases are commonly used to form volatile SiF_4. Although fluorine ions are reactive, chemical etching proceeds by reaction of fluorine radicals ($F^{\bullet}$), as the fractional production of radicals in plasma is orders of magnitude higher than ions. While SF_6 may be used on its own as an etch gas, fluorocarbons such as CF_4 are often used instead or in addition. The purpose of using fluorocarbons is to cause polymer build up on surfaces during the etch process by adsorption of non-volatile C_xF_y species (e.g. CF_2, C_2F_4). In order for etching to proceed these non-volatile polymers must be cleared from the substrate surface by ion sputtering or reaction with fluorine radicals to form volatile products (see fig. 3.6). As ion bombardment is directional, horizontal surfaces are preferentially cleared. This method allows the degree of anisotropy to be increased as chemical etching (fluorine radicals indicated by red dots in fig. 3.6) of the sidewalls is blocked by fluorocarbon polymer deposition (green dots in fig. 3.6). Note that for clarity reaction products are not shown in fig. 3.6.

It is critical to control the rate of polymer formation, as excessive polymerization will cause the etch process to stop altogether and the chamber to become contaminated. This happens when sputtering and volatile product formation are not be able to overcome the rate of polymer deposition. Polymerization can be decreased by adding oxygen to the etch gases, which reacts with C_xF_y to form volatile products and thus increase the so-called fluorine-to-carbon (F/C) ratio. Hydrogen, on the other hand, can be used to decrease the F/C ratio as it acts as a *radical* *scavenger*, reacting with fluorine radicals to form HF. In addition to controlling the F/C ratio, the effect of polymerization and resulting degree of anisotropy can be controlled by adjusting the voltage bias of the cathode and thus the rate of preferential polymer sputtering from horizontal surfaces.

ICP-RIE

A type of modern etcher known as inductively coupled plasma RIE (ICP-RIE), can produce high density plasmas at relatively low pressures as compared to diode configurations like the one shown in fig. 3.5. In such systems a helical coil of wire is wrapped around the exterior of a quartz tube, inside which the plasma is generated. An RF current through the coil drives an induced magnetic field, causing plasma generating electrons to spiral as they are accelerated, thus greatly increasing their path length as compared to purely linear acceleration. The increased path length and thus greater interaction with reactant gases leads to higher plasma generation efficiency. The higher fractional generation of ions and radicals, in turn, allows for lower pressure operation. In addition, the biasing voltage of the substrate can be independently controlled with respect to the voltage used to generate the plasma and thus does not rely on self-biasing. This means that the ion bombardment energy can be independently controlled, which is highly relevant when considering inhibitor-driven anisotropy. Operation at relatively low pressures also allows for much higher aspect ratio features to be etched, as a result of better control over ion directionality (less collisions in the gas bulk). ICP-RIE systems are increasingly preferred over diode-type etchers for these reasons. In fact, the dry etchers used for the work in this thesis are of the ICP-RIE type. For dielectric etching, such as the silicon dioxide etches discussed in sections 3.3.4 and 3.3.6, as well as the silicon nitride etch described in section 3.3.5, a SPTS Advanced Plasma System ICP-RIE is used. Silicon etching, such as in section 3.3.4 and section 3.3.6 is carried out using an Alcatel AMS 200 ICP-RIE. Both systems can be operated efficiently at a few tens of mTorr. The later system is capable of an important silicon etching process that exploits the well-controlled directionality of ICP-RIE (and is used for the etch in section 3.3.6) as well as the ability to adjust ion bombardment energy. This process is described below.

3.2.3 Bosch process

A particularly useful etch method utilizing ICP-RIE to produce high aspect ratio features in silicon was developed at Robert Bosch GmbH, and is known as the "Bosch process" [103]. This method may also be referred to as *time-multiplexed etching*, as it proceeds by a repetition of two discrete steps, shown in fig. 3.7(A-B). In the first step silicon is etched nearly isotropically using SF_6 and low energy ion bombardment (fig. 3.7(A)). In the second step, illustrated in fig. 3.7(B), a ∼10 nm fluorocarbon passivation layer is deposited, using C_4F_8 with no substrate bias (absence of ion bombardment). The first step is then repeated, clearing the passivation layer at the bottom of the trench, allowing the etch to proceed vertically (fig. 3.7(C)). Polymer, however, remains on the sidewalls from the previous etch due to the directionality of the ion

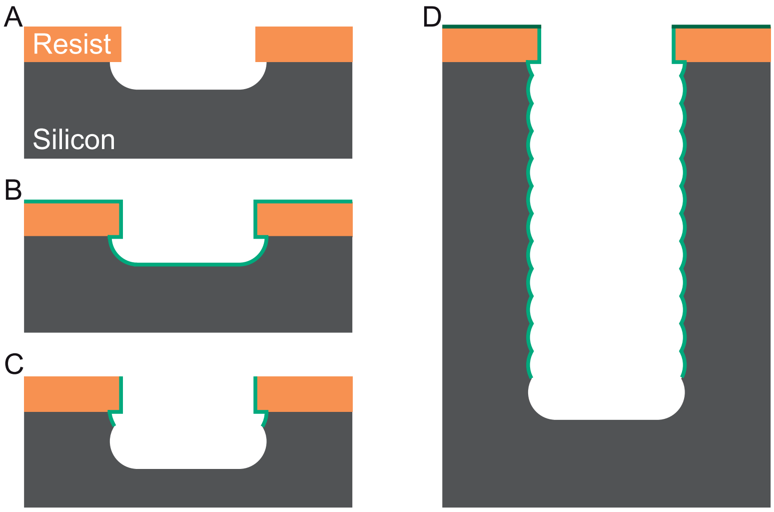

Figure 3.7 – **Bosch process:** (A) and (B) illustrate the two discrete steps of Bosch process etching, which involves RIE (A) followed by surface passivation with a fluorocarbon (green in (B)). RIE is then repeated (C) sputtering away the fluorocarbon layer at the bottom of the trench allowing the etch to continue. These steps are repeated until the desired etch depth is achieved. The feature profile at the end of the etch process is shown in (D). The fluorocarbon layer on top of the resist is illustrated in dark green to indicate that it has become hardened by many successive sputtering and redeposition steps.

sputtering, and they are thus protected from further etching. These steps alternate every ~5 seconds, and may be carried out hundreds of times. The resulting etch profile, shown in fig. 3.7(D), has a characteristic *scalloped* sidewall. The degree of this scalloping can be controlled by adjusting the duration of the etch and passivation steps. It should be noted that a mostly chemical silicon etch (isotropic) is required to achieve a very high selectivity to the resist layer (avoiding excessive sputtering of resist), allowing for etches hundreds of microns deep. It's also important to keep in mind that when etching high aspect ratio features the process can become diffusion limited, meaning that higher aspect ratio features on a wafer will etch more slowly than lower aspect ratio features. After many repeated fluorocarbon deposition and sputtering steps the polymerized layer on top of the resist becomes hardened (denoted by dark green in fig. 3.7(D)), normally requiring an oxygen plasma etch for removal. Bosch process is used to form the *mesa* structure described in section 3.3.6.

3.3 Device fabrication

Figure 3.8 provides a high level overview of the process developed to realize the optomechanical system detailed in chapter 2. Broadly speaking, this involves defining the microdisk structure (fig. 3.8(A-B)), creating a separation layer (fig. 3.8(C-D)), patterning the nanobeam (fig. 3.8(E-F)), and finally releasing the structure by removal of the separation layer as well as partial undercutting of the microdisk (fig. 3.8(G-H)). The microdisk must be designed to have low material absorption (section 3.1.2), low surface roughness and an optical mode centered near the upper edge of the wedge shaped perimeter to achieve a larger modal overlap with the nanobeam (sections 2.1.3 and 2.2.4). In terms of performance this translates to achieving high optical Q and maximizing the optomechanical frequency pulling factor, $G = \partial\omega_c/\partial x$, in terms of bringing the optical mode center as close as possible to the upper edge of the microdisk (section 2.1.3). Creating a good separation layer turns out to be a non-trivial problem for a number of reasons. First of all, it is necessary to completely remove this layer from the silicon dioxide (from here on SiO_2) pads where the nanobeam will be clamped (section 3.3.2), in order to avoid undercutting silicon nitride (from here on referred to as Si_3N_4, since we assume the type we use is close to this stoichiometric ratio) in the clamped region during the structural release step (as was the case for the initial device design, as discussed in appendix B.3). Second the layer must be compatible with LPCVD deposition of Si_3N_4 at ~800 °C (section 3.1.2), disqualifying the use of polymeric layers. Third, the layer should be removable with a chemistry that is highly selective to both SiO_2 and Si_3N_4 (section 3.3.6). Finally, the material should allow for a gap just tens of nanometers in height to be created between the nanobeam and microdisk. Polysilicon (section 3.1.2) was chosen

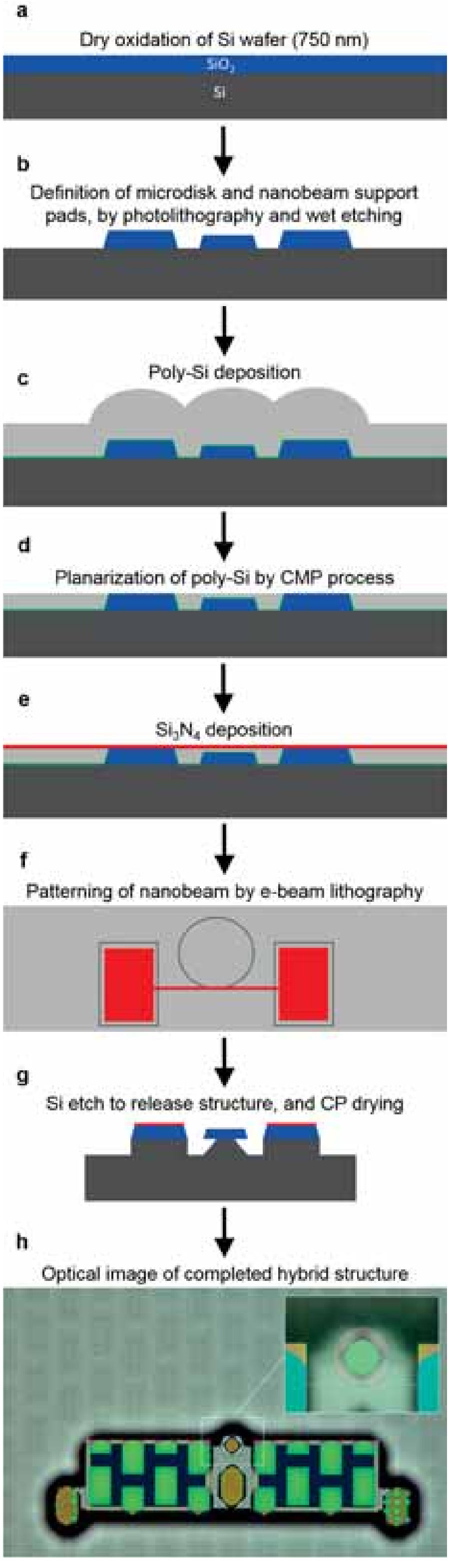

Figure 3.8 – **Fabrication process overview:** blue, red, green, and (light) gray indicate SiO_2, Si_3N_4, Al_2O_3 and Si, respectively. Details in section 3.3

as the material to meet these requirements, with CMP being used as the planarization method (section 3.3.3). Following CMP, Si_3N_4 is deposited (section 3.1.2) and patterned by e-beam lithography. The use of e-beam is critical as it allows very low edge roughness to be achieved (minimizing scatter of the evanescent optical field), precise (<100 nm) alignment to the microdisk (section 3.3.5), and writing of features on the nanoscale (such as in section 6.1.3). An additional benefit comes in the ability to use a resist that is rapidly dissolved in KOH (section 3.3.5), thus avoiding potential contamination from polymeric resists that could lead to increased optical absorption. Before releasing the device structure with KOH (section 3.3.6), the devices are elevated onto small islands as seen in fig. 3.8(H), using Bosch process (section 3.2.2), allowing an optical fiber to be coupled to the disk without coming into contact with the substrate. Before drying with CPD, a short HF etch is used to clean the sample surfaces and remove accumulated oxynitride from the nanobeam, which would otherwise result in increased mechanical dissipation as well as optical absorption.

3.3.1 Microdisk process

The process begins with an intrinsic FZ silicon wafer (section 3.1.1), on which a 750 nm film of SiO_2 is grown by dry oxidation, as described in section 3.1.2. The first mask in this process is used to define the microdisk resonator described in section 2.1.2, rectangular pads onto which the nanobeam ends are clamped (section 2.1.1) and alignment marks that are used for alignment of the subsequent lithography masks. The alignment markers are modified (see section 3.3.4) for alignment of the e-beam mask described in in section 3.3.5. The rectangular pads used to clamp the nanobeam are repeated across the entire wafer (see fig. 3.10) in order to produce a uniform topography, which is critical to achieving a uniform polishing rate, as described in section 3.3.3.

Wedged sidewall formation

It has long been known that wet etching of SiO_2 in HF ($SiO_2 + 6HF \rightarrow H_2[SiF_6] + 2H_2O$) can be utilized to form linear wedge profiles with varying angles [104]. This technique has been exploited in a number of works to realize high-Q optical microdisks [60, 105, 106]. The linear wedge profile of etched sidewalls can be understood to arise from the combination of two etch processes. One is the typical isotropic wet etch illustrated in fig. 3.9(A), and the second is a horizontal etch that propagates along the interface between the resist and SiO_2. The combination of these etch processes can be described in analogy to the formation of a *mach cone* that results when an objects velocity exceeds the speed of sound [107]. In the case of wet etching the linear wedge profile results from the superposition of a slower isotropic etch rate, u_i, and a faster lateral (interfacial) etch rate, u_l. The resulting wedged sidewall angle, shown in fig. 3.9(C) is then given by $\theta = arcsin(u_\mathrm{i}/u_\mathrm{l})$. As the lateral etch rate is a result of creep of the etchant solution (HF) at the interface between the resist and SiO_2, it is dependent on the adhesion strength of the resist. Residual tension in the resist and resist thickness likely also plays a role in this process. The observation of a "knee" feature, shown at the bottom of the wedged sidewall in fig. 3.9(B), that results for short etch times [60], indicates that the initial etch process is purely isotropic (fig. 3.9(A)) with u_l initially negligible. This suggests that u_l is likely driven by capillary forces causing the resist to peel back. Thus the resist must be sufficiently undercut to realize a purely linear sidewall. In principle if a given resist is sufficiently well bonded to the SiO_2 surface (high level of adhesion) a purely isotropic etch will result, while lower levels of adhesion will result in a wedge formation with the wedge angle, θ, decreasing with decreasing adhesion. It has been demonstrated that the lateral etch rate and thus the degree of linearity in the sidewall as well as the sidewall angle is independent of HF concentration but highly dependent on etch temperature [104]. Lower temperatures result in a near isotropic etch profiles and higher temperatures with a linear profile and decreasing sidewall angle. This may be attributed to decreased adhesion at higher temperatures, and may be an interesting avenue of exploration.

The first mask pattern is transferred by wet etching in buffered hydrofluoric acid (BHF), in order to create high-Q microdisks by the process described above. BHF is ideal for this process as it exhibits a selectivity between SiO_2 and Si greater than 1000:1 [108]. A variety of resists and adhesion promoters were tested, resulting in varying wedge angles (as well as Q-factors). The largest wedge angles of $\theta \sim 30°$ (rationale for using large wedge angles in section 2.1.3) were achieved using Microchemicals AZ 1512 resist following priming with hexamethyldisilazane (HMDS). HMDS is a resist adhesion promoter that causes silylation of the SiO_2 surface by attachment of $Si(CH_3)_3$ groups, which greatly increases its hydrophobicity. The methyl groups (CH_3) are assumed to form bonds with the polymeric photoresist. The first mask is exposed on 1.1 μm of Microchemicals AZ 1512 HS photoresist using a Karl Süss MA6 mask aligner, with an i-line filtered (365.4 nm) mercury-vapor lamp. Following development with Microchemicals AZ 726 MIF, a reflow step is carried out in an oven at 140 °C at ambient pressure, for 30 minutes. This raises the resist temperature near the glass transition point, allowing surface tension to smooth the resist boundaries, resulting in lower roughness on the etched sidewall and higher measured optical Q. Following a *descumming* step in O_2 plasma, the SiO_2 is etched in BHF

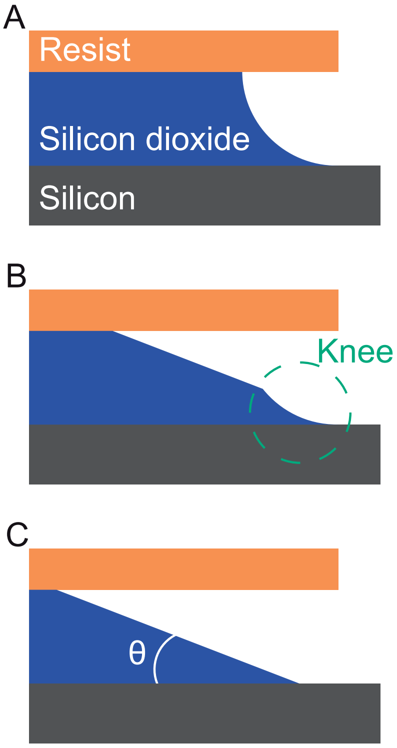

Figure 3.9 – **Formation of microdisk wedged sidewall:** Initially a characteristically isotropic sidewall profile is formed. As the resist is undercut, capillary forces drive an additional lateral etch at the interface between resist and SiO_2, with an intermediate profile illustrated in (B). A "knee" region is seen, which is a vestige of the initial isotropic etch. After some further etching a linear sidewall is realized (C), in analogy to the formation of a mach cone. The sidewall angle, θ, is dependent on the adhesion strength of the resist.

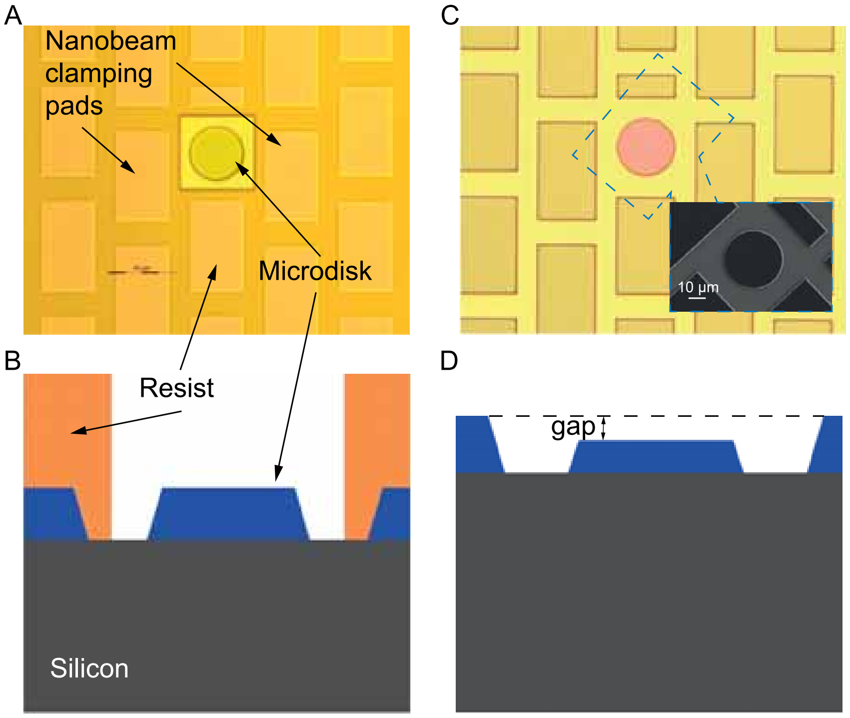

Figure 3.10 – **Microdisk thinning:** (A) shows a (optical microscope) top view of patterned SiO_2, after application of the second mask used to selectively etch the microdisk with respect to the pads where the nanobeam will be clamped. Resist protects the sacrificial structures, while a window is exposed around the microdisk. (B) illustrates this window in the resist with a cross-sectional view (SiO_2 colored blue). (C) is a top view after selective etching of the microdisk and removal of the resist. The altered color of the microdisk is indicative of thinning (alteration of the Bragg resonance), with the relative offset illustrated in cross-section in (D).

7:1 (NH_4F : HF = 87.5 : 12.5 %) for 20-25 minutes, resulting in a ~3.5 μm pattern biasing. Over-etching was required to remove the vestigial foot region described above, and resulted in higher optical Qs as compared to shorter etches. Following this etch, the resist is stripped by O_2 plasma ashing (a PE type process, as described in section 3.2.2).

Microdisk offset

A second mask and BHF etching step preferentially thins the microdisk with respect to the surrounding structures. This allows the microdisk to be recessed below the pads where the nanobeam will be clamped and defines the vertical gap between them, as shown in fig. 3.10(D). The mask covers all structures on the wafer except for the microdisk, leaving it exposed for etching (fig. 3.10(A)). It is patterned by the same process described for the first mask, except for the reflow step which is not necessary in this case. The microdisks are then etched in BHF for less than one minute (at an etch rate of ~80 nm/min), with a targeted thickness decrease of ~50 nm. The precise etch time is adjusted according to the desired nanobeam-microdisk gap. Following removal of the resist by O_2 ashing, the result is shown in fig. 3.10(C) and (D). Note that the microdisk reflects a different color than the surrounding pads due to its reduced thickness. Again, it should be mentioned that fig. 3.10 shows a matrix of sacrificial pads surrounding the disk. This matrix extends across the entire wafer and is only broken where microdisks or alignment marks (shown in fig. 3.15) are placed. As discussed in section 3.3.2, a uniform matrix of pads is necessary to achieve a flat surface when CMP processing the sacrificial layer.

The final result of microdisk fabrication is illustrated in fig. 3.10(D). Blue indicates (in profile) the patterned SiO_2 film, with the microdisk in the center and nanobeam support pads on either side. The offset between the microdisk and the pads is highlighted with a dashed line. Not shown are sacrificial pillars and alignment marks. In the next processing step, all structures are buried in a sacrificial layer of polysilicon, onto which a Si_3N_4 film will later be deposited.

3.3.2 Planarized sacrificial layer

After patterning by the two mask layers described in the previous section, the SiO_2 film is buried under a layer of sacrificial material. The sacrificial layer is used as a substrate for deposition and patterning of the Si_3N_4 film that will form the nanobeam. This layer is initially uneven because of its conformity to the underlying SiO_2 pattern. Before the Si_3N_4 layer is deposited it should be made exceptionally flat in order to avoid loss in tensile stress when the nanobeam is released. Moreover, it should be planarized in such a way that the SiO_2 pads where the nanobeam will be clamped are exposed while sacrificial material remains over top of the microdisk. This translates to a more stringent requirement for flatness - namely, that the deviation should be less than the offset between the microdisk and clamping pads (fig. 3.10(D)), which ranges from 20-50 nm. To remove the topography transferred from the underlying the SiO_2 and thin the sacrificial layer, a planarization technique known as CMP (described in section 3.3.3) is followed.

Polysilicon is chosen as the sacrificial material because it is isotropically etched at a high rate in KOH (see section 3.3.6) and thus can be used to undercut the nanobeam and the microdisk in a single step. It is well-suited to CMP and can withstand the high temperatures required for LPCVD Si_3N_4 ($\sim 800\,^\circ$C; see section 3.1.2). A $\sim$2.5 μm thick layer is deposited by LPCVD at $600\,^\circ$C using disilane as the reactant gas (described in section 3.1.2). In addition, immediately before polysilicon deposition, a 3 nm alumina (Al_2O_3) film is deposited on top of the SiO_2 using atomic layer deposition (ALD; described at the end of this section). This film later serves as an *etch-stop* layer, to protect the microdisk when etching the Si_3N_4 nanobeam. The alumina is referred to as an etch-stop because the fluorine-based RIE process described in section 3.3.5 etches it at a rate over 100× slower than Si_3N_4. Alumina is a general etch-stop material for RIE fluorine chemistry despite the fact that it is reactive, because the aluminum fluoride (AlF_3) product formed has very low volatility (recall that high volatility is critical in RIE: section 3.2.2). The polysilicon spacer layer between the Si_3N_4 and SiO_2, on the other hand, is only tens of nanometers thick and is rapidly etched by this process. Thus without the alumina layer, the etch would proceed through the polysilicon and into the SiO_2 microdisk, greatly degrading

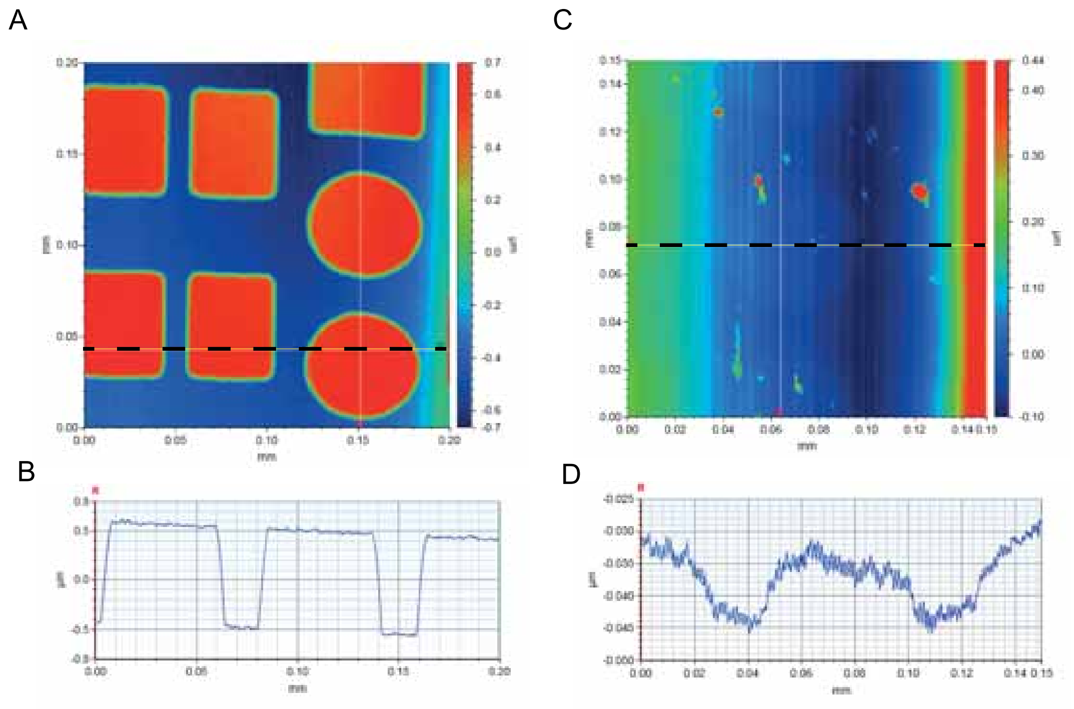

Figure 3.11 – **Sacrificial layer topography:** composite map taken with a Bruker Dektak XT mechanical profilometer, with a vertical resolution of ~2 nm, shown in (A) following deposition of polysilicon. (B) shows a single trace of the nanobeam clamping pad and microdisk, indicated by the dashed black line in (A), with a topographical variation following the underlying SiO_2 thickness. A map of the same area as in (A) is taken after the completion of the CMP process (C), with the microdisk faintly visible. In (D) a single trace through the dashed black line in (C) shows a variation of ~10 nm.

its performance. At the end of the fabrication process the alumina is removed, as it is readily dissolved in aqueous KOH ($Al_2O_3 + 2KOH + 3H_2O \rightarrow 2KAl(OH)_4$).

A profile of the pre-polished sacrificial layer is sketched in fig. 3.8(C). The alumina etch-stop film is indicated by green. Immediately above the etch-stop is the layer of polysilicon (gray). As a result of conformal deposition on the underlying SiO_2 structures, the surface of the polysilicon is uneven. This unevenness can be seen in the topographical map shown in fig. 3.11(A) and (B). This measurement is taken using a mechanical profilometer, which is essentially a contact version of atomic force microscopy, where a stylus is dragged along the wafer surface and its deflection is measurement by interferometry, achieving a vertical resolution of a few nanometers. Seen in the bottom of fig. 3.11(A) is a microdisk with a nanobeam clamping pad beside it, subsequent to polysilicon deposition. The image is formed from a composite of traces, with fig. 3.11(B) showing a single trace. The objective of the CMP process is to planarize this topography and remove polysilicon until the SiO_2 pads are exposed, while maintaining a thin layer above the recessed microdisk (fig. 3.8(D)). This procedure is complicated by the fact that the polishing rate varies across the wafer for the reasons discussed in section 3.3.3 and, importantly, that initially the polishing rate above the microdisk is faster than the rate above the adjacent nanobeam support pads, as a result of the lower feature density surrounding the microdisk (see section 3.3.3 for explanation). This results in a polysilicon layer which is thinner above the microdisk than at the nanobeam supports. This is visible in the profilometry trace shown in fig. 3.11(D), which is taken at the end of the CMP process. Note that fig. 3.11(C) scans the same area shown in fig. 3.11(A) and the microdisk is faintly visible due to the ~10 nm variation in height at the end of the process. To minimize this "dishing" effect (discussed in section 3.3.3), the support pads are brought as close the microdisk as possible (limited to ~15 μm by BHF over-etching (section 3.3.1) and necessary feature separation for the photolithography step).

To achieve the desired sacrificial layer, a two-step planarization method is used. In the first step Klebosol 30N50, a KOH-based slurry (PH ~11) containing silica particles with ~80 nm diameters, designed for fast polishing of polysilicon is used to remove the bulk of the material. This process is stopped when approximately 100 nm of polysilicon remains above the pads. The remaining material is removed using Klebosol 1598-25, a neutral slurry (PH 7) containing silica particles with ~30 nm diameters, designed for fine polishing and exhibiting a selectivity between polysilicon and SiO_2 of ~1:1. The selectivity is critical here because if polysilicon was polished at faster rate than SiO_2 (as would be the case with Klebosol 30N50) a further dishing effect would occur, clearing away the material above the microdisk and exposing it to damage. In fact Klebosol 1598-25 polishes SiO_2 slightly faster (~10%) than polysilicon which helps to reverse the initial dishing effect mentioned above. In addition to the selectivity consideration the smaller particles produce a fine polish, with a measured surface roughness of ~ 0.3 nm RMS.

The requirement to clear polysilicon from the nanobeam clamping pads during the final steps of CMP results in some thinning of the pads. Therefore the final gap between microdisk and nanobeam is smaller than originally defined by thinning of the microdisk in section 3.3.1. In order to precisely tune the gap, and ensure over-polishing does not occur, the thickness of the clamping pads is iteratively measured by reflectometry until the desired value is reached. At this point the sample is ready for Si_3N_4 deposition.

Atomic layer deposition

ALD is a deposition technique that allows for growth of extremely thin film layers, with control over thickness at the atomic level. Rather than introducing precursors simultaneously, as in CVD, in ALD the precursors are introduced sequentially forming monolayers on the substrate. The precursors are introduced to the reactor one at a time, with an inert gas purging step in between to remove any residual reactant gas. Each precursor is introduced for a sufficient time period to saturate all available surface sites. Thus each two-step reaction sequence deposits a known thickness of film, and the total thickness is determined linearly by the total number of steps.

In order to grow alumina, first water vapor is introduced to the chamber ensuring complete hydroxylation (–OH) of the surface (note this is generally redundant as the substrate is previously exposed to air and hydroxylation has already taken place). After purging is completed, trimethyl aluminum (TMA ; $Al(CH_3)_3$) is introduced and reacts with the adsorbed hydroxyl groups:

$$Al(CH_3)_3(g) + :Si–O–H(s) \rightarrow :Si–O–Al(CH_3)_2(s) + CH_4(g) \tag{3.3.1}$$

Here (g) and (s) indicate gas and solid phase, respectively and :Si indicates the silicon atom that is a component of the substrate. Excess TMA and methane (CH_4) are purged from the chamber and water vapor is once again introduced, reacting with the dangling methyl groups attached to the surface aluminum atoms, forming Al–O–Al bridges:

$$2H_2O(g) + :Si–O–Al(CH_3)_2(s) \rightarrow :Si–O–Al(OH)_2(s) + 2CH_4(g) \tag{3.3.2}$$

This process can then be repeated, with each two step reaction adding ~0.1 nm of thickness. This reaction sequence is typically carried out at ~300 °C [109] for optimal complete and self-limited results, although feasibility of the process has been demonstrated near room temperature [110].

3.3.3 Chemical-mechanical planarization

The process of chemical-mechanical planarization (or polishing) involves lapping of a dielectric using a colloidal solution containing abrasive particles, is a technique that has been used for centuries to polish glass lenses. CMP in its modern form traces back to the early 1960s when Monsanto developed a highly reproducible process of polishing wafers cut from a silicon rod, using an alkaline solution containing sub-micron SiO_2 particles [111]. Over the following decades the process was fine tuned to produce mirror-like surfaces with a very high degree of planarity and low number of defects, in silicon and SiO_2 [112, 113]. In 1993 CMP was first used by Intel in production of the Pentium chip, to planarize inter-layer dielectric (ILD) used to separate metalization layers [114].

The ILD planarization process shown in fig. 3.12(A) is one of the most common uses of CMP. After deposition and patterning of a conduction layer (shown in yellow) a dielectric spacer layer (shown in blue) is deposited by CVD, such that another another metalization layer may be added above. In order to avoid buildup of topography, and loss of pattern transfer fidelity, the dielectric layer is planarized after deposition. This process may then be repeated many times, resulting in a complex network of conduction layers. Note that the continued push towards smaller and smaller features comes with the additional requirement of meeting more and more stringent requirements for planarity.

Another common application of CMP is a process known as shallow trench isolation (STI), sketched in fig. 3.12(B). In this process insulating trenches are formed to isolate adjacent

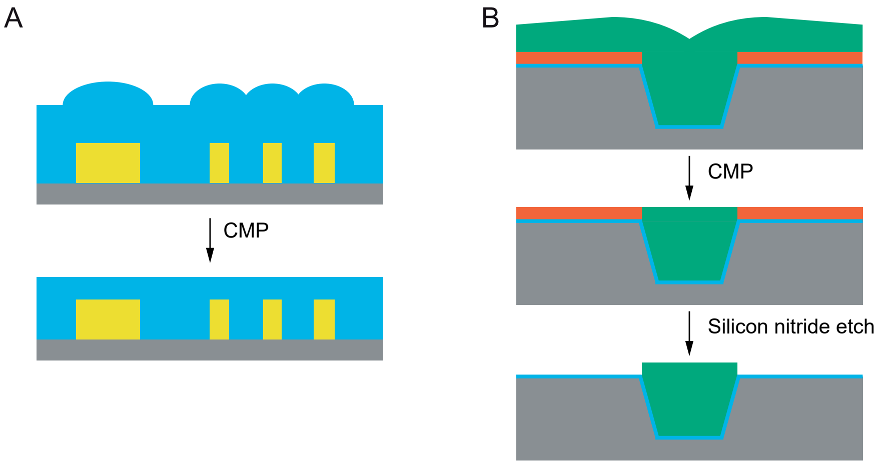

Figure 3.12 – **Inter-layer dielectric (ILD) and shallow trench isolation (STI) CMP processes:** The ILD process is briefly illustrated in (A), with the first step involving deposition of a dielectric material (blue) overtop of a patterned conduction layer (yellow). The dielectric is planarized by CMP, to remove topography, such that another conduction layer may be added. This process can be repeated many times to build a complex conduction network, with bridges in-between layers. An overview of STI is illustrated in (B), where Si_3N_4 (red) is deposited on an oxidized (blue) silicon (grey) wafer, a trench is etched, followed by oxidization of the trench (blue) and deposition of of an isolating material (green). CMP is used to planarize the isolating layer, with the polishing process stopping on the Si_3N_4 (which is used as a CMP etch-stop in this case). Finally Si_3N_4 is dry etched away, leaving the isolating trench which is typically used to isolate adjacent transistors.

transistors and reduce current leakage. First a thin SiO_2 layer (blue) is grown on a silicon wafer (grey), followed by CVD deposition of Si_3N_4 (red). A trench is formed by etching through these layers into the silicon and then insulating material is deposited by CVD, which may be SiO_2 or another dielectric material. CMP is then used to planarize the surface, with Si_3N_4 being used as a stop layer. Finally, a etch process is used to remove the Si_3N_4 and top insulator layer. This type of process is generally referred to as *damescene* - a term that also refers to the ancient Japanese art of producing fine jewelry consisting of complex inlaid patterns of various metals.

Beyond the common processes mentioned above, there are many niche applications of CMP. One such niche application is to produce the optomechanical device described in this chapter. In another application that is particularly useful, CMP has been used for the purpose of integrating MEMS with CMOS fabricated ICs on a single wafer [115]. This is done by first performing standard polysilicon MEMS fabrication in a trench. After the MEMS step, the trench is filled with SiO_2 and then the wafer is planarized such that standard CMOS processing can be carried out subsequently. At the end of the process the MEMS are released by etching away the SiO_2 around the devices.

Polishing mechanism

Material removal during a CMP process is a result of the synergistic combination of chemical surface modification, producing a softened layer, followed by removal of the surface material

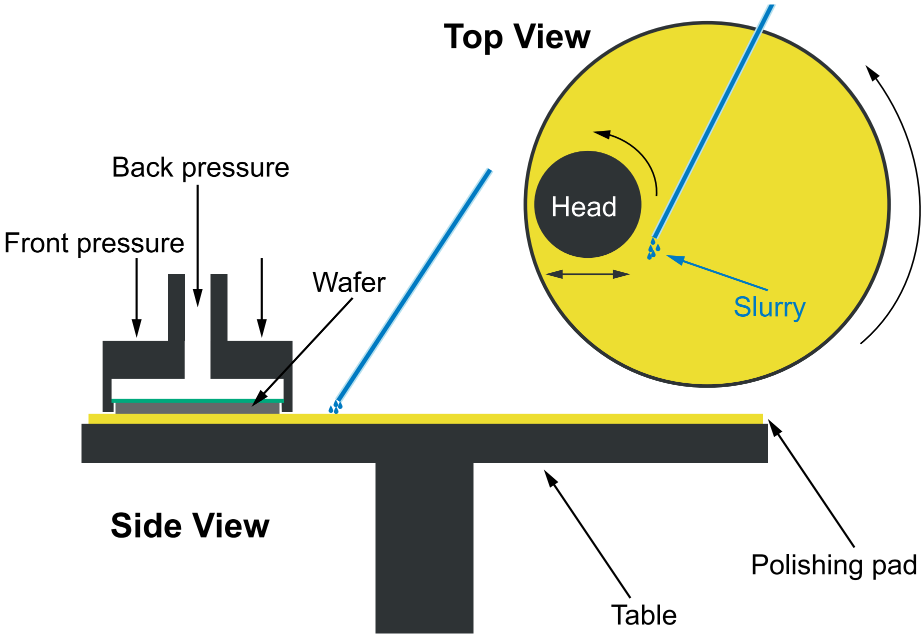

Figure 3.13 – **Schematic of a CMP system:** illustrated in top view at the right, with the rotating head pressed (front pressure) against a polyurethane polishing pad (yellow), attached to the spinning table. Slurry (blue) is dispensed at a fixed rate via a tube mounted near the edge of the polishing head. In the bottom left the apparatus is shown in side view, with the head drawn in cross-section, showing back pressure applied to the wafer view a gas-tight membrane (green).

by mechanical abrasion. Figure 3.13 illustrates a simple CMP system, consisting of a rotating table with a porous (typically polyurethane) polishing pad applied to the surface, and a rotating head where the wafer to be polished is mounted with the side to be polished facing the table. The head is brought into contact with the table using a tightly controlled force (referred to as the *front pressure*) and a water-based colloidal solution, called a *slurry*, containing silica particles tens of nanometers in diameter, is dispensed on the table at a controlled rate, as the table and head rotate. Grooves in the polishing pad facilitate efficient transport of the slurry to the wafer surface, while the fine porosity of the pad captures the silica particles used for abrasion. The porosity and mechanical stiffness of the pad play a major role in determining polishing rate and uniformity, and have been a subject of intensive study and development - particularly by Dow Corning. During polishing embedded particles are worn down, decreasing the polishing rate, and thus the pad must be regularly reconditioned throughout the process. Reconditioning is carried out by a second head which has fine diamond particles embedded in it, and is used to strip away surface pad material, exposing a fresh layer. As illustrated in fig. 3.13, an adjustable pressure can be applied to the back of the wafer (referred to as *back pressure*) to compensate for wafer bow and thereby achieve a uniform pressure across the wafer.

Polishing is carried out by chemical softening of the surface layer to be removed followed by mechanical abrasion. In the case of silicon or SiO_2 (as is of interest in this thesis), the chemical softening is a result of hydroxylation of surface silicon atoms, forming Si–OH bonds

[116]. This chemically weakened layer is then abraded by the silica particles contained in the colloidal slurry. In fact it has been demonstrated that polishing with slurries that lack water results in a near zero polishing rate [117]. The hydrolysis process is limited by diffusion of hydroxyl groups to the wafer surface, which can be enhanced by increasing temperature or PH. To facilitate faster removal rates, such slurries are typically made alkaline by the addition of KOH. As local friction leads to temperature increases, in more sophisticated CMP systems temperature stabilization may be employed.

A rather straightforward empirical equation of significant importance to CMP established long before the era of silicon manufacturing, in the context of glass polishing, is the Preston equation:

$$R = KPV \tag{3.3.3}$$

This states that the material removal rate, R, depends linearly on the local pressure, P, and local linear velocity of a point on the wafer, with respect to the polishing surface (the table in this case), V. The proportionality factor K is known as the Preston coefficient and lumps together a large number of factors, including chemical mechanisms and surface friction coefficients. Note that the modifier *local* with respect to pressure and velocity is of key importance, as discussed in the following two sections.

Another factor that must be considered in practice is the differing rates of hydroxylation, as a function of the radial position on the wafer. As can be seen in fig. 3.13, slurry is delivered to the edge of the wafer and transported to the center by grooves in the polishing pad. This means that in practice diffusion of hydroxyl groups at the edge of the wafer is higher than at the center. Using a slurry with a high PH and low density of particles may compensate for this effect, by operating in a regime where the removal rate coefficient, K, is limited by mechanical abrasion rather than hydroxylation. In principle, this effect as well as non-uniform polishing due to wafer bow (which is often not completely remedied by the application of backside pressure) may be compensated for by using the techniques discussed in the following two sections.

Local pressure

The dependence of local pressure on polishing rate is the mechanism behind the ability to achieve planarized surfaces by CMP. If we consider the topography in fig. 3.12(A) in the context of the CMP technique described above, it is clear that the extrusions experience a higher local pressure and thus polish at a faster rate. In the ideal case, after some time polishing the topography will be completely removed. In reality some topography always remains, as shown in the experimental measurements of fig. 3.11(C) and (D). Typically this residual topography arises from a non-uniform pattern density. As can be seen in fig. 3.10(A) and (C), the pattern density around the microdisk is somewhat lower than the density around the rectangular pads. This lower density results in a higher polishing pressure above the microdisk leading to a slight local concavity above it, as described in section 3.3.2. This type of feature is referred to as *dishing* and most often arises in CMP as a result of polishing two materials with differing polishing rates (for example when stopping on a bridging metal layer in an ILD process). This consideration is also discussed in section 3.3.2 and is one of the key reasons why a different slurry, with a selectivity between SiO_2 and polysilicon of ~1:1, is used in the final stage of polishing the sacrificial layer.

In general, to achieve uniform polishing rate across a wafer it is critical to have a uniform underlying pattern density (as shown in fig. 3.9). However, a density that varies radially across the wafer could in principle by used to compensate for the effect of wafer bow or non-uniform slurry delivery. On the other hand, practically this would be difficult as wafer bow will exhibit some variation from wafer to wafer and can be more easily (and dynamically) compensated for by the method described below.

Local velocity tuning

As described by Preston's equation the polishing rate for an arbitrary point on the wafer is dependent on its linear velocity with respect to the polishing pad. As we will see the ability to independently adjust the rotational velocities of the table (to which the pad is affixed) and head allow one to set a radially-dependent linear velocity for the wafer surface. To understand the effect of tuning the table and head angular velocities, given by ω_T and ω_H respectively, we refer to fig. 3.14. Here $\mathbf{r}_{CC}$ is the vector pointing from the center of the table to the center of the head and $\mathbf{r}_H$ is the vector pointing from the center of the head to an arbitrary point on wafer, P. The vector $\mathbf{r}_T$ is the sum of these vectors, $\mathbf{r}_T = \mathbf{r}_{CC} + \mathbf{r}_H$. We can thus determine the linear velocity of point P along the table surface as:

$$v_P = v_T + v_H = -\omega_T \times \mathbf{r}_T + \omega_H \times \mathbf{r}_H = -\omega_T \times \mathbf{r}_{CC} - \mathbf{r}_H \times (\omega_H - \omega_T) \tag{3.3.4}$$

Thus when the table and head angular velocities are matched, the linear velocity for all points on the wafer is the same. In this case, the linear velocity can be increased either by adjusting the distance between the center of table and head, $|\mathbf{r}_{CC}|$, increasing the angular velocities, or both. However, tuning the difference in rotational speeds provides a powerful tool to adjust the relative removal rates, according to Preston's equation, radially between the center and edge of the wafer, with $v(\mathbf{r}_H)$. This adjustment can be used to compensate for an uneven pressure resulting from the previously mentioned wafer bow or hydroxylation issues. Moreover, one could compensate for a radially varying pattern density using this adjustment. Note that this imbalance is set both by the relative angular velocities and the distance between the center of table and head. The imbalance may be increased by moving the head closer to the center of the table and vice versa.

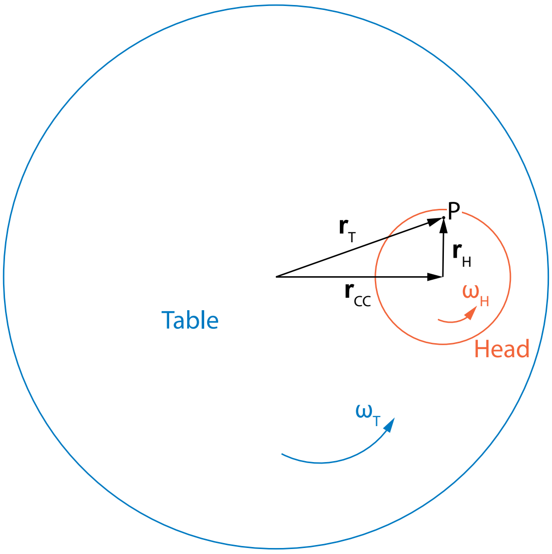

Figure 3.14 – **CMP polishing velocity:** A simplified drawing of CMP apparatus from top view, showing the polishing head in red and polishing table in blue, with rotational velocities ω_H and ω_T, respectively. Vectors $\mathbf{r}_{CC}$ and $\mathbf{r}_T$ have their origins at the center of the table. Point P is an arbitrary point on the polishing head (or wafer).

3.3.4 Excavation of e-beam alignment markers

In the original development stage the entire process was intended to be carried out by photolithography. Thus in the microdisk layer mask design (first mask), isolated markers for e-beam alignment were not included. However, the photolithography alignment markers, which can been seen in fig. 3.15, do include 20×20 μm boxes surrounding the cross feature, which are of the correct dimensions for e-beam alignment. However, the image recognition algorithm used locate the markers requires a 200×200 μm feature free area surrounding the box. Moreover, the marker should be raised or recessed with respect to the substrate by at least 2 μm in order to provide sufficient contrast. For these reasons a series of three lithography steps are required to transform the marker in fig. 3.15(A) to the e-beam compatible one in fig. 3.15(E). This process follows directly after Si_3N_4 deposition, and at this point the markers are buried under Si_3N_4 and polysilicon. The first lithography step clears these material layers by dry etching and follows the same process as used for the second microdisk disk mask in section 3.3.1, but without the need for adhesion promoter. The Si_3N_4 and polysilicon are etched in a single step with a non-selective SF_6 chemistry, using an Alcatel AMS 200 ICP-RIE. Critically, the etch is stopped at the interface between polysilicon and SiO_2 / crystalline silicon by the ALD deposited alumina layer (section 3.3.2). This is critical to avoid the SiO2 features being transfer into the underlying silicon, which would result in a non-uniform background for the (e-beam alignment) image recognition software. The result of this step after O_2 plasma ashing is shown in fig. 3.15(B).

In the second etch step we want to remove all the SiO_2 features from the box opened in the first step, save for the one shown with resist protection in the inset of fig. 3.15(C). This protected box will become the e-beam alignment marker. The mask is applied by the same process used for thinning the microdisk in section 3.3.1, and BHF wet etching is used to remove all the features surrounding the protected box. The result after removing the mask, which is a single SiO_2 surrounded by a featureless crystalline silicon substrate is seen in fig. 3.15(D) and (G). The alignment marker needed for e-beam has now been extracted, but the topography is too small to be recognized by the e-beam SEM mode and so one final step is required to increase its height.

The third mask has the same pattern as the first one, and is used to protect the wafer during a dry etch that uses the extracted SiO_2 box as a hard mask. The third mask is also applied in the same way as the first one. The Alcatel AMS 200 ICP-RIE is used to etch down 2 μm of silicon using an SF_6 process that exhibits a >10:1 selectivity to SiO_2. Thus the SiO_2 box is used as a hard mask and its shape is transferred to the underlying silicon. After removal of the mask, the completed alignment marker is shown in fig. 3.15(E), (F) and (H).

3.3.5 Nanobeam fabrication

To form the nanobeam, a 50-100 nm film of high-stress Si_3N_4 is deposited onto the planarized polysilicon layer - a film thickness roughly corresponding to the optical decay length of microdisk section 2.1.3. The film is deposited by LPCVD, using dichlorosilane and ammonia as described in section 3.1.2, producing a nearly stoichiometric Si_3N_4. High stoichiometry is important for two reasons. Firstly, it minimizes optical absorption that will otherwise be higher due to the presence of hydrogen and oxygen impurities in non-stoichiometric films, as is the case for lower temperature methods such as plasma-enhanced chemical vapor deposition (PECVD) [56]. Second, the ~1 GPa stress resulting from the LPCVD process is fundamental to achieving high mechanical quality factors as described in section 2.1.1 [47].

Alignment to microdisk mask

To maximize optomechanical coupling, it is necessary to fine tune the lateral beam-disk separation with 100 nm precision (see fig. 2.4C). In fact, moving the nanobeam laterally by 150 nm is enough to change the single-photon optomechanical coupling rate by approximately two, as can be seen in figure fig. 2.7. A typical wafer yielded 8 chips with 18 sample variants per chip. Due to this relatively low yield and the time intensive process of loading a sample into a ^{3}He buffer gas cryostat (chapter 5), it was worth taking considerable effort to ensure precise alignment calibration. Note that although the e-beam alignment marks are defined in the same mask as the microdisks, the wet etch process used (section 3.3.1) leads to an uncertainty in the microdisk diameter. Thus knowing the center value of the microdisk alone is not sufficient and precise calibration of the diameter is still required. Moreover, for shaped beams such as those described in section 6.1.3 it is also critical to know the distance between the clamping pads precisely, to ensure correct boundary conditions and avoid potential overhang of the Si_3N_4 which can lead to increased dissipation. Thus the SiO_2 feature dimensions must

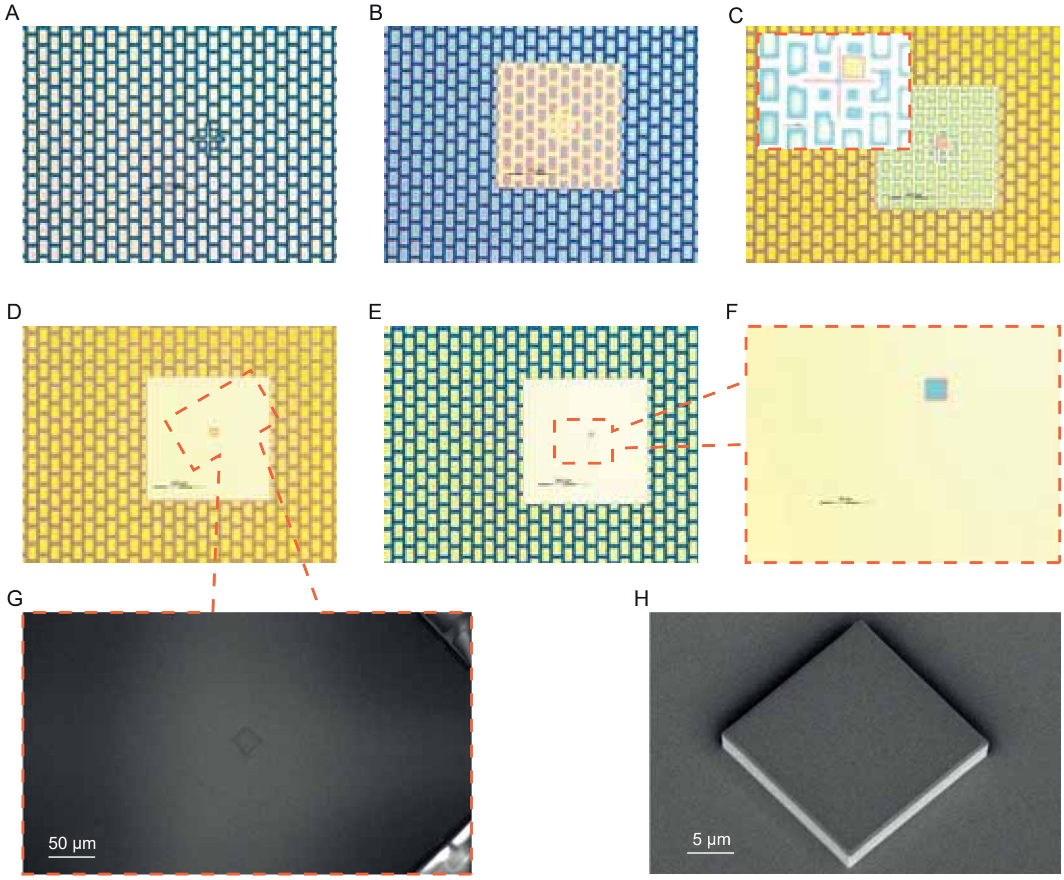

Figure 3.15 – **E-beam alignment marker excavation:** (A) shows a top view of SiO_2 photolithography alignment marker surrounded by sacrificial features and buried under polysilicon and Si_3N_4. In (B) the first mask, a 300×300 μm open around the alignment marker is seen following removal of polysilicon and Si_3N_4 by dry etching. Next the mask layer in (C) is applied, with one of the alignment marker boxes protected by resist (inset). BHF is used to remove the surround SiO_2 features and the result is shown in (D) and (G). A third mask (E) with the same opening as in (A) is used to protect the wafer while a dry etch transfers the box shape 2 μm down into the underlying silicon (hard mask process) with the result seen in (F) and (H).

be calibrated, either by simply measuring them using an optical microscope or by a more complex but higher precision method that is described in appendix B.1.

Alignment using mask aligners available in the CMi, such as the Süss MA6, results in an alignment error > ±1 μm, which is unacceptably large for the reasons mentioned above. Thus to ensure sufficient alignment precision e-beam lithography is used to define the beams, in conjunction with the alignment markers defined during SiO_2 patterning and uncovered following Si_3N_4 deposition (see details in section 3.3.4). In addition, e-beam writing allows us to realized features <100 nm, as described in chapter 4 and chapter 6. The resulting silicon markers in conjunction with the edge-detection based alignment algorithm included in the Vistec EBPG5000 operating software permits alignment of the Si_3N_4 mask with < ±100 nm precision. This can be partially attributed to the quality of the markers, which are defined by photolithography, it should also be mentioned that only global (wafer level) alignment is

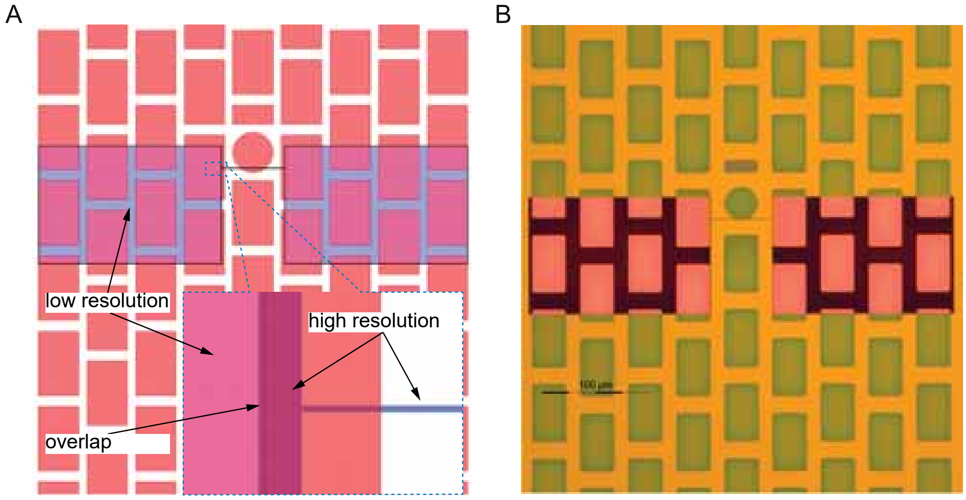

Figure 3.16 – **E-beam pattern for monolithic system:** (A) *bulk and sleeve* CAD pattern, with high resolution layer shown in dark purple and low resolution in light purple with black border. Surrounding SiO_2 structures appear red. (B) optical microscope top view of sample after etching of Si_3N_4 (pink and purple). Surrounding SiO_2 structures, including microdisk, appear green.

used as the error in estimating the microdisk dimensions is at a similar scale. Thus alignment precision of $< \pm 100$ nm is sufficient, and allows us to achieve an optical beam position by sweeping the offset over no more than three samples.

Resist patterning

Lithographic patterning of the Si_3N_4 layer that forms the nanobeams, support pads, and sample labels are patterned using hydrogen silsesquioxane (HSQ ; $[[HSiO_{3/2}]_n)$ in a carrier solvent of Methyl isobutyl ketone (MIBK). This negative tone resist is supplied by Dow Corning in concentrations of 2%,4% and 6% and identified by the product name XR-1541. This is one of the highest resolution resists available, capable of being pattern to features <10 nm by e-beam [118]. Upon exposure to an electron beam, UV light, or heat the small cage-like clusters of HSQ cross-link forming an extended network via Si–O–Si bonds, resulting in a hydrogen rich SiO_2-like compound [119]. The exact reaction mechanism is not known but it is thought to be a multi-step reaction with Si–H bonds being broken and the dangling silicon bonds reacting with water, linking the cages by Si–O–Si bond formation [119, 120]. When exposed to an alkaline solution HSQ exhibits a large difference in dissolution rates between the cross-linked and non-cross-linked portions and Tetramethylammonium hydroxide (TMAH) works particularly well for this purpose (development) [120]. In addition to the very high resolution achievable, HSQ is particularly well suited to this process as it is rapidly dissolved in KOH during the final steps of the process (section 3.3.6) ensuring a clean Si_3N_4 surface. Other types of polymeric resists may not be fully removed, leading to decreased mechanical and optical performance.

The patterns are written using a Vistec EBPG5000 e-beam tool equipped with 100 keV thermal field emission gun, focused by magnetic lenses. The tool sits in a room with temperature stabilization of 21±0.1 °C and active magnetic field cancellation. Written patterns are comprised of relatively low surface area nanobeam features (~ 200 μm^2/chip), and relative large clamping pads (~ 5×10^5 μm^2/chip), as well sample labels (~ 1×10^6 μm^2/chip). Only the nanobeams require a high resolution and so to keep the writing time at an acceptable level (typically ~ 1 hour/wafer), the pattern is separated into high resolution and low resolution parts, as shown in fig. 3.16(A). The *high resolution* pattern is written with on a 5 nm grid using a beam waist of ~ 10 nm and the *low resolution* pattern is written with a 50 nm grid and a beam waist of ~ 100 nm. For each pattern the tool is aligned using the markers described in section 3.3.4, and in order to account for any errors in the alignment, as well as thermal drift, a 500 nm overlap region is included at the boundary between the patterns (fig. 3.16(A)).

When attempting to write a high resolution pattern using an electron beam it's important to consider the forward scattering of electrons passing through the resist and the backscattering of electrons from the substrate that lead to distortion and broadening of patterns. The forward scattering process arises from electron-electron interactions, both in the resist and the substrate, which causes a deflection of the traveling electrons. When this occurs in the resist it causes an exposing dose to be delivered outside the pattern area. When using a high energy beam and thin resist with low electron density, as in our case, most electrons will pass through the resist, but a fraction will be elastically backscattered at broad angles and will deliver a dose to the resist on their path backwards. These two effects can be modeled as a sum of two Gaussian functions, representing the forward and backscattered electrons [121, 122], giving the following point spread function (PSF):

$$PSF(r) = \frac{1}{\pi(1+\eta)}\left(\frac{1}{\alpha^2}e^{-\frac{r^2}{\alpha^2}} + \frac{\eta}{B^2}e^{-\frac{r^2}{B^2}}\right) \tag{3.3.5}$$

with η being the contribution of backscattered electrons (on the order of 1), and α^2 and B^2 being the variance of the forward scattered and backscattered electrons, respectively. In thin resists α^2 is on the order of a few nanometers while B^2 is ~30 μm for a silicon substrate. The relative contribution of backscattered electrons must be calibrated for given substrate and resist. A piece of software called Beamer produced by GenISys is used to model the backscattered dose for the specific pattern being written and then dynamically adjusts the dose delivered across the pattern to account for backscatter. After exposure the resist is developed in 25% TMAH , which results in higher pattern contrast as compared with lower concentrations (which are inherently safer in terms of burn risks) [123].

Etching

The e-beam pattern is transferred to Si_3N_4 using an SPTS (manufacturer) Advanced Plasma System (APS) ICP-RIE, with a chemistry of SF_6 and CHF_3. This etch is optimized to provide smooth sidewalls when etching Si_3N_4, but offers poor selectivity to SiO_2 and etches HSQ and Si_3N_4 at approximately the same rate. For this reason a ~180 nm thick HSQ layer is used, with the typical Si_3N_4 layer to be etched ranging from 50-100 nm in thickness. In order to avoid significant over-etching, the etch end point is determined using optical emission spectroscopy (OES). OES monitors the intensity of spectral emission from etch products, in this case SiF, and the etch is stopped ~10 seconds after the emission begins to drop (indicating that the exposed Si_3N_4 has mostly been consumed). HSQ is not removed at the end of this process but is left in place until the KOH release step, where it is rapidly dissolved. In this way the HSQ helps to protect the nanobeam from contamination during the following steps where a resist is applied to the sample and used to etch down the substrate to allow fiber coupling.

3.3.6 Structural release

In the final steps of processing the Bosch process (section 3.2.3) is used to elevate the sample with respect to the substrate. The sample chips are then defined by partially cutting through the wafer with a silicon dicing saw. With the wafer still intact KOH etching releases the structure from polysilicon sacrificial layer, undercuts the perimeter of the microdisk and dissolves the HSQ used to pattern the nanobeam. A final cleaning step with dilute HF removes the surface SiO_2 layer from the nanobeam (silicon oxynitride) and microdisk. Directly following the cleaning the sample is dried using a tension-free drying technique known as critical point drying (CPD).

Mesa Etching

Before the nanobeam and microdisk are released, they are elevated from the surrounding wafer on a rectangular “mesa”. This later enables alignment of a straight tapered optical fiber to the microdisk [124] without introducing loss via contact with the substrate. Figure 3.17 shows the mesa structure at the end of processing. This ~50 μm tall structure is, naturally, defined using the Bosch process, but before this etch can proceed the sacrificial SiO_2 structures, as well as the Al_2O_3 etch stop layer must be removed. A single mask defined in a 5 μm mask of Microchemicals AZ 9260 resist is used for this process. The Si_3N_4 is etched away in the previous step, and at this point the top layer is polysilicon. This is removed with an anisotropic SF_6 etch, using the Alcatel AMS 200 ICP-RIE, and this process naturally stops on the Al_2O_3. The next etch is carried out in an SPTS APS ICP-RIE using C_4F_8 and H_2, which rapidly etches through the Al_2O_3 as well as SiO_2 but exhibits a high selectivity to silicon. At the end of this etch, just the crystalline silicon remains and the Bosch etch is carried out.

With the mesa process complete, the resist is left in place and the sample chips are defined using a silicon dicing saw. The wafer is diced half way through (~260 μm for a typical 525 μm thick wafer) by alignment to markers indicating the edge of the chips, that are defined in mesa mask layer. The dicing equipment is a DISCO (manufacturer) DAD 321 silicon dicing saw. The resist is left in place to protect the samples from silicon particles during the dicing.

Note that partial dicing is important as it leaves the wafer intact, enabling further processing using wafer-scale equipment. Following dicing the wafer is rinsed and the top layer of resist is removed by oxygen plasma ashing at high power (600W). Only the top layer of resist is removed in order to avoid exposing the HSQ, which still remains on the nanobeams, to plasma which would cause it to densify - potentially becoming insoluble in KOH. The remaining resist is removed with a hot (75 °C) bath of N-Methyl-2-pyrrolidone.

Nanobeam and microdisk

To release the nanobeam and undercut the microdisk, the partially diced wafer is immersed in aqueous 40% KOH at 45 °C, selectively removing polysilicon but also etching Si. The etch time is fine-tuned with two opposing criteria in mind: (1) to ensure that the microdisk is undercut sufficiently far from its rim to avoid optical losses and (2) to ensure that Si underneath the nanobeam clamping point is not etched away. A relatively low temperature (and slow) etch is used as it exhibits a high selectivity to SiO_2. This is critical to avoid unnecessarily increasing the coupling gap. For typical samples, with 15 μm radius disks, the etch time is 45 minutes. After etching, the wafer is immersed in 37% HCl to dissolve any potassium salts left behind from the KOH. Before drying the samples are briefly etched in 5% HF, for ~ 20 seconds. This is critical to achieving very clean samples. In fact, the addition of this step consistently reduces the mechanical dissipation rate by one half, from 20 Hz to 10 Hz. However, the step must be carefully timed to avoid over-etching the microdisks. Typically 3-5 nm of SiO_2 is removed - increasing the coupling gap by that amount.

After the HF etch, followed by rinsing, the wafer is transferred to high purity (VLSI grade) ethanol in a high pressure chamber used for critical point drying (Automegasamdri 915B). With the chamber sealed, the ethanol is purged with liquid CO_2. When purging is completed the temperature and pressure of the chamber is increased until the supercritical regime is reached. At this point the chamber pressure is slowly dropped with the CO_2 passing from the supercritical regime to gas phase. This tension-free drying method is necessary to avoid tension-induced stiction. With the drying complete the chips can now be carefully broken from the wafer using tweezers, in a process akin to dividing a Toblerone bar.

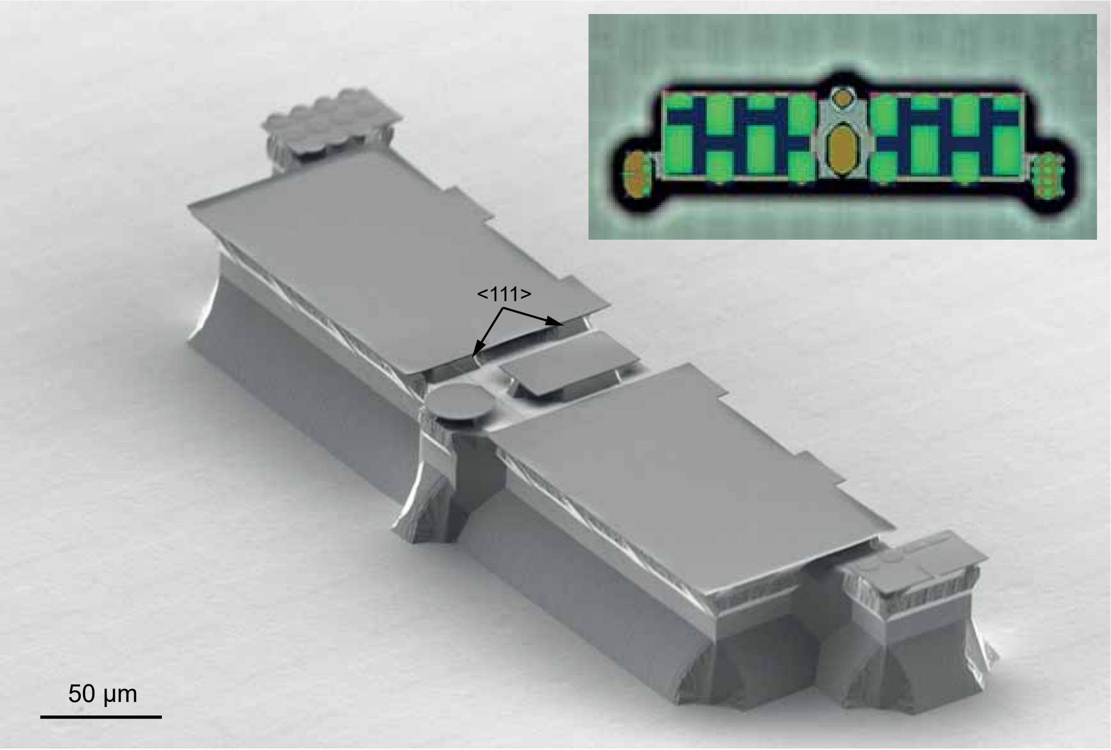

Figure 3.17 – **Monolithic structure at the end of processing:** is seen in a grey scale SEM of a structure with a similar beam design to that shown at the end of chapter 2. The <111> planes of the crystalline silicon, which are shielded from attack by KOH, are indicated. Correct orientation of the <111> plane with respect to the nanobeam clamping pads allows for a solid base beneath the clamping areas. A inset optical microscope image shows the top view of a similar sample at the end of processing with Si_3N_4 in blue and green, and SiO_2 in white (clear) and tan. Areas of Si_3N_4 over polysilicon appear blue and over SiO_2 (with silicon beneath) appear green. Areas of SiO_2 over silicon appear tan and suspended SiO_2 appears clear or white.

4 Quantum effects at room temperature

The radiation pressure interaction of light with mechanical oscillators has been the subject of intense theoretical research in the gravitational wave community [22, 126, 127], leading, for example, to an understanding of the quantum limits of interferometric position measurements. An important insight that could potentially help evade this limit is that the two noise sources that enforce it – quantum (measurement) back-action and imprecision – are in general correlated [128]. From the perspective of the light in the interferometer, quantum fluctuations in its amplitude quadrature drive the oscillator leading to quantum back-action, and the driven motion is imprinted onto the phase quadrature. Ultimately, this leads to correlations between the quantum fluctuations of the amplitude and phase quadratures, i.e. quantum correlations. Correlations thus established form a valuable resource: the optomechanical system may be viewed as an effective Kerr medium generating squeezed states of the optical field [129, 130], or the correlations can be directly employed for back-action cancellation [131–134]. The ability to utilize quantum correlations generated *in-situ* is conceptually identical to injection of squeezed light [133], while circumventing the challenge of realizing a near-unity coupling efficiency between the squeezed light source and the interferometer [135]. The burden of quantum efficiency in this case is shifted to the detector, a problem that is largely solved [136]. Thus, a room-temperature interferometer capable of harnessing in-situ correlations is a platform that may help extend the practical reach of quantum optics, with applications ranging from gravitational wave detection to chip-scale accelerometry.

In practice, owing to the weakness of the radiation pressure force, optomechanical quantum correlations are typically obscured by thermal motion. Only in recent years has this challenge been broached, by the development of cavity optomechanical systems [137], which combine an engineered high Q, *cryogenically-cooled* micromechanical oscillator with a high finesse optical (or microwave) cavity. In such systems, it is possible to realize a regime in which the motion of the oscillator is dominated – or nearly so – by quantum back-action [30, 31, 138]. This has enabled studies of various effects related to optomechanical quantum correlations, such as ponderomotive squeezing [46, 139–142] and motional sideband asymmetry (using

---

This chapter is adapted from [125]

autonomous [143–146] or measurement-based [46] feedback to cool the mechanical oscillator). Accessing this regime at *room-temperature* is difficult as the optical powers necessary to overwhelm thermal forces with back-action are typically accompanied by dynamic instabilities [147]. Various cross-correlation techniques have been proposed to relax these requirements and allow observation of quantum correlations near mechanical resonance [148, 149]. In a recent demonstration [150], such a technique was used in the regime of large measurement imprecision to unearth quantum correlations from beneath 60 dB of thermal noise. However, the generation of broadband quantum-noise-induced optomechanical correlations, that could simultaneously ameliorate the limits posed by imprecision and back-action on room-temperature interferometers [131–133, 151, 152], remains an outstanding challenge.

In this chapter we observe quantum correlations of light generated by its interaction with a room temperature nanomechanical oscillator coupled to a high finesse optical microcavity, and discuss how to use these correlations to realize a quantum-enhanced mechanical force sensor. The large bandwidth of the cavity and the exceptionally high Q/mass of the oscillator allows us to operate in a novel regime where the magnitude of quantum correlations is comparable to both sources of quantum noise – imprecision and back-action – at Fourier frequencies detuned as much as an octave from mechanical resonance. In a suitably chosen field quadrature, correlations manifest as a reduction or enhancement in the fluctuation spectrum at Fourier frequencies detuned from mechanical resonance. Though the fluctuations are contaminated by thermal noise and do not drop below the vacuum level – the condition for ponderomotive squeezing – their reduction provides a metrological advantage, since its origin is a coherent cancellation of quantum noises. Counter-intuitively, as a result of this coherence, we observe a 10% noise reduction despite the fact that back-action is 20 dB smaller, in equivalent phonon units (n_{QBA}), than thermal noise ($n_{\mathrm{th}} \approx k_B T/\hbar\Omega_{\mathrm{m}} \approx 10^6$). Indeed, at optimal Fourier frequencies, the fractional noise reduction scales as $\sqrt{n_{\mathrm{QBA}}/n_{\mathrm{th}}}$, distinguishing it from a classical noise correlations, and enabling an enhanced estimate of the quantum back-action force relative to standard 'calorimetric' measurements [30, 31, 138]. We conclude by showing how quantum correlations can be used to improve the signal-to-noise ratio of an off-resonant test force.

4.1 Concept of the experiment

Accessing the above physics requires the ability to resolve back-action-driven motion far from mechanical resonance, a regime traditionally studied for gravitational wave detectors, but only recently accessed experimentally, using high-cooperativity cryogenic micro-cavity optomechanical systems operating deep in the so-called bad cavity limit [28, 46, 153]. Our system was optimized for achieving this regime at room temperature as detailed in chapters 2 and 3. As shown in fig. 4.1, it consists of a Si_3N_4 nanomechanical beam coupled dispersively to a whispering gallery mode of a silica microdisk. The system exhibits a vacuum optomechanical coupling rate of $g_0 \approx 2\pi \cdot 60$ kHz for the fundamental, $\Omega_{\mathrm{m}} = 2\pi \cdot 3.4$ MHz flexural beam mode. In conjunction with the high room temperature mechanical quality factor, $Q_{\mathrm{m}} \approx 3 \cdot 10^5$ (giving

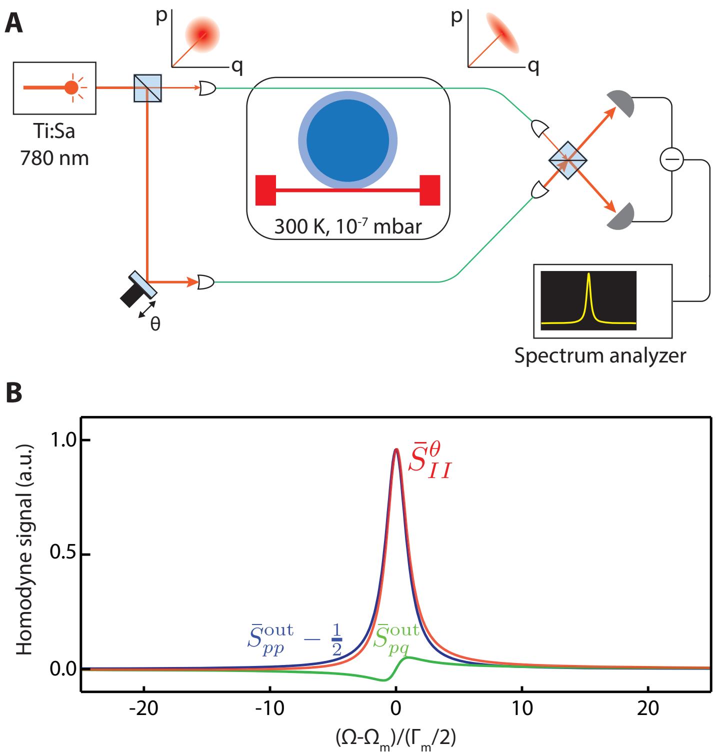

Figure 4.1 – **Optomechanical quantum correlations:** (A) Schematic of the experiment: The optomechanical system is formed by a Si_3N_4 nanobeam oscillator (red) evanescently coupled to SiO_2 microdisk cavity (blue). Both are maintained at room temperature ($T \approx 300\,\text{K}$) in a low pressure ($\approx 10^{-7}$ mbar) vacuum chamber. The cavity is probed on resonance with 780 nm light from a Ti:Sa laser. The transmitted field is read out with a homodyne detector with variable local oscillator phase θ. Amplitude and phase fluctuations of the light field are correlated after passing through the cavity, represented as squashing in a phase space cartoon. (B) Model of the homodyne photocurrent spectrum (normalized to vacuum noise, eq. (4.1.9)) for detection near the amplitude quadrature ($\theta \approx 0°$). The signal (red) has symmetric part (blue) due to physical motion and an asymmetric part (green) due to quantum correlations.

a damping rate of $\Gamma_\text{m} = \Omega_\text{m}/Q_\text{m} \approx 2\pi \cdot 12$ Hz), and a critically coupled cavity decay rate of $\kappa \approx 2\pi \cdot 4.5$ GHz, a near-unity single photon cooperativity of $C_0 = 4g_0^2/\kappa\Gamma_\text{m} \approx 0.27$ is attained. Importantly, the system operates in the broadband regime, i.e. $\kappa \gg \Omega_\text{m}$. Further details about the device used in this chapter can be found in appendix E.2.1.

In the experiment (outlined in fig. 4.1A), the optomechanical device is placed in a high-vacuum chamber and probed on resonance using a Ti:Sa laser. The motion of the oscillator, characterized by the Fourier transform of its displacement fluctuation $\delta x[\Omega]$, is imprinted on the transmitted phase quadrature as (see appendix E.1),

$$\delta p_\text{out}[\Omega] = -\delta p_\text{in}[\Omega] + \sqrt{2C\Gamma_\text{m}}\frac{\delta x[\Omega]}{x_\text{zp}} \tag{4.1.1}$$

where p_in is the phase quadrature of the input field, $x_\text{zp} = \sqrt{\hbar/2m\Omega_\text{m}}$ is the zero-point motion of the oscillator, and $C = C_0 n_c$ is the multi-photon cooperativity for the mean intracavity photon number n_c. The displacement has components from the ambient thermal environment, and quantum back-action,

$$\delta x[\Omega] = \delta x_{\mathrm{th}}[\Omega] + \delta x_{\mathrm{QBA}}[\Omega] \tag{4.1.2}$$

The thermal motion,

$$\delta x_{\mathrm{th}}[\Omega] = 2x_{\mathrm{zp}}\chi[\Omega]\sqrt{(n_{\mathrm{th}}+\tfrac{1}{2})/\Gamma_{\mathrm{m}}}\,\delta\xi[\Omega] \tag{4.1.3}$$

is due to a Langevin force of intensity proportional to the average thermal occupation n_{th}, and fluctuating as a white noise $\delta\xi$, characterized by,

$$\langle \delta\xi(t)\delta\xi(t')\rangle = \delta(t-t') \tag{4.1.4}$$

The force fluctuations are transduced into displacement fluctuations via the dimensionless susceptibility of the oscillator,

$$\chi[\Omega] \equiv \frac{\Omega_{\mathrm{m}}\Gamma_{\mathrm{m}}}{\Omega_{\mathrm{m}}^2 - \Omega^2 - i\Omega\Gamma_{\mathrm{m}}} = \frac{\chi_x[\Omega]}{m\Omega_{\mathrm{m}}\Gamma_{\mathrm{m}}} \tag{4.1.5}$$

where χ_x is the conventional susceptibility. The back-action driven motion,

$$\delta x_{\mathrm{QBA}}[\Omega] = 2x_{\mathrm{zp}}\chi[\Omega]\sqrt{2n_{\mathrm{QBA}}/\Gamma_{\mathrm{m}}}\,\delta q_{\mathrm{in}}[\Omega] \tag{4.1.6}$$

arises from quantum fluctuations in the amplitude quadrature of the input field, δq_{in}, characterized by

$$\langle \delta q_{\mathrm{in}}(t)\delta q_{\mathrm{in}}(t')\rangle = \frac{1}{2}\delta(t-t') \tag{4.1.7}$$

and leads to an additional phonon occupation, $n_{\mathrm{QBA}} = C$. Here we adopt the definition, $\delta q_{\mathrm{in}} = (\delta a_{\mathrm{in}} + \delta a_{\mathrm{in}}^{\dagger})/\sqrt{2}$, for the amplitude quadrature. This, in conjunction with the conventional correlator for the photon flux gives a factor of 1/2 in the correlator for the amplitude quadrature.

Because δq_{in} is written onto the output optical phase vis-a-vis back-action, the amplitude and phase quantum fluctuations of the output field are correlated. The magnitude of these quantum correlations is characterized by the symmetrized cross-correlation spectrum (see appendix E.1),

$$\begin{aligned}\bar{S}_{pq}^{\mathrm{out}}[\Omega] &\equiv \int \langle \tfrac{1}{2}\{\delta p_{\mathrm{out}}(t), \delta q_{\mathrm{out}}(0)\}\rangle e^{i\Omega t}\,dt \\ &= 2\eta\, n_{\mathrm{QBA}}\,\mathrm{Re}\,\chi[\Omega]\end{aligned} \tag{4.1.8}$$

which is proportional to the back-action occupation, and the overall detection efficiency η. The correlation changes sign across the mechanical resonance frequency because of the 180° phase change in the response of the oscillator to the quantum back-action force.

Phase-amplitude correlations can be experimentally accessed by measuring a linear superposition of both the amplitude and phase of the transmitted field. Proper choice of the superposition, exemplified by a homodyne detector, allows for a quantum-limited measurement of both quadratures. Specifically, the transmitted field interferes at a beam-splitter with a strong local oscillator field at a fixed phase offset θ, followed by balanced detection of the two output of the beam-splitter. In this case, the photocurrent I_θ, is proportional to the rotated field quadrature, $\delta q_\theta = \delta q \cos\theta + \delta p \sin\theta$. Its spectrum therefore contains contributions due to amplitude/phase vacuum noise, oscillator motion, and quantum correlations,

$$\bar{S}^{\theta}_{II}[\Omega] \propto \cos^2\theta\, \bar{S}^{\text{out}}_{qq}[\Omega] + \sin^2\theta\, \bar{S}^{\text{out}}_{pp}[\Omega] + \sin(2\theta)\, \bar{S}^{\text{out}}_{pq}[\Omega] \tag{4.1.9}$$

Here,

$$\begin{aligned} \bar{S}^{\text{out}}_{qq}[\Omega] &= \tfrac{1}{2} \\ \bar{S}^{\text{out}}_{pp}[\Omega] &= \tfrac{1}{2} + 8\eta C \left|\chi[\Omega]\right|^2 (n_{\text{tot}} + \tfrac{1}{2}) \end{aligned} \tag{4.1.10}$$

are, respectively, the transmitted amplitude quadrature spectrum (containing a copy of the incident vacuum fluctuations) and the transmitted phase quadrature spectrum (carrying in addition, the total motion of the oscillator transduced via the optomechanical interaction). The quantity $n_{\text{tot}} = n_{\text{th}} + n_{\text{QBA}}$ is the phonon occupation of the oscillator due to the combined effect of the thermal and back-action forces.

The homodyne photocurrent spectrum (in eq. (4.1.9)), expressed in terms of the mechanical response,

$$\begin{aligned} \bar{S}^{\theta}_{II}[\Omega] \propto\ & 1 + 16\eta C \left|\chi[\Omega]\right|^2 \left(n_{\text{tot}} + \tfrac{1}{2}\right) \sin^2\theta \\ & + 4\eta C\, \mathrm{Re}\,\chi[\Omega]\, \sin 2\theta \end{aligned} \tag{4.1.11}$$

consists of a measurement imprecision due to vacuum fluctuations of the detected quadrature This consists of a component due to the motion of the oscillator diminished by a $\sin^2\theta$ factor, and a component due to correlations between the imprecision and the quantum back-action ($\propto \sin 2\theta$). By exploiting its different dependence on the homodyne angle and Fourier frequency, the correlation term may be detected despite the large thermal motion of the oscillator at room-temperature. Specifically, near the amplitude quadrature ($\theta = 0°$) and at Fourier frequencies detuned from mechanical resonance ($|\Omega - \Omega_{\text{m}}| \gtrsim \Gamma_{\text{m}}$), the contribution of thermal and back-action forces is suppressed relative to the correlation term. Closer inspection shows that a necessary requirement for the correlation term to dominate eq. (4.1.11) is that the back-action force dominates over thermal force: $n_{\text{QBA}} \gtrsim n_{\text{th}}$.

The large thermal occupation of room temperature mechanical oscillators makes it technically challenging to achieve $n_{\text{QBA}} > n_{\text{th}}$. Nevertheless, even when $n_{\text{QBA}} \ll n_{\text{th}}$, the signature of quantum correlations can be discerned in the homodyne photocurrent spectrum at frequencies far detuned from mechanical resonance (alternate detection techniques have been demonstrated [46, 144], and proposed [154], to detect back-action-induced quantum correlations on mechanical resonance). For detunings $\delta \equiv \Omega - \Omega_{\text{m}}$ which are larger than Γ_{m} the homodyne

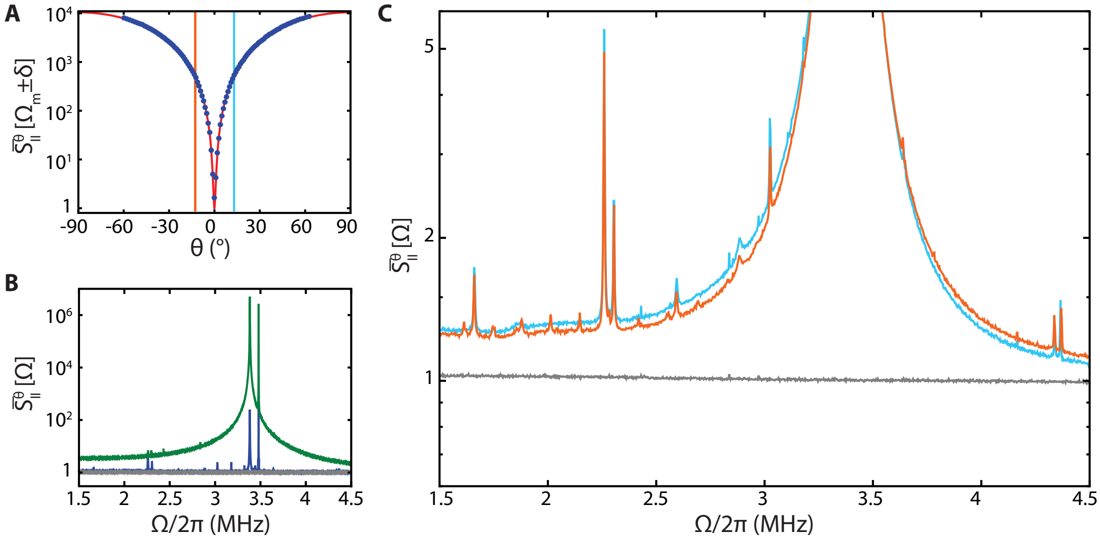

Figure 4.2 – **Asymmetry in homodyne spectrum:** (A) Resonant magnitude of the photocurrent signal, $\bar{S}^{\theta}_{II}[\Omega_\mathrm{m}]$ (normalized to shot-noise), as a function of the homodyne angle θ. Blue points are measurements. Red line is a fit to eq. (4.1.11). 40 dB suppression of the signal is achieved on the amplitude quadrature, limited by residual fluctuations in the homodyne angle ($\theta_\mathrm{RMS} < 0.57°$). (B) Example spectra taken near the phase (green) and amplitude (blue) quadratures. Also plotted is the background with the meter laser blocked (gray), dominated by LO shot noise (detector electronic noise is 10 dB below shot noise). For all measurements, feedback is used to stabilize the mechanical mode, as discussed in the main text. Note that the sharp peak at 3.5 MHz is due to thermal motion of the fundamental in-plane beam mode. (C) Magnified image of the spectrum at two quadratures, $\theta = \pm 13°$, highlighted with vertical lines in (A) (blue = $+13°$, yellow = $-13°$). The ~ 10% asymmetry between the two spectra at non-zero detuning arises due to quantum correlations (last term in eq. (4.1.11)). Larger asymmetry is observed at Fourier frequencies further from mechanical resonance, as predicted by eq. (4.1.12). The spectra are measured at an injected power of $P_\mathrm{in} = 280\,\mu$W.

photocurrent spectrum takes on a signature anti-symmetry with respect to both δ and θ [148, 149]

$$\begin{aligned}&\bar{S}^{\theta}_{II}[\Omega_\mathrm{m}+\delta]_{|\delta|\gg\Gamma_\mathrm{m}} \approx \\ &\quad 1 + 4\eta C\left(\frac{\Gamma_\mathrm{m}}{\delta}\right)^2 \sin^2\theta\left(n_\mathrm{th} + n_\mathrm{QBA} - \frac{\delta}{\Gamma_\mathrm{m}}\cot\theta\right)\end{aligned} \tag{4.1.12}$$

Note that such an anti-symmetry can also arise from quantum correlations established by injecting squeezed light into the optical cavity [155] (or classical correlations established by injecting a laser field with classical amplitude fluctuations [156, 157]). Figure 4.1B shows a model of the homodyne photocurrent spectrum for a quadrature close to the amplitude (i.e., $\theta \approx 0°$): the red trace represents the asymmetric spectrum observed at sufficiently large optical powers and the blue and green traces represent contributions due to thermal motion and quantum correlations, respectively.

4.2 Observation of quantum correlations

In the following we discuss homodyne measurements of a rotated quadrature of the field transmitted through the room temperature nanobeam-microdisk optomechanical system, with powers sufficient to resolve the asymmetry due to quantum correlations. In order to mitigate optomechanical instabilities, active radiation pressure feedback is used to damp the mechanical mode [138, 158]. For this purpose we employ an auxiliary 850 nm laser side-locked to an independent cavity mode (see appendix E.2.2). Cold-damping of this sort changes the mechanical susceptibility within the feedback bandwidth (1 kHz in this instance). Nevertheless, the total decoherence rate, and the ratio $n_{\mathrm{QBA}}/n_{\mathrm{th}}$, remains unchanged. Figure 4.2A shows the sensitivity of the homodyne interferometer as a function of the local oscillator phase θ. By operating with a modest input power of 25μW, we measure thermal motion of the oscillator with an (phonon-equivalent) imprecision, $n_{\mathrm{imp}} = (16\eta C)^{-1} \approx 1.2\cdot 10^{-4}$, that is approximately 40 dB below that at the SQL (i.e. $n_{\mathrm{imp}} = 1/4$) while operating on phase quadrature ($\theta = 90°$). As the local oscillator phase is swept towards the amplitude quadrature ($|\theta| \to 0°$), the apparent thermal motion is suppressed by about 40 dB. Figure 4.2B shows example photocurrent spectra measured close to the phase (green) and amplitude (blue) quadratures; the gray trace shows shot-noise of the homodyne detector, recorded by blocking the meter field. Excess amplitude noise in the output field is measured to be $\approx 1\%$ of shot-noise for the largest powers used in our experiments ($P \approx 100\mu$W), which we attribute to thermally driven fluctuations of the tapered fiber.

In order to visualize the asymmetry in the photocurrent spectra as predicted by eq. (4.1.12), we compare two spectra at homodyne angles symmetric about the amplitude quadrature, indicated by the blue (at angle $+\theta$) and yellow (at angle $-\theta$) vertical lines in fig. 4.2A. The corresponding spectra are shown in fig. 4.2C. An asymmetry of approximately 10% with respect to Fourier frequency, is observed at detunings $\delta \gtrsim 2\pi\cdot 100$ kHz, consistent with the theoretically predicted effect due to quantum correlations. Qualitatively, the observed asymmetry over a broad range of frequencies – more than a MHz on either side of resonance – indicates that the magnitude of quantum-noise-induced correlations is comparable to all sources of quantum noise at these frequencies.

The asymmetry in the observed spectrum (red in fig. 4.2C) traces its root to the detuning dependence of quantum correlations (green trace in fig. 4.1B, and third term in eq. (4.1.12)). In order to systematically investigate this asymmetry, we consider the ratio of the homodyne photocurrents at frequency offsets at $\pm\delta$ from mechanical resonance,

$$R_\theta \equiv \frac{\bar{S}^{\theta}_{II}[\Omega_{\mathrm{m}}+\delta]}{\bar{S}^{\theta}_{II}[\Omega_{\mathrm{m}}-\delta]} \tag{4.2.1}$$

Following eq. (4.1.12),

$$R_\theta = \frac{1+4\eta C n_{\mathrm{tot}}(\Gamma_{\mathrm{m}}\sin\theta/\delta)^2\,(1-(\delta/n_{\mathrm{tot}}\Gamma_{\mathrm{m}})\cot\theta)}{1+4\eta C n_{\mathrm{tot}}(\Gamma_{\mathrm{m}}\sin\theta/\delta)^2\,(1+(\delta/n_{\mathrm{tot}}\Gamma_{\mathrm{m}})\cot\theta)} \tag{4.2.2}$$

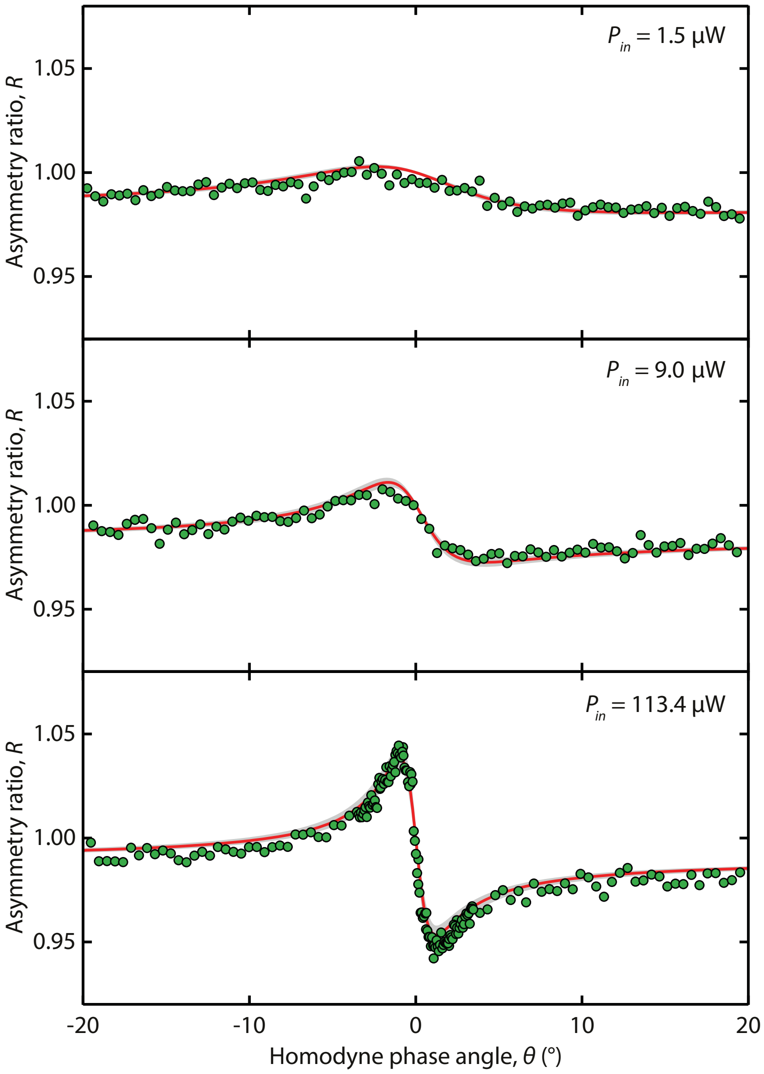

Figure 4.3 – **Asymmetry in spectrum as a function of homodyne angle:** Each plot shows asymmetry of the homodyne spectra, R_θ (eq. (E.1.17)), as a function of homodyne angle. From top to bottom, R_θ is plotted as the probe power (mean intracavity photon number) is increased: $P_{\text{in}} = 1.5, 9, 113.4\,\mu W$ ($n_c \approx 0.3\cdot10^4, 2.1\cdot10^4, 58\cdot10^4$). Red lines are a model employing only quantum noises and independently inferred values of the effective single-photon cooperativity, ηC_0; gray band shows interval corresponding to uncertainties in either parameter.

Note that quantum correlations render R_θ anti-symmetric in θ about amplitude quadrature ($\theta = 0°$), i.e.,

$$R_\theta - 1 \approx -(R_{-\theta} - 1) \tag{4.2.3}$$

It is therefore a robust experimental signature for the presence of quantum correlations, provided that excess amplitude and phase noise of the meter laser is sufficiently small (see appendix E.2.5 and [46]). R_θ is measured by recording the spectral power in windows of finite bandwidth symmetric about resonance ($\delta = \pm 2\pi\cdot 21\,\text{kHz}$, also see appendix E.2.3), as a function of the homodyne angle θ. fig. 4.3 shows R_θ for several probe powers. At low probe powers (i.e. low cooperativity, $C \approx 8 \cdot 10^2$), shown in the top panel of fig. 4.3, the anti-symmetric feature around the amplitude quadrature (i.e. $R_\theta - 1$) is relatively small due to the large measurement imprecision. As the probe power is increased, shown in the two subsequent panels of fig. 4.3, the relative contribution of quantum correlation increases, leading to a progressively larger anti-symmetry near amplitude quadrature. We note that classical sources of noise may also affect the anti-symmetric feature. For example, laser amplitude noise can establish classical amplitude-phase correlations leading to excess anti-symmetry [157], or anharmonicity of the mechanical oscillator can lead to structured thermal noise which at large Fourier frequency detuning modify the anti-symmetry [159]. These and various other sources of systematics were found to be negligible in our experiment (see appendices E.1.2, E.1.3 and E.2.5).

For the scenario in our experiments, where the back-action is large, but does not overwhelm thermal motion, i.e. $n_{\mathrm{th}} \gg n_{\mathrm{QBA}} \gg 1$, the visibility of the anti-symmetric feature in $R_{\theta\approx 0}$, is given by,

$$\Delta R \equiv \max R_\theta - \min R_\theta \approx 4\sqrt{\eta \frac{n_{\mathrm{QBA}}}{n_{\mathrm{th}}}} \tag{4.2.4}$$

Here the extrema are calculated with respect to both the readout angle θ and for detuning, $\delta \in (\Gamma_{\mathrm{m}}, 2\Gamma_{\mathrm{m}}\sqrt{\eta C n_{\mathrm{th}}})$ (see SI). The square-root scaling of ΔR is unique to quantum correlations (as opposed to correlations produced by classical noise), and makes possible the 10% asymmetry despite the the relatively small magnitude of quantum back-action in our room temperature experiment $n_{\mathrm{QBA}}/n_{\mathrm{th}} \approx 10^{-2}$. In fig. 4.4 we show measurements of ΔR versus power by analyzing a series of quadrature sweeps as shown in fig. 4.3. For all data, ΔR is extracted from the asymmetry in the same spectral window around $|\delta| \approx 2\pi \cdot 2 \cdot 10^3 \cdot \Gamma_{\mathrm{m}}$. The observed scaling agrees well with the square-root scaling predicted by eq. (E.1.16), shown as a red line in fig. 4.4 with parameters for C, η and n_{th} determined independently.

For comparison, it can be shown that for a laser with excess classical amplitude noise, characterized by an average thermal photon occupation C_{qq} in excess of shot-noise, the visibility of the anti-symmetric feature is given by (see appendix E.1.1),

$$\Delta R = 4\sqrt{\eta \frac{n_{\mathrm{QBA}}}{n_{\mathrm{th}}}(1 + 2C_{qq})} \tag{4.2.5}$$

Phenomenologically, when optical power is changed by attenuating the laser beam (as done in our experiment), excess amplitude noise scales as $C_{qq} \propto P$, leading to $\Delta R \propto P$. This linear scaling is in qualitative disagreement with the observations in fig. 4.4.

4.3 Quantum-noise cancellation for force sensing

Quantum correlations are a generic resource for enhancing the precision with which parameters of a system can be estimated [160]. In the context of force estimation using interferometric

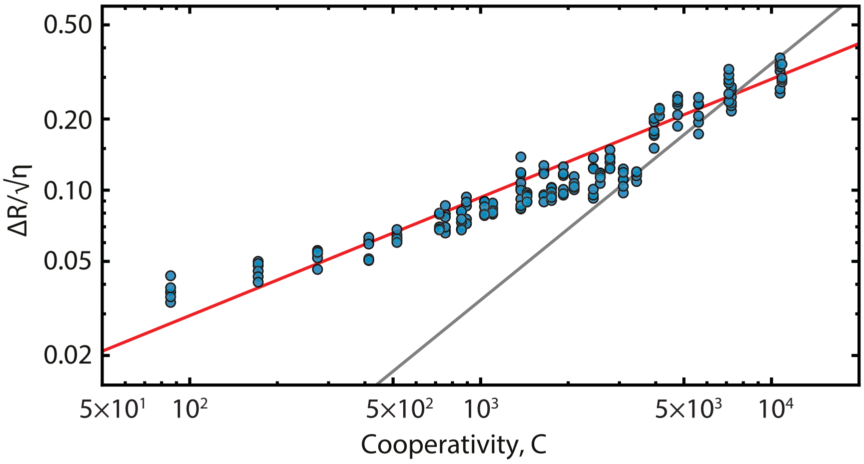

Figure 4.4 – **Visibility of quantum correlations versus laser power:** Measurement of ΔR (eq. (E.1.16)) as a function of laser power, referred to optomechanical cooperativity, C. Blue points are measurements taken for various detunings δ at each power. The red line is a prediction based on eq. (E.1.16), with a notably square-root dependence on power. The gray line is a linear fit to the data, which would apply if the correlations were entirely due to classical amplitude noise in the laser (see eq. (4.2.5)).

techniques, two techniques – injection of external correlations [128, 133, 135], and back-action evasion [127, 161, 162] – have been conventionally employed to surpass limits imposed by quantum noise of the optical field. A third alternative – correlations developed in-situ – can be directly used to derive a metrological advantage [132, 133]. For example, by performing a rotated-quadrature measurement of the cavity output field, an off-resonant external force (F_{ext}) applied to the mechanical oscillator, can be estimated with a precision better than that achievable with a phase quadrature measurement. As inferred from the homodyne photocurrent (eq. (4.1.11)), the apparent force experienced by the oscillator (i.e., the force estimator, F^{θ}_{est}) has a spectral density (see appendix E.3)

$$\begin{aligned}\bar{S}^{\text{est},\theta}_{FF}[\Omega] &= \bar{S}^{\text{ext}}_{FF}[\Omega] + \bar{S}^{\text{th}}_{FF}[\Omega] \\ &\quad + \bar{S}^{\text{imp},\theta}_{FF}[\Omega] + \bar{S}^{\text{QBA}}_{FF}[\Omega] + \hbar\cot\theta\frac{\operatorname{Re}\chi_x[\Omega]}{|\chi_x[\Omega]|^2}\end{aligned} \tag{4.3.1}$$

where we now employ the conventional susceptibility, $\chi_x[\Omega] \equiv [m(\Omega_{\text{m}}^2 - \Omega^2 - i\Omega\Gamma_{\text{m}})]^{-1}$. Equation (4.3.1) shows that the uncertainty in the estimate of F_{ext} has a classical component due to thermomechanical noise $\left(\bar{S}^{\text{th}}_{FF}\right)$ and a quantum component (second line in eq. (4.3.1)) due to phase quantum noise (imprecision), amplitude shot noise (back-action), and, correlations between the two. By detecting a rotated field quadrature ($\theta \neq 90°$), phase-amplitude correlations ($\propto \cot\theta$) can be used to reduce the uncertainty due to quantum noise, which has to be weighed against a concomitant reduction of the signal. In the limit of strong back-action $\bar{S}^{\text{QBA}}_{FF} \gg \bar{S}^{\text{imp},\pi/2}_{FF}$ (i.e. $C \gg 1$), and at an optimal measurement quadrature at angle θ_{opt}, this

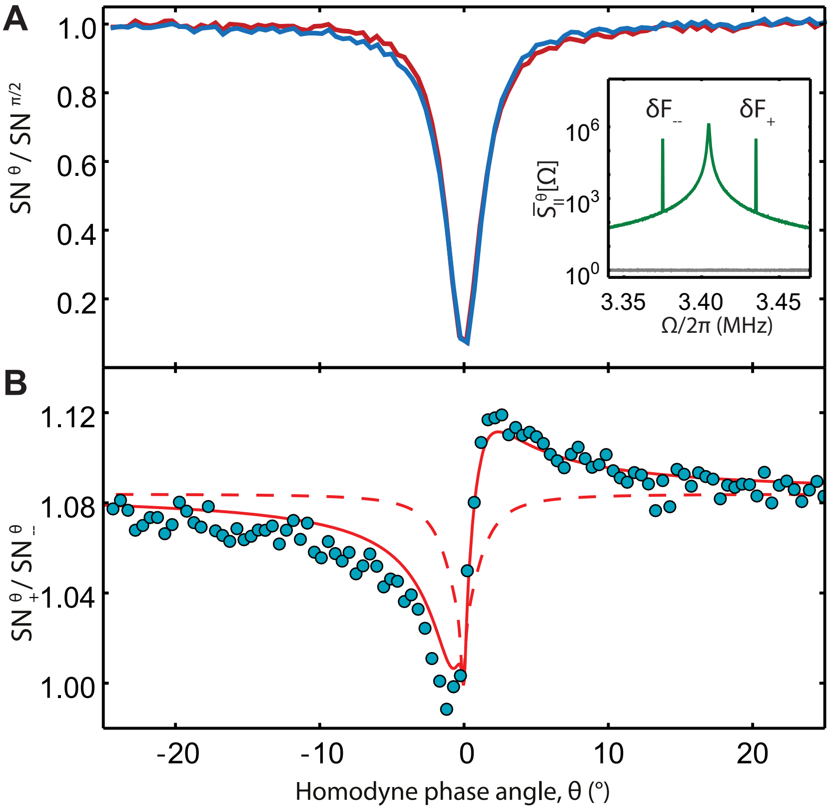

Figure 4.5 – **Quantum-enhanced force estimation:** (A) Inset: Homodyne photocurrent spectrum near phase quadrature showing the two balanced forces applied on the mechanical oscillator via radiation pressure from the auxiliary laser. Main: Red (blue) shows the signal-to-noise ratio of the force F_+ (F_-) normalized to its value for phase quadrature detection, i.e. $\mathrm{SN}^{\theta}_{+(-)}/\mathrm{SN}^{\pi/2}_{+(-)}$. The asymmetry between the two traces at $\theta \approx \pm 10°$ is due to quantum noise cancellation. Here the laser input power is $P_{\mathrm{in}} = 30\,\mu\mathrm{W}$. (B) Green shows $\mathrm{SN}^{\theta}_{+}/\mathrm{SN}^{\theta}_{-}$, extracted as a ratio of the blue and red traces in panel (A). For a force balanced in intensity and frequency offset from resonance, eq. (4.3.5) predicts that $\mathrm{SN}^{\theta}_{+}/\mathrm{SN}^{\theta}_{-} \propto R_\theta$. The solid red line is a prediction based on eq. (4.3.5) in conjunction with eq. (E.1.17), while red dashed shows the same model excluding the contribution from quantum correlations.

trade-off reduces to the simplified form (see appendix E.3),

$$\begin{aligned}\bar{S}^{\mathrm{est},\theta_{\mathrm{opt}}}_{FF}[\Omega] &= \bar{S}^{\mathrm{ext}}_{FF}[\Omega] + \bar{S}^{\mathrm{th}}_{FF}[\Omega] \\ &+ \bar{S}^{\mathrm{imp},\pi/2}_{FF}[\Omega] + \left[1 - \eta\left(\frac{\mathrm{Re}\,\chi_x[\Omega]}{|\chi_x[\Omega]|}\right)^2\right]\bar{S}^{\mathrm{QBA}}_{FF}[\Omega]\end{aligned} \tag{4.3.2}$$

Equation (4.3.2) shows that measurement back-action can be “erased” from the measured photocurrent at frequencies offset from mechanical resonance. The efficacy of this back-action erasure is limited by the detection efficiency, η. Note that, by contrast, *physical* back-action is suppressed in back-action evasion schemes [127].

In the presence of thermal noise, the signal-to-noise enhancement afforded by quantum correlations in eq. (4.3.2) is diminished by a factor of approximately $n_{\mathrm{th}}/n_{\mathrm{QBA}}$. We nevertheless observe the principle behind this quantum-enhancement, by applying a detuned radiation force $F_{\text{ext}}[\Omega_{\text{ext}}]$ via an auxiliary cavity field (see appendix E.2.2) and recording the signal-to-noise ratio,

$$\text{SN}^{\theta}[\Omega_{\text{ext}}] \equiv \frac{\bar{S}_{FF}^{\text{est},\theta}[\Omega_{\text{ext}}]}{\bar{S}_{FF}^{\text{est},\theta}[\Omega_{\text{ext}}] - \bar{S}_{FF}^{\text{ext}}[\Omega_{\text{ext}}]} \tag{4.3.3}$$

in the homodyne photocurrent versus θ. In the experiment, we choose a two-tone force of the form,

$$F_{\text{ext}}[\Omega] = F_{+}\delta[\Omega_{\text{m}} + \delta] + F_{-}\delta[\Omega_{\text{m}} - \delta] \tag{4.3.4}$$

centered around resonance, so that one of the forces provides a reference for the signal-to-noise ratio. We denote by $\text{SN}_{\pm}^{\theta}$, the definition of the signal-to-noise ratio in eq. (4.3.3) applied to each of the two force components ($F_{\pm}$). Figure 4.5A shows the variation of $\text{SN}_{\pm}^{\theta}$ for each of the forces $F_{\pm}$ (carefully balanced, as shown in inset) as the homodyne readout angle is varied. The effect of quantum correlations in the optical field is to cancel back-action at intermediate measurement quadratures ($0° < |\theta| < 90°$), leading to an enhancement or suppression of $\text{SN}_{\pm}^{\theta}$ at these optimal quadratures. For a fixed measurement setting (i.e. fixed value of C, θ, δ), it can be seen that quantum noise cancellation leads to an enhanced signal-to-noise ratio for F_{+} relative to F_{-}, or vice versa. The absolute value of the enhancement is given by the ratio,

$$\frac{\text{SN}^{\theta}[\Omega_{\text{m}} + \delta]}{\text{SN}^{\theta}[\Omega_{\text{m}} - \delta]} \approx \frac{1}{R_{\theta}} \frac{|\chi_x[\Omega_{\text{m}} + \delta]|^2}{|\chi_x[\Omega_{\text{m}} - \delta]|^2} \frac{\langle F_{+}^2 \rangle}{\langle F_{-}^2 \rangle}. \tag{4.3.5}$$

This ratio is plotted in fig. 4.5B. The observed anti-symmetric dependence on θ is directly related to R_{θ} (eq. (E.1.17)). The offset from unity at $\theta = \pm 90°$ is due to imperfect balance of the two forces. The maximum deviation (at $\theta \approx \pm 10°$) of approximately 6% is less than the absolute signal loss shown in fig. 4.5A. It nevertheless provides a measure of the improvement obtained in the ability to estimate a force with and without quantum noise cancellation.

4.4 Conclusion

To summarize, we have demonstrated a room-temperature cavity-enhanced interferometer where quantum correlations of light are generated *in-situ* via the radiation pressure interaction between light and the effective harmonic motion of the cavity. We show that these correlations manifest as a 10% cancellation of quantum noise in a homodyne measurement away from phase quadrature – "variational measurement" – of the optical field over an octave in frequency about 3 MHz from the optical carrier. The absolute magnitude of quantum noise cancellation is shown to scale as the square root of the ratio of the back-action to thermal force acting on the mechanical oscillator. Finally, by applying an external force to the oscillator, we demonstrate how quantum noise cancellation leads to an increase in the signal-to-noise ratio for the external force. In future experiments, where back-action is the dominant force noise, the "variational" measurement technique, applied here at room temperature, can be used to surpass the standard quantum limit for a linear force measurement. This remains a long-standing pursuit in the gravitational wave community, and was recently demonstrated in a micro-cavity optomechanical system at dilution refrigerator temperatures to obtain a displacement sensitivity beyond the finite-efficiency standard quantum limit [163].

5 Feedback cooling from cryogenic temperatures

Feedback control of mechanical oscillation is found in many applications, ranging from stabilizing the ~kg test mass in a gravity-wave interferometer [164] to trapping/cooling of atomic [165] and sub-atomic particles [166]. A basic approach uses a sensor to track the oscillator's position and an actuator to convert the measurement record into a continuous ('real-time') feedback force. Recently the quantum limits of continuous feedback [167] have been explored, enabling remarkable demonstrations such as microwave Fock state generation [168] and persistent Rabi oscillations in a superconducting qubit [169]. These protocols employ a 'weak measurement' capable of tracking a quantum state as rapidly as it decoheres due to measurement back-action [170]. For mechanical oscillators, ideal weak position measurements [171] have in fact been available since the advent of the laser, in the context of shot-noise-limited interferometry [22]. Only recently, however, with the confluence of low-loss, cryogenic micromechanics and on-chip, integrated photonics explored in cavity optomechanics [21], has it been feasible to consider their application to quantum feedback protocols [32, 33]. The main challenge is thermal noise, which places stringent requirements on the timescale in which the measurement must take place.

Feedback cooling [32, 158, 165, 172] is a well-studied control protocol that illustrates both the utility and the challenge of quantum feedback applied to mechanical systems. In feedback cooling protocols, a mechanical oscillator undergoing thermal Brownian motion is steered towards its ground state by minimizing a measurement of its displacement, S_x (here expressed as a power spectral density [171] evaluated at the oscillator frequency, Ω_m). A conventional strategy [158] is to apply a feedback force proportional to the measurement's time derivative (estimating the oscillator's velocity). The resultant damping acts to reduce (cool) the motion of the oscillator until it coincides with the measurement imprecision, S_x^imp. Cooling the oscillator until it spends most of the time in its ground state (a phonon occupancy of $n_\mathrm{m} < 1$) is possible if S_x^imp remains lower than the zero-point fluctuations of the damped oscillator, i.e., if $S_x^\mathrm{imp} \lesssim S_x^\mathrm{zp}/n_\mathrm{th}$ (see appendix F.1.3) where S_x^zp is the spectral density of intrinsic (absent feedback) zero-point fluctuations and n_th is the phonon occupancy of the thermal bath.

This chapter is adapted from [28]

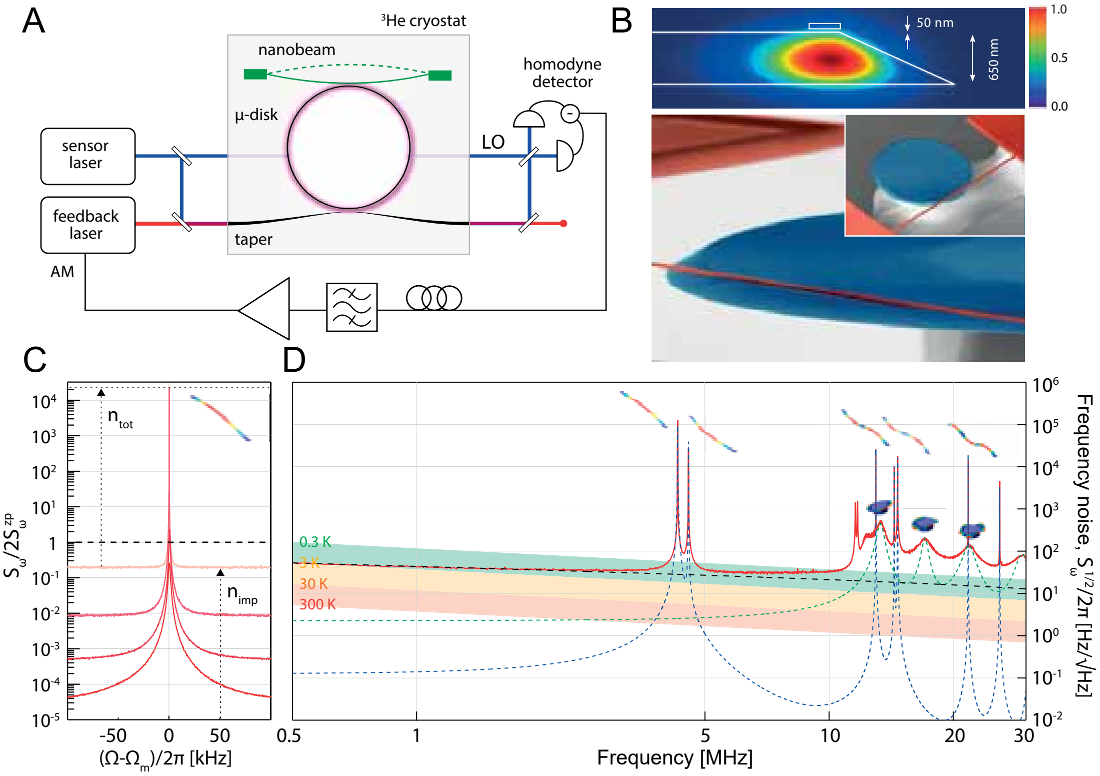

Figure 5.1 – **Measuring and controlling the position of a nanomechanical beam using a near-field optomechanical transducer:** (a) Whispering gallery modes of a SiO_2 microdisk are excited using a tapered optical fiber driven by a pair of tunable diode lasers. Displacement of a Si_3N_4 nanobeam, sampling the evanescent mode volume of the microdisk, is recorded in the phase of the transmitted sensor field using a balanced homodyne detector. Radiation pressure feedback is applied by modulating the amplitude of the feedback laser with an electrically processed copy of the homodyne photocurrent. Sample and fiber are both embedded in a ^{3}He cryostat operating at 4.4 K. (b) Above: Finite element model of the optical mode (field amplitude). Optomechanical coupling is proportional to the field intensity gradient at the position of the beam. Below: SEM image of the optomechanical system. (c) Thermomechanical noise spectrum of the fundamental beam mode, measured with varying intracavity photon number. (d) Broadband extraneous (shot-noise-subtracted) homodyne signal expressed as apparent cavity frequency noise. Solid red corresponds to measurement data. Dashed blue, green, and black lines correspond to estimated contributions from nanobeam thermomechanical, microdisk thermomechanical, and microdisk thermorefractive noise, respectively. Colored bands denote the imprecision required for $\Gamma_{\mathrm{meas}} = \Gamma_{\mathrm{th}}$: $S_\omega^{\mathrm{imp}} = g_0^2\hbar Q_{\mathrm{m}}/2k_B T$, assuming $g_0^2 \propto 1/\Omega$ and $Q_{\mathrm{m}} = 7.6\cdot 10^5$.

($S_x^{\mathrm{zp}} = 4x_{\mathrm{zp}}^2/\Gamma_{\mathrm{m}}$ is given by the ratio of the ground-state variance $x_{\mathrm{zp}}^2 = \hbar/(2m\Omega_m)$ and the mechanical damping rate Γ_{m}, where $\hbar$ is the reduced Planck's constant and m is the effective mass of the oscillator.) In the frequency domain, this amounts to resolving the intrinsic thermal displacement $S_x \approx 2n_{\mathrm{th}}S_x^{\mathrm{zp}}$ with a signal-to-noise of $S_x/S_x^{\mathrm{imp}} \gtrsim 2n_{\mathrm{th}}^2$. In the time domain, it corresponds to resolving the zero-point motion at a characteristic "measurement" rate [171]

$$\Gamma_{\mathrm{meas}} \equiv \frac{x_{\mathrm{zp}}^2}{2S_x^{\mathrm{imp}}} \gtrsim \frac{\Gamma_{\mathrm{th}}}{8}, \tag{5.0.1}$$

where $\Gamma_{\mathrm{th}} \approx \Gamma_{\mathrm{m}} n_{\mathrm{th}}$ is the oscillator's thermal decoherence rate. Eq. 5.0.1 implies the ability to resolve a displacement of x_{zp} in the timescale over which a single phonon enters from the thermal bath, $\tau_{\mathrm{th}} \approx \Gamma_{\mathrm{th}}^{-1}$. This is a technically daunting challenge because of the small x_{zp} and large Γ_{th} of typical engineered mechanical oscillators. As a consequence, despite the success of autonomous feedback [23–25], ground-state cooling using measurement-based feedback has yet to be demonstrated.

An additional, fundamental caveat at once compounds the challenge of ground state cooling and hints at the underlying virtue of quantum feedback: Heisenberg's uncertainty principle predicts that a weak ($\Gamma_{\mathrm{meas}} \ll \Omega_{\mathrm{m}}$) continuous position measurement with an imprecision of $S_x^{\mathrm{zp}}/2$ will produce a stochastic 'back-action' force that disturbs the position of the oscillator by at least the same amount [171]. By inference, an imprecision of $n_{\mathrm{imp}} \equiv S_x^{\mathrm{imp}}/2S_x^{\mathrm{zp}}$ equivalent bath quanta results in an effective increase of the thermal bath occupation by $n_{\mathrm{ba}} \geq 1/16 n_{\mathrm{imp}}$ (see appendix F.1.3). This penalty would appear to prohibit ground-state cooling, as it entails substantially heating the oscillator to achieve the necessary measurement precision. Remarkably, however, feedback counteracts back-action [173], so that a phonon occupancy of $n_{\mathrm{m}} \approx 2\sqrt{n_{\mathrm{imp}}(n_{\mathrm{ba}} + n_{\mathrm{th}})} - 1/2 < 1$ (see appendix F.1.2) can still be achieved [32, 172]. The limiting case of $n_{\mathrm{m}} \to 0$ is approached when the measurement record is dominated by back-action-induced fluctuations. This occurs when the measurement is maximally efficient [170], i.e., when the measurement rate, $\Gamma_{\mathrm{meas}} = \Gamma_{\mathrm{m}}/16 n_{\mathrm{imp}}$, approaches the effective thermal decoherence rate, $\Gamma_{\mathrm{tot}} \approx (n_{\mathrm{th}} + n_{\mathrm{ba}})\Gamma_{\mathrm{m}} \geq \Gamma_{\mathrm{meas}}$. To meet this condition for a typical engineered oscillator, a linear position sensor must achieve an imprecision far ($\sim n_{\mathrm{th}}$ times) below the natural scale set by the 'standard quantum limit' (SQL) [171] ($n_{\mathrm{imp}} = n_{\mathrm{ba}} = 1/4$), while maintaining back-action near the uncertainty limit: $4\sqrt{n_{\mathrm{ba}} n_{\mathrm{imp}}} \geq 1$.

Coupling micromechanical oscillators to optical cavities has emerged as a promising route to meeting the above requirements. Transduction in such 'cavity-optomechanical systems [21] arises from a parametric coupling, $G = \partial\omega_{\mathrm{c}}/\partial x$, between the position of the oscillator and the resonance frequency ω_{c} of a cavity. For broadband sensing, characterized by a cavity decay rate $\kappa \gg \Omega_{\mathrm{m}}$, a resonant laser field passing through the cavity acquires a phase shift $2G\delta x/\kappa$; this can be resolved in a homodyne interferometer with a quantum-noise-limited imprecision of $S_x^{\mathrm{imp}} = (8G^2 n_c \eta/\kappa)^{-1}$, where n_{c} is the mean intracavity photon number and $\eta \in [0,1]$ is the effective photon collection efficiency (see appendix F.2). The associated measurement rate is given by $\Gamma_{\mathrm{meas}} = 4g_0^2 n_{\mathrm{c}}\eta/\kappa \equiv \Gamma_{\mathrm{m}} \cdot C_0 n_{\mathrm{c}}\eta$, where $g_0 \equiv G x_{\mathrm{zp}}$ is the vacuum optomechanical coupling rate and $C_0 \equiv 4g_0^2/\kappa\Gamma_{\mathrm{m}}$, the 'single-photon cooperativity' [21], characterizes the per-photon measurement rate. To achieve efficient measurements, contemporary cavity-optomechanical systems combine the state-of-the-art in high-Q nanomechanics and microphotonics [21]. As a consequence, imprecision below that at the SQL [45, 55, 174], as well as quantum-back-action (i.e., radiation pressure shot noise [22]) [30, 175] has recently been observed. In none of these experiments, however, was $\Gamma_{\mathrm{meas}} \approx \Gamma_{\mathrm{th}}$ demonstrated at the photodetector, owing to a combination of large thermal occupation, extraneous imprecision, optical loss, and dynamic instabilities. (We note that an electromechanical device operating deep in the 'good-cavity' limit, $\kappa \ll \Omega_{\mathrm{m}}$, has recently achieved $\Gamma_{\mathrm{meas}} > \Gamma_{\mathrm{th}}$ [176]; however, the use of a far- off-resonant probe here results in strong dynamic coupling of the optical and mechanical mode.)

Our study is carried out using the system described in chapters 2 and 3, consisting of a 65 μm × 400 nm × 70 nm (effective mass $m \approx 2.9$ pg) nanobeam placed ~ 50 nm from the surface of a 30 μm diameter microdisk. The microdisk is optically probed using a low-loss ($\approx 6\%$) fiber-taper pumped by a tunable diode laser. Displacement of the nanobeam is observed in the phase of the transmitted cavity field using a balanced homodyne interferometer. We interrogate two optical modes: a 'sensor' mode (used for readout) at $\lambda_\mathrm{c} \approx 775$ nm that exhibits an intrinsic decay rate of $\kappa_0 \approx 2\pi \cdot 0.44$ GHz and a 'feedback' mode (used for radiation pressure actuation) at $\lambda_\mathrm{c} \approx 843$ nm for which $\kappa_0 \sim 2\pi \cdot 1$ GHz. For the mechanical oscillator, we use the $\Omega_\mathrm{m} \approx 2\pi \cdot 4.3$ MHz fundamental out-of-plane mode of the nanobeam. The optomechanial coupling strength between the oscillator and the sensor mode is $g_0 \approx 2\pi \cdot 20$ kHz, corresponding to a frequency pulling factor of $G \approx 2\pi \cdot 0.70$ GHz/nm for the estimated zero-point amplitude of $x_\mathrm{zp} \approx 29$ fm. Our experiments are conducted in a ^{3}He buffer gas cryostat [24] at a bath temperature of $T \approx 4.4$ K ($n_\mathrm{th} \simeq k_\mathrm{B} T/\hbar\Omega_\mathrm{m} \approx 2.1 \cdot 10^4$) and at gas pressures below 10^{-3} mbar. Ringdown measurements reveal a mechanical damping rate of $\Gamma_\mathrm{m} \approx 2\pi \cdot 5.7$ Hz ($Q_\mathrm{m} \approx 7.6 \cdot 10^5$). Our system thus allows for a near-unity cooperativity of $C_0 \approx 0.64$.

All position sensors are limited by extraneous thermal noise. In optical-cavity-based sensors, major sources include thermomechanical and thermorefractive fluctuations of the cavity substrate [45]. These result in excess cavity frequency noise, $S_\omega^\mathrm{imp,ex}$, and limit the measurement rate to:

$$\Gamma_\mathrm{meas} = \frac{g_0^2/2}{S_\omega^\mathrm{imp,shot} + S_\omega^\mathrm{imp,ex}} = \frac{\Gamma_\mathrm{m}/16}{n_\mathrm{imp}^\mathrm{shot} + n_\mathrm{imp}^\mathrm{ex}} \tag{5.0.2}$$

where $S_\omega^\mathrm{imp,shot}$ is the photocurrent shot noise referred to an apparent cavity resonance frequency noise and $n_\mathrm{imp}^\mathrm{shot(ex)} \equiv S_\omega^\mathrm{imp,shot(ex)}/2S_\omega^\mathrm{zp}$. Fig. 5.1d shows the extraneous noise floor of our sensor over a broad range of frequencies. We obtained this spectrum by subtracting shot noise from a measurement made with a large intracavity photon number, $n_\mathrm{c} > 10^5$. (To mitigate dynamic instabilities, this measurement was conducted using ~ 10 mbar of gas pressure at an elevated temperature of 15.7 K.) High- and low-Q noise peaks correspond to thermal motion of the nanobeam and the microdisk, respectively. Near the fundamental noise peak, we observe an extraneous frequency noise of $S_\omega^\mathrm{imp,ex} \approx (2\pi \cdot 30\mathrm{Hz}/\sqrt{\mathrm{Hz}})^2$, corresponding to a displacement imprecision of $S_x^\mathrm{imp,ex} \approx (4.3 \cdot 10^{-17}\mathrm{m}/\sqrt{\mathrm{Hz}})^2$. We identify this as a combination of thermorefractive noise [45], diode laser frequency noise [21], and off-resonant thermal motion of the in-plane nanobeam mode at 4.6 MHz. Owing to the large zero-point motion of the oscillator, $S_\omega^\mathrm{zp} \equiv 4g_0^2/\Gamma_\mathrm{m} = (2\pi \cdot 6.7\,\mathrm{kHz}/\sqrt{\mathrm{Hz}})^2$ ($S_x^\mathrm{zp} = (0.95 \cdot 10^{-14}\mathrm{m}/\sqrt{\mathrm{Hz}})^2$), the equivalent bath occupancy of $S_x^\mathrm{imp,ex}$ has an exceptionally low value of $n_\mathrm{imp}^\mathrm{ex} \approx 1.0 \cdot 10^{-5}$, nearly 44 dB below that at the SQL. The associated measurement rate, $\Gamma_\mathrm{m}/16 n_\mathrm{imp}^\mathrm{ex} \approx 2\pi \cdot 36$ kHz, is equal to the thermal decoherence rate at an experimentally accessible temperature of 1.3 K, implying

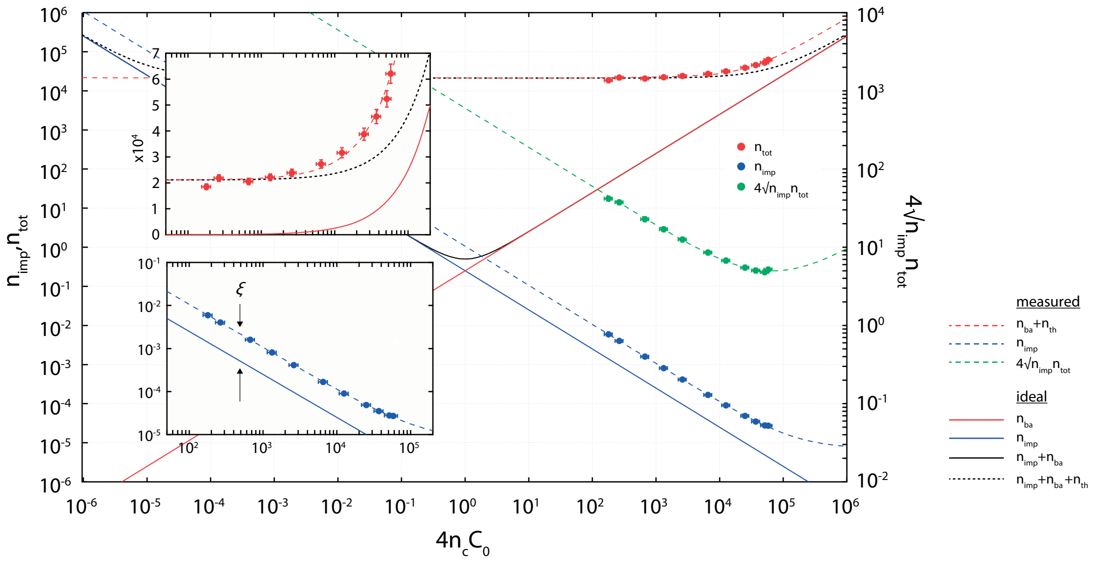

Figure 5.2 – **Measurement imprecision and back-action versus intracavity photon number:**. Red, blue, and green points correspond to measurements of total effective bath occupation, $n_{\mathrm{tot}} = n_{\mathrm{th}} + n_{\mathrm{ba}}$, measurement imprecision referred to an equivalent bath occupation, n_{imp}, and apparent imprecision-back-action product, $4\sqrt{n_{\mathrm{tot}} n_{\mathrm{imp}}}$, respectively. Short-dashed red, blue, and black lines correspond to models of $n_{\mathrm{ba}} = C_0 n_{\mathrm{c}}$, $n_{\mathrm{imp}} = 1/16 C_0 n_{\mathrm{c}}$, and their sum, $n_{\mathrm{ba}} + n_{\mathrm{imp}}$, respectively. Dash-dotted black line represents the apparent bath occupation $n_{\mathrm{tot}} + n_{\mathrm{imp}}$. Long-dashed red and blue lines highlight excursion from their counterparts due to extraneous back-action, $C_0^{\mathrm{ex}} = 0.56$, extraneous imprecision, $n_{\mathrm{imp}}^{\mathrm{ex}} = 0.70 \cdot 10^{-5}$, and imperfect detection efficiency, $\xi = 0.23$, as described in the main text. Green line models the apparent imprecision-back-action product using Eq. 5.0.3. Insets highlight the measurement region.

that ground state cooling ($\Gamma_{\mathrm{meas}} < \Gamma_{\mathrm{th}}/8$) should be accessible at 10 K.

The sensor's performance is limited by optical loss, photothermal and radiation pressure instabilities, and extraneous sources of measurement back-action. We investigate these constraints by recording the measurement imprecision, n_{imp}, and the total effective bath occupation, $n_{\mathrm{tot}} \equiv n_{\mathrm{th}} + n_{\mathrm{ba}}$, as a function of intracavity photon number, comparing their product to the uncertainty-limited value, $4\sqrt{n_{\mathrm{imp}} n_{\mathrm{tot}}} \geq 1$ (fig. 5.2). Two considerations are crucial: First, in order to efficiently collect photons from the cavity, it is necessary to increase the taper-cavity coupling rate to $\kappa_{\mathrm{ex}} \gtrsim \kappa_0$, thereby increasing the cavity decay rate to $\kappa = \kappa_0 + \kappa_{\mathrm{ex}}$. We operate at a near-critically coupled ($\kappa_{\mathrm{ex}} = \kappa_0$) value of $\kappa \approx 2\pi \cdot 0.91$ GHz, reducing the single photon cooperativity to $C_0 \approx 0.31$ in exchange for an output coupling efficiency of $\eta_c = (\kappa - \kappa_0)/\kappa \approx 0.52$. Second, in order to minimize S_x^{imp}, it is necessary to maximize n_{c} while avoiding dynamic instabilities. We accomplish this by damping the oscillator using radiation pressure feedback. Feedback is performed by modulating the intensity of the feedback laser with an electronically amplified and delayed copy of the homodyne photocurrent. A feedback phase of $-3\pi/2$ is chosen by tuning the total delay, $\tau \approx 172\,\mathrm{ns}$, such that the feedback-induced spring effect is minimized [44] (see appendices F.2.1 and F.3). The resulting viscous radiation pressure gives rise to a well-known cooling effect ('cold-damping' [158]), reducing the phonon occupancy of the mechanical mode to a mean value of $n_{\mathrm{m}} \approx n_{\mathrm{tot}}\Gamma_{\mathrm{m}}/(\Gamma_{\mathrm{m}} + \Gamma_{\mathrm{fb}})$, where Γ_{fb} is the optically-induced damping rate.

Measurements of the oscillator's thermal motion are shown in Fig. 5.1c. We determine $n_{\rm tot}$ and $n_{\rm imp}$ by fitting each noise peak to a Lorentzian with a linewidth of $\Gamma_{\rm eff} = \Gamma_{\rm m} + \Gamma_{\rm fb} + \Gamma_{\rm ba}$ (including a minor contribution from dynamic back-action, $\Gamma_{\rm ba}$; see appendices F.2.1 and F.3), a peak amplitude of $S_\omega(\Omega_m) \approx 2n_{\rm tot}(\Gamma_{\rm m}/\Gamma_{\rm eff})^2 S_\omega^{\rm zp}$, and an offset of $S_\omega^{\rm imp} = 2n_{\rm imp}S_\omega^{\rm zp}$. For low input power, $n_c \ll n_{\rm th}/C_0$, we observe that the effective bath occupation is dominated by thermalization to the cryostat, $n_{\rm tot} \approx n_{\rm th}$, and that imprecision scales as $n_{\rm imp} = (16\xi C_0 n_c)^{-1}$, where $\xi \approx 0.23$. ξ represents the ideality of the measurement, and includes both optical losses and reduction in the cavity transfer function due to mode splitting (see appendix F.3.5). Operating with higher input power — ultimately limited dynamic instability of higher-order beam modes — the lowest imprecision we observe is $n_{\rm imp} = 2.7(\pm 0.2)\cdot 10^{-5}$, corresponding to an imprecision 39.7 ± 0.3 dB below that at the SQL (see appendix F.4 for uncertainties). The associated measurement rate, $\Gamma_{\rm meas} = 2\pi\cdot(13\pm 1)$ kHz, is a factor of 9.2 lower than the rate of thermal decoherence to the ambient 4.4 K bath, $\Gamma_{\rm th} = 2\pi\cdot 120$ kHz. Significantly, this value is within 15% of the requirement for ground-state cooling.

For large measurement strengths, quantum back-action [30] should in principle exceed the ambient thermal force, scaling as $n_{\rm ba} = C_0 n_{\rm c}$ (see appendix F.2.2). As shown in Fig. 5.2 (red data), our system deviates from this ideal behavior due to extraneous back-action, manifesting as an apparent excess cooperativity, $C_0^{\rm ex} \approx 0.56$, and limiting the fractional contribution of quantum back-action to $C_0/(C_0 + C_0^{\rm ex}) \approx 35\%$. Similar behavior for high-order mechanical modes suggests that photo-absorption is the cause of this excess heating, as does our observation that $C_0^{\rm ex}$ is markedly higher at lower cryostat temperatures — consistent with the reduction of thermal conductivity in amorphous glasses below 10 K (see appendix F.3.1). Including extraneous back-action, we model the apparent imprecision-back-action product (green curve in Fig. 5.2) as

$$4\sqrt{n_{\rm imp}n_{\rm tot}} = \sqrt{\frac{1}{\xi}\left(1 + \frac{n_{\rm th}}{C_0 n_{\rm c}} + \frac{C_0^{\rm ex}}{C_0}\right)\left(1 + \frac{n_{\rm c}}{n_{\rm c}^{\rm ex}}\right)}, \tag{5.0.3}$$

where $n_{\rm c}^{\rm ex} \equiv (16\xi C_0 n_{\rm imp}^{\rm ex})^{-1}$ is the photon number at which $n_{\rm imp}^{\rm shot} = n_{\rm imp}^{\rm ex}$. Using $n_{\rm c} \approx 5\cdot 10^4 \ll n_{\rm c}^{\rm ex}$, we observe a minimum value of $4\sqrt{n_{\rm imp}n_{\rm tot}} \approx 5.0$, corresponding to a measurement efficiency of $\Gamma_{\rm meas}/\Gamma_{\rm tot} \approx 0.040$.

To illustrate the utility of this high efficiency, we increase the strength of the feedback used to cold-damp the oscillator in Fig 5.1c. The limits of cold-damping are well-studied [32, 165]. Ignoring back-action due to the weakly driven ($n_c < 100$) feedback optical mode, the phonon occupancy of the cooled mechanical mode depends on the balance between coupling to thermal, measurement, and feedback reservoirs at rates $\Gamma_{\rm th}$, $\Gamma_{\rm m} n_{\rm ba}$, and $g_{\rm fb}\Gamma_{\rm m} n_{\rm imp}$, respectively, where $g_{\rm fb} \equiv \Gamma_{\rm fb}/\Gamma_{\rm m}$ is the open loop feedback gain (see appendix F.1.2):

$$n_{\rm m} + \frac{1}{2} = \frac{1}{1+g_{\rm fb}}n_{\rm tot} + \frac{g_{\rm fb}^2}{1+g_{\rm fb}}n_{\rm imp} \geq 2\sqrt{n_{\rm imp}n_{\rm tot}}. \tag{5.0.4}$$

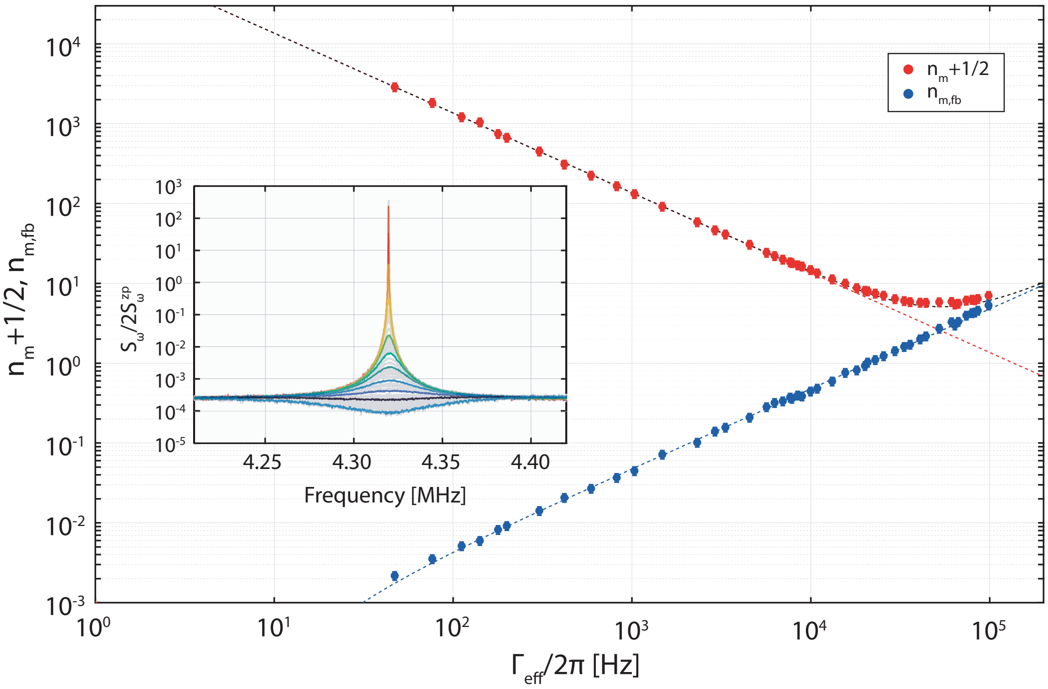

Figure 5.3 – **Radiation pressure feedback cooling to near the ground state:** Blue and red points correspond to measurements of the phonon occupancy of the mechanical mode, n_m (plus a phonon-equivalent zero-point energy of 1/2) and its component due to feedback of measurement noise $n_\mathrm{m,fb} = n_\mathrm{imp} g_\mathrm{fb}^2/(1+g_\mathrm{fb})$, respectively, as a function of effective damping rate, $\Gamma_\mathrm{eff} = (1+g_\mathrm{fb})\Gamma_\mathrm{m}$. Red, blue, and black dashed lines correspond to models of components in Eq. 5.0.4: $n_\mathrm{tot}/(1+g_\mathrm{fb})$, $n_\mathrm{m,fb}$, and $n_\mathrm{m}+1/2$, respectively, using experimental parameters $\Gamma_\mathrm{m} = 2\pi\cdot 5.7$ Hz, $n_\mathrm{tot} = 2.4\cdot 10^5$, and $n_\mathrm{imp} = 2.9\cdot 10^{-4}$, respectively. Inset: in-loop mechanical noise spectra for various feedback gain settings; fits to these spectra were used to infer blue and red points.

(here $\Gamma_{\mathrm{ba}} \ll \Gamma_{\mathrm{fb}}$ has been assumed). n_{m} is minimized for an optimal gain of $g_{\mathrm{fb}} = \sqrt{n_{\mathrm{tot}}/n_{\mathrm{imp}}}$, which corresponds to suppressing S_x to S_x^{imp} (yellow curve in Fig. 5.3, inset). Notably, for $C_0^{\mathrm{ex}} = 0$, $n_{\mathrm{m}} < 1$ requires $n_{\mathrm{imp}} < 1/2n_{\mathrm{th}}$. Results in Fig. 5.2 suggest that $n_{\mathrm{m}} \approx 2$ should be achievable.

Fig. 5.3 shows the result of feedback cooling using a measurement with an imprecision far below that at the SQL. We emphasize that for this demonstration, imprecision was deliberately limited to $n_{\mathrm{imp}} \approx 2.9 \cdot 10^{-4}$ in order to reduce uncertainties due to extraneous heating and due to the off-resonant tail of the thermal noise peak at 4.6 MHz (which limits applicability of Eq. 5.0.4 to effective damping rates of $\Gamma_{\mathrm{eff}} = (1 + g_{\mathrm{fb}})\Gamma_{\mathrm{m}} \lesssim 2\pi \cdot 200$ kHz). Feedback gain was controlled by changing the magnitude of the electronic gain, leaving all other parameters (e.g. laser power) fixed. We also note that the Markovianity condition $\tau \ll 2\pi/\Gamma_{\mathrm{th}}$ is satisfied by the feedback delay [165]. Fitting the closed loop noise spectrum (Fig. 5.3, inset) to a standard Lorentzian noise squashing model [177], we estimate the phonon occupancy of the mechanical mode from the formula $n_{\mathrm{m}} + 0.5 \approx \Gamma_{\mathrm{eff}} \cdot (S_\omega(\Omega_{\mathrm{m}}) + S_\omega^{\mathrm{imp}})/2S_\omega^{\mathrm{zp}}$, where S_ω^{imp} denotes the off-resonant background. Accounting for extraneous back-action, we infer a minimum occupation of $n_{\mathrm{m}} \approx 5.3 \pm 0.6$ (see appendix F.4 for uncertainties) at an optimal damping rate of $\Gamma_{\mathrm{eff}} \approx 2\pi \cdot 52$ kHz, corresponding to a ground state probability of $1/(1 + n_{\mathrm{m}}) \approx 16\%$. This value agrees well with the prediction based on Eq. 5.0.4 and Fig. 5.2. Notably, for larger feedback strengths, shot noise "squashing" [167] leads to an apparent reduction of S_x, while n_{m} physically increases. The discrepancy can be resolved with an out-of-loop measurement [165, 177], at the cost of reduced measurement efficiency.

Collectively, our results establish new benchmarks for linear measurement and control of a mechanical oscillator. Employing an optomechanical sensor with readout imprecision nearly 40 dB below that at the SQL, we have shown that traditional radiation pressure cold-damping [158] can be used to cool a nanomechanical oscillator to a mean phonon occupancy of ≈ 5.3; this represents a 40-fold improvement over previous reports [164, 177, 178], and invites comparison [179, 180] to the recent success of autonomous feedback (sideband) cooling [23–25]. Looking forward, high efficiency optomechanical sensors open the door to a variety of feedback applications such back-action evasion [173] and mechanical squeezing [33].

6 Outlook

The experimental achievements described in chapter 4 and chapter 5 can be largely attributed to the ability exploit the large zero-point motion and low dissipation rates afforded by Si_3N_4 nanobeams, while at the same time achieving a moderate frequency pulling factor, $G = \partial\omega_c/\partial x$. The latter is achieved by placing the nanobeam a distance from an optical resonator less than its evanescent decay length. The planar top surface of the microdisk allowed us to achieve an overlap with the optical field, in terms of the resonator path length, of ~10% (section 2.2.6). These effects combined, allowed us to achieve a single photon cooperativity, $C_0 = (G \cdot x_{zp})^2/(\kappa\Gamma)$, on the order of 1 at room temperature. The high linearity of the microdisk, able to support a cavity photon number on the order of 10^4, allows us to realize a back-action noise contribution at the level of ~10% of thermal noise at room temperature, while at cryogenic temperatures back-action noise dominates.

Looking towards the future, we would like to enter a new regime where back-action noise is dominant at room-temperature. With such a system the results described in [46], could be taken out of the cryostat and into the everyday world. Namely, it would be possible to realize mechanically-mediated (ponderomotive) squeezing of light as well as quantum enhanced force metrology. Such improvements could also lead to the ability to laser cool a mechanical mode to near its ground state occupancy by external feedback control (as described in chapter 5). Such a future seems compellingly close, but so far significant increases to cooperativity have remained elusive.

As discussed in chapter 2 the system architecture allows for a large range of variation in the placement of the nanobeam - both vertically and laterally. Moreover, the width and thickness of the beam are free parameters. However, in terms of cooperativity it seems that in practice a gain in one factor always comes with a corresponding loss in another. This is readily apparent in section 2.2.6(C). In this case we compare systems with microdisks that vary significantly in their thickness (430 vs 630 nm), with all other factors being equal. We see that for 800 nm wide beams g_0 differs by a factor of ~2.5, and if we were to assume κ is unaffected (as is the case for the bare microdisks) this would give an increase in C_0 of $2.5^2 \approx 6$. However, what we observe is a difference of ~1.5. Moreover, and counter intuitively, it is the sample with lower g_0

that exhibits the larger cooperativity. Here what is gained in g_0^2 is completely lost to increased optical dissipation. This is not an isolated example, but a consistent trend observed when reducing the gap between the beam and disk, when varying the beams thickness, or width, and when thinning the disk. The trend is always the same: it seems that the optomechanical world conspires to keep us fixed at $C_0 \sim 1$.

If we ask ourselves what is behind this phenomenon it seems there are two obvious potential mechanisms. One is that scattering losses from beam are the dominant optical loss mechanism in our system, and as the intensity of the field interacting with the beam increases so too does the scattering. This might seem like a reasonable claim but it doesn't seem to capture the scaling described above, which does not scale linearly with the intensity (with intensity being inferred from G). This leads to the more likely conclusion that we are observing a waveguiding behavior, with light being guided out from the microdisk via the nanobeam. Thus when the microdisk is thinned in the example above we not only increase the intensity of the field in the nanobeam, but potentially also more closely match the propagation constants.

It should be mentioned that waveguiding is not just a speculative claim. In experiment we can actually observe, through the microscope, light scattering at the point where the nanobeam meets the silicon support. The question is not whether it's happening, but whether it is the dominant loss mechanism in our system. The scaling behavior seems to suggest that it is. If we are to assume this is the reality that confronts us, we have two possible routes forward: try to improve the apparently free parameter of mechanical dissipation or face the waveguiding problem head on. Serendipitously, recent work involving localized modes of Si_3N_4 membranes has opened a compelling path forward in terms of the former route, with our recent work in this direction described in the following section. Still, it seems wise to also look towards alternative strategies, which are discussed in section 6.2. Following these considerations, a practical implementation of an optomechanical electrometer, using the device architecture developed in this thesis, is discussed and experimentally characterized.

6.1 Very low dissipation nanobeams

When considering the effect of dissipation dilution in section 2.1.1, it was recognized that if we assume a purely sinusoidal mode shape when solving for the Q enhancement factor then the predicted enhancement is orders of magnitude higher than what is observed in practice. This is a result of considerations at the clamped boundary, where the displacement profile takes on an additional curvature, in order to meet the flat clamped boundary condition. In fact this turns out to be the primary loss mechanism in such devices, and when taking this into account the Q enhancement is expressed as:

$$\frac{Q}{Q_0} \approx (\underbrace{2\lambda}_{\text{boundaries}} + \underbrace{\pi^2 n^2 \lambda^2}_{\text{antinodes}})^{-1}, \tag{6.1.1}$$

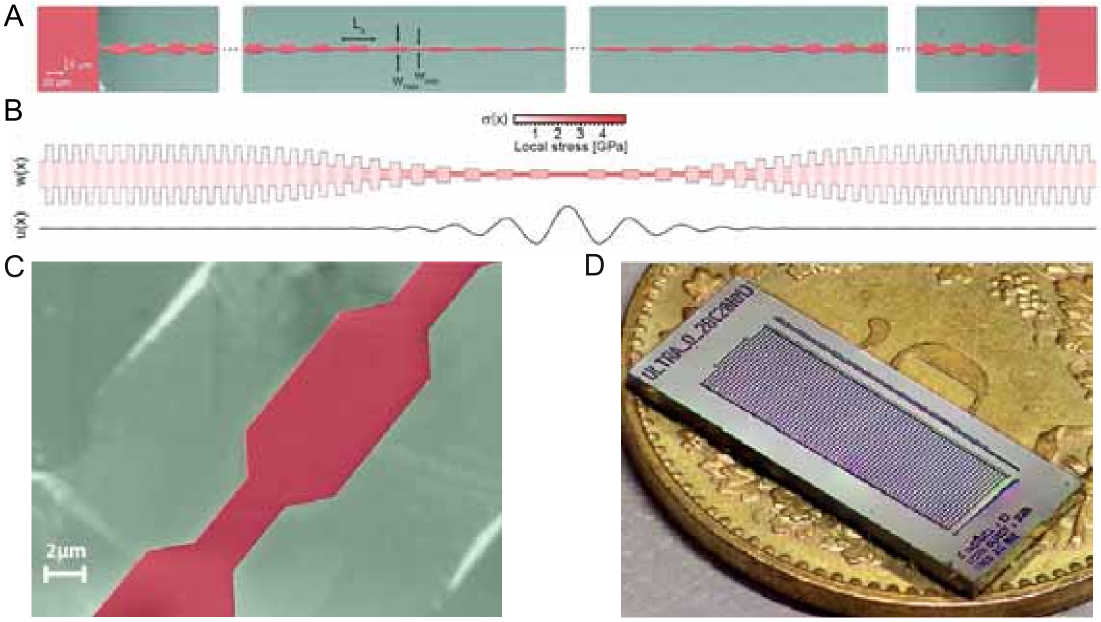

Figure 6.1 – **Soft-clamped nanobeam geometry:** shown with a segmented SEM image in (A), and illustrated for a 60 unit cell device, with color indicating the local stress value, in (B). In (B) the tapered beam envelope, that focuses stress toward the center of the structure, is readily apparent. The displacement profile of the localized mode of interest shown in black. (C) is an SEM zoomed in on a single unit cell of the sample in (A). In (D) a chip containing 76 beams can be seen (highlighting the macro nature of these devices).

with $\lambda = \frac{h}{L}\sqrt{E_0/12\sigma}$. This situation is highly suggestive that clever design might be able to reduce the contribution of boundary curvature to dissipation. In fact, a way to reduced it almost to zero was first demonstrated in high-stress Si_3N_4 membranes one year ago [181]. The concept involves embedding a membrane in a phononic crystal such that the envelope of the displacement profile, for an effectively high order mode, decays exponentially toward the clamped boundaries. The authors referred to this effect as *soft-clamping* as it relies on weak localization of the mode to avoid introducing additional curvature at the nodes.

6.1.1 Soft-clamped beams

The soft-clamping strategy developed in membrane resonators is equally applicable to beam resonators and thus we have worked to exploit this effect as a method to realize higher cooperativity in our optomechanical system. Figure 6.1(B) illustrates the geometry we have employed to realize soft-clamping in Si_3N_4 nanobeams (red), with the resulting displacement profile for the localized mode of interest shown in black, below. We note that the displacement profile is near zero at the boundaries. Above in fig. 6.1(A) is a segmented SEM (necessary due to the extremely large aspect ratio of the beam) of the fabricated structure. Figure 6.1(C) shows a zoom in on a unit cell of the beam, and Figure 6.1(D) shows the chip on which the beams are fabricated, highlighting that the beams are macro-scale in one dimension (the length). Fabricated beams have been realized with thicknesses of 20 nm and commensurate lengths as large as 7 mm (an astounding aspect ratio of almost half a million). In this work an additional

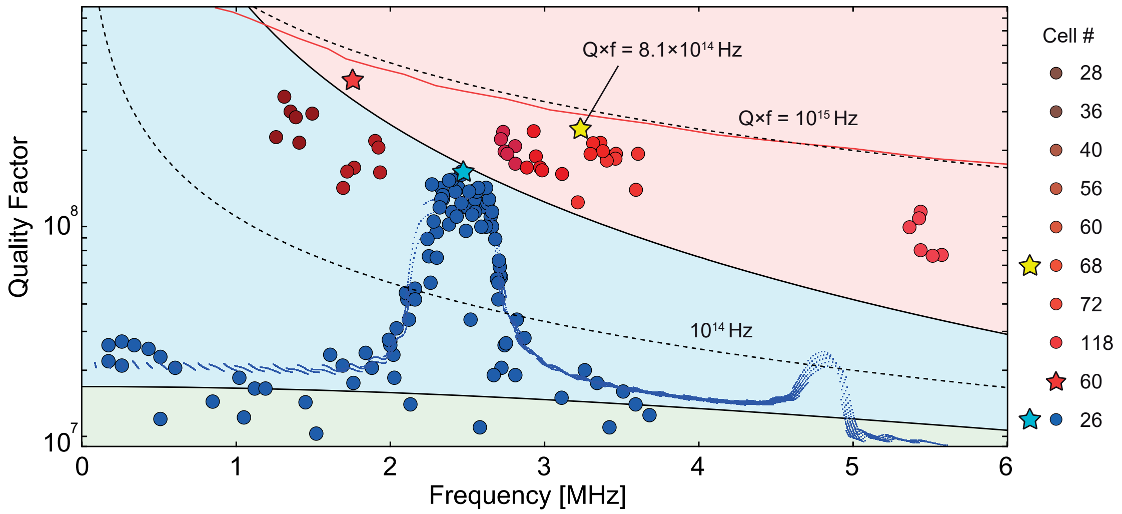

Figure 6.2 – **Measured quality factors for soft-clamped nanobeams:** recorded from thermal noise ringdown measurements using a lensed fiber interferometer in a high vacuum chamber. Blue circles indicate the modes of an non-tapered 2.6 mm long soft-clamped beam, with varying defect length and bandgap at ~2.5 MHz. Circles in varying shades of red correspond tapered 4 mm long soft-clamped beams with the number of unit cells varying from 28 (dark red) to 118 (light red). The yellow star indicates the highest Q×f product measured, for a beam with 68 unit cells and the red star indicates a 7mm long tapered beam with 60 unit cells. The red line and blue dashed line are numerical models. All measurements here are for 20 nm thick beams.

twist has been added to the concept developed by [181], which is to taper the envelope of the nanobeam in order to increase stress at its center, where the mode of interest is localized. Referring back to eq. (6.1.1), we recall that stress is in fact the origin of dissipation dilution and so this stress focusing leads to a further enhancement of the Q, which is fundamentally limited by the yield stress of the material - in this case ~6 GPa.

Figure 6.2 shows experimental thermal noise ringdown measurements of localized nanobeam modes, taken with a lensed fiber interferometer, in a high vacuum ($< 10^{-6}$ mbar) chamber. The data in blue circles captures the measurement of 40 different beams of varying defect length, and fixed unit cell length, for a non-tapered localized beam 2.6 mm in length. It can be observed for defect lengths outside the bandgap region the Q values correspond that of a normal (non-localized) rectangular beam. Q is enhanced within the bandgap region, saturating near the theoretical Q of a beam with a purely sinusoidal displacement profile (an "unclamped" beam, as in eq. (2.1.2)), represented by the solid black line. Red circles indicate localized modes of tapered beams 4 mm in length with a varying number of unit cells. These measurements illustrate the ability to achieve Qs higher than for an unclamped rectangular beam, by stress engineering. Here the maximum Q×f product achieved, of 8.1×10^{14} Hz, is two orders of magnitude higher than we have achieved for rectangular beams at similar frequencies (as shown in figure fig. 2.2).

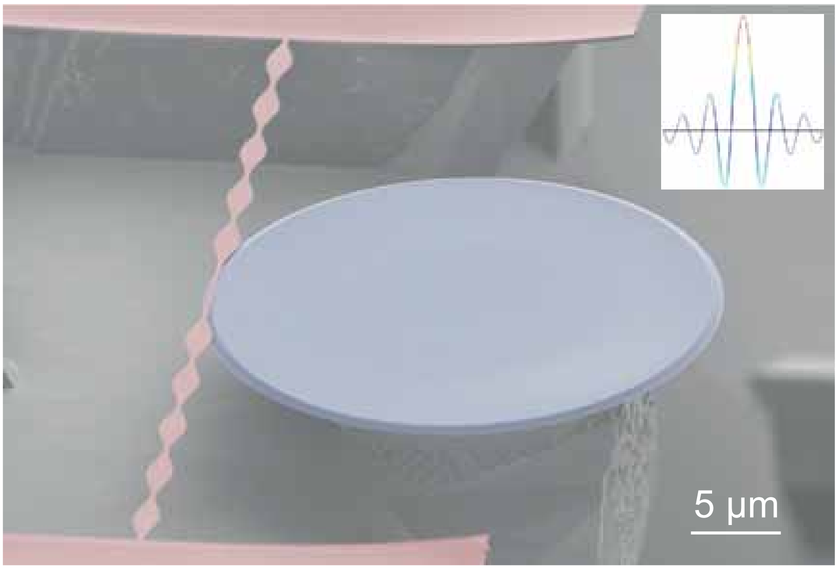

Figure 6.3 – **Integrated soft-clamped nanobeam:** with the SiO_2 microdisk false-colored blue and the Si_3N_4 colored red. Here a 39.1 MHz mode is localized in a 60 μm long beam.

6.1.2 Integration of localized beams

The results discussed in the previous section were achieved for isolated beams (not integrated with a microdisk), and naturally the goal is to make use of these astoundingly high mechanical Q values by integrated the beams into an optomechanical system. The extreme lengths of these beams (4 mm) makes this a significant challenge, as the correspondingly low fundamental mode frequencies and are thus highly susceptible to collapse onto the disk surface. Prior to the work in the previous section an attempt was made to integrate short soft-clamped beams into our optomechanical system, with the resulting structure is shown in fig. 6.3. Collapse of the beam was avoided by designing it to have our typical beam length of 60 μm (and 80 nm thick). The unit cell has a sinusoidal envelop, and in the device shown here utilizes 5 unit cells per side to localize the 11th out-of-plane harmonic. The fundamental mode frequency is 3.8 MHz, as is typical for this system, and the localized 11^{th} harmonic at 39.1 MHz. Calibrating from the optomechancial coupling rates to these two modes, the ratio of masses, $m_{\text{eff},11}/m_{\text{eff},1}$, is found to be 0.35. The Q×f products for these harmonics are 1.13×10^{12} and 5.13×10^{12}, respectively. This value matches, and does not exceed, the measured Q×f product for the 11^{th} harmonic of rectangular beams of this length (see fig. 2.2). Thus we do not we do not benefit from increased dissipation dilution, as the beams in the previous section do. This is a result of the weak effect of boundary induced losses for beams with this aspect ratio (L/h) and nodal spacing, as can be inferred from eq. (6.1.1). For very thin beams, on the order of 10 nm, this would likely show an appreciable effect. Regardless, such high frequency localized beams may be of interest when attempting to reach the sideband-resolved regime.

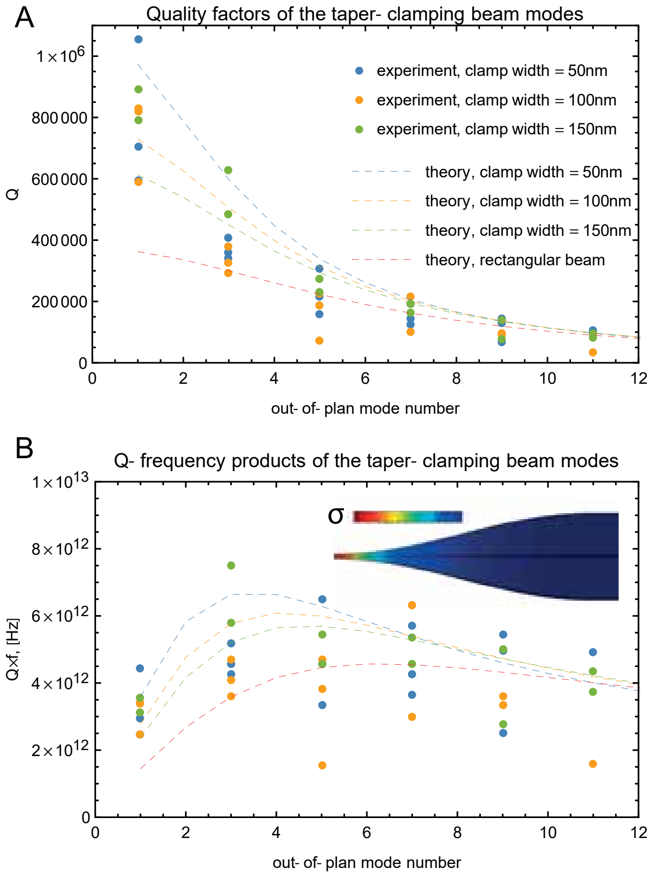

Figure 6.4 – **Tapered clamping point beams:** utilize local stress enhancement near the clamping points to reduce dissipation. (A) shows a comparison between Q values found by analytical calculation (dashed lines) and measurement for 60 μm long, 300 nm wide beams. In (B) the corresponding Q×f products are compared.

6.1.3 Tapered clamping point beams

We consider, once again, the primary source of dissipation in rectangular, stressed beams, which originates from additional curvature enforced by the flat clamped boundary conditions at the ends of the beam. This region of high curvature, which is captured in the first term of eq. (6.1.1), accounts for a tiny fraction of the total beam length. On the other hand, the stored energy of a rectangular beam is evenly distributed across its length and is proportional to its total volume. Considering this situation, one may recognize that if the beam is locally narrowed at its clamping points, such that its total volume is negligibly reduced, the local stress will be enhanced while the total stored energy is unaffected. An enhancement of the local stress in the region of high curvature leads to an alteration of the first λ term in eq. (6.1.1), now defined by $\lambda_{\mathrm{cl}} = \frac{h}{L}\sqrt{E_0/12\sigma_{\mathrm{cl}}}$, where the subscript indicates a local value in the clamping region. Given the situation that loss is dominated by λ_{cl}, tapering the beam locally near the clamped ends will reduce the dissipation proportional to the square root of stress enhancement $\sqrt{\sigma_{\mathrm{cl}}/\sigma}$. This trick has been employed to enhance the Q of 60 μm long, 300 nm wide beams by creating a ~1.5 μm long sinusoidal taper in the clamping region, as illustrated in fig. 6.4(B). Here the

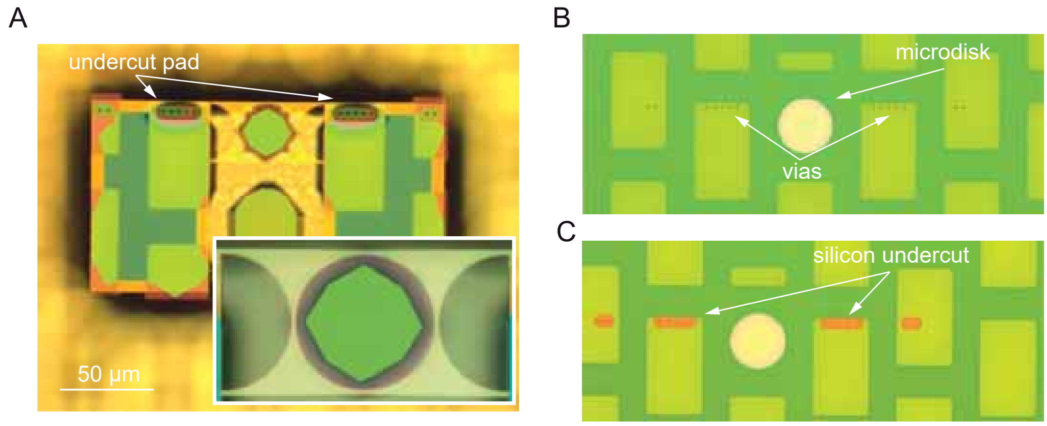

Figure 6.5 – **Ribbon type optomechanical device** (A) Shows a ribbon type "nanobeam" with a circle cut out at the center to allow the sacrificial layer to be etched, as well as to reduce mass. (B) and (C) shows the fabrication steps that allow the edge of the clamping pads to be undercut, as seen in (A). This process consists of etching vias through the SiO_2 pads and isotropically etching the silicon underneath using XeF_2 gas (see appendix B.2).

stress enhancement is roughly proportional to the ratio of the beam width to taper width, $\sigma_{\mathrm{cl}}/\sigma \propto w_{\mathrm{beam}}/w_{\mathrm{clamp}}$. The amount of tapering that can be practically achieved is limited by the yield stress of film, which in this case is ~6 GPa. Thus starting from a pre-stress of 900 MPa, the most aggressively tapered beam, with $w_{\mathrm{cl}} = 50$ nm, achieves a local stress of $\sigma_{\mathrm{cl}} \approx 5.4$ GPa, with a corresponding Q enhancement of ~2.4. While this is a modest improvement as compared to the results for localized modes, it may be of considerable interest when working with materials where the pre-stress is far below the yield stress.

6.2 Increasing optical mode overlap

The origin of high coupling efficiency in our optomechanical device, as compared to other near-field systems, is the relatively large spatial overlap we achieve as a result of placing the nanobeam overtop of the planar microdisk. As we explored in section 2.2.6, for our typical system with a 15 μm radius disk, the overlap is ~10 μm. This is approximately 10% of the disk circumference. If this could be made 100%, we would increase the frequency pull factor, G, by 10 and thus the factor in cooperativity by 100 (here neglecting the increased mass). This is an intriguing possibility, but one that hasn't been pursued in earnest at this point because it requires that the fiber couples to the bottom of the disk. In existing designs this access is blocked, as can been seen in fig. 3.17. The silicon beneath the clamping pads prevents this coupling situation.

In an effort to get around this problem, the process described in appendix B.2, is used to produce an overhanging region at the edge of the nanobeam clamping pads. This result can be in seen in fig. 6.5(A), where the overhanging region is indicated and includes small holes, which are used in the process to undercut the pads. These pads are aligned with the <111> silicon crystal plane, which is not attacked during the KOH etch used to undercut the

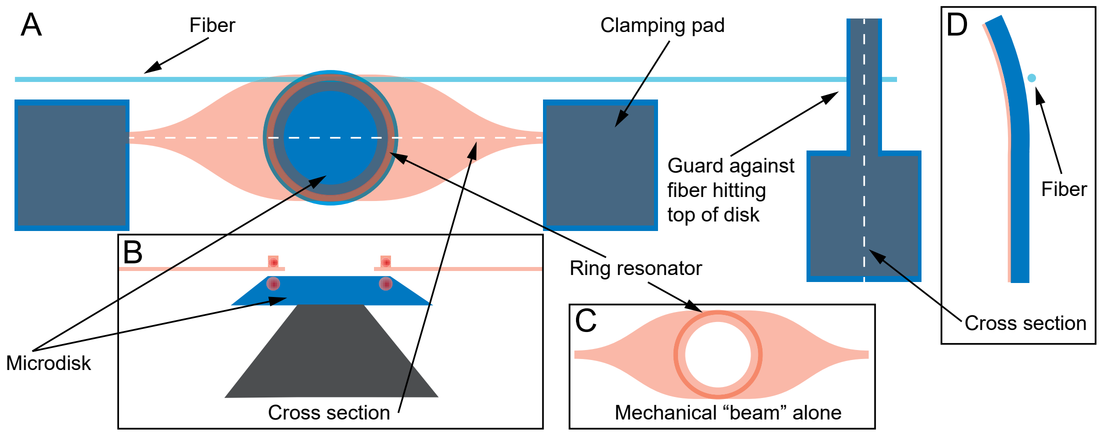

Figure 6.6 – **Waveguiding mechanical element** (A) Shows a top view of the system, consisting of a Si_3N_4 ribbon type resonator (C) with a ring resonator built on top - intended to hybridize with the microdisk mode. The ribbon is tapered towards the ends to allow the clamping pads to be recessed relative to the microdisk, thus allowing fiber access. A cross section of the ring resonator above the microdisk is illustrated in (B). In order to prevent the fiber from accidentally hitting the top of the structure an overhanging piece of SiO_2 extends past the microdisk edge (D). The cantilever is designed to curl upwards under the tensile stress of the Si_3N_4 on top, to avoid direct contact with the fiber. Note that the length of beam (C) is compressed for easy representation.

disk and remove the sacrificial material. In order to create an overhang, holes (vias) were etched through the SiO_2 pads (fig. 6.5(B)) and the silicon underneath the holes was etched isotropically using XeF_2 gas (fig. 6.5(C)). Following these steps the remainder of the process, starting with the Si_3N_4 etch was carried out as normally. This isotropic etch creates a region where the silicon can be attacked during the KOH etch, leading to the final result in fig. 6.5(A). The mechanical design, seen in the inset, was ribbon-like with a circle cut out at the center to allow the underlying sacrificial layer to be etched away (as well as to reduce the mass). While this process has worked in principle, it results in a very precarious situation when coupling with a fiber. Movement of the fiber is not well controlled and it inevitably hits the top surface of the disk. In the case of this kind of structure contact with the fiber will lead to collapse. So far we have not been able to detect a mechanical signal in these samples.

6.2.1 Ring resonator on mechanical beam

Here an alternative process to realize complete overlap with the optical mode is proposed, which combines a potential solution to the nanobeam waveguiding problem mentioned at the start of this chapter. The system, illustrated in fig. 6.6, is comprised of a wide beam (ribbon) that completely overlaps the microdisk but tapers at its end points such that the clamping structures can be offset relative to the disk. This configuration allows taper access to the bottom side of the disk. In order to avoid accidental contact by the taper to the top of the disk, SiO_2 cantilevers are positioned to extend past the edge of the disk (see fig. 6.6(D)). The tensile Si_3N_4 on the top surface causes the cantilevers to curl upwards, avoiding the complication of the fiber being in contact with them. The beam has a ring waveguide patterned on the top surface, to avoid output coupling of light. This design can be achieved quite easily using LPCVD deposition SiO_2 or Si_3N_4 with a few nanometer layer of Al_2O_3 to act as an etch stop. Numerical optimization of this structure would be very efficient using FEM, as axial symmetric boundary conditions can be used. Some care will need to be taken in considering the effect of the relative stress between the Si_3N_4 beam and ring resonator. Fortunately, LPCVD deposition allows for a large variation in the deposited stress (including stress-free SiO_2 for e.g.). This type of system may not only solve the output coupling problem but may lead to high interaction strengths making use of mode hybridization. Moreover, such a architecture may, counter intuitively, help in solving problems of stiction. This could be approached by making the center region of at the top of the microdisk intentionally rough in order to minimize the overlapping surface area. As a note the circular cutout in the center of the beam is not strictly needed and a solid beam may be advantageous in avoiding stiction. As a further note, the length of the beam as shown in fig. 6.6 is highly compressed for easy representation. Naturally with a relatively stiff waveguide on top of the beam, nodes should be relatively far from the center to avoid unnecessary mechanical losses.

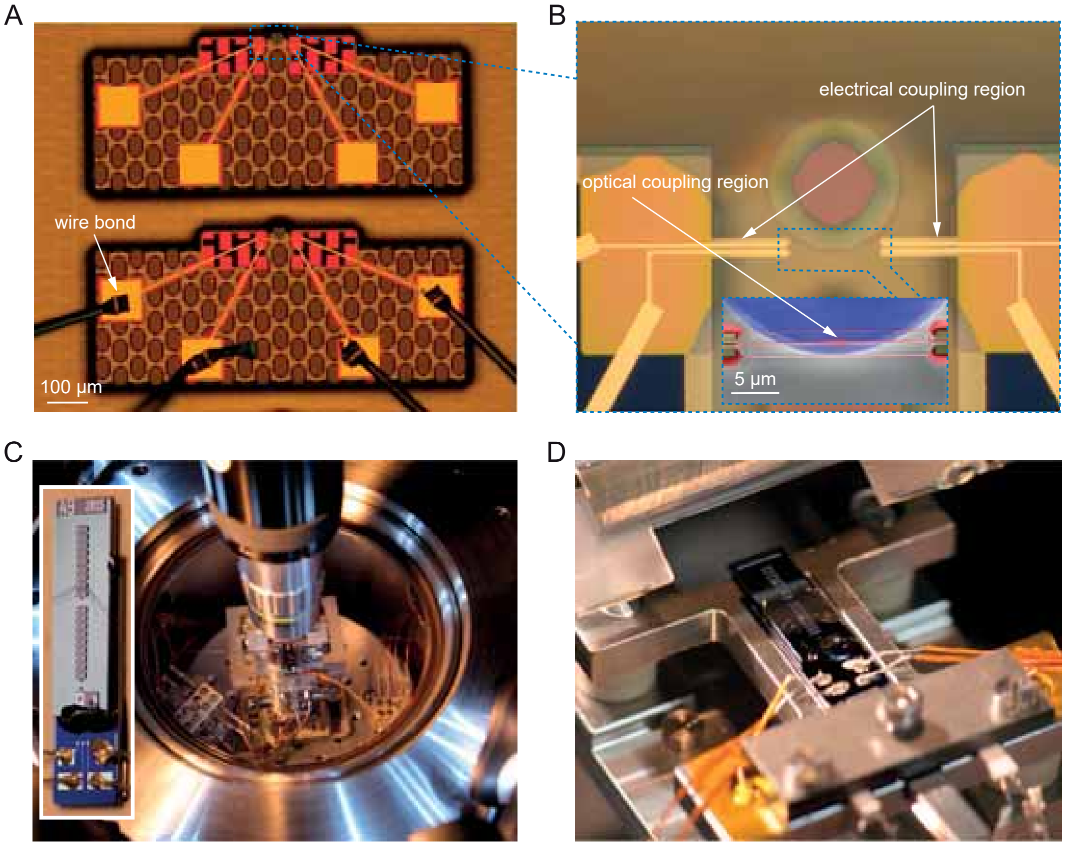

Figure 6.7 – **Electrometer: device and measurement setup** (A) Shows two adjacent devices with wires bonded to one. In (B) a close up of the coupling region is seen, including a false colored SEM showing the nanobeam locally widened where it couples to the microdisk. (C) The sample is mounted to a carrier chip to which wires are soldered, and embedded in a high vacuum chamber. Inset shows a close up of the device chip mounted to a carrier chip. (D) A close up of the chip on the vacuum stage, with a tapered fiber suspended above (mounted to a glass fork).

6.3 An optomechanical electrometer

Here we consider a novel extension to the near-field device architecture that has been developed and experimentally utilized in this thesis, for the purpose of sensing an external force. As detailed in chapters 2, 4 and 5, this system exhibits unusually low imprecision. In fact, it seems to be in a class of its own at room-temperature, achieving an imprecision more than three orders of magnitude below that at the SQL (chapter 2). The high Q/m ratio of silicon nitride nanobeams makes them well suited to external force sensing applications, as discussed in section 1.1.1. Furthermore, monolithic integration along with the use of sacrificial layers and e-beam lithography makes this process well suited to building in further complexity. These strengths combined suggest that this architecture may be well suited to developing a new class of practical sensors. A new incarnation of the device that allows for electro-optic coupling, by means of a circuit that electrically displaces the nanobeam, is described here.

In this context, we seek to couple weak oscillating charges to the nanobeam, which can be optically read out via the microdisk resonator. Electrical coupling to the nanobeam is accomplished by via the dielectrophoretic force, which is the phenomenon that causes a polarizable object to experience a force when subjected to a non-uniform electric field. The electric field polarizes the object and exerts a force on the poles, along the field gradient. To accomplish this, electrodes are placed on either side of the nanobeam and are vertically offset as shown in figure 2. This type of configuration was originally demonstrated in the absence of an optical cavity [72]. Applying a DC electric field induces a dipole in the nanobeam, and when an oscillating electric field is also applied across the electrodes the nanobeam experiences a corresponding oscillating force.

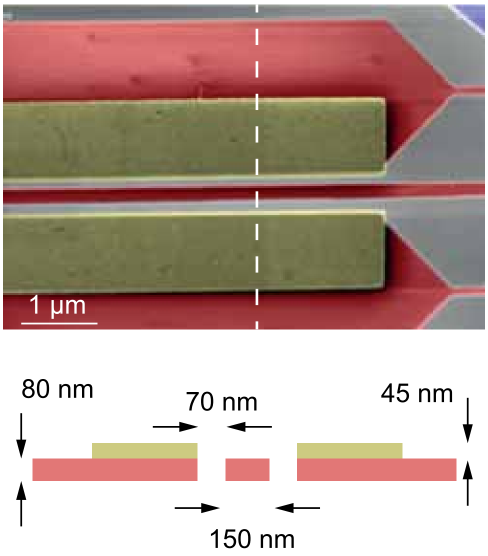

Figure 6.8 – **Electrometer: electrode configuration** A false color SEM shows a close up of one of the electrode pairs, with Si_3N_4 in red and platinum in yellow. The cross section is illustrated below, following the dashed line in the SEM

The process used to construct the optomechanical device (chapter 3) has been adapted to place electrodes on either side of the nanobeam as described above. The resulting system is shown in fig. 6.7. A lift-off metalization process using platinum forms the electrodes. Platinum is chosen due to its highly unreactive nature, making it compatible with acids, bases, and oxygen plasma used during process steps following lift-off. The mechanical nanobeam that sits between the electrodes is designed to be narrow in the region of the electrodes and is widened in the region that overlaps with the evanescent field of the microdisk. Since the dielectrophoretic force is proportional to the electric field in magnitude, it is advantageous to make the beam narrow where it is coupled to the electrodes (see fig. 6.8) in order to allow for reduction of the gap between electrodes. Conversely, widening the beam in the region of the microdisk serves to enhance the coupling to the whispering gallery mode (this design is similar to that shown in appendix E.2.1). The electrodes are separated into two sections such that they do not interfere with the optical field (which would naturally lead to high losses). The electrodes themselves sit on suspended silicon nitride beams that are designed to be very narrow at the center (~50 nm), where they overlap with the microdisk, to avoid introducing extraneous mechanical noise to the optical readout.

Applying a DC electric field results in a vertical displacement of the nanobeam, which in turn leads to a shift in the optical mode frequency. This effect is demonstrated in fig. 6.9, and can be used to construct an optical switch or a high-speed tunable optical filter. Note that although the applied voltage is rather high, at 15 V, the energy required to induce this shift is just $U \sim 0.5(0.8\text{fF})(15\text{V})^2 = 90\text{fJ}$ (here the FEM simulated capacitance value of 0.8 fF is used). Note that the very small capacitance value implies that such an optical switch could be operated at very high frequencies, given by the cutoff frequency $f_\text{c} = 1/(2\pi RC) \sim\ 200\text{THz} \cdot \text{Ohms}/R$

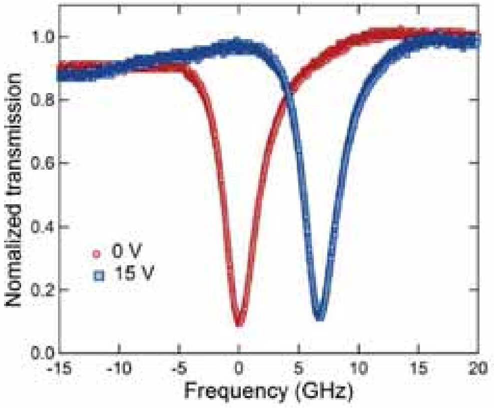

Figure 6.9 – **Electrometer: use as a tunable optical cavity** Demonstration of the potential to use this device as a high-speed tunable optical filter or switch. The voltage value indicates a DC voltage applied to the electrodes

While a DC field causes a dielectrophoretic force that displaces the beam, the derivative of this force results in an electrically induced spring constant, which leads to a shift in the nanobeams eigenmode frequencies. In the case of the geometry shown here the result is spring stiffening for the out-of-plane mode and spring softening for the in-plane mode. Since the fundamental in-plane mode is initially at higher frequency the result of applying a DC field is to tune the modes toward an avoid crossing. This effect can be seen in fig. 6.10(A). At the avoided crossing the initially orthogonal modes become hybridized and their optomechanical coupling rates become equal (fig. 6.10(B)).

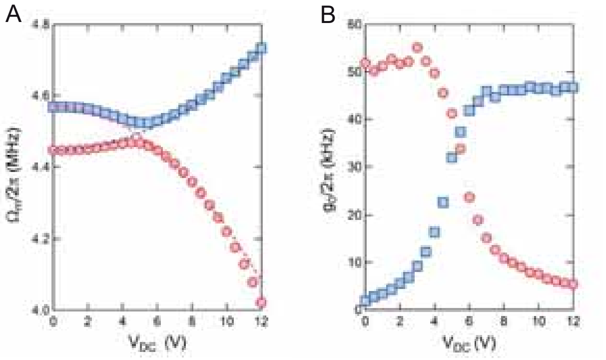

Figure 6.10 – **Electronically mediated intermodal coupling** In (A) the fundamental in-plane and out-of-plane nanobeam modes are tuned through the avoided crossing and (B) hybridization is observed via their modified coupling rates

Beyond static tuning of the intermodal mechanical and optomechanical coupling rates, it follows that dynamic fields applied across the electrodes may be used to imprint a signal onto the nanobeam's motion - on or off resonance. In this scenario the nanobeam mediates electro-optic transduction. This presents a compelling practical application to read out very small electrical signals, as the optomechanical system in question has extraordinary sensitivity to mechanical motion. In fact the ability to resolve broadband thermomechanical noise from a 4.3 MHz, 10 pg nanobeam with a Q over 300 000 has been demonstrated at room-temperature (see section 2.2.2). Assuming the ability to resolve off-resonant thermomechanical noise we estimate the minimum resolvable spectral density for a fluctuating charge applied to the device's electrodes at various RF frequencies, as shown in fig. 6.11. Here the resolvable charge fluctuation is dependent on the applied DC field, which defines the strength of the induced dipole. Impressively, the extrapolated resolution of $3.2 \times 10^{-4}\mathrm{e}/\sqrt{\mathrm{Hz}}$ is less than an order of magnitude away from the state-of-the-art of $5.3 \times 10^{-5}\mathrm{e}/\sqrt{\mathrm{Hz}}$ achieved using cryogenic RF-single electron transistors [182]. Importantly, in our case this sensitivity can be achieved at room temperature.

In this initial work, we have demonstrated the ability to dynamically tune the mechanical intermodal coupling, as well the mode frequencies electronically, as demonstrated in fig. 6.10(A). Moreover, the optomechanical coupling can be dynamically adjusted electronically (fig. 6.10(B)). However, what is truly compelling about this system is the ability to leverage exquisite displacement sensitivity in order to read out tiny RF charge fluctuations at room temperature (fig. 6.11). The device in its current form already approaches state-of-the-art sensitivities, which can in principle be improved by orders of magnitude with a parallel plate coupling scheme. This would involve placing one electrode on the central beam and another electrode over top, bridging the two side beams. This direction presents a pathway towards achieving an electrometer that has unprecedented sensitivity and can be operated across a very broad temperature range.

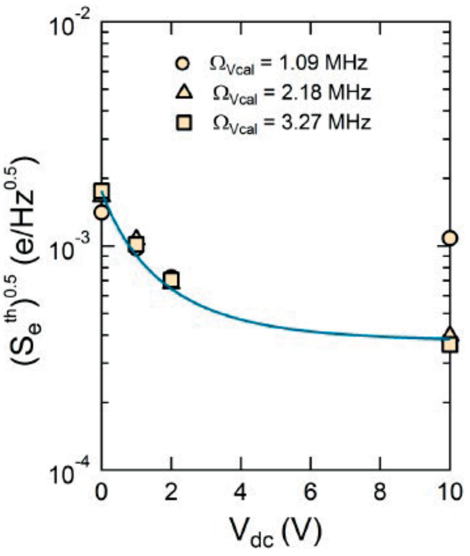

Figure 6.11 – **Electrometer: sensitivity to RF charge fluctuations** over a range of RF frequencies, as a function of DC bias voltage

It should also be mentioned that this configuration allows for a very simple implementation of measurement based feedback, analogous to that carried out in chapter 5. However, in this case the photodetector signal is used to actuate the beam via the electrodes. This is interesting as it avoids the need for light modulators and is thus more amenable to on-chip implementation. Moreover, the feedback phase can be easily flipped simply by changing the sign of the DC bias. This type of feedback was briefly carried out and seen to work as expected, although no comprehensive efforts were made to explore its limits.

6.4 Final words

The results presented in the previous sections suggest that there is good reason to be hopeful about the future of the device architecture explored in this thesis. The ability to reduce mechanical dissipation by orders of magnitude is a demonstrable reality. The open question for future exploration is how to leverage this insight when faced with the problem of stiction. When considering the 4 mm long beams discussed in this chapter and the ~30 nm gaps utilized in current versions of our system it is clearly a formidable challenge. However, as discussed in section 6.2.1 there are other possible routes towards realizing back-action dominated systems at room-temperature. Moreover, these routes are likely complimentary. Coupling more efficiently to the cavity may allow one to increase the coupling gap, in turn making it possible to utilize larger and more compliant mechanical devices. Realizing an optomechanical system dominated by quantum noise at room-temperature is a noble goal, and it will certainly open a new vista on experimental possibilities. Moreover, there seems to be great promise in utilizing these devices as practical sensors. For those willing to take up and solve the inevitable challenges ahead, there is much to be excited about.

A Sample designs

This appendix describes the typical sample chip layout for the devices described in chapter 2 (with the fabrication process described in chapter 3), the specific details of samples used for major manuscripts, and a set of data characterizing how relevant optomechanical parameters depend on varying beam width, beam position, and optical mode. Figure A.1 shows a CAD rendering of a typical chip layout, with numbering and 'Wild card samples' labels added. An inset photo taken with a macro lens shows three adjacent samples, with 500 μm spacing between them. As can be seen in the image, the samples are elevated with respect to the chip substrate in order to allow coupling with a tapered fiber.

A typical sample chip has dimensions of approximately 5 by 13 mm with 21 total samples, as shown in fig. A.1. The bottom of the chip contains a unique chip indicator (in this case 'A') and the top of the chip indicates the wafer from which the chip originates. The first two samples, labeled as 'Wild card samples', were generally used to test new designs that were likely to have problems (e.g. the design shown in fig. 6.5). Samples 1 to 9 were used to perform a parametric sweep of some type, which was usually the lateral position of the nanobeam with respect to the disk. Sample 10 was always dedicated to a bare disk, with no mechanics, such that a reference optical Q measurement could be made. Samples 11-19 were then used to perform a second parametric sweep. Typically such a chip would contain two beam designs: one used for samples 1 to 9 and another used for samples 11-19.

A.1 Sample chips used for major publications

This section provides details for the sample chips used in the major publications that resulted from this thesis work. The samples used for characterization in chapter 2 and published in [153] are not explicitly mentioned here, as a large number were used and later re-purposed for thermal annealing tests.

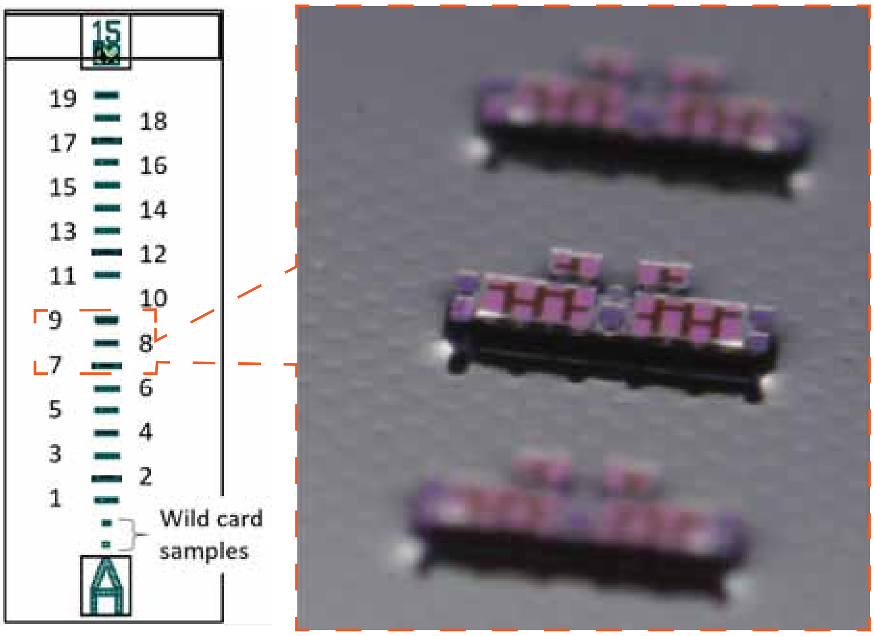

Figure A.1 – **Typical monolithic sample chip layout** with a CAD rendering of the chip shown on the left and a close up photograph of the samples on the right. The numbering and label "Wild card samples" have been added to the CAD rendering for illustrative purposes.

A.1.1 Measurement-based control of a mechanical oscillator at its thermal decoherence rate

This sample was one of the first working samples produced, and was used for the experimental work described in chapter 5. This work was published in Nature in August 2015 under the title *Measurement-based control of a mechanical oscillator at its thermal decoherence rate*. The sample originates from wafer *13.09.17* (early wafers used date labels) and chip *01 10* (early chips used binary labels). The chip CAD rendering is shown in fig. A.2(A), with the sample used circled in blue. The microdisk was produced by photolithography, has a 30^o wedge angle, is 600 nm thick and has a radius of 14.9 μm. The sample exhibits an intrinsic linewidth of $\kappa_0 \approx 2\pi \cdot 0.44$ GHz. The nanobeam is 70 nm thick, 400 nm wide, and 65 μm long. Its fundamental out-of-plane resonance is at 4.3 MHz, with a mechanical damping rate of $\Gamma_\mathrm{m} \approx 2\pi \cdot 5.7$ Hz at 4K (mechanical Q is very poor at room-temperature for this sample). It is suspended approximately 50 nm above the microdisk, with a frequency pulling factor of $G \approx 2\pi \cdot 0.70$ GHz/nm and optomechanical coupling rate of $g_0 \approx 2\pi \cdot 20$ KHz.

A.1.2 Appearance and disappearance of quantum correlations in measurement-based feedback control of a mechanical oscillator

The experiments involving this sample were published in PRX in January of 2017, with the title *Appearance and disappearance of quantum correlations in measurement-based feedback control of a mechanical oscillator*. The wafer used to produce these samples is *A1* and the

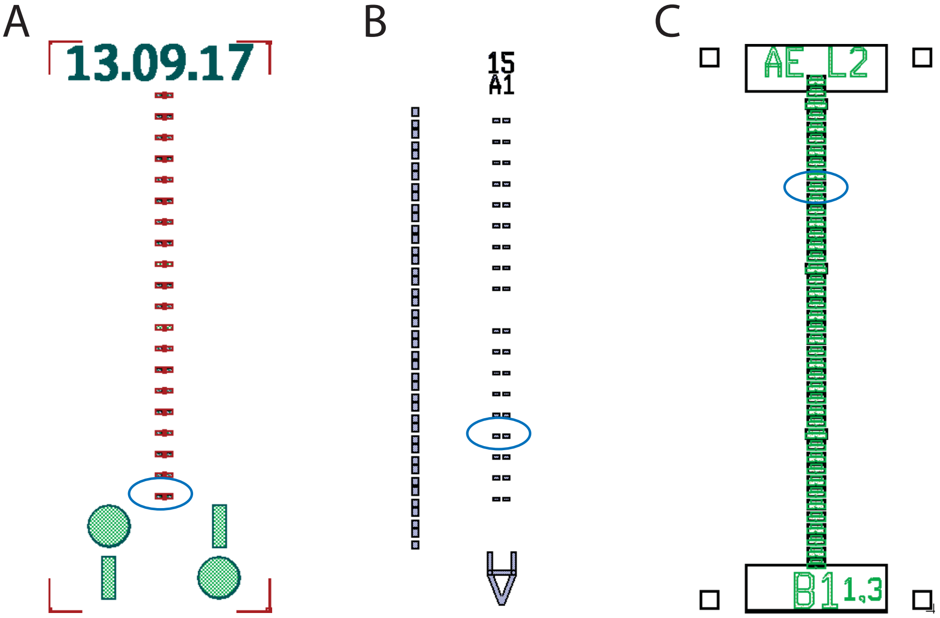

Figure A.2 – **Chips used in major manuscripts** with the specific samples used circled in blue. (A) is the chip used for the experiments in chapter 5, published in Nature as *Measurement-based control of a mechanical oscillator at its thermal decoherence rate.* (B) was used for the experiments published in PRX as *Appearance and disappearance of quantum correlations in measurement-based feedback control of a mechanical oscillator.* (C) was used for the experiments published in PRX with the title *Quantum correlations of light from a room-temperature mechanical oscillator*, also detailed in chapter 4.

chip used for experiments is *A down* (here 'down' indicates that the letter is rotated to be upside down). The chip and sample of interest are shown in fig. A.2(B). The microdisk was produced by photolithography, has a 30^o wedge angle, is 620 nm thick and 13.6 μm in radius. The intrinsic optical linewidth is $\kappa_0 \approx 2\pi \cdot 0.25$ GHz. The nanobeam is 80 nm thick, 400 nm wide, and 60 μm long. Its fundamental out-of-plane resonance is at 4.3 MHz, with a mechanical damping rate of $\Gamma_\mathrm{m} \approx 2\pi \cdot 7$ Hz at 4K (approximately 15 Hz at room-temperature). The separation gap between the nanobeam and microdisk is ~ 55 nm and the optomechanical coupling rate is $g_0 \approx 2\pi \cdot 23$ KHz.

A.1.3 Quantum correlations of light from a room-temperature mechanical oscillator

This sample was used for observation of quantum back-action-induced correlations of light at room-temperature, as described in chapter 4. The work was published in PRX in September of 2017 with the title *Quantum correlations of light from a room-temperature mechanical oscillator.* The chip of interest, with label *B1 1,3* ('B1' indicates the design and '1,3' the location on the wafer) was produced from wafer *AE L2.* These samples, as opposed to the others above, were produced with e-beam microdisks and spacing between samples of 250 μm rather than 500 μm. This higher sample density is clearly visible in the CAD rendering of the chip (fig. A.2(C)). This type of chip has a total of 41 samples, with the specific sample of interest

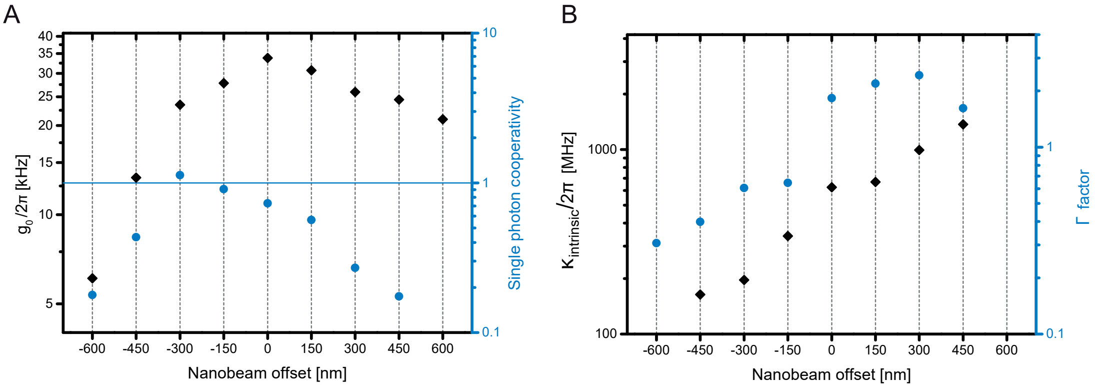

Figure A.3 – **400 nm wide beam: fundamental TM optomechanical coupling and optical dissipation** for varying lateral positions of the nanobeam. In (A) the single photon optomechanical coupling and cooperativity for the first out of plane mechanical mode is shown with respect to lateral positioning around the point of maximum coupling. (B) shows the exponential rise in optical dissipation as the beam is moved towards the center of the microdisk.

in this case being number 34. The e-beam microdisk has a 10^o wedge angle, is 350 nm thick and has a radius of 20 μm. The microdisk has an intrinsic optical linewidth of $\kappa_0 \approx 2\pi \cdot 2.2$ GHz. This surprisingly large linewidth is speculated to arise from increased waveguiding in the nanobeam as a result of the lower optical mode effective index and better matching to the optical modes of the nanobeam. The nanobeam is 80 nm thick, 200 nm wide with a 400 nm wide center defect (see fig. E.1), and 70 μm long. The fundamental out-of-plane mode sits at 3.4 MHz and has a damping rate of $\Gamma_m \approx 2\pi \cdot 7$ Hz at room-temperature. The separation gap between the nanobeam and microdisk is ~ 55 nm, with an optomechanical coupling rate of $g_0 \approx 2\pi \cdot 60$ KHz.

A.2 Dependence of optomechanical parameters on beam width, beam position and optical mode selection

This section provides a more extensive set of characterization data to supplement the data in chapter 2. All samples in this section were produced from a single wafer and so they share many parameters. All samples have SiO_2 microdisks that are 630 ±10 nm thick, 30 ±0.2 μm in diameter and have a 30^o sidewall angle. The microdisks are produced by photolithography, as described in chapter 3. The LPCVD Si_3N_4 used to form the nanobeams is 60 ±2 nm thick, with a pre-stress of ~1 GPa. All nanobeams are 60 ±0.01 μm long and have vertical gap from the microdisk of 25 ±5 nm.

The data in fig. A.3 shows the optomechanical coupling rate, cooperativity, optical loss rate and Γ factor (optical loss rate over mode splitting) for varying lateral positions of the nanobeam. Here data is only shown for the fundamental TM mode. All samples have beams that are 400 nm wide. The 0 offset position in fig. A.3 indicates the position where simulation predicts the highest coupling rate. This corresponds to the nanobeam center being positioned above the upper edge of the microdisk sidewall. This results in an overlap with the optical mode,

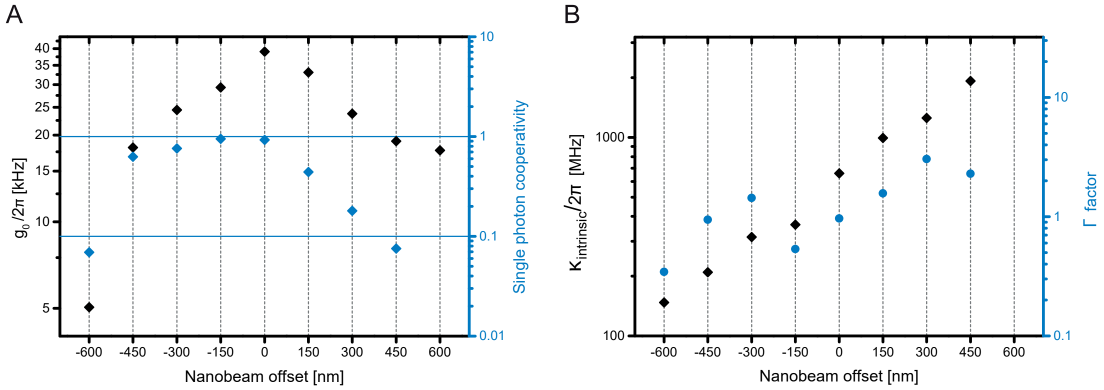

Figure A.4 – **400 nm wide beam: fundamental TE optomechanical coupling and optical dissipation** for varying lateral positions of the nanobeam. In (A) the single photon optomechanical coupling and cooperativity for the first out of plane mechanical mode is shown with respect to lateral positioning around the point of maximum coupling. (B) shows the exponential rise in optical dissipation as the beam is moved towards the center of the microdisk.

of about 10 μm (see section 2.2.6), which drops rapidly as the beam is moved further from the center of the disk (negative offset values). As discussed in the thesis body, when the beam is moved towards the center of the microdisk from the outmost positon (-600 nm), g_0 rises rapidly but so too does the optical loss rate. The combination of these two effects results in an optimal cooperativity that occurs for g_0 that is below the maximum value (here for offset of -300 nm).

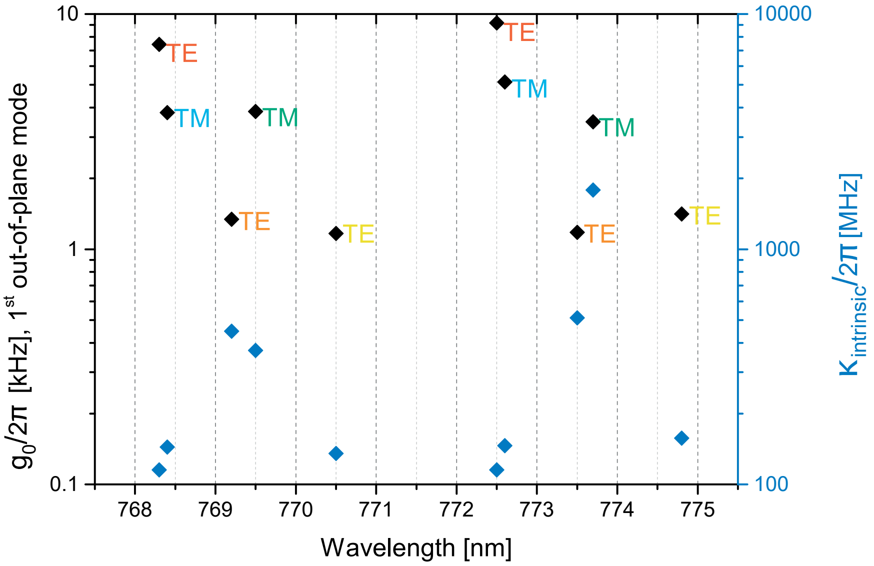

Figure A.5 – **200 nm wide beam: optomechanical coupling for higher order optical modes** The optomechanical coupling rates for higher order TM and TE polarization modes are shown over one free spectral range. Color coding is used to identify different mode families.

The same general behavior is seem for the fundamental TE mode in fig. A.4. However, in this case cooperativity remains nearly constant for offsets between -450 nm and 0 nm, with the change in g_0^2 being compensated by a commensurate change in $\kappa_{\text{intrinsic}}$. Interestingly, for both polarization modes a maximum cooperativity of unity is reached. Even more curious, simulation predicts that g_0 for the TE mode should be a factor of two smaller than what was measured in experiment. The simulation predictions were accurate for samples with larger coupling gaps, but for the small gaps (~25 nm) of these samples the perturbative simulation approach described in chapter 2 may not be sufficient. For example, if the electric field in the air gap between the nanobeam and microdisk is enhanced this would not be captured by the model. This could be explored with a 3D finite-difference time-domain model.

Figure A.5 shows the measured the coupling rates to higher order TE and TM polarization modes, for a 200 nm wide nanobeam offset by -450 nm from the ideal coupling point. The result in fig. A.5, shows coupling to the fundamental out-of-plane mechanical over one free spectral range for the observed optical mode families, for both TM and TE polarizations. Note that the mode indices are not known experimentally, and color coding in the plot is used to differentiate different mode families, which are separated by ~4.5 nm.

In experiment the ratio of optomechanical coupling between the in plane and out of plane modes often becomes important. For example, in the case of feedback cooling contamination of the noise floor by the in plane mode can limit the degree to which the out of plane mode can be cooled. Ideally, in this scenario the in plane mode would have far lower coupling strength than the out of plane mode. In this context fig. A.6 shows this coupling ratio for and illustrates the intuitive result that when coupling is maximized for the out of plane mode coupling to the in plane mode is minimized. The sharp feature in the scatter plot of $g_{0,\text{OP}}/\ g_{0,\text{IP}}$ near the zero offset (for both TM (A) and TE (B) modes) suggests that finely stepping the beam offset near zero would allow one to produce a sample with almost no in plane coupling.

The data presented in fig. A.3 and fig. A.4 was also taken for samples with beam widths of 200,

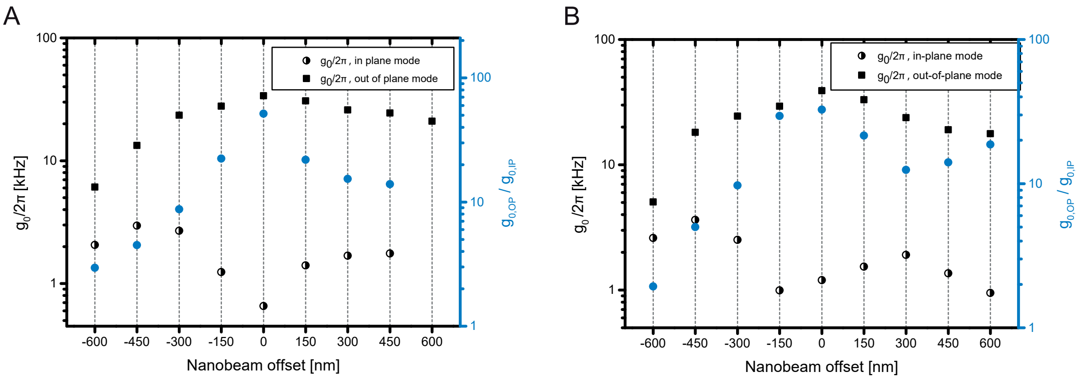

Figure A.6 – **400 nm wide beam: optomechanical coupling to in plane and out of plane mechanical modes** The ratio of optomechanical coupling rates is shown for excitation of the fundamental TM (A) and TE (B) polarization modes.

600, and 800 nm. The equivalent data for these samples is given in fig. A.7, fig. A.8 and fig. A.9, respectively.

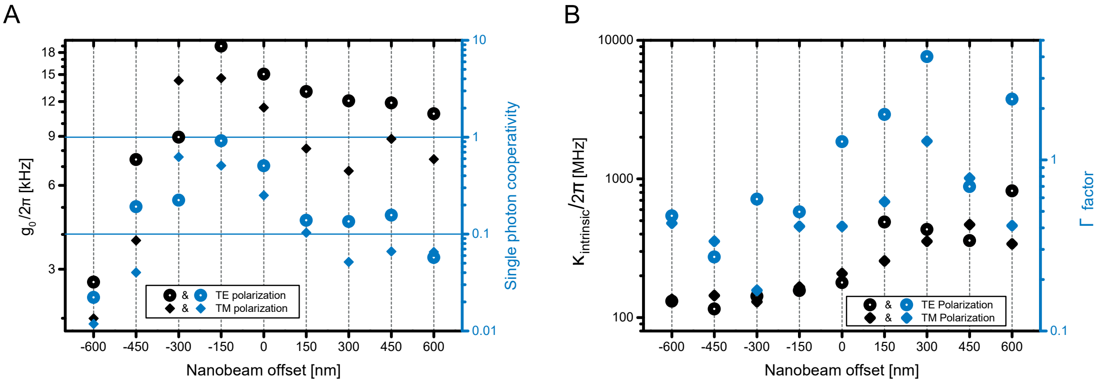

Figure A.7 – **200 nm wide beam: fundamental TM and TE optomechanical coupling and optical dissipation** for varying lateral positions of the nanobeam. In (A) the single photon optomechanical coupling and cooperativity for the first out of plane mechanical mode is shown with respect to lateral positioning around the point of maximum coupling. (B) shows the dependence of optical dissipation with the lateral position of the beam

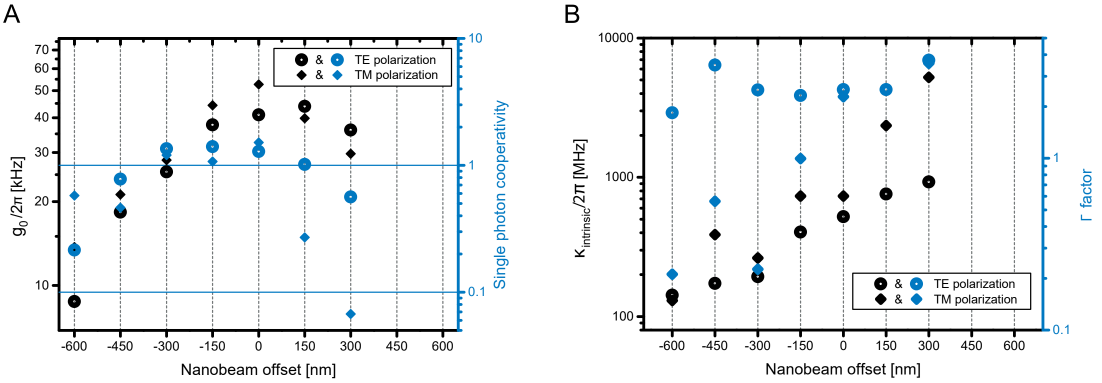

Figure A.8 – **600 nm wide beam: fundamental TM and TE optomechanical coupling and optical dissipation** for varying lateral positions of the nanobeam. In (A) the single photon optomechanical coupling and cooperativity for the first out of plane mechanical mode is shown with respect to lateral positioning around the point of maximum coupling. (B) shows the dependence of optical dissipation with the lateral position of the beam

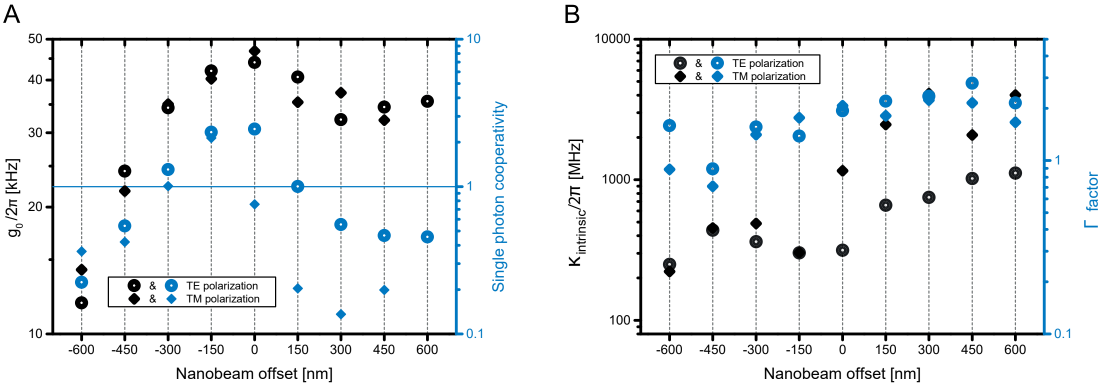

Figure A.9 – **800 nm wide beam: fundamental TM and TE optomechanical coupling and optical dissipation** for varying lateral positions of the nanobeam. In (A) the single photon optomechanical coupling and cooperativity for the first out of plane mechanical mode is shown with respect to lateral positioning around the point of maximum coupling. (B) shows the dependence of optical dissipation with the lateral position of the beam

B Monolithic device fabrication addendum

The following section details the calibration process used to determine the microdisk radius and nanobeam clamping pad separation, which is crucial for the e-beam writing step (and correct placement of the nanobeams). Next a process developed in an effort to mitigate heating effects, by avoiding optical absorption at the nanobeam clamping points, is described. The remaining sections deal with various caveats that have been encountered during the fabrication process. The earliest one was a fundamental problem with the initial design, which assumed the nanobeams could be clamped on polysilicon. It turned out that polysilicon was significantly undercut during the release stage of the process, which severely impacted their performance. For this reason, the method described in section 3.3.1 was developed. Appendix B.4 describes the problem that arises during KOH etching if the clamping pads are made too small or the etch is carried out for too long of a period (namely undercutting of the nanobeam supports). Appendix B.5 details early problems encountered when attempting to carry out the microdisk thinning step described in section 3.3.1. Finally, efforts made to anneal the Si_3N_4 film, in order to realize lower absorption and potentially high Q, are described in appendix B.6.

B.1 Calibration of e-beam alignment to microdisk and clamping pads

Figure B.1(A) showing a calibration mask pattern written in HSQ prior to the mask used for pattering Si_3N_4, described in section 3.3.5. During etching of the SiO_2 layer that defines the microdisk as well as the clamping pads for the nanobeam, it is necessary to over-etch significantly in order to achieve a linear wedged sidewall (as described in section 3.3.1), which is fundamental to achieving high Q performance. Typically the etch time was set to 25 minutes, leading to a 3.5 μm biasing of the pattern. However, the precise bias varied between 3.3-3.7 μm which likely depended on the chemical conditions of BHF bath (which is a communal bath) as well as the adhesion conditions of the photoresist, which can vary based on temperature fluctuations and wafer surface conditions. The end result is that the exact dimensions of the

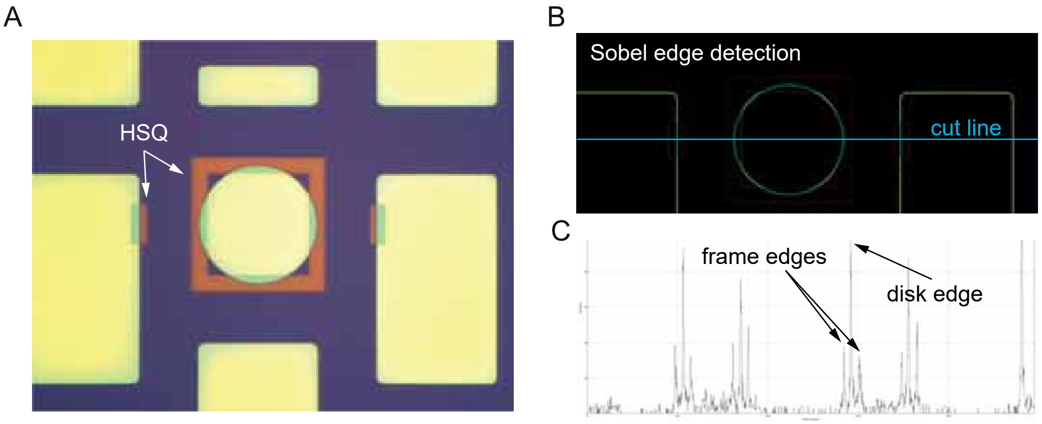

Figure B.1 – **E-beam alignment calibration process for monolithic system:** (A) Optical microscope image of alignment and size calibration pattern (brown/green) written in HSQ over top of microdisk and nanobeam clamping pads. (B) Image in (A) is transformed by Sobel edge detection method. (C) Grayscale map of blue cut line shown in (B), allowing for precise calibration of nanobeam clamping pad separation and microdisk diameter.

microdisk, as well as the spacing between the nanobeam clamping pads could not be assumed with the requisite precision required to achieve an alignment uncertainty to the nanobeam of <100 nm, as desired.

One simple solution to the problem of uncertainty in the feature dimensions is to measure them with a microscope in the CMi (with some microscopes being equipped with a software package that allows measurement). Since the dimensional variation across a wafer is very small, it is only necessary to measure a representative set of features. However, this method relies on the microscope itself being well calibrated and even in the best case is limited to an uncertainty of ±200 nm.

In order to avoid uncertainty in the microscope calibration and in an attempt to improve the resolution with which the SiO_2 feature dimensions could be determined, a self-calibrated process was used. The mask pattern shown in fig. B.1(A) was aligned to the markers described in section 3.3.4 and written in HSQ by e-beam, using a 5 nm grid. Thus the pattern features could be used for length calibration in analysis (for example the spacing between the small rectangular boxes in fig. B.1(A) are spaced by exactly 60 μm. The contrast generated by interference pattern between the edges of the SiO_2 features and HSQ was exploited by an edge detection method known as *sobel edge detection*, which approximates the intensity gradient at each point on the image. This process was carried out in ImageJ (an open source image processing software), with the resulting image shown in fig. B.1(B). As can be seen in the cut through line of fig. B.1(C), the edges of the SiO_2 are precisely delineated by a spike in the intensity gradient. Using this method it was possible to achieve an alignment precision between the SiO_2 and Si_3N_4 layers <100 nm.

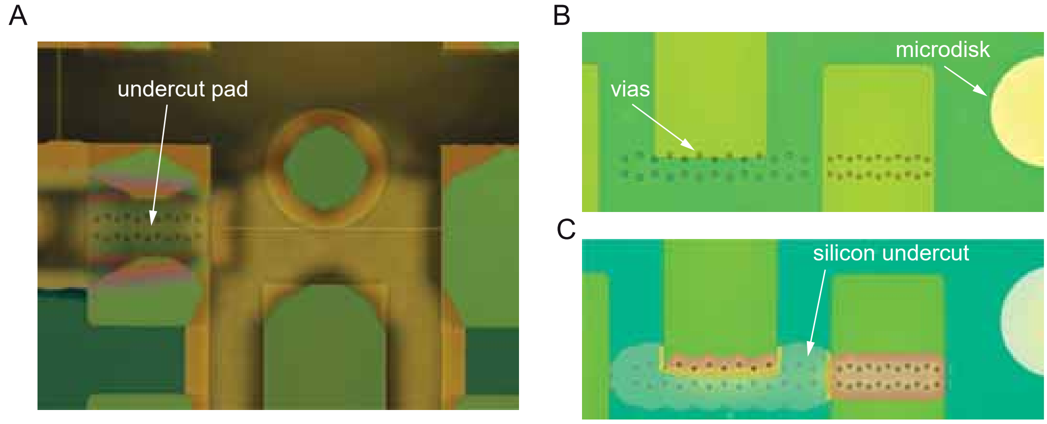

Figure B.2 – **Creating a channel beneath the clamping pad:** (A) shows a nanobeam clamped to a SiO_2 pad that has a channel etched out beneath it, along the beam's axis. (B) Shows vias etched into the Si_3N_4 and SiO_2 layers, prior to Si_3N_4 etching. These vias allowed XeF_2 gas (no plasma) to access the silicon underneath, etching isotropic cavities, as seen in (C). The purple and light blue in (C) indicate the presence of a cavity underneath.

B.2 Creating a suspended channel under the clamping pads

As was mentioned in chapters 5 and 6, we have long suspected that light being guided away from the cavity by the nanobeam is producing the heating effects we observe. Light may be absorbed in the beam causing direct heating, and/or it may cause heating at the clamping points upon absorption by the silicon substrate. Efforts toward improving the Si_3N_4 stoichiometry, as detailed in appendix B.6, sought to address the former mechanism. To address the latter issue we sought to suspend the SiO_2 clamping pad on one side of the cavity, as seen in fig. B.2(A). The concept of this was that light could continue to propagate before being absorbed, such that the heat source was far from the nanobeam clamping point.

In order to create this channel the KOH used in the final undercut step needed access to the <100> plane. This was accomplished in a two-step process that consisted of patterning 1 μm diameter holes into the Si_3N_4 and SiO_2 layers by dry etching, and with the resist still in place to protect the Si_3N_4, XeF_2 gas was diffused through the holes in order to attack the silicon underneath. The result of this process is shown in fig. B.2(C). The holes were staggered in order to avoid creating a line where the film could easily fracture. We note that in (A), after KOH etching, the SiO_2 pad is still robustly clamped on either side of the channel. However, an apparent birefringent effect is seen in the colors at the edge of the channel, suggesting a stress gradient. Although the modification did not lead to an apparent reduction in heating, the process was used to make the structure in fig. 6.5(A).

B.3 Initial design with polysilicon spacer layer

A key requirement during the planarization process described in section 3.3.2 is that at the end of the process the pads where the nanobeam will be clamped must be cleared of polysilicon.

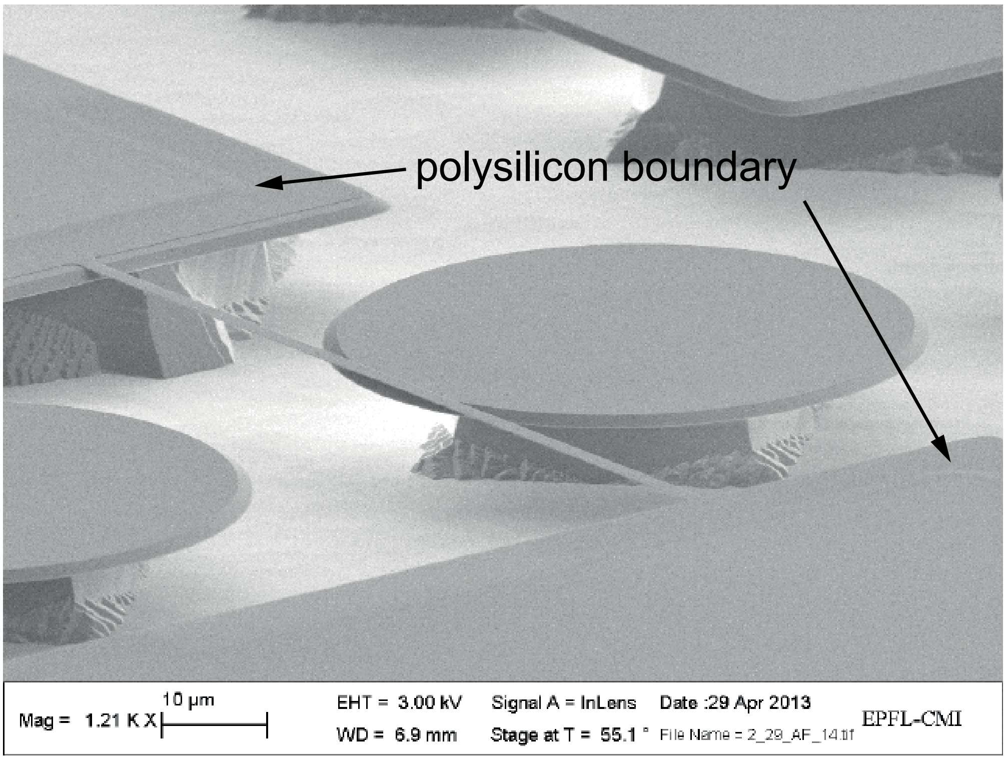

Figure B.3 – **Undercut of polysilicon in initial monolithic system design:** SEM shows completed sample, following KOH undercut and drying. As indicated the SEM the polysilicon spacer layer has been undercut by approximately 10 μm, and the Si_3N_4 has collapsed onto the SiO_2, completely removing the gap between microdisk and nanobeam.

This, in turn, means that the microdisk must be initially thinned with respect to the pads such that the necessary offset can be achieved. When the process was initially run preferential thinning of the microdisk was not used and instead a thin layer of polysilicon (~50-100 nm) was left above the pads at the end of the CMP process. This thin layer was intended to define the gap.

It was anticipated that the polysilicon would be partially undercut at the clamping points, but it was expected that this would be acceptably small and not lead to increased dissipation. However, as can be seen in fig. B.3 the polysilicon was undercut by ~ 10 μm and after drying (with CPD) the Si_3N_4 has collapsed onto the SiO_2. The collapse of the Si_3N_4 is particularly problematic as it completely removed the gap between microdisk and nanobeam.

In order to solve this problem the strategy of creating an offset in the SiO_2 layer was developed, avoiding undercut of the Si_3N_4 during the release step. In the new process polysilicon is technically not a spacer layer, but a sacrificial layer. The space between the structures is defined primarily by the microdisk thinning step and secondarily by the (unavoidable) polishing of the clamping pads, as described in section 3.3.2.

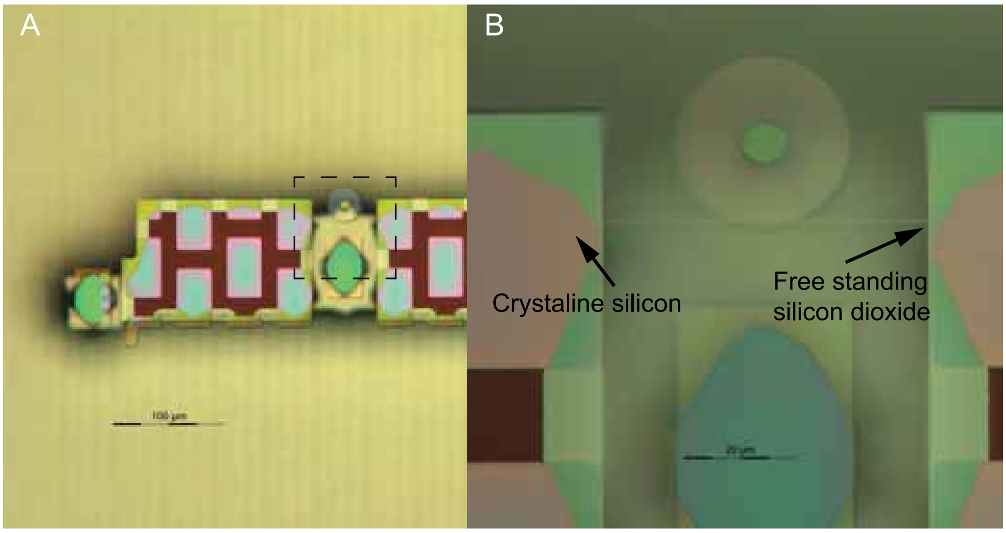

Figure B.4 – **Undercutting of nanobeam clamping pads during KOH release:** shown in (A) and (B), where the silicon substrate (pink) has started to recede behind the nanobeam clamping point, creating a free-standing edge of the SiO_2 clamping pad.

B.4 Excessive undercutting of nanobeam clamping pads

During the structural release step described in section 3.3.6 the sacrificial polysilicon spacer layer is removed, freeing the nanobeam. In addition, during this process the crystalline silicon beneath the microdisk must be also be partially etched away to avoid interference with the optical mode that would lead to excessive loss. Practically, it was determine that an undercut >5 μm avoided introducing additional losses from the silicon pillar. However, a balance needed to be achieved between sufficient undercutting of the microdisk and excessive undercutting of the supporting SiO_2 nanobeam clamping pads. The pads were aligned with the <111> crystal plane to protect the underlying silicon from direct attack, but the KOH could still attack from the edges of the pad. After a sufficient etch time the silicon would begin to recede behind the point where the nanobeam is clamped, as can be seen in fig. B.4(B). It is critical to avoid this effect, as the SiO_2 is under compressive stress (see section 3.1.2) and with sufficient undercut this stress will be released in the overhanging region, leading to loss of tensile stress in the nanobeam. A 45 minute etch in 40% KOH at 45 ° achieved the desired balance between these processes, with a 5-6 μm undercut of the microdisk while keeping the silicon intact under the nanobeam clamping region, as can be seen in fig. 2.9, for example.

B.5 BHF leakage under resist undercut during microdisk thinning

In section 3.3.1 the process used to offset the microdisk with respect to the surrounding pads by preferentially etching the microdisk in BHF is described. This involves exposing resist using a mask that creates an opening around the microdisk and covers the rest of the structures on the wafer. The wafer is then immersed in BHF for then than 1 minute, with the exact time being calibrated to thin the disk by ~50 nm. Initial attempts to run this process used 5 μm

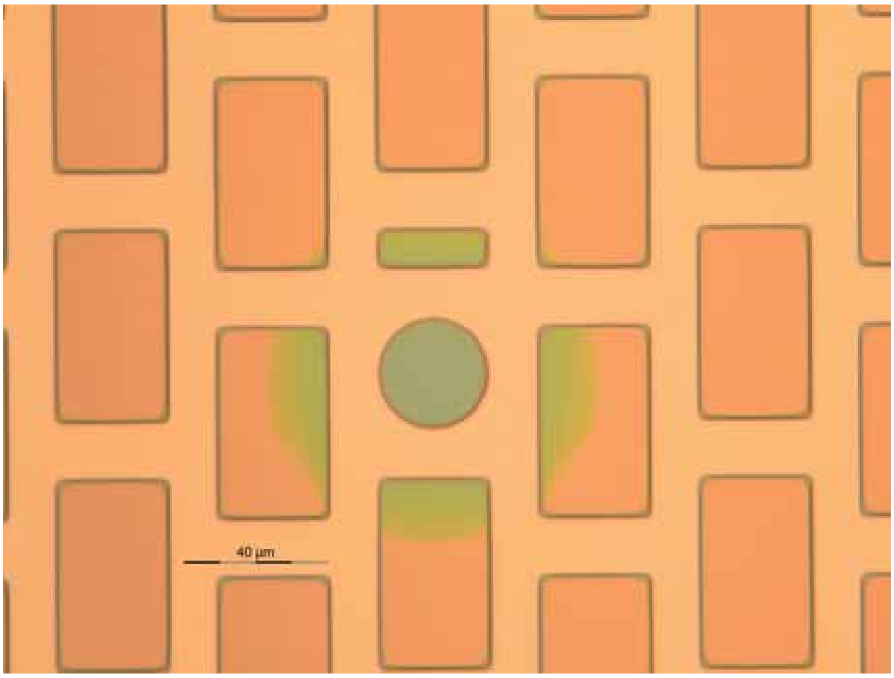

Figure B.5 – **Leakage of BHF during microdisk thinning:** Initial attempts to thin the microdisk preferentially, as described in section 3.3.1, using MicroChemicals AZ 9260 resist. The halo effect seen in the microscope, taken after removal of the resist, shows that the BHF leaked underneath the resist mask during etching and attacked the surrounding pads (used for clamping the nanobeam).

thick MicroChemicals AZ 9260 resist. This resist was originally chosen as it allows for spinning thicker layers than AZ 1512 HS, which is limited to 2 μm thicknesses. The thicker layer was expected to result in better conformality to the SiO_2 topography, and avoid leakage of BHF underneath the mask. In fact, as can be seen in fig. B.5, a conformal layer was not achieved with AZ 9260 and BHF leaked under the mask during the thinning process. This mean that the nanobeam clamping pads were thinned at the edges, as can be seen from the halo effect, and the offset was effectively lost.

In the end it was necessary to a 2 μm layer of AZ 1512, following application of HMDS adhesions promoter (as described in section 3.3.1). A reflow step was carried out in an oven at 140 °C, for 30 minutes in order to improve conformality to the structures. This method allowed for preferential thinning of the disk with no undercut of the resist mask.

B.6 Thermal annealing

Mechanical heating effects, such as those observed in the work of chapter 5 were suspected to arise from excessive absorption in the Si_3N_4 due to residual hydrogen content. Despite the near ideal stoichiometry of the LPCVD Si_3N_4 (section 3.1.2 we hoped that some further improvement could be made by annealing at temperatures above the deposition temperature (ideally >1000 °C). Annealing was attempted both during the processing, following Si_3N_4

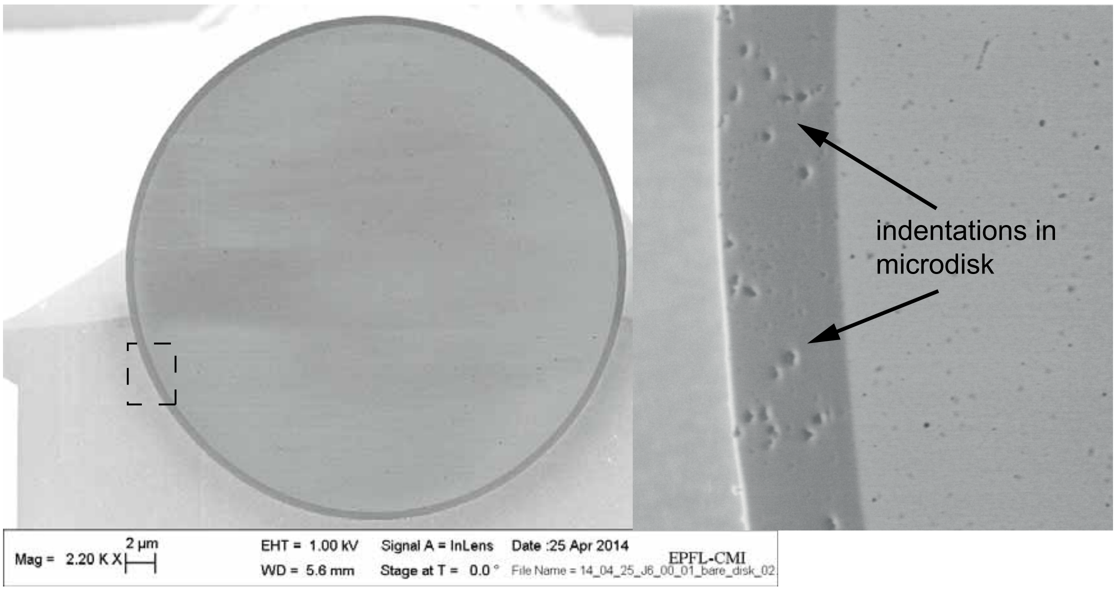

Figure B.6 – **Attempt to anneal silicon nitride during processing in tube furnace at 1050 °C:** for 24 hours with N_2 gas flow. After removal of the Si_3N_4 and polysilicon layers indentations could be observed in the microdisk surface, under SEM. This are attributed to the polysilicon grains, under compressive stress, pushing into the soften SiO_2 during the process.

deposition, and after completed fabrication can of the sample. Unfortunately, in both cases these attempts failed and the reasons are discussed below.

Annealing after silicon nitride deposition

A first attempt at annealing was made following deposition of Si_3N_4, placing the wafer in a LPCVD tube furnace at 1050 °C, with N_2 gas flow, for 24 hours. After annealing, the Si_3N_4 and polysilicon layers were removed and the microdisks were inspected under SEM, with the results shown in fig. B.6. It can be observed that large indentations were formed in the microdisk surface as a result of this process. We attribute this to a softening of the SiO_2 combined with the compressive stress and granular nature of the polysilicon (section 3.1.2). Likely the compressed columnar grains of the polysilicon pressed into and deformed the SiO_2 during the anneal. This stress induced damage raises the question of where it could be possible to first release the compressive tension in the polysilicon by initially annealing at 600 °C as described in section 3.1.2 (before Si_3N_4 deposition) and then anneal the Si_3N_4 at 1050 °C. This method has not been attempted and could be an interesting avenue for exploration.

Annealing of samples at the end of the fabrication process

As annealing during the fabrication process was not successful, attempts were made to anneal the structures at the end of fabrication. Figure B.7 shows the result of such an attempt, using a specialized annealing tube furnace at 1200 °C, with N_2 gas flow, for 24 hours. As should be

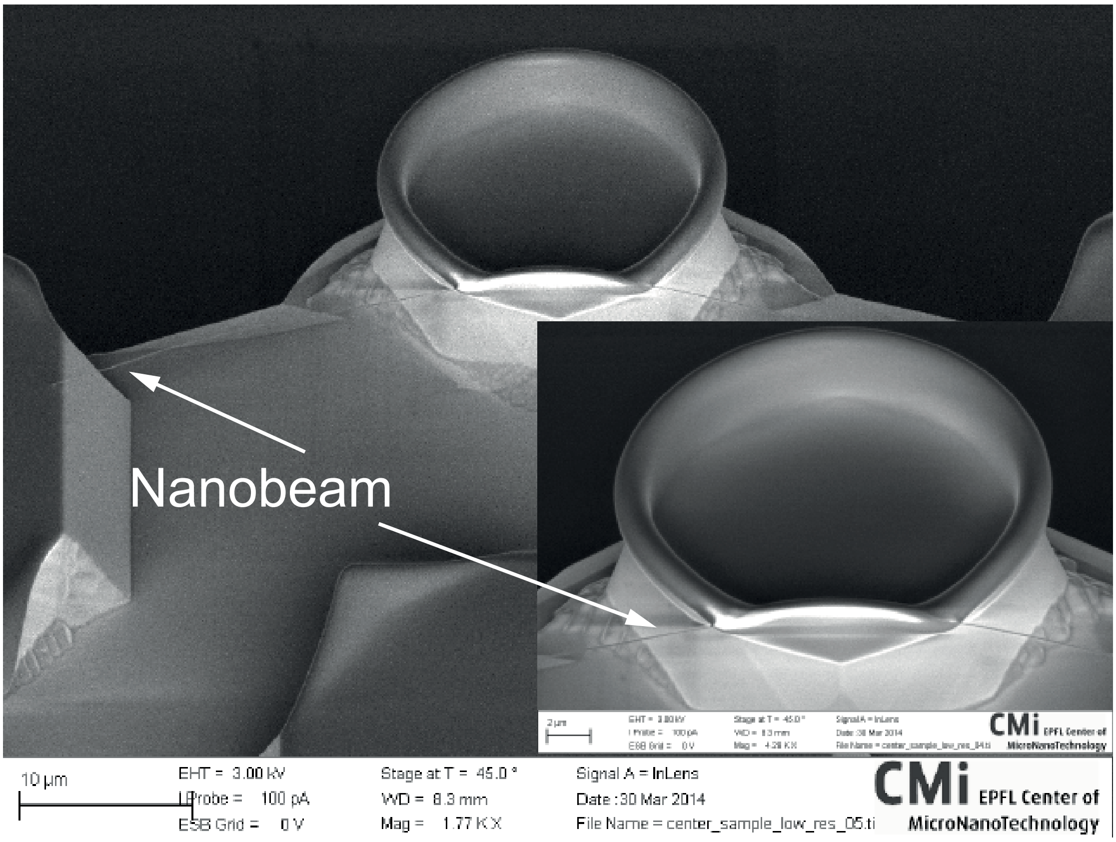

Figure B.7 – **Attempt to anneal completed samples in a tube furnace at 1200 °C:** for 24 hours with N_2 gas flow. As can be observed the suspended rim of the microdisk curled upwards and formed a torus shape, at the same time enveloping the nanobeam. The result was not successful.

clear the result was not successful. It can be seen that the suspended edge of the microdisk curled into a torus shape, and moreover enveloped the nanobeam in SiO_2. This result can be thought of as analogous to the method used to form microtoroidal resonators described in [57], where a microdisk is rapidly heated by exposure to a high intensity CO_2 laser pulse.

Despite the result being unsuccessful, it perhaps raises the question of whether such a method could be used to produce an alternate version of the system described in this thesis that integrates a microtoroid. Since slow formation in a furnace should be rather well controlled as compared to heating with a laser pulse, it may be possible to achieve this result if the right gap distance between the microdisk and nanobeam is used along with precise control over the microdisk overhang. The advantage would be the ability to achieve optical Q factors more than an order of magnitude higher for the same mode volume (~ radius) as compared to microdisks. However, it should be said that presumably such a system would be quite challenging to realize in practice.

Other attempts were made to anneal completed samples at lower temperatures, using a process known as rapid thermal annealing (RTA). This process uses high intensity IR lamps to directly heat a wafer, or sample, with the temperature measured by a pyrometer and used to feedback control the lamp intensity. Here temperatures used ranged from 700-1000 °C. Distortion of the geometry could not be directly observed and so the samples were iteratively measured between annealing tests to confirm that nanobeam had not become stuck to the disk. In this case it was found that temperatures above 850 °C consistently lead to the nanobeam becoming stuck. It should be kept in mind that the separation gaps in these samples are 20-50 nm and so even a small deformation of the microdisk would lead to collapse. It might seem unlucky that the disk would always curl towards the disk rather than away, but this effect is likely a result of the wedged microdisk sidewall, which would favor an upward curling in a compressively stressed film.

C E-beam microdisks fabrication

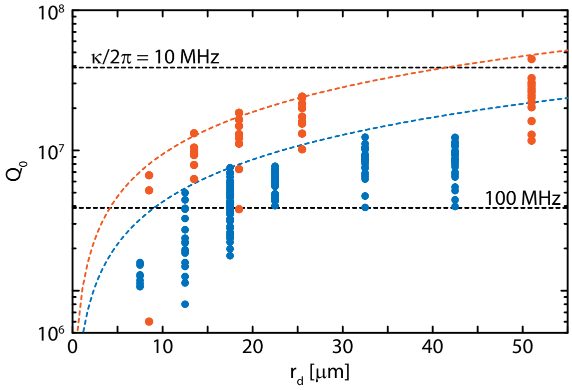

Figure C.1 – **Comparison between microdisks made by photolithography and e-beam lithography:** Intrinsic (undercoupled) Q-factors for a set of microdisks with oxide thickness of 700 nm and varying radii. TM and TE modes are not distinguished. The set shown in red is produced by e-beam lithography and in blue by photolithography. Dashed grey lines indicate corresponding resonance linewidths, $\kappa = 2\pi c/(\lambda Q_o)$, at $\lambda = 780$ nm (the measurement wavelength).

Fabrication of e-beam microdisks follows closely the process used for making microdisks by photolithography as detailed in section 3.3.1. Microdisks fabricated by this method are a compelling replacement for the monolithic fabrication process, as they exhibit approximately an order of magnitude higher Q for the same radius and thickness, as compared to the photolithography produced variants used throughout much of this thesis work. As optomechanical cooperativity scales inversely with the optical dissipation rate, if it is possible to integrate these disks without significantly losing in the frequency pulling factor than these would be a compelling replacement. Moreover, they may facilitate making an integrated sideband-resolved device (with mechanical frequency being higher than the optical dissipation rate). This cannot be practically achieved currently, as the bare linewidth of a 15 μm radius photolithography microdisk is ~ 100 MHz. On the other hand, a 100 MHz mode in a nanobeam with intrinsic stress of 900 MPa has a nodal spacing of ~2 μm, whereas the optimal overlap length for a 15 μm radius is ~10 μm (see section 2.2.6). This means that a significant trade off in optomechanical coupling would be required (roughly a factor of 4, leading to a ~16 times lower cooperativity). Even more problematic is that at these high frequencies stress-induced dissipation dilution has a negligible effect (section 2.1.1).

We recall the comparison between the two types of microdisks mentioned briefly in chapter 2

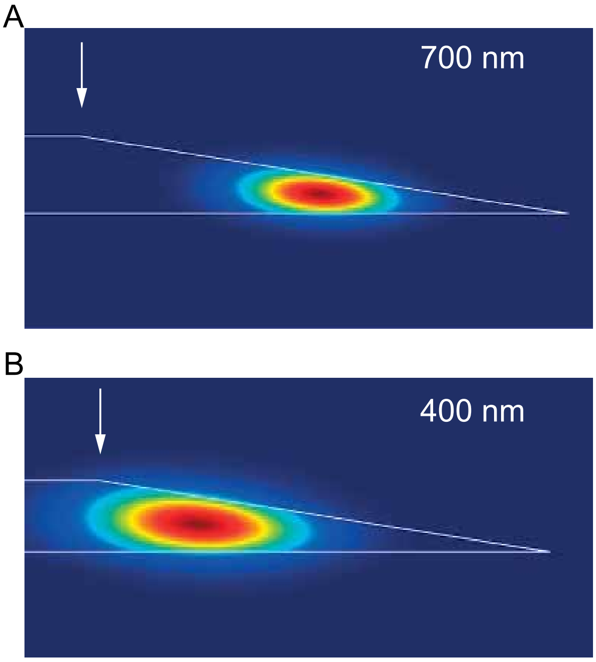

Figure C.2 – **FEM simulation of fundamental TE mode location with varying SiO_2 thickness:** FEM simulations show the location of fundamental TE mode at $\lambda = 780$ nm for 700 nm thick (A) and 400 nm thick (B) SiO_2 microdisks with a radius of 15 μm. The wedge angle is 10°, corresponding to the sidewall profile of microdisks fabricated with this e-beam process. Arrows indicate the upper edge of the wedge, where the mode is ideally centered in the optomechanical system, in order to realize maximum overlap with the nanobeam.

and shown in fig. C.1, with e-beam microdisks illustrated in red and those produced by photolithography in blue. The thickness in both cases is 700 nm. A complication that arises when integrating the e-beam type microdisks is that, as produced currently, they have a typical wedge angle of 10°, as compared with the photolithography type with an angle of 30°. As described in chapter 2, in order to maintain a high overlap between the optical mode and nanobeam, the center of the optical mode should coincide with the same radial position as the upper edge of the microdisk. The steep wedge angle of photolithography microdisks allows this condition to be realized for a large range of thicknesses, up to ~1 μm. However, the shallow angle of e-beam microdisks causes the mode to sit far into the wedge region for thickness above ~400 nm, greatly reducing the overlap with the nanobeam. This effect is clearly seen in the FEM simulations of fundamental TE modes for microdisks with a 15 μm radius and 10 ° wedge angle. Thus in such systems the microdisk must be made very thin, as is the case for the samples used in chapter 4, with a thickness of 350 nm. This results in a low effective refractive index, which does not significantly impact the Q when the microdisks are measured on their own, but when a nanobeam is brought into the near-field the Q drops precipitously. We cannot say for sure the origin of this effect, but it's a fair guess that it is a result of a closer matching of the mode index to that of the nanobeam, leading to guiding of light out of the resonator and into the nanobeam (it could also be attributed to increased scattering). Either of these effects may be remedied by using extremely thin nanobeams, but so far this avenue has not been explored, and for the time being integrated devices utilizing e-beam microdisks do not exhibit the high Qs that one would expect. For example the device used in chapter 4 has a radius of 15 μm and an under-coupled cavity decay rate of $\kappa \approx 2\pi \cdot 2.2$ GHz. From fig. C.1 we can see that the microdisk on its own has a decay rate of $\kappa \approx 2\pi \cdot 30$ MHz - almost two orders of magnitude lower. Careful modeling of this effect will likely be necessary if this issue is to be mitigated in future versions of the device.

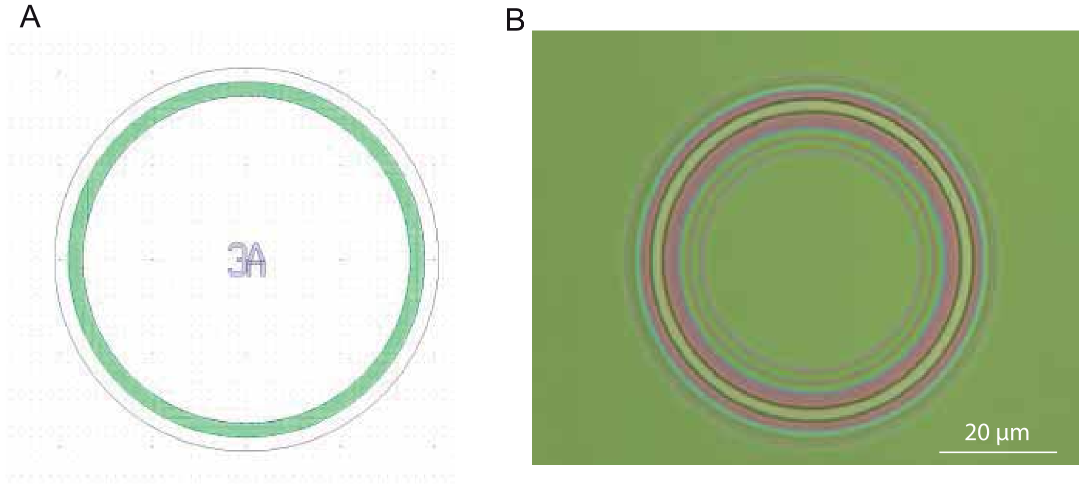

Figure C.3 – **E-beam microdisks process:** with the three mask layers shown in (A). The first mask, used to define the microdisk, is the green ring which is written by e-beam in ZEP 520A resist. The next mask (optional), in blue, is similarly defined and used to etch labels (or other features as seen in fig. C.5) into the microdisk. The final mask outline in black is used to elevate the microdisk with respect to the substrate, as shown in fig. C.4. (B) is an optical microscope image of the microdisk following BHF etching, with mask 1 still in place. The yellow ring corresponds to the green pattern in (A). The colored rings inside this ring are interference fringes from the sloped sidewall of the microdisk.

C.0.1 Fabrication process

First mask process

The fabrication process utilizes a negative tone polymeric resist made by Zeon Corporation, known as ZEP 520A, which exhibits good stability to wet etches like BHF. The initial mask layer is shown in green in fig. C.3(A), for a single microdisk. In order to keep the e-beam writing process efficient a thin ring, 1.5 μm wide, is written. A dry oxidized FZ silicon wafer (section 3.1) is used for the process and prior to coating the resist, the wafer is dehydrated and primed with HMDS (section 3.3.1) in an oven at 125 °C. ZEP 520A 100% is spin coated at 1500 rpm for 3 minutes, resulting in a resist thickness of ~600 nm. Following spin coating the wafer is baked at 180 °C for 5 minutes, to remove residual solvents. The mask layer is exposed to a dose of 245 μC/cm^2 using a Vistec EBPG5000 e-beam system with 100 kV acceleration. The mask is fractured on a 5 nm grid and the dose is delivered with 4x multipass in order to reduce line edge roughness (each pass delivers 1/4 of the total dose). Following exposure the resist is immersion developed in Amyl acetate for 70 seconds, and development is stopped by immersion in 9:1 MiBK:IPA for 60 seconds. The wafer is then baked in an oven at atmospheric pressure and 140 °C for 30 minutes, to reflow the resist and further reduce pattern roughness (this step also serves to remove solvent residue in preparation for wet etching). Prior to wet etching, a low power (200W) oxygen plasma for 20 seconds is used to remove any resist residues in the cleared area. Immersion etching of the SiO_2 is carried out in a bath of BHF 7:1 (NH_4F : HF = 87.5 : 12.5 %) for 10 minutes. Note that this etch is much shorter than the 25 minute one used for photolithography microdisks as the lateral etch rate is nearly three times faster (which is the cause of the more shallow wedge angle - see section 3.3.1 for more

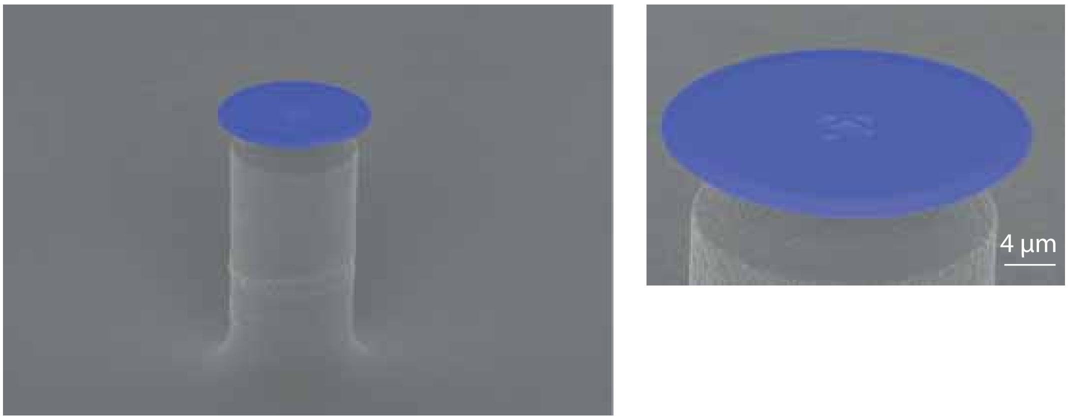

Figure C.4 – **Standalone disks written by e-beam:** with false coloring (blue) to indicate the SiO_2. The pillar defined by Bosch process in mask 3 can be seen on the left side. Note that following etching to undercut the microdisk the pillar shrinks to be smaller in radius than the microdisk (it is initially larger). The label "3A" can be seen etched into the center of the microdisk.

details). The resulting pattern at the end of wet etching is seen in the microscope image of fig. C.3(B). Here the yellow ring is the mask pattern, seen in green in fig. C.3(A), the purple region is where SiO_2 has been completely cleared, and the ring patterns seen at the center are interference fringes caused by sloping sidewall of the microdisk. Note that resist is still in place in this image. Finally, the resist is removed by oxygen plasma ashing at high power (600W) for 10 minutes.

Second mask process (optional)

At this point the process can be carried on to produce optomechanical device samples, as detailed in appendix D, or the microdisks can be made into standalone devices. In the latter case the process detailed above for patterning ZEP 520A can be repeated to place labels on the microdisks, as shown in the blue mask layer in fig. C.3(A). However, in this case the pattern is transferred by ICP-RIE dry etching (section 3.2.2) and reflow is not required. The oxygen plasma step is still used to remove resist residues following development. Dry etching is carried out with an SPTS APS (manufacturer and model) ICP-RIE using C_4F_8 as the enchant gas, with H_2 used to enhance polymerization and increase anisotropy (section 3.2.2). Normally the etch time is calibrated to achieve a etch depth of ~50 nm, which is sufficient to resolve the markers (seen in fig. C.4), although this can be adjusted as desired. As with the first mask resist is removed by oxygen plasma ashing at high power (600W) for 10 minutes.

Third mask process (Elevation and undercut of the microdisk)

In order to couple to the microdisk with an optical fiber it must be elevated with respect to the substrate. Also, as mentioned at the beginning of this chapter, the microdisk must be sufficiently undercut in order to avoid optical losses to the supporting pillar. The step of elevating the resonator is accomplished using the Bosch process detailed in section 3.2.3, and the undercutting step is carried out by KOH wet etching, as described in section 3.3.6. The Bosch process is used to etch down the substrate ~50 μm with respect to the microdisk and a resist layer at least a few microns thick is required. For this step 5 μm of MicroChemicals AZ 9260 is spin coated at 6800 rpm, following a dehydration bake at 160 °C for 5 minutes. A *softbake* follows the spin coating to remove residual solvent before photolithography is used to expose the mask layer shown in black in fig. C.3(A). This is just a circle with a radius that is enlarged by 2 μm with respect to the ring used to define the microdisk in mask 1. Note that SiO_2 still surrounds the microdisk, as seen in fig. C.3(B), and thus the circle used for Bosch process should fit within the region where SiO_2 has been cleared. It should be large enough that photolithography alignment imprecision (±2 μm) does not cause the disk to be exposed and etched, but not too large such that SiO_2 remains outside the disk and blocks it from being coupled to at the end of the process. The mask is exposed using a Süss MA6 mask aligner, with a 1000W i-line filtered mercury-vapor lamp for 25 seconds, in hard contact. The resist is then sprayed developed with MicroChemicals AZ 726 MIF for 70s. Exposure to low power (200W) oxygen plasma for 20 seconds removes any photoresist residues in the cleared area. Dry etching with the same chemistry and equipment used for mask 2 clears SiO_2 from the rest of the wafer (Bosch process does not effectively etch SiO_2), with the etch time dependent on the SiO_2 thickness. Bosch process is used to etch down 50 μm of silicon, using an Alcatel AMS 200 ICP-RIE (the name of specific recipe used in the CMi is *soi_acc*++++), and takes 15 minutes to etch this depth). Before removing the resist, the wafer is diced half way through (~260 μm for a typical 525 μm thick wafer) by alignment to markers indicating the edge of the chips, which can be defined in either mask 1 or 2. The dicing equipment is a DISCO (manufacturer) DAD 321 silicon dicing saw. The resist is left in place to protect the microdisks from silicon particles during the dicing. Following dicing the wafer is rinsed and resist is removed by oxygen plasma ashing at high power (600W) for 15 minutes (note that the wafer is still in one piece). Undercut of the disk proceeds by etching in aqueous 40% KOH at 45 °C, with the time dependent on the radius of the disks (for 15 μm radii 45 minutes is sufficient). After etching, the wafer is immersed in 37% HCl to dissolve any potassium salts left behind from the KOH. The chips can now be carefully broken from the wafer using tweezer, in a process akin to dividing a Toblerone bar. It is recommended to perform one more step to clean the SiO_2, which can be done with the entire wafer or with individual chips: this wet etching in 5% HF for 30 seconds. This process removes removes ~10 nm of SiO_2, leaving an *optically clean* surface - avoiding any additional losses that would be introduced by contaminants on the surface.

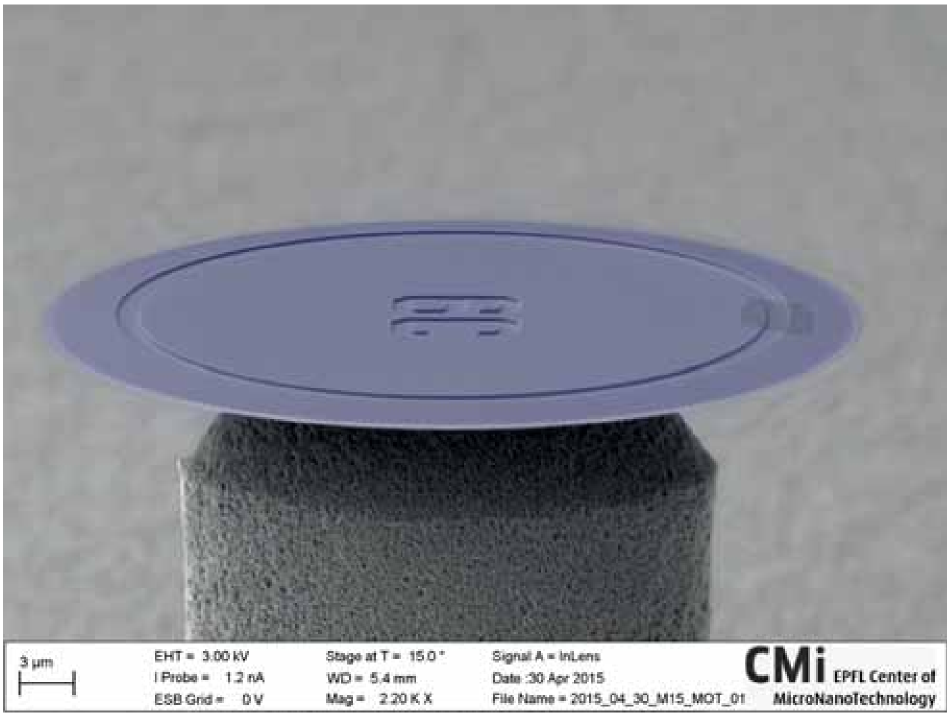

Figure C.5 – **Possibility to use e-beam microdisks for 2D optomechanics:** a version of the structure in fig. C.4 is modified to include a 50 nm deep and 1 μm wide channel around its perimeter (SiO_2 false colored to blue). The image is modified to show the concept of applying a flake of 2D material over this channel to create a suspended mechanical structure, where its motion would be optically coupled to the microdisk mode.

An alternative use for the second mask

Note that although the second mask process described above was introduced in the context of applying labels for identification of different microdisks, it can be used to etch other types of features into the surface. One interesting example is shown in fig. C.5, where a shallow channel, ~50 nm deep and 1 μm wide, has been etched into the microdisk, in a ring shape following its perimeter. The image has been modified to show the concept of depositing a flake of 2D material over the channel, which would be free to oscillate over the suspended region. Such a device could in principle be used to make an optomechanical system using 2D materials. A somewhat similar concept has been demonstrated to form a mechanically compliant capacitor plate made of graphene deposited over a shallow etched circle [183]. The concept shown in fig. C.5 has not been explored further but could be an interesting avenue to consider in the future.

D Fabrication process monolithic device with e-beam microdisks

The following sections detail the fabrication process for the sample used in the experiment described in chapter 4 [125], referred to as B1 1,2 #34. Here B1 refers to the wafer, 1,2 to the specific chip, and #34 to the specific sample on the chip. This is a modified version of the process described in chapter 3, which has been altered to include microdisks made using e-beam rather than photolithography

As described in chapter 3, the process starts with a 525 μm thick, 100 mm diameter, float zone grown, intrinsic Si wafer (see chapter 3). A tube furnace is used to grow a 750 nm SiO_2 layer in a pure O_2 environment (dry oxidized). For the samples used in the manuscript the SiO_2 thickness was reduced to 450 nm, by buffered hydrofluoric acid etching, before the start of the process.

Mask 1

Process tag: HAE M1 (hybrid all e-beam process, mask 1). Note that *all e-beam* refers to the fact that both the microdisk and nanobeam patterns are defined by e-beam. In fact, the other masks utilized are transfered by photolithography

Process objective: Define alignment markers that are used for all subsequent e-beam masks. Of specific note: these markers combined with calibration of the microdisk radius allow for precise alignment (<50 nm) between the microdisk and nanobeam, which is critical for maximizing coupling between the mechanical and optical modes.

GDS number: 1

HAE M1 Run Card

Step	Process step description	Equipment	Operation	Notes
1	HMDS adhesion promoter priming	YES III priming oven	HMDS vapor coating at ~10 mBar and 125 °C	Allow wafers to thermalize (~5 minutes) before engaging vacuum
2	Coat with high contrast photoresist	EV Group EVG150 resist processing system (100mm)	Coat 2 μm MicroChemicals AZ 1512 HS (spin at 1800 rpm)	Edge bead removal used. Softbake at 110 °C for 90s.
3	Expose mask 1	Süss MA6/BA6 mask aligner	Hard contact exposure for 3.5s	1000W Hg lamp, hard contact for 10s before exposure
4	Photoresist development	EV Group EVG150 resist processing system (100mm)	Spray develop with AZ 726 MIF for 70s	Post bake at 112 °C for 90s
5	Oxygen plasma ashing (descum)	PVA TePla plasma system	Plasma treatment for 20s (~50 nm photoresist removed)	2.45 GHz, 200W, 200 sccm O_2
6	Plasma etching of SiO_2	SPTS APS inductively coupled plasma etcher	Etch through 750 nm SiO_2 layer (*SiO_2 3:1* recipe, 3 mins)	$He/H_2/C_4F_8$ chemistry
7	Plasma etching of Si	Alcatel AMS 200 inductively coupled plasma etcher	Etch ~2.5 μm into Si (*Si Opto* recipe, 3 mins)	SF_6 chemistry
8	Oxygen plasma ashing of photoresist	PVA TePla plasma system	Plasma treatment for 10 mins	2.45 GHz, 600W, 400 sccm O_2
9	Piranha etching of photoresist residues	Temperature controlled Ultrafab wetbench	Immerse wafer in solution for 10 minutes	30% H_2O_2 added to H_2SO_4 (1:7) maintained at 100 °C

Mask 2

Process tag: HAE M2 (hybrid all e-beam process, mask 2)

Process objective: Define the SiO_2 microdisks that will be integrated with nanobeams in the final samples, by e-beam lithography. Also defined in this mask are the photolithography alignment markers. Here positive photoresist is used and an opening is created whereby the underlying SiO_2 can be etched using buffered hydrofluoric acid.

GDS numbers: 2 and 3 (high resolution (5 nm grid) and low resolution (50 nm grid), respectively). Note that a *bulk and sleeve* technique is used for e-beam writing to reduce write time: features are divided into a 1 μm wide feature boundary (the *sleeve*) and the remaining *inside* of the features (the *bulk*).

HAE M2 Run Card

Step	Process step description	Equipment	Operation	Notes
1	HMDS adhesion promoter priming	YES III priming oven	HMDS vapor coating at ~10 mBar and 125 °C	Allow wafers to thermalize (~5 minutes) before engaging vacuum
2	Coat with positive e-beam photoresist	ATMsse OPTIspin SB20 manual spin coater	Coat 600 nm Zeon Corporation ZEP520A (spin at 1500 rpm)	Post bake at 180 °C for 5 mins
3	Expose mask 2	Vistec EBPG5000 e-beam system @ 100 kV	Expose with 245 $\mu C/cm^2$ dose, and 4x multipass (to minimize line edge roughness)	GenISys Beamer software used for fracturing and application of proximity effect correction ($\eta = 0.5$)
4	Photoresist development	Petri dishes	Immersion develop with Amyl acetate for 70s, and rinse in 9:1 MiBK:IPA for 60s	
5	Photoresist reflow	YES-PB curing oven	Bake at 140 °C for 30 mins at atmospheric pressure	Allow to cool at least 5 mins before proceeding
6	Oxygen plasma ashing (descum)	PVA TePla plasma system	Plasma treatment for 20s (~50 nm photoresist removed)	2.45 GHz, 200W, 200 sccm O_2
7	Buffered hydrofluoric acid (BHF) wet etching	Plade Six Sigma wet bench with recirculating bath	Immersion in BHF for 10 mins	40% NH_4F and 49% HF in 7:1 volume ratio
8	Oxygen plasma ashing of photoresist	PVA TePla plasma system	Plasma treatment for 10 mins	2.45 GHz, 600W, 400 sccm O_2
9	Piranha etching of photoresist residues	Temperature controlled Ultrafab wetbench	Immerse wafer in solution for 10 minutes	30% H_2O_2 added to H_2SO_4 (1:7) maintained at 100 °C

Mask 3

Process tag: HAE M3 (hybrid all e-beam process, mask 3)

Process objective: Define the *sacrificial* SiO_2 microdisks, which will not be integrated with nanobeams in the final samples, by photolithography. Here positive photoresist is used and an opening is created whereby the underlying SiO_2 can be etched using buffered hydrofluoric acid. The purpose of creating these *sacrificial* microdisks, which cover the entire wafer, is to provide a uniform topography that is critical to achieving a uniform polishing rate during chemical mechanical planarization. The process is nearly the same as mask 2, except that photolithography is used instead of e-beam (since the microdisks will not be utilized). Here HMDS priming is not done as the resist adheres much better than ZEP520A used in mask 2, and we want to achieve a similar sidewall angle in both cases.

GDS number: 4

HAE M3 Run Card

Step	Process step description	Equipment	Operation	Notes
1	Coat with high contrast photoresist	EV Group EVG150 resist processing system (100mm)	Coat 2 μm MicroChemicals AZ 1512 HS (spin at 1800 rpm)	Edge bead removal used. Softbake at 110 °C for 90s.
2	Expose mask 3	Süss MA6/BA6 mask aligner	Hard contact exposure for 3.5s	1000W Hg lamp, hard contact for 10s before exposure
3	Photoresist development	EV Group EVG150 resist processing system (100mm)	Spray develop with AZ 726 MIF for 70s	Post bake at 112 °C for 90s
4	Photoresist reflow	YES-PB curing oven	Bake at 140 °C for 30 mins at atmospheric pressure	Allow to cool at least 5 mins before proceeding
5	Oxygen plasma ashing (descum)	PVA TePla plasma system	Plasma treatment for 20s (~50 nm photoresist removed)	2.45 GHz, 200W, 200 sccm O_2
6	Buffered hydrofluoric acid (BHF) wet etching	Plade Six Sigma wet bench with recirculating bath	Immersion in BHF for 10 mins	40% NH_4F and 49% HF in 7:1 volume ratio
7	Oxygen plasma ashing of photoresist	PVA TePla plasma system	Plasma treatment for 10 mins	2.45 GHz, 600W, 400 sccm O_2
8	Piranha etching of photoresist residues	Temperature controlled Ultrafab wetbench	Immerse wafer in solution for 10 minutes	30% H_2O_2 added to H_2SO_4 (1:7) maintained at 100 °C

Mask 4

Process tag: HAE M4 (hybrid all e-beam process, mask 4)

Process objective: Thin the SiO_2 microdisks relative to the bulk SiO_2 in order to define the gap between the microdisks and nanobeams (note that nanobeams will be clamped to the bulk SiO_2 layer). Here an opening in positive photoresist is created around the microdisk such that it can be selectively etched relative to the bulk SiO_2 using buffered hydrofluoric acid.

GDS numbers: 5 (repeated for 6 and 7). This process can be repeated N times (here N=3), for $2^N - 1$ different disk thicknesses. For example, here a disk can be thinned with a single mask (ie. gds 5,6, or 7), by two masks (ie. gds 5 & 6, 5 & 7, or 6 & 7), or by three masks (ie. gds 5 & 6 & 7). This allows for making many different gaps between microdisks and nanobeams on the same wafer, which is important for optimizing performance.

HAE M4 Run Card

Step	Process step description	Equipment	Operation	Notes
1	Coat with high contrast photoresist	EV Group EVG150 resist processing system (100mm)	Coat 2 μm MicroChemicals AZ 1512 HS (spin at 1800 rpm)	Edge bead removal used. Softbake at 110 °C for 90s.
2	Expose mask 4	Süss MA6/BA6 mask aligner	Hard contact exposure for 3.5s	1000W Hg lamp, hard contact for 10s before exposure
3	Photoresist development	EV Group EVG150 resist processing system (100mm)	Spray develop with AZ 726 MIF for 70s	Post bake at 112 °C for 90s
4	Oxygen plasma ashing (descum)	PVA TePla plasma system	Plasma treatment for 20s (~50 nm photoresist removed)	2.45 GHz, 200W, 200 sccm O_2
5	Buffered hydrofluoric acid (BHF) wet etching	Plade Six Sigma wet bench with recirculating bath	Immersion in BHF for 24s, 32s, or 40s (for gds 5, 6, or 7, respectively)	40% NH_4F and 49% HF in 7:1 volume ratio
6	Oxygen plasma ashing of photoresist	PVA TePla plasma system	Plasma treatment for 10 mins	2.45 GHz, 600W, 400 sccm O_2
7	Piranha etching of photoresist residues	Temperature controlled Ultrafab wetbench	Immerse wafer in solution for 10 minutes	30% H_2O_2 added to H_2SO_4 (1:7) maintained at 100 °C

Thin film deposition

Process tag: HAE FD (hybrid all e-beam process, film deposition)

Process objective: After thinning of the microdisks with mask set 4, a 1.5 μm thick poly-Silicon layer is deposited by low-pressure chemical vapor deposition (LPCVD) at 600 °C. The poly-Silicon will serve as the sacrificial layer between the microdisks and nanobeams. Before this step the wafer undergoes RCA cleaning, followed by atomic layer deposition (ALD) of 2 nm of Al_2O_3 (this will serve as an etch stop for mask 5, step 7). After deposition of poly-Silicon, chemical mechanical planarization (CMP) is used to thin the material until the surface of the bulk SiO_2 is reached. This surface will provide a place for the ends of the nanobeams to be clamped. Following CMP, RCA cleaning is performed, 2 nm of Al_2O_3 is deposited by ALD (an etch stop for mask 7, step 5), and finally 80 nm of Si_3N_4 is deposited by LPCVD at 800 °C (producing a near stoichiometric film, with intrinsic stress of ~900 MPa).

Mask 5

Process tag: HAE M5 (hybrid all e-beam process, mask 5)

Process objective: After deposition of Al_2O_3, poly-Silicon, Al_2O_3, and Si_3N_4 the e-beam alignment markers defined in mask 1 must be uncovered. This means etching away these deposited materials which have *buried* the markers.

GDS number: 8

HAE M5 Run Card

Step	Process step description	Equipment	Operation	Notes
1	Coat with high contrast photoresist	EV Group EVG150 resist processing system (100mm)	Coat 2 μm MicroChemicals AZ 1512 HS (spin at 1800 rpm)	Edge bead removal used. Softbake at 110 °C for 90s.
2	Expose mask 5	Süss MA6/BA6 mask aligner	Hard contact exposure for 3.5s	1000W Hg lamp, hard contact for 10s before exposure
3	Photoresist development	EV Group EVG150 resist processing system (100mm)	Spray develop with AZ 726 MIF for 70s	Post bake at 112 °C for 90s
4	Oxygen plasma ashing (descum)	PVA TePla plasma system	Plasma treatment for 20s (~50 nm photoresist removed)	2.45 GHz, 200W, 200 sccm O_2
6	Plasma etching of Si_3N_4 and Al_2O_3	SPTS APS inductively coupled plasma etcher	Etch through 80 nm Si_3N_4 layer and the 2 nm Al_2O_3 underneath (*SiO_2 3:1* recipe, 2 mins)	$He/H_2/C_4F_8$ chemistry
7	Plasma etching of poly-Silicon	Alcatel AMS 200 inductively coupled plasma etcher	Etch away poly-Silicon that has filled the alignment markers defined in mask 1 (*Si Opto* recipe, 5 mins)	Note that the poly-Silicon is *over-etched*, as the Al_2O_3 underneath provides a stopping layer. SF_6 chemistry
8	Oxygen plasma ashing of photoresist	PVA TePla plasma system	Plasma treatment for 10 mins	2.45 GHz, 600W, 400 sccm O_2
9	Piranha etching of photoresist residues	Temperature controlled Ultrafab wetbench	Immerse wafer in solution for 10 minutes	30% H_2O_2 added to H_2SO_4 (1:7) maintained at 100 °C

Mask 6

Process tag: HAE M6 (hybrid all e-beam process, mask 6)

Process objective: Thin local sections of Si_3N_4 using buffered hydrofluoric acid, such that samples with differing Si_3N_4 thicknesses can be produced on the same wafer.

GDS numbers: 9 (repeated for 10). As with mask 4, this process can be repeated N times, for $2^N - 1$ different nanobeam thicknesses. Here only two thicknesses were desired.

HAE M6 Run Card

Step	Process step description	Equipment	Operation	Notes
1	HMDS adhesion promoter priming	YES III priming oven	HMDS vapor coating at ~10 mBar and 125 °C	Allow wafers to thermalize (~5 minutes) before engaging vacuum
2	Coat with positive e-beam photoresist	ATMsse OPTIspin SB20 manual spin coater	Coat 600 nm Zeon Corporation ZEP520A (spin at 1500 rpm)	Post bake at 180 °C for 5 mins
3	Expose mask 6	Vistec EBPG5000 e-beam system @ 100 kV	Expose with 245 μC/cm^2 dose, and 4x multipass (to minimize line edge roughness)	GenISys Beamer software used for fracturing and application of proximity effect correction ($\eta = 0.5$)
4	Photoresist development	Petri dishes	Immersion develop with Amyl acetate for 70s, and rinse in 9:1 MiBK:IPA for 60s	
5	Photoresist reflow	YES-PB curing oven	Bake at 140 °C for 30 mins at atmospheric pressure	Allow to cool at least 5 mins before proceeding
6	Oxygen plasma ashing (descum)	PVA TePla plasma system	Plasma treatment for 20s (~50 nm photoresist removed)	2.45 GHz, 200W, 200 sccm O_2
7	Buffered hydrofluoric acid (BHF) wet etching	Plade Six Sigma wet bench with recirculating bath	Immersion in BHF for 27 mins (depends on desired Si_3N_4 thickness; etch rate ~0.75 nm/min	40% NH_4F and 49% HF in 7:1 volume ratio
8	Oxygen plasma ashing of photoresist	PVA TePla plasma system	Plasma treatment for 10 mins	2.45 GHz, 600W, 400 sccm O_2
9	Piranha etching of photoresist residues	Temperature controlled Ultrafab wetbench	Immerse wafer in solution for 10 minutes	30% H_2O_2 added to H_2SO_4 (1:7) maintained at 100 °C

Mask 7

Process tag: HAE M7 (hybrid all e-beam process, mask 7)

Process objective: Etch nanobeam patterns in Si_3N_4 by plasma etching. Nanobeams are aligned to underlying microdisks with a precision of <50 nm, using the alignment markers defined in masks 1 and 6.

GDS numbers: 11 and 12 (high resolution (5 nm grid) and low resolution (50 nm grid), respectively). Note that a *bulk and sleeve* technique is used for e-beam writing to reduce write time: features are divided into a 1 μm wide feature boundary (the *sleeve*) and the remaining *inside* of the features (the *bulk*).

HAE M7 Run Card

Step	Process step description	Equipment	Operation	Notes
1	Buffered hydrofluoric acid (BHF) surface preparation	Plade Six Sigma wet bench with recirculating bath	Immersion in BHF for 30 s	Used to strip surface Silicon oxy-nitride layer (better resist adhesion). 40% NH_4F and 49% HF in 7:1 volume ratio
2	Coat with negative e-beam photoresist	ATMsse OPTIspin SB20 manual spin coater	Coat 180 nm Dow Corning XR1541 006 (*HSQ 6%*; spin at 1000 rpm)	
3	Expose mask 7	Vistec EBPG5000 e-beam system @ 100 kV	Expose with 1700 $\mu C/cm^2$ dose	GenISys Beamer software used for fracturing and application of proximity effect correction ($\eta = 1.5$)
4	Photoresist development	Petri dishes in fume hood	Immersion develop with 25% Tetramethylammonium hydroxide (TMAH) for 90s, and rinse in H_2O	
5	Plasma etching of Si_3N_4	SPTS APS inductively coupled plasma etcher	Etch through 80 nm Si_3N_4 layer and stop on the 2 nm Al_2O_3 underneath (*Si_3N_4 smooth* recipe, ~30s)	End point detection via optical spectrometry is used. CHF_3/SF_6 chemistry

Mask 8

Process tag: HAE M8 (hybrid all e-beam process, mask 8)

Process objective: Using photolithography define a mesa type feature that elevates the sample relative to the rest of the chip. This is necessary such that an optical fiber can be brought near to the microdisk, for coupling during experiment, without having the fiber touch the chip (which would cause loss of the out-coupled photons). Following this etch, the remaining fabrication steps including chip dicing, undercut, cleaning, and release are carried out. Note that the HSQ e-beam resist from mask 7 is left on the sample as it will be stripped during step 10.

GDS number: 13

HAE M8 Run Card

Step	Process step description	Equipment	Operation	Notes
1	Coat with high contrast photoresist	EV Group EVG150 resist processing system (100mm)	Coat 5 μm MicroChemicals AZ 9260 (spin at 6800 rpm)	Dehydrate at 160 °C for 5 mins. Softbake at 115 °C for 6 mins. Edge bead removal used
2	Expose mask 8	Süss MA6/BA6 mask aligner	Hard contact exposure for 25s	1000W Hg lamp, hard contact for 10s before exposure
3	Photoresist development	EV Group EVG150 resist processing system (100mm)	Spray develop with AZ 726 MIF for 70s	No post bake
4	Oxygen plasma ashing (descum)	PVA TePla plasma system	Plasma treatment for 20s (~50 nm photoresist removed)	2.45 GHz, 200W, 200 sccm O_2
5	Plasma etching of bulk SiO_2	SPTS APS inductively coupled plasma etcher	Etch through 450 nm SiO_2 layer (*SiO_2 3:1* recipe, 2.5 mins)	$He/H_2/C_4F_8$ chemistry
6	Deep reactive ion etching of Si	Alcatel AMS 200 inductively coupled plasma etcher	Etch down Si surrounding samples, such that the sample is elevated ~50 μm relative to the substrate (*soi_acc++++* recipe, 15 mins)	SF_6 and C_4F_8 chemistry, in pulsed mode
7	Dicing of samples from wafer	Disco DAD 321 Silicon dicing saw	Cut into 5 x 12 mm sample chips	Cut half way through wafer (~260 μm), such that chips can be broken from the wafer at the end of processing
8	Oxygen plasma ashing of hardened photoresist surface layer	PVA TePla plasma system	Plasma treatment for 1 min	2.45 GHz, 600W, 400 sccm O_2
9	Wet etching of photoresist	Temperature controlled Ultrafab wetbench	Immerse wafer in solution for 10 minutes	Dow Microposit remover 1165 maintained at 70 °C
10	Buffered hydrofluoric acid (BHF) wet etching of SiO_2	Plade Six Sigma wet bench with recirculating bath	Immersion in BHF for 7 mins	Removal of SiO_2 under nanobeam and surrounding microdisk. 40% NH_4F and 49% HF in 7:1 volume ratio
11	Potassium hydroxide (KOH) wet etching of poly-Silicon and Si	Plade Six Sigma wet bench with recirculating bath	Immersion in bath for 45 mins	Removal of SiO_2 under nanobeam and surrounding microdisk. Structural release of sample, by etching poly-Silicon and Silicon under nanobeams and microdisks. 40% KOH at 45 °C

Step	**Process step description**	**Equipment**	**Operation**	**Notes**
12	Neutralization of Potassium salts with hydrochloric acid (HCl)	Plade Six Sigma wet bench with recirculating bath	Immersion in bath for 2 hours	37% HCl
13	Surface cleaning of Si_3N_4 and SiO_2 with hydrofluoric acid (HF)	Arias wet bench with Teflon petri dishes	Immersion in solution for 30 seconds (etch ~10 nm SiO_2 and ~2 nm Si_3N_4)	Process strips Silicon oxynitride from the nanobeam surface, minimizing material loss tangent. 5% HF diluted from 50% stock
14	Critical point drying (CPD) of the released sample	Automegasamdri 915B CO_2 CPD	Start process with sample immersed in VLSI grade EtOH (replaced by CO_2 in sealed, high pressure chamber)	CPD is necessary to avoid stiction

E Addendum: Chapter 4

E.1 Theoretical model for optomechanically induced quantum correlations

We consider here an optomechanical system consisting of an optical cavity, whose intracavity field is described by the amplitude $a(t)$, dispersively coupled to a mechanical oscillator of effective mass m, whose position is described by $x(t)$. Following standard linearization procedure [21], the fluctuations in either variable, denoted δa and δx respectively, satisfy the equations of motion,

$$\begin{aligned} \delta \dot{a} &= \left(i\Delta - \frac{\kappa}{2}\right)\delta a + iG\bar{a}\delta x + \sqrt{\eta_c \kappa}\delta a_{in} + \sqrt{(1-\eta_c)\kappa}\delta a_0 \\ m\left(\delta\ddot{x} + \Gamma_m \delta\dot{x} + \Omega_m^2 \delta x\right) &= \delta F_{\mathrm{th}} + \hbar G\bar{a}(\delta a + \delta a^\dagger). \end{aligned} \tag{E.1.1}$$

Here $\delta F_{\mathrm{th}}$is the thermal force noise, G is the cavity frequency pull parameter (the dispersive optomechanical coupling strength). The noise variables $\delta a_{\mathrm{in},0}$ describe the fluctuations in the cavity input at the coupling port and the port modelling internal losses. The cavity coupling efficiency $\eta_c = \kappa_{\mathrm{ex}}/\kappa$, describes the relative strength of the external coupling port. The steady state intracavity photon number, $n_c = \bar{a}^2$ is given by,

$$n_c = \frac{4\eta_c}{\kappa}\frac{P_{\mathrm{in}}/\hbar\omega_L}{1+4\Delta^2/\kappa^2},$$

where P_{in} is the injected probe power at optical frequency ω_L.

In the frequency domain, mechanical motion is described by susceptibility to the applied force,

$$x[\omega] = \chi_x[\Omega]F[\Omega] = \frac{1}{m(\Omega_m^2 - \Omega^2 - i\Omega\Gamma_m[\Omega])}F[\Omega], \tag{E.1.2}$$

where $\Gamma_m[\Omega]$ is frequency dependent damping rate generalizing the velocity-proportional dissipation model in the eq. (E.1.1). For the out-of-plane flexural modes of a Si_3N_4 nanos-

---

This appendix is adapted from [125]

tring $\Gamma_m[\Omega] \approx \Omega_m\Gamma_m/\Omega$ [159], where Γ_m without argument denotes the oscillator resonance linewidth.

For the following it is convenient to introduce the normalized position, $\delta z := \delta x/x_{\mathrm{zp}}$, the single- and multi- photon optomechanical coupling rates, $g_0 := Gx_{\mathrm{zp}}$ and $g := g_0\sqrt{n_c}$, and the single- and multi- photon cooperativities, $C_0 := 4g_0^2/\kappa\Gamma_m$ and $C := C_0 n_c$; $x_{\mathrm{zp}} = \sqrt{\hbar/2m\Omega_m}$ is the zero-point variance in the position of the mechanical oscillator.

In the experimentally relevant situation of resonant probing ($\Delta \approx 0$) and bad cavity limit ($\Omega_m \gg \kappa$), the equation of motion for the cavity field in eq. (E.1.1) assumes the form,

$$\delta a[\Omega] \approx \frac{2ig}{\kappa}\delta z[\Omega] + \frac{2}{\sqrt{\kappa}}\left(\sqrt{\eta_c}\delta a_{\mathrm{in}}[\Omega] + \sqrt{1-\eta_c}\delta a_0[\Omega]\right),$$

Using the input-output relation [7], $\delta a_{\mathrm{out}} = \delta a_{\mathrm{in}} - \sqrt{\eta_c\kappa}\delta a$, the transmitted fluctuations,

$$\delta a_{\mathrm{out}}[\Omega] = (1-2\eta_c)\delta a_{\mathrm{in}}[\Omega] - 2\sqrt{\eta_c(1-\eta_c)}\,\delta a_0[\Omega] - i\sqrt{\eta_c C\Gamma_m}\,\delta z[\Omega], \tag{E.1.3}$$

carries information regarding the total mechanical motion δz consisting of the thermal motion and the quantum back-action driven motion, i.e.,

$$\delta z[\Omega] = \delta z_{\mathrm{th}}[\Omega] + \delta z_{\mathrm{QBA}}[\Omega].$$

Here and henceforth, we define the quadratures of the optical field δa,

$$\delta q(t) = \frac{1}{\sqrt{2}}\left(\delta a(t) + \delta a^\dagger(t)\right), \qquad \delta p(t) = \frac{1}{i\sqrt{2}}\left(\delta a(t) - \delta a^\dagger(t)\right). \tag{E.1.4}$$

The back-action motion is given by,

$$\delta z_{\mathrm{BA}}[\Omega] = \sqrt{2C\Gamma_m}\chi_z[\Omega]\left(\sqrt{\eta_c}\,\delta q_{\mathrm{in}}[\Omega] + \sqrt{1-\eta_c}\,\delta q_0[\Omega]\right), \tag{E.1.5}$$

where $\delta q_{\mathrm{in},0}$ are the amplitude quadrature fluctuations from the two cavity input ports and $\chi_z[\Omega] = \hbar\chi_x[\Omega]/x_{\mathrm{zp}}^2$ is the oscillator susceptibility in new units,

$$\chi_z[\Omega] = \frac{2\Omega_m}{(\Omega_m^2 - \Omega^2 - i\Omega\Gamma_m[\Omega])} \underset{|\Omega-\Omega_m|\ll\Omega_m}{\approx} \frac{1}{(\Omega_m - \Omega) - i\Gamma_m/2}. \tag{E.1.6}$$

Note that in the main manuscript, we make use of $\chi = \chi_x$.
Inserting eq. (E.1.5) in eq. (E.1.3), the two quadratures of the cavity transmission are,

$$\begin{aligned}
\delta q_{\mathrm{out}}[\Omega] &= (1-2\eta_c)\delta q_{\mathrm{in}}[\Omega] - 2\sqrt{\eta_c(1-\eta_c)}\,\delta q_0[\Omega] \\
\delta p_{\mathrm{out}}[\Omega] &= (1-2\eta_c)\delta p_{\mathrm{in}}[\Omega] - 2\sqrt{\eta_c(1-\eta_c)}\,\delta p_0[\Omega] \\
&\quad - \sqrt{2\eta_c C\Gamma_m}\left[\delta z_{\mathrm{th}}[\Omega] + \sqrt{2C\Gamma_m}\chi_z[\Omega]\left(\sqrt{\eta_c}\,\delta q_{\mathrm{in}}[\Omega] + \sqrt{(1-\eta_c)}\delta q_0[\Omega]\right)\right].
\end{aligned} \tag{E.1.7}$$

For a general quadrature at angle θ, defined by,

$$\delta q^{\theta}_{\text{out}}[\Omega] := \delta q_{\text{out}}[\Omega]\cos\theta + \delta p_{\text{out}}[\Omega]\sin\theta, \tag{E.1.8}$$

it follows that,

$$\begin{aligned}\left\langle \delta q^{\theta}_{\text{out}}[\Omega]\delta q^{\theta}_{\text{out}}[-\Omega]\right\rangle = &\cos^2\theta\left\langle \delta q_{\text{out}}[\Omega]\delta q_{\text{out}}[-\Omega]\right\rangle \\ &+\sin^2\theta\left\langle \delta p_{\text{out}}[\Omega]\delta p_{\text{out}}[-\Omega]\right\rangle \\ &+\sin(2\theta)\,\text{Re}\left\langle \delta q_{\text{out}}[\Omega]\delta p_{\text{out}}[-\Omega]\right\rangle .\end{aligned} \tag{E.1.9}$$

The homodyne photocurrent spectrum is related to this correlator via,

$$\begin{aligned}&\bar{S}^{\theta}_{II}[\Omega]\cdot 2\pi\delta[0] \propto \bar{S}^{\theta,\text{out}}_{qq}[\Omega]\cdot 2\pi\delta[0] = \frac{1}{2}\left\langle \{\delta q^{\theta}_{\text{out}}[\Omega],\delta q^{\theta}_{\text{out}}[-\Omega]\}\right\rangle, \\ \text{i.e.,}\quad &\bar{S}^{\theta}_{II}[\Omega] = \cos^2\theta\,\bar{S}^{\text{out}}_{qq}[\Omega] + \sin^2\theta\,\bar{S}^{\text{out}}_{pp}[\Omega] + \sin(2\theta)\,\bar{S}^{\text{out}}_{pq}[\Omega].\end{aligned} \tag{E.1.10}$$

The relevant spectra of the output field quadratures is explicitly given by,

$$\begin{aligned}\bar{S}^{\text{out}}_{qq}[\Omega] &= \tfrac{1}{2} \\ \bar{S}^{\text{out}}_{pp}[\Omega] &= \tfrac{1}{2} + 2\eta_c C\Gamma_m\left(\bar{S}^{\text{th}}_{zz}[\Omega] + \bar{S}^{\text{BA}}_{zz}[\Omega]\right) \\ \bar{S}^{\text{out}}_{pq}[\Omega] &= \eta_c C\Gamma_m \text{Re}\,\chi_z[\Omega].\end{aligned}$$

Inserting these in eq. (E.1.10), we arrive at the homodyne photocurrent spectrum (normalized to electronic shot noise and omitting the negligible contribution from detector electronic noise),

$$\bar{S}^{\theta}_{II}[\Omega] = 1 + 4\eta C\Gamma_m\left(\bar{S}_{zz}[\Omega]\sin^2\theta + \frac{1}{2}\sin(2\theta)\,\text{Re}\,\chi_z[\Omega]\right). \tag{E.1.11}$$

Note that henceforth (as in the main manuscript) photocurrent spectra are implicitly normalized to shot noise. Using the fluctuation-dissipation theorem [184] to relate the thermal and back-action force noise to mean phonon occupations n_{th} and n_{BA} respectively, the spectral density of the total motion,

$$\bar{S}_{zz}[\Omega] = \left|\chi_z[\Omega]\right|^2\left(\Gamma_m[\Omega]n_{\text{th}} + \Gamma_m n_{\text{QBA}}\right), \tag{E.1.12}$$

where, $n_{\text{th}} = k_B T/\hbar\Omega_m \gg 1$ is the average thermal occupation, and, $n_{\text{QBA}} = C = C_0 n_c$ is the average occupation due to (quantum) back-action arising from vacuum fluctuations in the input amplitude quadrature.

E.1.1 Analytical expression for asymmetry ratio R, and visibility ΔR

In the regime when $n_{\text{QBA}} \ll n_{\text{th}}$ the correlation term in the eq. (E.1.11) is small compare to the shot noise + thermomechanical noise $4\eta C\Gamma_m\bar{S}_{zz}$. Therefore, in order to visualize the correlations we consider $R(\theta,\delta)$, the ratio of the homodyne spectral densities symmetrically detuned to the high and low frequencies from the mechanical resonance

$$R(\theta,\delta) \equiv \frac{\bar{S}^{\theta}_{II}[\Omega_m+\delta]}{\bar{S}^{\theta}_{II}[\Omega_m-\delta]}. \tag{E.1.13}$$

In the limit of $\delta \ll \Omega_m$ the thermomechanical motion spectrum $\bar{S}_{zz}[\Omega]$ is symmetric about Ω_m and $\mathrm{Re}\,\chi[\Omega]$ is antisymmetric, so $R(\theta,\delta)$ only deviates from 1 due to the correlation term

$$R(\theta,\delta)|_{\delta\ll\Omega_m} \approx 1+\frac{4\eta C\Gamma_m \sin(2\theta)}{1+4\eta C\Gamma_m \bar{S}_{zz}[\Omega_m+\delta]\sin^2\theta}\mathrm{Re}\,\chi_z[\Omega_m+\delta]. \tag{E.1.14}$$

Maximization/minimization of R given by the eq. (E.1.14) over θ yields

$$\Delta R(\delta) \equiv \max_{\theta} R(\theta,\delta) - \min_{\theta} R(\theta,\delta) = 2\frac{4\eta C\Gamma_m \mathrm{Re}\,\chi[\Omega_m+\delta]}{\sqrt{1+4\eta C\Gamma_m \bar{S}_{zz}[\Omega_m+\delta]}} \approx 4\frac{\eta C/n_{\mathrm{th}}}{\sqrt{(\delta/2\Gamma_m n_{\mathrm{th}})^2+\eta C/n_{\mathrm{th}}}}, \tag{E.1.15}$$

$$\Delta R(\delta) = 4\sqrt{\frac{\eta C}{n_{\mathrm{th}}}} \text{ if } \Gamma_m \ll \delta \ll 2\Gamma_m\sqrt{\eta C n_{\mathrm{th}}}. \tag{E.1.16}$$

Considering broad frequency ranges, however, one has to account for the deviation of χ_x from a single-pole Lorenzian and for the thermal force noise being not perfectly white. Up to the 1-st order in $(\bar{S}_{zz}[\Omega_m+\delta]-\bar{S}_{zz}[\Omega_m-\delta])$

$$R(\theta,\delta) \approx 1+\frac{4\eta C\Gamma_m}{1+4\eta C\Gamma_m \bar{S}_{zz}[\Omega_m+\delta]\sin^2\theta}\left(\sin(2\theta)\mathrm{Re}\,\chi_z[\Omega_m+\delta]+\frac{1}{2}\sin^2\theta(\bar{S}_{zz}[\Omega_m+\delta]-\bar{S}_{zz}[\Omega_m-\delta])\right). \tag{E.1.17}$$

In the approximation of eq. (E.1.14) $R_\theta - 1$ is antisymmetric in the quadrature angle θ, with magnitude being proportional to $\sqrt{\eta\, n_{\mathrm{QBA}}/n_{\mathrm{th}}}$. For δ further from the mechanical resonance the antisymmetric part of $R_\theta - 1$ still has the same meaning, but it becomes superimposed with a symmetric in θ classical contribution.

E.1.2 Effect of excess laser noise and detuning

In addition to vacuum fluctuations in the input amplitude quadrature, classical fluctuations in the amplitude quadrature can lead to phase-amplitude correlations in the cavity transmission. Additionally, detuning deviations causing a finite Δ/κ can transduce classical phase fluctuations in the input to excess phase-amplitude correlations in the output.

In order to analyse the two possible classical contributions on the same footing, we consider the quadratures of the cavity transmission, $\delta q_{\mathrm{out}}, \delta p_{\mathrm{out}}$ for the case of a finite detuning $|\Delta| \ll \kappa$.

In this regime, eq. (E.1.7) contains corrections of order Δ/κ, viz.,

$$\begin{aligned}
\delta q_{\text{out}}[\Omega] &= (1-2\eta_c)\delta q_{\text{in}}[\Omega] - 2\sqrt{\eta_c(1-\eta_c)}\delta q_0[\Omega] \\
&\quad + \frac{2\Delta}{\kappa}\left(\sqrt{2\eta_c C\Gamma_m}\delta z[\Omega] + 2\eta_c\delta p_{\text{in}}[\Omega] + 2\sqrt{\eta_c(1-\eta_c)}\delta p_0[\Omega]\right) \\
\delta p_{\text{out}}[\Omega] &= (1-2\eta_c)\delta p_{\text{in}}[\Omega] - 2\sqrt{\eta_c(1-\eta_c)}\delta p_0[\Omega] - \sqrt{2\eta_c C\Gamma_m}\delta z[\Omega] \\
&\quad - \frac{2\Delta}{\kappa}\left(2\eta_c\delta q_{\text{in}}[\Omega] + 2\sqrt{\eta_c(1-\eta_c)}\delta q_0[\Omega]\right),
\end{aligned} \tag{E.1.18}$$

where the total motion $\delta z = \delta z_{\text{th}} + \delta z_{\text{BA}}$, with,

$$\begin{aligned}
\delta z_{\text{BA}}[\Omega] = \sqrt{2C\Gamma_m}\Bigg[&\left(\sqrt{\eta_c}\delta q_{\text{in}}[\Omega] + \sqrt{1-\eta_c}\delta q_0[\Omega]\right) \\
&+4i\frac{\Omega\Delta}{\kappa^2}\left(\sqrt{\eta_c}\delta p_{\text{in}}[\Omega] + \sqrt{1-\eta_c}\delta p_0[\Omega]\right)\Bigg],
\end{aligned} \tag{E.1.19}$$

the motion induced by the quantum and the classical fluctuations in the input laser field. Excess noise in the input amplitude and phase quadratures is modelled by white noise with intensity C_{qq} and C_{pp} respectively, so that,

$$\bar{S}^{\text{in}}_{qq}[\Omega] = \frac{1}{2} + C_{qq}, \qquad \bar{S}^{\text{in}}_{pp}[\Omega] = \frac{1}{2} + C_{pp}. \tag{E.1.20}$$

Using eqs. (E.1.18) and (E.1.19) in the definition of the homodyne spectrum (eq. (E.1.10)) to leading order in Δ/κ, the shot-noise normalized balanced homodyne spectrum is:

$$\begin{aligned}
\bar{S}^{\theta}_{II}[\Omega] \approx 1 + 4\eta C\Gamma_m \Bigg[&\left(\bar{S}^{\text{th+QBA}}_{zz}[\Omega] + \bar{S}^{\text{CBA,q}}_{zz}[\Omega] + \bar{S}^{\text{CBA,p}}_{zz}[\Omega]\right)\sin(\theta')^2 + \frac{1}{2}\sin(2\theta')\text{Re}\,\chi_z[\Omega] + \\
&+\sin(2\theta')\sqrt{\eta_c}(1-2\eta_c)C_{qq}\text{Re}\,\chi_z[\Omega] + 2\sin(\theta')^2\sqrt{\eta_c}(1-2\eta_c)\frac{4\Omega_m\Delta}{\kappa^2}C_{pp}\text{Im}\,\chi_z[\Omega]\Bigg],
\end{aligned} \tag{E.1.21}$$

where $\theta' \approx \theta - 4\Delta/\kappa$ is the quadrature angle rotated by the cavity. The effect of excess noise is two-fold. Firstly, classical amplitude (phase) noise C_{qq} (C_{pp}) causes additional classical back-action motion $\bar{S}^{\text{CBA,q}}_{xx}$ ($\bar{S}^{\text{CBA,p}}_{xx}$), leading to excess back-action occupations,

$$n_{\text{CBA,q}} = C_0 n_c C_{qq}, \qquad n_{\text{CBA,p}} = C_0 n_c\left(\frac{4\Omega_m\Delta}{\kappa^2}\right)^2 C_{pp}. \tag{E.1.22}$$

Secondly, classical amplitude noise, and phase noise transduced via finite detuning, establish excess correlations, as can be seen from the last two terms in the eq. (E.1.21). It is important to note that the contribution of excess phase noise C_{pp} to the measured homodyne signal is effectively suppressed for the current experimental parameters since $\Delta\cdot\Omega_m/\kappa^2 = \mathcal{O}(10^{-4})$. Finally, when laser noise is insignificant, the role of a residual detuning from the cavity, i.e. $\Delta \neq 0$, is to rotate the detected quadrature by an angle $\arctan(4\Delta/\kappa)$, without leading to any artificial asymmetry.

Classical amplitude noise leads to excess correlations, which results in a larger anti-symmetry in R. The size of the anti-symmetry is quantified by ΔR. Following the definition in eq. (E.1.15), and using the expression for the homodyne spectrum in the presence of laser noise (eq. (E.1.21)), it can be shown that,

$$\Delta R(\delta) = 4\sqrt{\frac{\eta C}{n_{\mathrm{th}}}(1+2C_{qq})} \text{ for } \Gamma_m \ll \delta \ll 2\Gamma_m\sqrt{\eta C n_{\mathrm{th}}}, \tag{E.1.23}$$

and for an overcoupled cavity ($\eta_c \approx 1$). Thus, the magnitude of the anti-symmetric feature in R (shown in fig. 4 in the main manuscript) is increased by the average thermal photon occupation of the amplitude quadrature.

In addition, the overall scaling of ΔR with probe power is qualitatively different. In order to see this, we consider an arrangement (as in the experiment) where the laser field a_{las} is attenuated by a variable beam-splitter of transmissivity η_{bs}, to derive the field that excites the optical cavity, a_{in}. Thus,

$$\delta a_{\mathrm{in}}[\Omega] = \sqrt{\eta_{\mathrm{bs}}}\,\delta a_{\mathrm{las}}[\Omega] + \sqrt{1-\eta_{\mathrm{bs}}}\,\delta a_{\mathrm{bs}}, \tag{E.1.24}$$

where, δa_{bs}, is the vacuum noise from the remaining open input port of the beam-splitter. This equation, together with the definition of C_{qq} (eq. (E.1.20)), allows us to relate the amplitude quadrature excess noise in the cavity input field to that of the laser, viz.

$$C_{qq}^{\mathrm{in}} = \eta_{\mathrm{bs}} C_{qq}^{\mathrm{las}} = \frac{P_{\mathrm{in}}}{P_{\mathrm{las}}} C_{qq}^{\mathrm{las}}, \tag{E.1.25}$$

$P_{\mathrm{in}}(P_{\mathrm{las}})$ is the mean optical power of the input (laser) field. Thus, when the cavity input power (P_{in}) is varied by attenuating a laser operating at a fixed output power (P_{las}), the amplitude noise at the cavity input scales proportional to the power. Inserting this in eq. (E.1.23) shows that in this case, $\Delta R \propto P_{\mathrm{in}}$, when $C_{qq}^{\mathrm{in}} \gg \frac{1}{2}$.

E.1.3 Effect of homodyne phase fluctuations

The measured dependence $R(\theta)$ for $\delta/2\pi = 21$ kHz, shown at the fig. 3 of the main text, exhibit sharp variation with θ around amplitude quadrature, with maxima and minima of the high-power measurements being as close as 1-2° to $\theta = 0$. Correspondingly, in order to be able to resolve these features ensuring low residual fluctuations of the homodyne angle is essential.

In order to see the effect of homodyne angle instability on $R(\theta)$, consider the homodyne detection with θ fluctuating as $\theta(t) = \theta_0 + \delta\theta(t)$

$$\delta q^{\theta}(t) = \delta q(t)\cos(\theta(t)) + \delta p(t)\sin(\theta(t)) \approx \delta q^{\theta_0}(t) + \delta\theta(t)\delta q^{\theta_0+\pi/2}(t), \tag{E.1.26}$$

where $\delta q^{\theta_0}(t)$ is the signal of a perfectly stable homodyne at the angle θ_0 and $\delta q^{\theta_0+\pi/2}(t)$ is such signal at the orthogonal quadrature. The signal spectral density

$$\bar{S}_{II}^{\theta}[\Omega] = \bar{S}_{II}^{\theta_0}[\Omega] + \bar{S}_{II}^{\theta_0+\pi/2}[\Omega] * S_{\delta\theta}[\Omega], \tag{E.1.27}$$

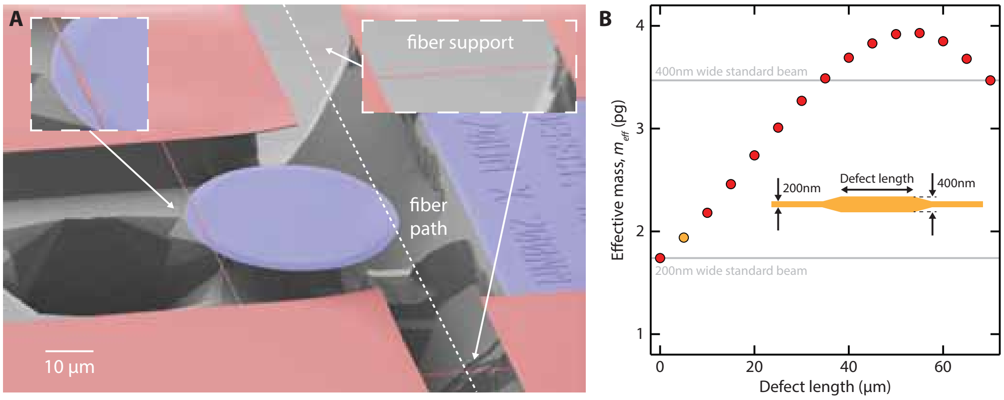

Figure E.1 – (A) False colored scanning electron micrograph of the device design used in this work. Si_3N_4 is indicated in red and SiO_2 in blue. (B) Finite element calculation of effective mass for defect beam design, as a function of the defect length. The data point in orange indicates the defect length (5 μm) of the experimental device; see text for details.

where $S_{\delta\theta}[\Omega]$ is the homodyne angle fluctuations spectrum and $*$ denotes convolution

$$\bar{S}_{II}^{\theta_0+\pi/2}[\Omega] * S_{\delta\theta}[\Omega] = \frac{1}{2\pi}\int d\Omega' \bar{S}_{II}^{\theta_0+\pi/2}[\Omega-\Omega'] S_{\delta\theta}[\Omega']. \tag{E.1.28}$$

In the presented experiment the homodyne angle fluctuations were mainly confined to low frequency (suppressed withing the bandwith of 300 Hz by feedback loop), so $S_{\delta\theta}[\Omega']$ can be treated as a delta-function

$$\bar{S}_{II}^{\theta_0+\pi/2}[\Omega] * S_{\delta\theta}[\Omega] \approx \langle\delta\theta^2\rangle \bar{S}_{II}^{\theta_0+\pi/2}[\Omega]. \tag{E.1.29}$$

Neglecting terms $\langle\delta\theta^2\rangle$ compare to 1 the eq. (E.1.11) is modified as

$$\bar{S}_{II}^{\theta}[\Omega] = 1 + 4\eta C\Gamma_m \left(\bar{S}_{zz}[\Omega](\sin^2\theta + \langle\delta\theta^2\rangle\cos^2\theta) + \frac{1}{2}\sin(2\theta)\,\mathrm{Re}\,\chi_z[\Omega]\right). \tag{E.1.30}$$

Correspondingly, due to the impossibility to completely suppress thermal noise on amplitude quadrature, ΔR is diminished by the fraction $\langle\delta\theta^2\rangle/(\theta_{opt})^2$, where $\theta_{opt} \ll 1$ is the angle at which R reaches maximum. For the bottom panel of the manuscript fig. 3 $\sqrt{\langle\delta\theta^2\rangle} \approx 0.4°$, $\theta_{opt} \approx 1.2°$, resulting in the homodyne instability effect on R as $\langle\delta\theta^2\rangle/(\theta_{opt})^2 < 10\%$. Larger δ or smaller input power result in larger θ_{opt} and improve this constraint further.

E.2 Experimental details

E.2.1 Experimental platform

The device measured in this work consists of an SiO_2 whispering gallery mode microdisk with a high-stress Si_3N_4 nanobeam centered in the near-field of the microdisk (see chapters 2 and 3. For the devices used here both the mechanical and optical resonator shapes are defined by electron-beam lithography (appendix D). The bare microdisks exhibit very high finesse of $\sim 10^5$ – nearly an order of magnitude higher than microdisks produced by photolithography. However, in this implementation we do not access this high finesse regime when the nanobeam is placed in the near-field of the disk. We attribute this to the 80 nm thickness of the Si_3N_4, which is conjectured to lead to excessive scattering and/or waveguiding. The microdisk is $40\,\mu$m in diameter, $\sim$ 350 nm thick, and has a wedged sidewall of $\sim 10^{o}$ (see section 3.3.1 and appendix C).

In this rendition of the device the nanobeam has been designed with a central defect that allows for increased overlap with the optical mode while minimizing the effective mass ($m_{\text{eff}} \approx$ 1.94 pg). The optical mode of the microdisk samples approximately $9\,\mu$m of the beam at its center (see section 2.2.6), however we utilize a defect that is tapered within the sampling region as this resulted in lower optical loss and overall higher C_0 than longer defects. This effect may be attributed to the reduced scattering loss on account of a softer dielectric boundary seen by the optical mode. Figure E.1B shows the defect geometry and the effect of defect length on the effective mass of the fundamental out-of-plane mode. The beam is 70 μm long and consists of a narrow (200 nm) beam with a wider (400 nm) rectangular defect at the center which tapers linearly into the thin beam at an angle of $\sim 12^{o}$. The defect length of the device used in this paper is 5 μm, which exhibits an effective mass only 11% larger than that of a standard 200 nm wide beam.

As shown in Figure E.1A, two short beams of Si_3N_4 with dimensions $20 \times 0.2 \times 0.08\,\mu$m are also placed across the channel on either side of the microdisk to support the tapered optical fiber and increase the overall mechanical stability of the experiment.

E.2.2 Measurement setup

The essential layout of the experiment is shown in fig. E.2. The sample is placed in a high vacuum chamber, at a pressure of $\sim 10^{-7}$ mbar, and room temperature. Light is coupled in and out of the microdisk cavity using a tapered optical fiber, the position of which is adjusted using piezo actuators to achieve critical coupling into the cavity (i.e. $\eta_c \approx 0.5$).

Two lasers are employed in the experiment – a TiSa laser (MSquared Solstis) with wavelength centered around 780 nm which is the *meter* beam, and an auxiliary 850 nm external cavity diode laser (NewFocus Velocity) which is the *feedback* beam. Both beams are combined before the cavity and separated after it using dichroic beamsplitters. The feedback beam is detected on an avalanche photodetector (APD), while the meter beam is fed into a length- and power-balanced homodyne detector. A small portion of the meter beam – stray reflection from the dichroic beam-splitter – is directed onto an APD.

Both lasers are actively locked to their independent cavity resonances using the APD signal. For the meter beam, a lock on cavity resonance ($|\Delta| \lesssim 0.1 \cdot \kappa$) is implemented using the Pound-Drever-Hall technique. For the feedback beam, a part of the APD signal is used directly to implement a lock red-detuned from cavity resonance.

The other part of the feedback beam APD signal is used to perform moderate feedback cooling of the mechanical oscillator. Specifically, the photosignal is amplified, low-pass filtered and phase-shifted, before using it to amplitude modulate the same laser. As in conventional cold damping [158], the phase-shift in the feedback loop is adjusted to synthesise an out-of-phase radiation pressure force that damps the mechanical oscillator. At the nominal feedback laser power of $5\,\mu$W, a damping rate of 1 kHz is realized; the associated increase in the mechanical decoherence rate due to injected imprecision noise was measured to be below 5%.

The path length difference of the homodyne interferometer is actively stabilized using a two-branch piezo translation system. Demodulation of the homodyne signal at PDH frequency also produced interference fringes suitable for locking the homodyne angle near the amplitude quadrature (i.e. $\theta = 0$). The residual homodyne angle fluctuations could be estimated $\theta_{\mathrm{RMS}} \lesssim 1^{\mathrm{o}} \approx 0.017\,\mathrm{rad}$, inferred from the suppression of thermomechanical signal-to-noise ratio on amplitude quadrature of $\approx 10^{-4}$ compared to the phase quadrature. An offset DC voltage is applied to the homodyne error signal for deterministic choice of detection quadrature.

Since the feedback cooling exclusively relies on the auxiliary diode laser, the homodyne measurements on the 780 nm meter beam are completely out-of-loop and does not contain electronically-induced correlations.

E.2.3 Data analysis

In each experimental run, corresponding to the data shown in one panel of Figure 3 of the main text, the meter laser is locked to cavity resonance at fixed input power, and a series of homodyne photocurrent spectra are taken at various settings of the homodyne angle θ. From independently measured mechanical and optical parameters of the sample, together with the known input power, the homodyne detection efficiency is inferred in each run by the thermomechanical signal-to-shot-noise ratio (shot noise level was measured by blocking the signal interferometer arm). To account for a small quadrature rotation by the cavity the nominal $\theta = 0$ quadrature was inferred from the minimum in the transduction of thermomechanical noise.

In order to experimentally access the asymmetry ration R_θ discussed in the main text, R_θ is

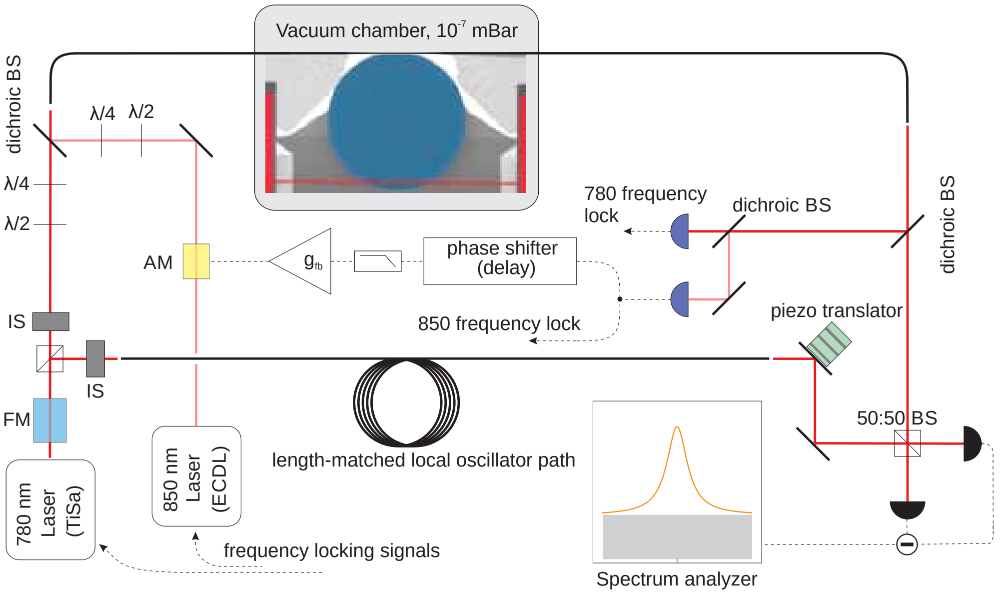

Figure E.2 – Schematic of the experimental setup. Abbreviations: AM – amplitude modulator, FM – frequency modulator, BS – beam splitter, IS – intensity stabilizer.

estimated from an integral over a finite bandwidth $\Delta\Omega$, i.e.,

$$R_\theta = \int_{\Omega_m+\delta-\Delta\Omega/2}^{\Omega_m+\delta+\Delta\Omega/2} \bar{S}_{II}^{\theta}[\Omega]\,d\Omega \Big/ \int_{\Omega_m-\delta-\Delta\Omega/2}^{\Omega_m-\delta+\Delta\Omega/2} \bar{S}_{II}^{\theta}[\Omega]\,d\Omega\,. \tag{E.2.1}$$

Theoretically, there is some freedom in the choice of the detuning offset δ and integration bandwidth $\Delta\Omega$, since the relative contribution of the quantum interference term to the detected signal is maximum within a broad range of detunings $\Gamma_{\text{eff}} \ll \delta \ll 2\Gamma_m\sqrt{\eta C\, n_{\text{th}}}$; here $\Gamma_{\text{eff}} \approx 2\pi\cdot 1\,\text{kHz}$ is the effective damping rate due to feedback. For typical experimental conditions in this work $1\ \text{kHz} \ll \delta/2\pi \ll 500\ \text{kHz}$. Figure E.3 shows the ratio R_θ extracted for various choices of the detuning offset and integration bandwidth. Figure 3 of the main manuscript depicts data extracted for the choice $\delta = 2\pi\cdot 56\,\text{kHz}$ and $\Delta\Omega = 2\pi\cdot 20\,\text{kHz}$.

In the demonstration of external force estimation in the main manuscript, the signal-to-noise ratio for the applied force δF_{ext} is defined by,

$$\text{SN}_{\pm}^{\theta} \equiv \bar{S}_{II}^{\theta}[\Omega_{\text{F}} \pm \delta] \big/ \bar{S}_{II}[\Omega_{\text{F}} \pm \delta]|_{\delta F_{\text{ext}}=0}\,; \tag{E.2.2}$$

i.e., the signal is the photocurrent noise at the frequencies where the force is applied ($\Omega_{\text{F}} \pm \delta$), while the noise is the photocurrent noise at the same frequencies without the force. Practically, we estimate both contributions from finite bandwidth integrals over the relevant part of the photocurrent spectrum: for the signal, the photocurrent signal is integrated over a finite bandwidth $\Delta\Omega_{\text{F}}$ around the applied force, while to estimate the noise, we choose to take averages of the photocurrent spectrum over finite bandwidth $\Delta\Omega_{\text{N}}$, on either side of the

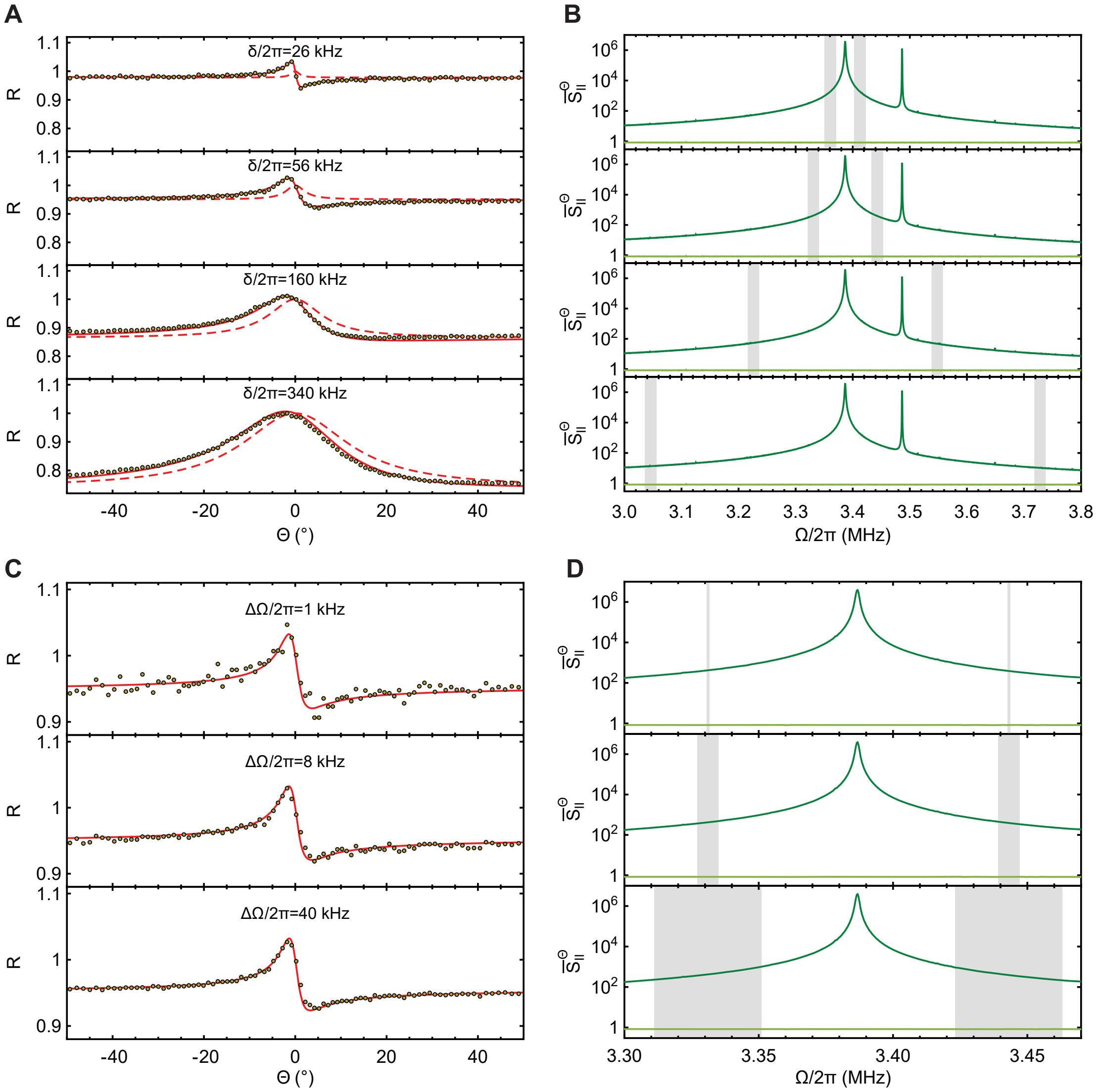

Figure E.3 – (A,C) Illustration of the variation of the experimental asymmetry ratio $R(\theta)$ for different offsets δ at fixed integration bandwidth $\Delta\Omega\pi = 20$ kHz (A) and for different integration bandwidths $\Delta\Omega$ at fixed offset $\delta/2\pi = 56$ kHz (C). Solid and dashed red curves show theoretical predictions accounting and not accounting for the quantum back-action-imprecision correlations. (B,D) Plots show the integration bands used for calculation of the $R(\theta)$ on the left (shaded gray regions). Dark green is a mechanical spectrum at an intermediate homodyne quadrature and light green is the local oscillator trace showing the shot noise level. The data was taken at $P_{\text{in}} = 200$ μW.

applied force, without turning off the force. Specifically,

$$\mathrm{SN}_{\pm}^{\theta} = \int_{\Omega_{\mathrm{F}}\pm\delta-\Delta\Omega_{\mathrm{F}}/2}^{\Omega_{\mathrm{F}}\pm\delta+\Delta\Omega_{\mathrm{F}}/2} \bar{S}_{II}^{\theta}[\Omega]\,d\Omega \Bigg/ \frac{1}{2}\left(\int_{\Omega_{\mathrm{F}}\pm\delta+\delta\Omega_{\mathrm{N}}-\Delta\Omega_{\mathrm{N}}/2}^{\Omega_{\mathrm{F}}\pm\delta+\delta\Omega_{\mathrm{N}}+\Delta\Omega_{\mathrm{N}}/2} \bar{S}_{II}^{\theta}[\Omega]\,d\Omega + \int_{\Omega_{\mathrm{F}}\pm\delta-\delta\Omega_{\mathrm{N}}-\Delta\Omega_{\mathrm{N}}/2}^{\Omega_{\mathrm{F}}\pm\delta-\delta\Omega_{\mathrm{N}}+\Delta\Omega_{\mathrm{N}}/2} \bar{S}_{II}^{\theta}[\Omega]\,d\Omega\right). \tag{E.2.3}$$

The integration bands used for the Figure 5 in the main text are shown at the Figure E.4.

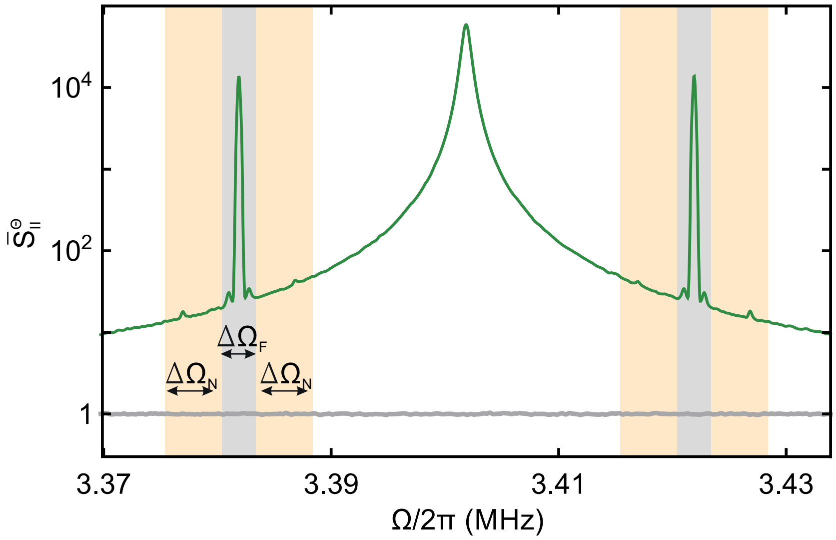

Figure E.4 – Integration bands used in the definition of the signal-to-noise ratio SN^{θ} in the main manuscript. The signal bands are shaded gray ($\Delta\Omega_F = 3\,\mathrm{kHz}$), the bands for noise estimation are shaded orange ($\Delta\Omega_N = 5\,\mathrm{kHz}$).

E.2.4 Role of broadband mechanical susceptibility

Within the theoretical description,adopted in the main text, that relies on single-pole Lorenzian mechanical susceptibility and white thermal noise, the variation of the asymmetry ratio, $\Delta R = \max_\theta R_\theta - \min_\theta R_\theta$, can be directly related to the $n_{\mathrm{QBA}}/n_{\mathrm{th}}$ as given by the eq. (E.1.16). In the present experiment, however, back-action-imprecision correlations are produced in the broad span of frequencies on the order of hundreds of kHz, which makes eq. (E.1.16) not directly applicable at large detunings δ. As is illustrated by the fig. E.3A, at large δ the experimental $R_\theta - 1$ shows deviations from the antisymmetric shape given by eq. (E.1.14) and should be described by the eq. (E.1.17) containing a contribution symmetric in θ. In order to make the data analysis in the main text more transparent we choose $\delta = 21$ kHz, which is small enough so that eq. (E.1.16) holds with sufficient accuracy.

E.2.5 Laser noise

A MSquared Solstis Ti:Sa laser was used for the measurements presented in the manuscript. The amplitude noise of the laser was characterized via direct photo-detection. In a frequency band 3 MHz wide around the mechanical frequency, $\Omega_m = 2\pi\cdot 3.4\,\mathrm{MHz}$ at the highest employed power 100 μW the classical amplitude noise level was < 1% of the shot noise (see Figure E.5B). This means that, $C_{qq} < 5\times 10^{-3}$, implying a negligible contribution to excess classical correlations and a negligible fraction of classical back-action motion, $n_{\mathrm{CBA,q}} < 0.005\cdot n_{\mathrm{QBA}}$, compared to quantum back-action.

Laser phase noise was upper-bounded using a self-heterodyne measurement [185] with a 400 m fiber delay line. The self-heterodyne signal can described by the formula (after shifting the

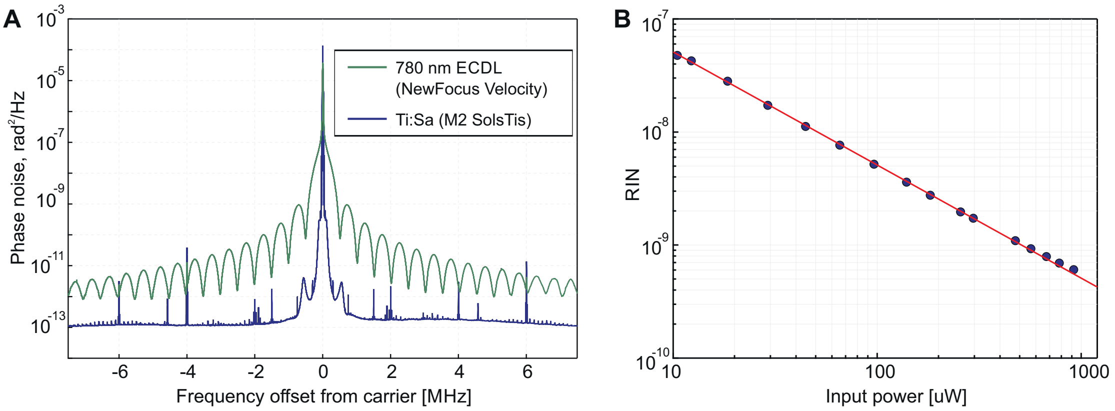

Figure E.5 – (A) Phase noise about the carrier, measured using an imbalanced Mach-Zehnder interferometer (self-heterodyning). Blue color shows the measurement for the employed Ti:Sa, whose phase noise contribution can be estimated to be $\leq 2\cdot 10^{-13}\,\mathrm{rad}^2/\mathrm{Hz}$ around the mechanical frequency $\approx 3.4\,\mathrm{MHz}$, corresponding to frequency noise $\leq 2\mathrm{Hz}^2/\mathrm{Hz}$. The noise peaks at ca. 250 kHz are attributed to the laser's relaxation oscillation frequency. Green shows a commercial diode laser (NewFocus Velocity) for comparison, exhibiting at least 20 dB times more phase noise at similar frequencies. The noise measurement for the TiSa laser clearly indicates absence of the $\sin^2(\Omega\tau_0)$ pattern, visible in the measurement for the diode laser and expected for the classical laser noise interference, showing that the phase noise of the TiSa lasers was not observed. (B) Amplitude noise of the Ti:Sa characterised as relative intensity noise integrated over a 3 MHz bandwidth around the mechanical frequency for the used Ti:Sa laser. The solid line shows fit with $1/P$ dependence, characteristic of shot noise limited behavior.

beat-note to zero frequency)

$$\bar{S}_{II}[\Omega] \propto \frac{\pi}{2}\delta[\Omega] + \sin^2\left(\frac{\Omega\tau_0}{2}\right)\bar{S}_{\phi\phi}[\Omega], \tag{E.2.4}$$

where τ_0 is the delay and $\bar{S}_{\phi\phi}[\Omega]$ is the laser phase noise spectral density. The measured signal for the laser is shown at the Figure E.5A, where the vertical scale is calibrated using the known mean photon flux in the beat note carrier. For the Ti:Sa laser (the blue curve in Figure E.5A) the absence of the characteristic $\sin^2(\Omega\tau_0)$ interference pattern suggests that laser phase noise is below the sensitivity of the measurement. Although the laser is expected to be quantum-noise-limited at frequencies well above the relaxation oscillation frequency ($\approx 400\,\mathrm{kHz}$), our measurements can only provide a conservative upper-bound for the frequency noise to be at the level of $2\,\mathrm{Hz}^2/\mathrm{Hz}$ (in comparison, frequency noise of a commercial external cavity diode laser, also shown in Figure E.5A, is 20 dB larger). This upper bound on the excess phase noise, together with large optical linewidth (κ) strongly suppresses the influence of C_{pp} and leads to an estimated back-action motion that is below a factor 0.0025 compared to the quantum mechanical contribution. Intrinsic cavity frequency noise, for example from thermoelastic [186] or thermorefractive [187] processes, can also lead to a finite value of C_{pp}. In the current experiments, broadband measurements of cavity transmission on phase quadrature suggests a conservative upper bound of $C_{pp} < 10$ at frequencies around Ω_m. Using a length-balanced homodyne interferometer for detection, classical phase noise in the measurement imprecision could also be bounded by 0.1%.

E.3 Quantum-enhanced force sensitivity

Consider estimation of an arbitrary force, δF, acting on the mechanical oscillator. The homodyne photocurrent spectrum carries information about the force eq. (E.1.10), viz.

$$\bar{S}^{\theta}_{II}[\Omega] = 1 + 4\eta C\Gamma_m \left[\left|\chi_x[\Omega]\right|^2 \left(\bar{S}_{FF}[\Omega] + \bar{S}^{\mathrm{QBA}}_{FF}[\Omega]\right)\sin^2\theta + \frac{1}{2}\sin(2\theta)\mathrm{Re}\chi_x[\Omega]\right]. \tag{E.3.1}$$

The spectrum of the applied force $\bar{S}_{FF}[\Omega]$ can be estimated from the photocurrent spectrum via,

$$\begin{aligned}\bar{S}^{\mathrm{est},\theta}_{FF}[\Omega] &:= \frac{\bar{S}^{\theta}_{II}[\Omega]}{4\eta C\Gamma_m\left|\chi_x[\Omega]\right|^2\sin^2\theta}\\ &= \bar{S}_{FF}[\Omega] + \bar{S}^{\mathrm{QBA}}_{FF}[\Omega] + \underbrace{\frac{1}{4\eta C\Gamma_m\left|\chi_x[\Omega]\right|^2\sin^2\theta}}_{\bar{S}^{\mathrm{imp},\theta}_{FF}} + \cot\theta\,\frac{\mathrm{Re}\,\chi_x[\Omega]}{\left|\chi_x[\Omega]\right|^2}.\end{aligned} \tag{E.3.2}$$

Here, the first term represent the spectral density to be estimated. The second term, positive at all frequencies, is the contamination in the measurement record due to quantum back-action. The third, also positive term, is the imprecision due to shot-noise in the detection. The last term is due to quantum correlations between the back-action and imprecision in homodyne measurement record that can be negative at some frequencies, providing for reduced uncertainty in the ability to estimate the force.

Note that precisely on resonance ($\Omega = \Omega_m$), and/or, for phase quadrature homodyne measurement ($\theta = \pi/2$), correlations do not contribute to the estimator; so any reduction in uncertainty can only be expected away from resonance for quadrature-detuned homodyne measurement.

For a fixed probe strength, i.e. fixed cooperativity C, there exists a frequency dependent homodyne phase at which the correlation and the imprecision $\bar{S}^{\mathrm{imp},\theta}_{FF}$ achieve an optimal trade-off. This optimal angle $\theta_{\mathrm{opt}}[\Omega]$ is determined by,

$$\cot\theta_{\mathrm{opt}}[\Omega] = -2\eta C\Gamma_m\mathrm{Re}\,\chi_x[\Omega] = 4\eta C\frac{\Omega_m\Gamma_m(\Omega^2-\Omega_m^2)}{(\Omega^2-\Omega_m^2)^2+(\Omega\Gamma_m[\Omega])^2}. \tag{E.3.3}$$

At this optimal angle, the spectrum of the force estimator takes the form,

$$\bar{S}^{\mathrm{est},\theta_{\mathrm{opt}}}_{FF}[\Omega] = \bar{S}_{FF}[\Omega] + \bar{S}^{\mathrm{QBA}}_{FF}[\Omega] + \frac{1}{4\eta C\Gamma_m\left|\chi_x[\Omega]\right|^2} - \eta C\Gamma_m\left(\frac{\mathrm{Re}\,\chi_x[\Omega]}{\left|\chi_x[\Omega]\right|}\right)^2. \tag{E.3.4}$$

Noting that the third term is simply $\bar{S}^{\mathrm{imp},\pi/2}_{FF}$, and that $\bar{S}^{\mathrm{QBA}}_{FF}[\Omega] = C\Gamma_m$, this equation can be re-expressed in the suggestive form,

$$\bar{S}^{\mathrm{est},\theta_{\mathrm{opt}}}_{FF}[\Omega] = \bar{S}_{FF}[\Omega] + \bar{S}^{\mathrm{imp},\pi/2}_{FF}[\Omega] + \bar{S}^{\mathrm{QBA}}_{FF}[\Omega]\left[1-\eta\left(\frac{\mathrm{Re}\,\chi_x[\Omega]}{\left|\chi_x[\Omega]\right|}\right)^2\right]. \tag{E.3.5}$$

Thus, at the optimal detection angle, *quantum correlations conspire to cancel quantum back-action (in the measurement record) and reduce the error in the force estimation* compared to the conventional choice $\theta = \pi/2$, for which correlations are absent and

$$\bar{S}_{FF}^{\mathrm{est},\pi/2}[\Omega] = \bar{S}_{FF} + \bar{S}_{FF}^{\mathrm{imp},\pi/2}[\Omega] + \bar{S}_{FF}^{\mathrm{QBA}}[\Omega]. \tag{E.3.6}$$

E.3.1 Correlation enhanced thermal force sensing

In the case of an oscillator in thermal equilibrium quantum correlations can yield improved sensitivity in the detection of the thermal force. In such a case the signal is the thermal force noise, i.e. $\bar{S}_{FF} = \bar{S}_{FF}^{\mathrm{th}}$. Assuming that the recorded periodogram of the photocurrent has converged to the theoretical power spectrum, the homodyne angle dependent uncertainty in the spectral estimation of the thermal force may be defined by,

$$\epsilon_\theta[\Omega] := \bar{S}_{FF}^{\mathrm{est},\theta}[\Omega] - \bar{S}_{FF}^{\mathrm{th}}[\Omega]. \tag{E.3.7}$$

If consider the ratio of uncertainties for the phase quadrature measurement ($\theta = \pi/2$) and for the measurement at a detuned detuned quadrature θ,

$$\xi_{\mathrm{th}}[\Omega] = \frac{\epsilon_{\pi/2}[\Omega]}{\epsilon_\theta[\Omega]} = \frac{\bar{S}_{FF}^{\mathrm{imp},\pi/2}[\Omega] + \bar{S}_{FF}^{\mathrm{QBA}}[\Omega]}{\frac{\bar{S}_{FF}^{\mathrm{imp},\pi/2}[\Omega]}{\sin^2\theta} + \cot\theta \frac{\mathrm{Re}\,\chi_x[\Omega]}{|\chi_x[\Omega]|^2} + \bar{S}_{FF}^{\mathrm{QBA}}[\Omega]}, \tag{E.3.8}$$

the sensitivity enhancement due to back-action cancellation takes place when $\xi > 1$ for θ such that $\frac{\bar{S}_{FF}^{\mathrm{imp},\pi/2}[\Omega]}{\sin^2\theta} + \cot\theta \frac{\mathrm{Re}\,\chi_x[\Omega]}{|\chi_x[\Omega]|^2} < \bar{S}_{FF}^{\mathrm{imp},\pi/2}[\Omega] < \bar{S}_{FF}^{\mathrm{imp},\pi/2}[\Omega]$.

The enhancement in sensitivity attained for measurement at the frequency-dependent optimal quadrature θ_{opt}, compared to the conventional measurement on phase quadrature, is quantified by,

$$\xi_{\mathrm{th}}[\Omega] = \frac{\epsilon_{\pi/2}[\Omega]}{\epsilon_{\theta_{\mathrm{opt}}}[\Omega]} = \frac{\bar{S}_{FF}^{\mathrm{imp},\pi/2}[\Omega] + \bar{S}_{FF}^{\mathrm{QBA}}[\Omega]}{\bar{S}_{FF}^{\mathrm{imp},\pi/2}[\Omega] + \bar{S}_{FF}^{\mathrm{QBA}}[\Omega]\left[1 - \eta\left(\mathrm{Re}\,\chi_x[\Omega]/\left|\chi_x[\Omega]\right|\right)^2\right]} \approx \left[1 - \eta\left(\frac{\mathrm{Re}\,\chi_x[\Omega]}{\left|\chi_x[\Omega]\right|}\right)^2\right]^{-1}, \tag{E.3.9}$$

where the last approximation is valid when $\bar{S}_{FF}^{\mathrm{QBA}}[\Omega] \gg \bar{S}_{FF}^{\mathrm{imp},\pi/2}[\Omega]$, i.e. in the limit of large co-operativity $C \gg 1$ and for frequency offsets around the mechanical resonance $|\Omega - \Omega_m|/\Gamma_m \ll 2\sqrt{\eta}C$. In this regime $\xi[\Omega] > 1$ and quantum-enhanced force sensitivity can be realized, with the enhancement factor being limited by the finite detection efficiency η and the imaginary part of the mechanical susceptibility. The back-estimated factors $\xi_{\mathrm{th}}[\Omega]$ for the parameters of our experiment are shown at the Figure E.6 and demonstrate thermal force sensitivity enhancement up to 25%.

The ability to better estimate the thermal force over a broad range of frequencies may open up opportunities for probing the structure of the weak thermal environment that the oscillator is coupled to.

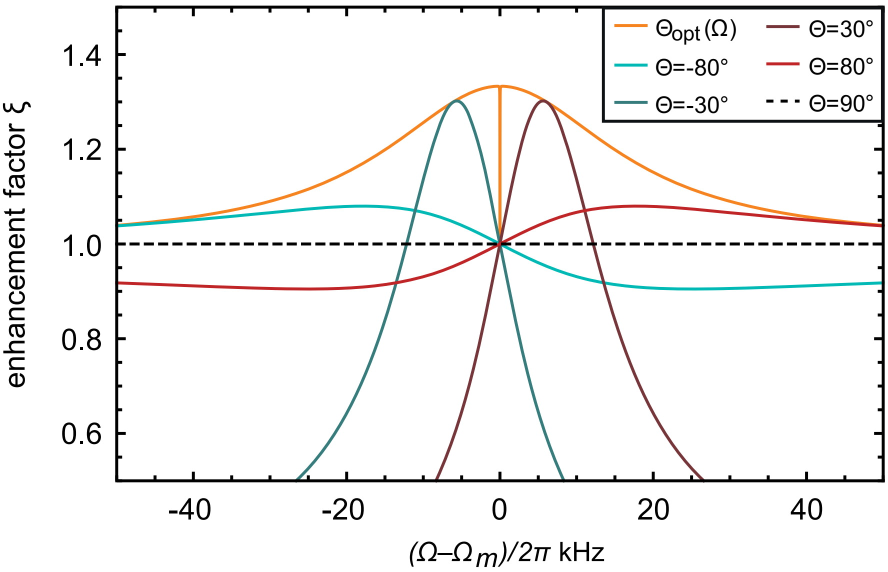

Figure E.6 – Quantum-enhanced sensitivity to thermal force for the parameters realized in the current experiment, assuming input power = 25 μW. Plot shows the enhancement factor $\xi_\theta[\Omega]$, defined in eq. (E.3.8) and eq. (E.3.9), as a function of Fourier frequency and homodyne angle θ. The dashed black line corresponds to $\xi_{\pi/2}[\Omega]$, where force is estimated by phase quadrature detection, where back-action-imprecision correlations are absent. As the homodyne angle is detuned from phase quadrature, enhancement of up to 25% can be observed, limited by the detection efficiency of similar magnitude. The yellow curve shows the theoretically ideal detection scheme, where the homodyne angle is frequency dependent (eq. (E.3.3)), so that broadband enhancement is realized.

E.3.2 Correlation enhanced external force sensing

If an optomechancial system is used for external incoherent force detection, the thermal force itself becomes a part of the noise background. We now consider the sensitivity enhancement in such a case, i.e. $\bar{S}_{FF} = \bar{S}^{\mathrm{ext}}_{FF} + \bar{S}^{\mathrm{th}}_{FF}$, and the error is,

$$\epsilon_\theta[\Omega] := \bar{S}^{\mathrm{est}}_{FF}[\Omega] - \bar{S}^{\mathrm{ext}}_{FF}[\Omega]. \tag{E.3.10}$$

The corresponding expression for the sensitivity enhancement,

$$\xi_{\mathrm{ext}}[\Omega] = \frac{\epsilon_{\pi/2}[\Omega]}{\epsilon_{\theta_{\mathrm{opt}}}[\Omega]} = \frac{\bar{S}^{\mathrm{imp},\pi/2}_{FF}[\Omega] + \bar{S}^{\mathrm{th}}_{FF}[\Omega] + \bar{S}^{\mathrm{QBA}}_{FF}[\Omega]}{\bar{S}^{\mathrm{imp},\pi/2}_{FF}[\Omega] + \bar{S}^{\mathrm{th}}_{FF}[\Omega] + \bar{S}^{\mathrm{QBA}}_{FF}[\Omega]\left[1-\eta\left(\mathrm{Re}\,\chi_x[\Omega]/\left|\chi_x[\Omega]\right|\right)^2\right]}, \tag{E.3.11}$$

indicates an additional constraint to be met due to the presence of the thermal force – the quantum back-action force needs to be comparable to the thermal force.

For room temperature experiments to date, the regime $n_{\mathrm{QBA}}/n_{\mathrm{th}} \ll 1$ (with $n_{\mathrm{th}} \gg 1$) has been relevant, so, again for the case $\bar{S}^{\mathrm{QBA}}_{FF} \gg \bar{S}^{\mathrm{imp},\pi/2}_{FF}$,

$$\xi_{\mathrm{ext}}[\Omega] \approx 1 + \eta \frac{n_{\mathrm{QBA}}}{n_{\mathrm{th}}} \left(\frac{\mathrm{Re}\,\chi_x[\Omega]}{\left|\chi_x[\Omega]\right|}\right)^2, \tag{E.3.12}$$

and quantum-enhanced sensitivity to external force can be realized far off resonance, if QBA is significant compared to thermal noise.

In future experiments, where $n_{\mathrm{QBA}}/n_{\mathrm{th}} \gg 1$ may be achieved, the improvement for external force sensitivity scales as,

$$\xi_{\mathrm{ext}}[\Omega] \approx \frac{1}{1-\eta(\mathrm{Re}\,\chi_x/\left|\chi_x\right|)^2}\left[1-\mathscr{O}\left(\frac{n_{\mathrm{th}}}{n_{\mathrm{QBA}}}\right)\right], \tag{E.3.13}$$

so that arbitrarily large enhancement may be realized far off resonance, limited by the detection efficiency.

F Addendum: Chapter 5

a glossary of variables is provided at the end of this section, on page 185

Note on convention

For any variable X, $\bar{X}$ denotes its classical steady state value, and $\delta X(t) = X(t) - \bar{X}$, the fluctuation from that steady state. We define the Fourier transform of an operator $X(t)$ by

$$\tilde{X}(\Omega) := \int_{-\infty}^{+\infty} X(t) e^{i\Omega t}\, dt. \tag{F.0.1}$$

Following standard definition [184], we employ the symmetrized spectral density,

$$\bar{S}_{XX}(\Omega) := \int_{-\infty}^{\infty} \frac{1}{2} \langle \delta X(t)\, \delta X(0) + \delta X(0)\, \delta X(t) \rangle\, e^{i\Omega t}\, dt, \tag{F.0.2}$$

to describe the spectral distribution of the variance of the operator-valued process, $\delta X(t)$. The single-sided spectral density is then given by (strictly for $\Omega \geq 0$)

$$S_X(\Omega) = 2\, \bar{S}_{XX}(\Omega). \tag{F.0.3}$$

To make contact with experiment and with the main text, we hereafter adopt the single-sided convention unless otherwise necessary for clarity.

F.1 Theory of feedback cooling of a harmonic oscillator

Consider a harmonic oscillator, whose motion is described by position coordinate $x(t)$, moving in a harmonic potential of frequency Ω_m. We specialize to a case in which the oscillator is subject to three stochastic forces: a thermal force (F_{th}) associated with the ambient environment, a 'back-action' force (F_{ba}) associated with the oscillator's coupling to a measurement

---

This appendix is adapted from [28]

device, and a feedback force (F_{fb}) that controls the oscillator. The dynamics of this system are described by the Langevin equation [1],

$$\begin{aligned} & m\left(\ddot{x}+\Gamma_{\mathrm{m}}\dot{x}+\Omega_{\mathrm{m}}^2 x\right) = F_{\mathrm{th}}+F_{\mathrm{ba}}+F_{\mathrm{fb}} \\ \Rightarrow\ & \underbrace{\left(\Omega_{\mathrm{m}}^2-\Omega^2-i\Omega\Gamma_{\mathrm{m}}\right)}_{:=\chi_{\mathrm{m}}(\Omega)^{-1}}\tilde{x} = m^{-1}\left(\tilde{F}_{\mathrm{th}}+\tilde{F}_{\mathrm{ba}}+\tilde{F}_{\mathrm{fb}}\right). \end{aligned} \tag{F.1.1}$$

where χ_{m} is the intrinsic mechanical susceptibility (note that, for notational convenience in section F.2, we have scaled the conventional expression for χ_{m} by m). See Sec. F.1.5 for a discussion of the role of dephasing as a decoherence mechanism in addition to energy damping.

We adopt the following model for the back-action and feedback forces:

$$\tilde{F}_{\mathrm{ba}} = -m\chi_{\mathrm{ba}}(\Omega)^{-1}\,\tilde{x}+\tilde{F}_{\mathrm{ba,th}} \tag{F.1.2a}$$

$$\tilde{F}_{\mathrm{fb}} = -m\chi_{\mathrm{fb}}(\Omega)^{-1}\,\tilde{y}+\tilde{F}_{\mathrm{fb,th}}. \tag{F.1.2b}$$

Each force has two components: a ‘dynamic’ component, characterized by a linear susceptibility, that contains correlations with the oscillator’s position, and an effective thermal component. Notably, the dynamic component of the feedback force is linear in an apparent (measured) position, $\tilde{y}=\tilde{x}+\tilde{x}_{\mathrm{imp}}$, where $\tilde{x}_{\mathrm{imp}}$ is the measurement imprecision. Hereafter, for simplicity, we neglect the dynamic portion of the back-action force. We revisit this approximation in detail in section F.2.1.

F.1.1 Optimal feedback cooling

In feedback cooling, we are interested in minimizing the mean phonon occupancy of the oscillator, viz.

$$\min_{\chi_{\mathrm{fb}}}(2n_{\mathrm{m}}+1) = \min_{\chi_{\mathrm{fb}}}\sqrt{\left\langle\frac{x^2}{x_{\mathrm{zp}}^2}\right\rangle\left\langle\frac{p^2}{p_{\mathrm{zp}}^2}\right\rangle-\left\langle\frac{xp+px}{2x_{\mathrm{zp}}p_{\mathrm{zp}}}\right\rangle}, \tag{F.1.3}$$

where $x_{\mathrm{zp}}^2=\frac{\hbar}{2m\Omega_{\mathrm{m}}}$, and $x_{\mathrm{zp}}p_{\mathrm{zp}}=\frac{\hbar}{2}$. For a thermal state, the constraint reduces to

$$\min_{\chi_{\mathrm{fb}}}\frac{\langle x^2\rangle}{x_{\mathrm{zp}}^2}. \tag{F.1.4}$$

The problem described herein — that of a linear system driven by weak-stationary Gaussian noise (Eq. (F.1.1)), and controlled by linear measurement and actuation (Eq. (F.1.2a)), with the aim of minimizing a quadratic cost function (Eq. (F.1.4)) — is an archetype of the *linear*

---

[1] we adopt a Brownian motion description of the oscillator position, as opposed to a Lindblad one, in spite of the well-known non-positivity of the former [188, 189]; this choice is justified by their mutual concordance at sufficiently large temperatures $T\gtrsim\frac{\hbar\Gamma_m}{k_B}=\mathcal{O}(10^{-10}\,\mathrm{K})$ [190, 191]. Note that there exist non-Markovian noise models that preserve the positivity of the evolution [192].

quadratic gaussian (LQG) paradigm of classical control theory [193–195]. Recently, such problems have been formalized and studied in the quantum mechanical context [196, 197].

The optimal feedback filter, χ_{fb}, can be solved for exactly in our case. From Eq. (F.1.1) and Eq. (F.1.2a) (and neglecting χ_{ba}), the oscillator position and measurement record are

$$\begin{aligned}\left(\chi_{\text{m}}^{-1}+\chi_{\text{fb}}^{-1}\right)\tilde{x} &= m^{-1}\left(\tilde{F}_{\text{th}}+\tilde{F}_{\text{ba,th}}+\tilde{F}_{\text{fb,th}}\right)-\chi_{\text{fb}}^{-1}\tilde{x}_{\text{imp}}\\ \left(\chi_{\text{m}}^{-1}+\chi_{\text{fb}}^{-1}\right)\tilde{y} &= m^{-1}\left(\tilde{F}_{\text{th}}+\tilde{F}_{\text{ba,th}}+\tilde{F}_{\text{fb,th}}\right)+\chi_{\text{m}}^{-1}\tilde{x}_{\text{imp}}.\end{aligned} \tag{F.1.5}$$

Identifying the effective mechanical susceptibility, $\chi_{\text{eff}}^{-1} := \chi_{\text{m}}^{-1}+\chi_{\text{fb}}^{-1}$ and total effective thermal force, $S_F^{\text{tot}} = S_F^{\text{th}}+S_F^{\text{ba}}+S_F^{\text{fb,th}}$, Eq. (F.1.5) implies

$$\begin{aligned}S_x(\Omega) &= |\chi_{\text{eff}}|^2\left(m^{-2}S_F^{\text{tot}}+|\chi_{\text{fb}}|^{-2}S_x^{\text{imp}}\right)\\ S_y(\Omega) &= |\chi_{\text{eff}}|^2\left(m^{-2}S_F^{\text{tot}}+|\chi_{\text{m}}|^{-2}S_x^{\text{imp}}\right).\end{aligned} \tag{F.1.6}$$

for the (single-sided) spectral density of the position and measurement records.

The LQG problem can be stated concretely as (using double-sided spectra temporarily)

$$\min_{\chi_{\text{fb}}}\int_{-\infty}^{\infty}\bar{S}_{xx}(\Omega)\,\frac{d\Omega}{2\pi}. \tag{F.1.7}$$

The solution to this variational problem is given by the Euler-Lagrange equation,

$$\frac{\mathscr{D}\bar{S}_{xx}}{\mathscr{D}\chi_{\text{fb}}}=0, \tag{F.1.8}$$

where $\mathscr{D}$ stands for the variational (Gateaux) derivative. This is most effectively solved in terms of the magnitude $|\chi_{\text{fb}}|$ and phase $\phi_{\text{fb}} = \arg\chi_{\text{fb}}$ of the optimal filter; resulting in the solution,

$$\begin{aligned}\phi_{\text{fb}}(\Omega) &= \arctan\frac{\operatorname{Im}\chi_{\text{m}}}{\operatorname{Re}\chi_{\text{m}}}\\ |\chi_{\text{fb}}(\Omega)|\,\frac{\bar{S}_{FF}^{\text{tot}}}{m^2} &= |\chi_{\text{m}}(\Omega)|^{-1}\,\bar{S}_{xx}^{\text{imp}}.\end{aligned} \tag{F.1.9}$$

F.1.2 Practical feedback cooling

The optimal filter Eq. (F.1.9) affects cooling by inverting the open-loop susceptibility χ_{m}, and so relies on the ability to realize a $Q \sim 10^6$ electronic filter at room temperature, which is experimentally challenging. Moreover, such a filter is not intrinsically robust to perturbations in χ_{m}.

Thus in practice, it is easiest to implement $\phi_{\text{fb}} = \pi/2$ across the mechanical oscillator bandwidth, and choose $|\chi_{\text{fb}}|^{-1} \propto \Omega$, i.e.,

$$\chi_{\text{fb}}(\Omega)^{-1} = -i\Omega\Gamma_{\text{fb}}(\Omega), \tag{F.1.10}$$

where ideally the feedback gain $\Gamma_{\text{fb}}(\Omega) = g_{\text{fb}}\Gamma_m$, with g_{fb} the dimensionless gain of the filter. The ensuing effective susceptibility,

$$\chi_{\text{eff}}^{-1} := \chi_{\text{m}}^{-1} + \chi_{\text{fb}}^{-1} = \Omega_{\text{m}}^2 - \Omega^2 + i\Omega \underbrace{\Gamma_{\text{m}}(1 + g_{\text{fb}})}_{:=\Gamma_{\text{eff}}}, \tag{F.1.11}$$

is characterized by a modified damping rate, Γ_{eff} (cf. Sec. F.1.4 for a discussion of the effects of a non-ideal loop phase in the feedback).

To see how this damping leads to cooling, we reconsider the three components of the thermal environment: (1) an ambient reservoir with which the oscillator equilibrates, (2) a reservoir constituted by stochastic measurement back-action, and (3) a reservoir constituted by stochastic fluctuations of the feedback actuator. For a high-Q oscillator, each reservoir can be assigned a thermal noise equivalent occupation: n_{th}, n_{ba} and n_{fb} respectively, where $n_{\text{th}} + \frac{1}{2} = \frac{1}{2}\coth(\hbar\Omega_{\text{m}}/2k_B T)$ in terms of the ambient bath temperature, T. Thus the total effective thermal force may be expressed:

$$S_{\text{F}}^{\text{tot}}(\Omega) = \left(n_{\text{th}} + n_{\text{ba}} + n_{\text{fb}} + \tfrac{1}{2}\right) \cdot m^2 |\chi_{\text{m}}(\Omega_m)|^{-2} \cdot 2S_x^{\text{zp}}(\Omega_{\text{m}}). \tag{F.1.12}$$

where we have introduced for convenience the (peak) position spectral density in the ground state:

$$S_x^{\text{zp}}(\Omega_{\text{m}}) = \frac{4x_{\text{zp}}^2}{\Gamma_{\text{m}}}. \tag{F.1.13}$$

We further introduce the imprecision quanta, n_{imp}, as the apparent thermal occupation associated with noise in the measurement:

$$S_x^{\text{imp}}(\Omega) = n_{\text{imp}} \cdot 2S_x^{\text{zp}}(\Omega_{\text{m}}). \tag{F.1.14}$$

Thus the spectra of physical position and the measurement record, Eq. (F.1.6), are given by

$$\begin{aligned} \frac{S_x(\Omega)}{2S_x^{\text{zp}}(\Omega_{\text{m}})} &= \frac{(n_{\text{th}} + n_{\text{ba}} + n_{\text{fb}} + \frac{1}{2})\Omega_{\text{m}}^2\Gamma_{\text{m}}^2 + n_{\text{imp}}\, g_{\text{fb}}^2 \Omega^2 \Gamma_{\text{m}}^2}{(\Omega_{\text{m}}^2 - \Omega^2)^2 + \Omega^2\Gamma_{\text{eff}}^2} \\ \frac{S_y(\Omega)}{2S_x^{\text{zp}}(\Omega_{\text{m}})} &= \frac{(n_{\text{th}} + n_{\text{ba}} + n_{\text{fb}} + \frac{1}{2})\Omega_{\text{m}}^2\Gamma_{\text{m}}^2 + n_{\text{imp}} \left((\Omega_{\text{m}}^2 - \Omega^2)^2 + \Omega^2\Gamma_{\text{m}}^2\right)}{(\Omega_{\text{m}}^2 - \Omega^2)^2 + \Omega^2\Gamma_{\text{eff}}^2}. \end{aligned} \tag{F.1.15}$$

The mean phonon occupancy of the cooled oscillator is then given by

$$\begin{aligned} 2n_{\text{m}} + 1 &= \int_0^\infty \frac{S_x(\Omega)}{x_{\text{zp}}^2} \frac{d\Omega}{2\pi} \\ \Rightarrow\ n_{\text{m}} &= \frac{(n_{\text{th}} + n_{\text{ba}} + n_{\text{fb}} + \frac{1}{2}) + n_{\text{imp}} g_{\text{fb}}^2}{1 + g_{\text{fb}}} - \frac{1}{2}. \end{aligned} \tag{F.1.16}$$

In the relevant limit of $n_{\text{th}} \gg \frac{1}{2}$, a minimum of

$$\begin{aligned} n_{\text{m,min}} &\approx 2\sqrt{(n_{\text{th}} + n_{\text{ba}} + n_{\text{fb}})\, n_{\text{imp}}} - \frac{1}{2} \\ &\approx \frac{1}{2\hbar}\sqrt{S_F^{\text{tot}}(\Omega_{\text{m}})\, S_x^{\text{imp}}(\Omega_{\text{m}})} - \frac{1}{2} \end{aligned} \tag{F.1.17}$$

is attained at an optimal gain of

$$g_{\text{fb,opt}} \approx \sqrt{\frac{n_{\text{th}} + n_{\text{ba}} + n_{\text{fb}}}{n_{\text{imp}}}}, \tag{F.1.18}$$

as anticipated by Eq. (F.1.9).

In particular, for the experimentally relevant case of $n_{\text{th}} \gg n_{\text{fb}}$, the conventional condition for ground state cooling, $n_{\text{m}} < 1$, translates to

$$n_{\text{imp}} < \frac{9}{16}(n_{\text{th}} + n_{\text{ba}})^{-1}. \tag{F.1.19}$$

Finally, in the regime where feedback cooling is strong ($g_{\text{fb}} \gg 1$) and quantum-limited ($n_{\text{fb}} = 0$), intuition can be garnered by noticing that Eq. (F.1.16) can be expressed as the detailed balance condition, $\left(n_{\text{m}} + \frac{1}{2}\right)\Gamma_{\text{eff}} = (n_{\text{th}} + n_{\text{ba}})\Gamma_{\text{m}} + n_{\text{imp}}\Gamma_{\text{fb}}$. This suggests that cooling as affected by feedback can be understood as a thermodynamic process which proceeds by the reduction of entropy of the mechanical oscillator to a level ultimately set by the entropy due to the imperfect estimation of the mechanical position.

F.1.3 Limits due to stochastic back-action

In section F.2.4, it is shown that stochastic back-action associated with a cavity-optomechanical position measurement is bound by the imprecision-back-action product: $\hbar^2 S_x^{\text{imp}} S_F^{\text{ba}} = 16 n_{\text{imp}} n_{\text{ba}} \geq 1$. Imposing this limit, Eq. (F.1.19) implies that a necessary condition for ground-state cooling is

$$n_{\text{imp}} < (2n_{\text{th}})^{-1}. \tag{F.1.20}$$

Notably, from Eq. (F.1.14), the associated condition on the measurement imprecision becomes

$$S_x^{\text{imp}} < \frac{S_x^{\text{zp}}}{n_{\text{th}}} = \frac{4x_{\text{zp}}^2}{n_{\text{th}}\Gamma_{\text{m}}} = \frac{4x_{\text{zp}}^2}{\Gamma_{\text{th}}}, \tag{F.1.21}$$

where $\Gamma_{\text{th}} := \Gamma_{\text{m}} n_{\text{th}}$ is the thermal decoherence rate. Notably Eq. (F.1.21) corresponds to an imprecision $n_{\text{th}}/2$ times below that at the standard quantum limit (Eq. (F.2.22)), or equivalently, as a measurement rate [184, 198]

$$\Gamma_{\text{meas}} := \frac{x_{\text{zp}}^2}{2S_x^{\text{zp}}} = \frac{\Gamma_{\text{m}}}{16 n_{\text{imp}}} > \frac{\Gamma_{\text{th}}}{8} \tag{F.1.22}$$

F.1.4 Effect of non-ideal filter phase

In the experimentally implemented feedback filter Eq. (F.1.10), the phase has to satisfy $\arg\left[\chi_{\rm fb}(\Omega)^{-1}\right] = -(2n+1)\,\frac{\pi}{2}$ for all relevant Fourier frequencies, for efficient cold damping (here n is an integer). Note that to satisfy the condition for Markovian feedback, the total time delay $\tau := \phi_{\rm fb}(\Omega_{\rm m})/\Omega_{\rm m}$ has to satisfy, $\tau < 2\pi/\Gamma_{\rm th}$, thus constraining the largest phase warp tolerable.

To achieve minimal dispersion, the delay is implemented by a combined optical/electronic delay line (cf. Sec. F.3). Here we consider the effect of any residual dispersion and/or non-ideal phase, which we model by,

$$\begin{aligned}\chi_{\rm fb}(\Omega)^{-1} &= \exp\left[-i\left((2n+1)\frac{\pi}{2}+\delta\phi_{\rm fb}(\Omega)\right)\right]\Omega g_{\rm fb}(\Omega)\Gamma_{\rm m}\\ &= -i\Omega g_{\rm fb}(\Omega)\Gamma_{\rm m}\, e^{-i\delta\phi_{\rm fb}(\Omega)}.\end{aligned} \tag{F.1.23}$$

The corresponding effective susceptibility,

$$\chi_{\rm eff}(\Omega)^{-1} = \Omega_{\rm eff}(\Omega)^2 - \Omega_m^2 - i\Omega\Gamma_{\rm eff}(\Omega), \tag{F.1.24}$$

features feedback-induced damping, and an additional frequency shift,

$$\begin{aligned}\Gamma_{\rm eff}(\Omega) &= \Gamma_{\rm m}\left[1+g_{\rm fb}(\Omega)\cos\delta\phi_{\rm fb}(\Omega)\right]\\ \Omega_{\rm eff}(\Omega) &= \Omega_m\left[1-g_{\rm fb}(\Omega)\,\frac{\Omega\Gamma_{\rm m}}{\Omega_{\rm m}^2}\,\sin\delta\phi_{\rm fb}(\Omega)\right]^{1/2}.\end{aligned} \tag{F.1.25}$$

Thus, deviations from an ideal phase profile can be observed in the feedback-induced frequency shift, while a non-flat gain profile results in a susceptibility that is no longer Lorentzian.

In the experiment, we measure $\tau = 174\,$ns, implying a linear phase dispersion amounting to $\delta\phi_{\rm fb}(\Omega_{\rm m}+\Gamma_{\rm eff}) - \delta\phi_{\rm fb}(\Omega_{\rm m}-\Gamma_{\rm eff}) \approx 0.3\,$rad. The resulting fractional frequency shift $|(\Omega_{\rm eff}-\Omega_{\rm m})/\Omega_{\rm m}| \approx 10^{-3}$ contributes negligibly to the estimation of the final occupation, while the contribution from the uncertainty in $\Gamma_{\rm eff}$ can be shown to result in a 5% uncertainty in the final occupation.

F.1.5 Dephasing as a decoherence mechanism for the oscillator

In Eq. (F.1.1), the damping rate $\Gamma_{\rm m}$ was assumed to arise from a generic coupling of the oscillator to an environment, giving rise to energy relaxation. In this section, we provide a model that distinguishes between two potential sources of such a coupling, namely, energy relaxation and dephasing, and discuss their relevance to our experiment.

To discuss the relevant intrinsic decoherence mechanisms that the mechanical oscillator is susceptible to, it is convenient to work in terms of the oscillator ladder operators $b, b^\dagger$ defined by,

$$b := \frac{1}{2}\left(\frac{x}{x_{\mathrm{zp}}} + i\frac{p}{p_{\mathrm{zp}}}\right)$$
$$\text{s.t. } [b, b^\dagger] = 1.$$

The free oscillator, described by the hamiltonian,

$$H = \hbar\Omega_m\left(b^\dagger b + \frac{1}{2}\right),$$

is assumed to decohere via two mechanisms:

1. energy damping affected by its contact with a thermal bath at temperature T. In this case, the oscillator state ρ undergoes changes whereby oscillator quanta decay into the bath i.e., $\rho \to b\rho b^\dagger$, or the bath stimulates thermal fluctuations in the oscillator, i.e., $\rho \to b^\dagger \rho b$. Since the bath is assumed to be Markovian, and in thermal equilibrium at all times, these two processes take place with a probability per unit time given by [184, 199], $\Gamma_- = \Gamma_1(n_{\mathrm{th}} + 1)$ and $\Gamma_+ = \Gamma_1 n_{\mathrm{th}}$ respectively.
2. dephasing, wherein the environment acts by measuring the oscillator's average phonon number $N = b^\dagger b$ at random times, with a probability per unit time given by Γ_2. This entails the jump $\rho \to N\rho N$, which unlike damping, does not cause exchange of quanta with the environment. We identify Γ_2 with the dephasing rate of the oscillator.

These two processes imply that the system state ρ evolves according to the Lindblad equation [199],

$$\dot{\rho} = -\frac{i}{\hbar}[H + F_{\mathrm{ext}}(t)x, \rho] + \Gamma_- \mathscr{D}[b]\rho + \Gamma_+ \mathscr{D}[b^\dagger]\rho + \Gamma_2 \mathscr{D}[N]\rho, \tag{F.1.26}$$

where $\mathscr{D}[O]\rho = O\rho O^\dagger - \frac{1}{2}\{O^\dagger O, \rho\}$. In writing the Lindblad terms for the individual decoherence channels, we have modeled energy damping and dephasing as Markovian process into independent baths with white spectrum. Note that for later discussion, we have assumed an external Newtonian force F_{ext} to be driving the oscillator.

Switching to the Heisenberg picture, and employing standard trace identities, this master equation implies the following equation of motion for the mean amplitude,

$$\frac{d\langle b\rangle}{dt} := \mathrm{Tr}[b\dot{\rho}] = -(i\Omega_m + (\Gamma_1 + \Gamma_2))\langle b\rangle + x_{\mathrm{zp}}F_{\mathrm{ext}}(t). \tag{F.1.27}$$

Note that due to the assumption made in Eq. (F.1.26), white frequency noise, which by definition acts on very fast time scales compared to the system dynamics, the effect of dephasing is to contribute an effective linewidth $\Gamma_m = \Gamma_1 + \Gamma_2$. In specific experiments where the frequency noise may not be white, and are characterized by a non-zero correlation time, an appropriate treatment using a Langevin equation may alter this prediction. In the extreme case where the frequency drift is very slow, the effect of dephasing would be rendered irrelevant.

Since Eq. (F.1.27) is a linear equation, the quantum regression theorem [199, 200] guarantees that the susceptibility of the two-time correlator $\langle x(t)x(0)\rangle$ to the corresponding correlator of external Langevin forces, is of the form employed in Eq. (F.1.1), except that now $\Gamma_m = \Gamma_1 + \Gamma_2$. This implies that a coherent response measurement of the mechanical oscillator, for example by driving it with a chirped radiation pressure force, would reveal a susceptibility with the total linewidth Γ_m.

However, the effect of dephasing can be seperated from that of energy damping, by an additional measurement that probes the decay of the average coherent phonon number $\langle N\rangle_{\mathrm{coh}} := \langle N\rangle - n_{\mathrm{th}}$, for example by ringdown. The master equation Eq. (F.1.26) implies in this case,

$$\frac{d\,\langle N\rangle_{\mathrm{coh}}}{dt} = -\Gamma_1\,\langle N\rangle_{\mathrm{coh}}\,, \tag{F.1.28}$$

which is consistent with the initiuton that dephasing does not involve exchange of quanta with the environment. Thus in principles $\Gamma_2 = \Gamma_{\mathrm{response}} - \Gamma_{\mathrm{ringdown}}$, asuming that additional sources of decoherence, other than the ones considered here, are absent.

In practice, we do not observe a departure between ringdown and spectral measurements of the linewidth, which is consistent with observations on a similar oscillator in our own group [201], and others [202].

Finally, we make a related, if somewhat tangential, observation regarding the implication of Eq. (F.1.27) for dynamic back-action Sec. F.2.1. The increased linewidth predicted in Eq. (F.1.27) would imply a modification of the strength of linear optomechanical phenomena like parametric amplification and back-action cooling – indeed, if the frequency noise is white, it decorrelates the mechanical amplitude from the mean optical back-action force.

F.2 Readout and feedback using a cavity

In our system, the mechanical oscillator is dispersively coupled to an optical cavity mode. The cavity field exerts a radiation pressure force on the oscillator; the unitary nature of this interaction affects a phase shift of the cavity field commensurate with the amplitude of mechanical motion.

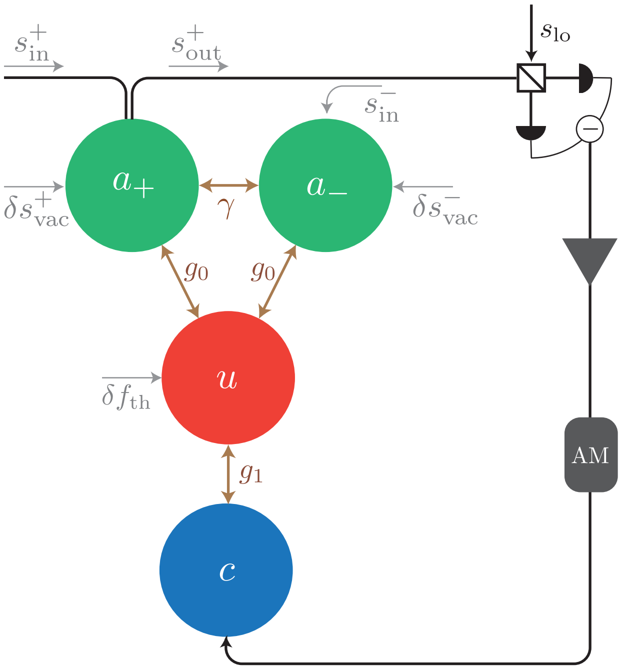

Supplementary Figure F.1 – Schematic of the relevant input, output and couplings between the various subsystems in the experiment.

We adopt the following set of coupled Langevin equations to model the dynamics of the cavity mode (characterized by the slowly varying amplitude of the intracavity field, a) and the mechanical mode (characterized by its normalized position, $u := x/x_{\text{zp}}$):

$$\begin{aligned}\dot{a}_+ &= \left(i\Delta_0 - \frac{\kappa}{2}\right)a_+ + \frac{i\gamma}{2}a_- + i g_0 u a_+ + \sqrt{\eta_c\kappa}\, s_{\text{in}}^{+} + \sqrt{(1-\eta_c)\kappa}\,\delta s_{\text{vac}}^{+}\\ \dot{a}_- &= \left(i\Delta_0 - \frac{\kappa}{2}\right)a_- + \frac{i\gamma}{2}a_+ + i g_0 u a_- + \sqrt{\eta_c\kappa}\, s_{\text{in}}^{-} + \sqrt{(1-\eta_c)\kappa}\,\delta s_{\text{vac}}^{-}\end{aligned} \tag{F.2.1a}$$

$$\ddot{u} + \Gamma_{\text{m}}\dot{u} + \Omega_{\text{m}}^2 u = \delta f_{\text{th}} + f_{\text{ba}} + f_{\text{fb}}. \tag{F.2.1b}$$

Notably, in Eq. (F.2.1a) we use a two-mode model to describe the microdisk cavity. Subscripts + and − refer to whispering gallery modes propagating along ('clockwise') and against ('counter-clockwise') the conventional direction (+) of the injected field, respectively. The two modes are coupled at a rate γ by scattering centers [203], leading to a characteristic splitting of the optical resonance (cf. Eq. (F.2.5) and Sec. F.3.5). Motivated by the geometrical nature of the interaction, we assume that both modes share a common vacuum optomechanical coupling rate, g_0.

Light is physically coupled to the microdisk cavity using an optical fiber [203]. In Supplementary Figure F.1 and Eq. (F.2.1a), we model this coupler as a two port waveguide. Fields entering(exiting) the 'clockwise' port, $s^+_{\text{in(out)}}$, couple directly to the clockwise cavity mode. Fields entering(exiting) the 'counter-clockwise' port, $s^-_{\text{in(out)}}$, couple directly to the counter-clockwise mode. The cavity-waveguide coupling rate is $\kappa_{\text{ex}} = \eta_c\kappa$, where $\kappa = \kappa_{\text{ex}} + \kappa_0$ is the total cavity decay rate and κ_0 is the intrinsic cavity decay rate. In addition, each cavity mode is driven through its intrinsic decay channel by a vacuum state with amplitude $\delta s^\pm_{\text{vac}}$. Input field amplitudes are here normalized so that $P^\pm_{\text{in}} = \hbar\omega^\pm_\ell |s^\pm_{\text{in}}|^2$ is the injected power. $\Delta_0 = \omega_{\text{c}} - \omega^\pm_\ell$ denotes the detuning of the drive field carrier frequency, $\omega^\pm_\ell$, from the center frequency of the optical mode doublet, ω_c.

The dynamics of the mechanical oscillator are governed by Eq. (F.2.1b). Note that owing to the dimensionless form of u, generalized forces $f_{\text{th,ba,fb}}$ have dimensions of $(\text{time})^{-2}$; the actual forces (cf. Sec. F.1), in units of Newtons, are given by $F_i = m x_{\text{zp}} f_i$ ($i \in \{\text{th, opt, fb}\}$). Using this convention, the thermal Langevin force is given by

$$\delta f_{\text{th}} = \Omega_{\text{m}}\Gamma_{\text{m}}\sqrt{2(2n_{th}+1)}\,\xi_{\text{th}}, \quad \text{where} \quad n_{\text{th}} = \frac{1}{2}\coth\left(\frac{\hbar\Omega_{\text{m}}}{2k_B T}\right) \tag{F.2.2}$$

and ξ_{th} the is unit variance white noise process modeling the bath fluctuations.

We model the measurement back-action force as the radiation pressure imparted by the excited mode doublet $a_\pm$:

$$f_{\text{ba}} = \Omega_{\text{m}} g_0 (a^\dagger_+ a_+ + a^\dagger_- a_-). \tag{F.2.3}$$

We likewise model the feedback force as the radiation pressure imparted by an independent, auxiliary cavity mode with amplitude c and optomechanical couplng rate g_1:

$$f_{\text{fb}} = \Omega_{\text{m}} g_1\, c^\dagger c. \tag{F.2.4}$$

In the following treatment, both optical modes are driven by optical fields entering the clockwise port of the optical fiber. The field driving mode doublet $a_\pm$ is refered to as the 'sensor' field. The field driving mode c is referred to as the 'feedback' field. The counter-clockwise port of the optical fiber is used to monitor the transmitted sensor field, but is otherwise left open. We hereafter confine our attention to the back-action force associated with the cavity mode $a_\pm$.

Steady state. When the cavity is excited by the sensor field, the static component of the ensuing radiation pressure force displaces the oscillator to a new steady-state position, $\bar{u}$, and leads to a renormalization of the laser-cavity detuning to $\Delta = \Delta_0 + g_0\bar{u}$. In practice the frequency of the sensor field is stabilized so that $\Delta = 0$. In this case the steady state intracavity field amplitude ($\bar{a}$) and oscillator position are given by

$$\begin{aligned} &\bar{a}_+ = \sqrt{n_+},\ \ \bar{a}_- = i\sqrt{n_-} \text{ and } \bar{u} = \frac{g_0}{\Omega_\mathrm{m}}(n_+ + n_-), \\ \text{where } &n_+ = \frac{4\eta_\mathrm{c}}{\kappa}\frac{P_\mathrm{in}^+/\hbar\omega_\mathrm{c}}{(1+\gamma^2/\kappa^2)^2} \text{ and } n_- = \left(\frac{\gamma}{\kappa}\right)^2 n_+. \end{aligned} \tag{F.2.5}$$

denote the mean intracavity photon number of the clockwise and counter-clockwise modes, respectively. Note that when describing Figure 2 in the main text, we associate the intravity photon number with that of the clockwise mode, i.e. $n_\mathrm{c} = n_+$.

Splitting of the cavity resonance can be observed spectroscopically in the normalized steady state transmission. Using the input-output relation $\bar{s}_\mathrm{out}^+ = \bar{s}_\mathrm{in}^+ - \sqrt{\eta_\mathrm{c}\kappa}\,\bar{a}_+$ gives

$$\left|\frac{\bar{s}_\mathrm{out}^+}{\bar{s}_\mathrm{in}^+}\right|^2 = \frac{P_\mathrm{out}^+}{P_\mathrm{in}^+} = 1 - \eta_\mathrm{c}\kappa^2\frac{\left(\Delta^2 + (\gamma/2)^2 + (\kappa/2)^2\right) - \eta_\mathrm{c}\left(\Delta^2 + (\kappa/2)^2\right)}{\left(\Delta^2 - (\kappa/2)^2 - (\gamma/2)^2\right)^2}, \tag{F.2.6}$$

which is used in Sec. F.3.5.

Fluctuations. Fluctuations of the cavity field, $\delta a = a - \bar{a}$, and the mechanical position, $\delta u = u - \bar{u}$, are coupled according to Eq. (F.2.1). To first order:

$$\delta\dot{a}_\pm = \left(i\Delta - \frac{\kappa}{2}\right)\delta a_\pm + \frac{i\gamma}{2}\delta a_\mp + i g_0 \bar{a}_\pm\,\delta u + +\sqrt{\eta_\mathrm{c}\kappa}\,\delta s_\mathrm{in}^- \pm +\sqrt{(1-\eta_\mathrm{c})\kappa}\,\delta s_\mathrm{vac}^\pm \tag{F.2.7a}$$

$$\delta\ddot{u} + \Gamma_\mathrm{m}\delta\dot{u} + \Omega_\mathrm{m}^2\delta u = \delta f_\mathrm{th} + \delta f_\mathrm{fb} + g_0\Omega_\mathrm{m}\sum_{j=\pm}(\bar{a}_j\delta a_j^\dagger + \bar{a}_j^*\delta a_j). \tag{F.2.7b}$$

The ensuing radiation pressure force fluctuations

$$\delta f_\mathrm{ba} = g_0\Omega_\mathrm{m}\sum_{j=\pm}(\bar{a}_j\delta a_j^\dagger + \bar{a}_j^*\delta a_j) \tag{F.2.8}$$

contain both a dynamic and stochastic component, as detailed in section F.2.1 and F.2.2, respectively.

Taking the Fourier transforms of Eq. (F.2.7) recasts the optomechanical interaction in terms of optical(mechanical) susceptibilities, $\chi_{\mathrm{a(m)}}$:

$$\begin{aligned}\chi_{\mathrm{a}}^{(\gamma)}(\Omega)^{-1}\,\delta\tilde{a}_{\pm} = i g_0 \left(\bar{a}_{\pm} + \frac{i\gamma}{2}\chi_{\mathrm{a}}^{(0)}\,\bar{a}_{\mp}\right)\delta\tilde{u} \\ + \sqrt{(1-\eta_{\mathrm{c}})\kappa}\left(\delta\tilde{s}_{\mathrm{vac}}^{\pm} + \frac{i\gamma}{2}\chi_{\mathrm{a}}^{(0)}\,\delta\tilde{s}_{\mathrm{vac}}^{\mp}\right) \\ + \sqrt{\eta_{\mathrm{c}}\kappa}\left(\delta\tilde{s}_{\mathrm{in}}^{\pm} + \frac{i\gamma}{2}\chi_{\mathrm{a}}^{(0)}\delta\tilde{s}_{\mathrm{in}}^{\mp}\right)\end{aligned} \tag{F.2.9a}$$

$$\left(\chi_{\mathrm{m}}(\Omega)^{-1} + \chi_{\mathrm{fb}}(\Omega)^{-1} + \chi_{\mathrm{ba}}(\Omega)^{-1}\right)\delta\tilde{u} = \delta\tilde{f}_{\mathrm{th}} + \delta\tilde{f}_{\mathrm{fb,th}} + \delta\tilde{f}_{\mathrm{ba,th}}. \tag{F.2.9b}$$

Here χ_{fb} and χ_{ba} are the modification to the intrinsic mechanical susceptibility due to feedback and dynamic back-action, respectively. Likewise $f_{\mathrm{fb,th}}$ and $f_{\mathrm{ba,th}}$ represent effectively thermal components of the feedback and measurement back-action forces, respectively, adopting the notation from Sec. F.1. Before elaborating, we emphasize the following simplifications in the experimentally relevant 'bad-cavity' limit, $\kappa \gg \Omega_{\mathrm{m}}$, assuming a resonantly driven cavity ($\Delta = 0$) and adopting the dissipative feedback strategy described in Sec. F.1.2:

$$\begin{aligned}\chi_{\mathrm{a}}^{(0)}(\Omega)^{-1} &:= -i(\Omega+\Delta) + \frac{\kappa}{2} \approx \frac{\kappa}{2} \\ \chi_{\mathrm{a}}^{(\gamma)}(\Omega)^{-1} &:= \frac{\chi_{\mathrm{a}}^{(0)}(\Omega)^{-1}}{\chi_{\mathrm{a}}^{(0)}(\Omega)^{-2} + (\gamma/2)^2} \approx \frac{\kappa}{2}\left(1 + \frac{\gamma^2}{\kappa^2}\right) \\ \chi_{\mathrm{m}}(\Omega)^{-1} &:= \Omega_{\mathrm{m}}^2 - \Omega^2 - i\Omega\Gamma_{\mathrm{m}} \\ \chi_{\mathrm{fb}}(\Omega)^{-1} &:= \Omega_{\mathrm{fb}}^2(\Omega) - i\Omega\Gamma_{\mathrm{fb}}(\Omega) \approx -i\Omega\Gamma_{\mathrm{m}}(1+g_{\mathrm{fb}}) \\ \chi_{\mathrm{ba}}(\Omega)^{-1} &:= \Omega_{\mathrm{ba}}^2(\Omega) - i\Omega\Gamma_{\mathrm{ba}}(\Omega) \approx 0.\end{aligned} \tag{F.2.10}$$

F.2.1 Dynamic back-action

When the cavity is driven away from resonance ($\Delta \neq 0$), correlations between the radiation pressure back-action force and the mechanical position give rise to a well known dynamic radiation pressure back-action force [204]. In the high-Q ($\Omega_{\mathrm{m}} \gg \Gamma_{\mathrm{m}}$), bad-cavity ($\kappa \gg \Omega_{\mathrm{m}}$) limit relevant to our experiment, dynamic back-action manifests as a displaced mechanical frequency (the optical spring effect) and passive cold-damping [204]. Accounting for cavity mode splitting, the optically-induced spring shift ($\Delta\Omega_{\mathrm{ba}}$) and damping rate ($\Gamma_{\mathrm{ba}}$) are given by:

$$\Delta\Omega_{\mathrm{ba}} := \Omega_{\mathrm{ba}}(\Omega_{\mathrm{m}}) - \Omega_{\mathrm{m}} \approx \frac{2g_0^2}{\kappa}\frac{4\eta_{\mathrm{c}}P_{\mathrm{in}}^{+}}{\kappa\hbar\omega_{\mathrm{c}}}\sum_{j=\pm}\frac{(\kappa/2)^3(\Delta + j\gamma/2)}{\left[(\Delta + j\gamma/2)^2 + (\kappa/2)^2\right]^2} \tag{F.2.11a}$$

$$\Gamma_{\mathrm{ba}}(\Omega_{\mathrm{m}}) \approx \frac{\Omega_{\mathrm{m}}}{4\kappa}\cdot\frac{2g_0^2}{\kappa}\frac{4\eta_{\mathrm{c}}P_{\mathrm{in}}^{+}}{\kappa\hbar\omega_{\mathrm{c}}}\sum_{j=\pm}\frac{\kappa^5(\Delta - j\gamma/2)}{\left[(\Delta + j\gamma/2)^2 + (\kappa/2)^2\right]^3}. \tag{F.2.11b}$$

Eq. (F.2.11a) is used in conjunction with Eq. (F.2.6) to estimate g_0 in section Sec. F.3.3. Note that both terms vanish for resonant probing.

F.2.2 Stochastic back-action

When the cavity is driven on resonance ($\Delta = 0$), the thermal component of the radiation pressure back-action force takes the form

$$\begin{aligned}\delta \tilde{f}_{\mathrm{ba,th}} = \frac{8 g_0 \Omega_{\mathrm{m}}}{\sqrt{\kappa}\left(1+\gamma^2/\kappa^2\right)} \Big\{ & \left(\sqrt{n_+} + \frac{\gamma}{\kappa}\sqrt{n_-}\right)\sqrt{\eta_{\mathrm{c}}}\,\delta \tilde{q}^{+}_{\mathrm{in}} + \left(\sqrt{n_+} + \frac{\gamma}{\kappa}\sqrt{n_-}\right)\sqrt{1-\eta_{\mathrm{c}}}\,\delta \tilde{q}^{+}_{\mathrm{vac}} \\ & - \left(\frac{\gamma}{\kappa}\sqrt{n_+} - \sqrt{n_-}\right)\sqrt{\eta_{\mathrm{c}}}\,\delta \tilde{p}^{-}_{\mathrm{in}} - \left(\frac{\gamma}{\kappa}\sqrt{n_+} - \sqrt{n_-}\right)\sqrt{1-\eta_{\mathrm{c}}}\,\delta \tilde{p}^{-}_{\mathrm{vac}} \Big\},\end{aligned} \tag{F.2.12}$$

where $q(p)$ denote the amplitude(phase) quadrature of each field: $\delta s = \delta q + i\delta p$. In Eq. (F.2.12), we have retained the explicit dependence on $n_\pm$ in order to emphasize their role in weighting the various noise components. We note that as a consequence of the scattering process, (amplitude)phase fluctuations entering the (clockwise)counter-clockwise mode are converted to intensity fluctuations by two pathways.

Assuming that the drive field is shot-noise limited in its amplitude quadrature ($\bar{S}^{\mathrm{in}}_{qq} = \frac{1}{2}$) and that the cavity is otherwise interacting with a zero temperature bath ($\bar{S}^{\mathrm{vac}}_{qq} = \frac{1}{2} = \bar{S}^{\mathrm{vac}}_{pp}$), we find that the effective thermal occupation of the remaining 'quantum' stochastic back-action is given by

$$n_{\mathrm{ba}} = C_0 \frac{1}{1+\gamma^2/\kappa^2}(n_+ + n_-) = C_0 n_+; \tag{F.2.13}$$

here expressed in terms of the 'single-photon cooperativity' parameter,

$$C_0 := \frac{4 g_0^2}{\kappa \Gamma_{\mathrm{m}}}. \tag{F.2.14}$$

F.2.3 Measurement imprecision

The cavity transmission, $\delta \tilde{s}^{+}_{\mathrm{out}} = \delta \tilde{s}^{+}_{\mathrm{in}} - \sqrt{\eta_{\mathrm{c}}\kappa}\,\delta \tilde{a}_+$, at $\Delta = 0$ is given by,

$$\begin{aligned}\delta \tilde{s}^{+}_{\mathrm{out}} = -i\sqrt{\eta_{\mathrm{c}}}\frac{2 g_0 \sqrt{n_+}}{\sqrt{\kappa}}\left(\frac{1-\gamma^2/\kappa^2}{1+\gamma^2/\kappa^2}\right)\delta \tilde{u} + \left(1 - \frac{2\eta_{\mathrm{c}}}{1+\gamma^2/\kappa^2}\right)\delta \tilde{s}^{+}_{\mathrm{in}} - i\frac{2\eta_{\mathrm{c}}(\gamma/\kappa)}{1+\gamma^2/\kappa^2}\,\delta s^{-}_{\mathrm{in}} \\ - \frac{2\sqrt{\eta_{\mathrm{c}}(1-\eta_{\mathrm{c}})}}{1+\gamma^2/\kappa^2}\left(\delta \tilde{s}^{+}_{\mathrm{vac}} + i\frac{\gamma}{\kappa}\delta \tilde{s}^{-}_{\mathrm{vac}}\right).\end{aligned} \tag{F.2.15}$$

As depicted in fig. F.1, the transmitted field is amplified in a balanced homodyne receiver with a coherent local oscillator (LO) s_{lo}. The fields transmitted at either ports of the homodyne beam-splitter are,

$$\begin{pmatrix}\tilde{s}_1 \\ \tilde{s}_2\end{pmatrix} = \frac{1}{\sqrt{2}}\begin{pmatrix}1 & i \\ i & 1\end{pmatrix}\begin{pmatrix}s_{\mathrm{lo}} \\ \delta \tilde{s}^{+}_{\mathrm{out}}\end{pmatrix}; \tag{F.2.16}$$

the optical intensities detected by independent identical photodetectors are, $\delta\tilde{I}_i = \tilde{s}_i^\dagger \tilde{s}_i$ $(i = 1, 2)$. The operator corresponding to the resulting subtracted homodyne intensity is,

$$\delta\tilde{I}_{\mathrm{hom}} = \delta\tilde{I}_1 - \delta\tilde{I}_2 = 2|s_{\mathrm{lo}}|\left(\delta\tilde{p}^+_{\mathrm{out}}\cos\theta_{\mathrm{lo}} - \delta\tilde{q}^+_{\mathrm{out}}\sin\theta_{\mathrm{lo}}\right), \tag{F.2.17}$$

where $|s_{\mathrm{lo}}|$ is the amplitude of the large coherent LO field, and θ_{lo} the relative mean phase between the LO and the cavity transmission. The path length of the LO arm is electronically locked to maintain $\theta_{\mathrm{lo}} \approx 0$, so that the homodyne signal picks out the phase quadrature of the cavity transmission. For photodetectors with gain G_{d} (A/W) and quantum effeciency η_{d}, the resulting shot-noise-normalized spectrum of photocurrent fluctuations is given by [205]:

$$\begin{aligned} S_i^{\mathrm{hom}}(\Omega) &= G_{\mathrm{d}}^2\eta_{\mathrm{d}}\left(1 + \eta_{\mathrm{d}}\frac{\langle: \delta\tilde{I}_{\mathrm{hom}}(\Omega)\,\delta\tilde{I}_{\mathrm{hom}}(-\Omega) :\rangle}{\langle I_{\mathrm{hom}}\rangle}\right) \\ &= G_{\mathrm{d}}^2\eta_{\mathrm{d}}\left(1 + \eta_{\mathrm{d}}\eta_c\frac{16g_0^2 n_+}{\kappa}\left(\frac{1-\gamma^2/\kappa^2}{1+\gamma^2/\kappa^2}\right)^2 S_u(\Omega)\right). \end{aligned} \tag{F.2.18}$$

Using Eq. (F.1.14) and $u \equiv x/x_{\mathrm{zp}}$, the shot noise floor of the homodyne photocurrent spectrum can be expressed as an equivalent thermal bath occupation,

$$n_{\mathrm{imp}} = \left(\frac{1}{16\eta_{\mathrm{c}}\eta_{\mathrm{d}}C_0 n_+}\right)\left(\frac{1+\gamma^2/\kappa^2}{1-\gamma^2/\kappa^2}\right)^2. \tag{F.2.19}$$

Note that mode splitting causes the optical susceptibility (Eq. (F.2.7)) to flatten near resonance, leading to divergence of Eq. (F.2.19) when $\gamma = \kappa$.

F.2.4 The uncertainty principle and the standard quantum limit

Eq. (F.2.13) and Eq. (F.2.19) imply that a cavity-optomechanical position measurement is bound by the imprecision-back-action product,

$$4\sqrt{n_{\mathrm{imp}}n_{\mathrm{ba}}} = \frac{1}{\hbar}\sqrt{S_x^{\mathrm{imp}}S_F^{\mathrm{ba}}} \geq 1. \tag{F.2.20}$$

Using Eq. (F.1.12) and Eq. (F.1.13), we identify

$$S_x^{\mathrm{imp}} = n_{\mathrm{imp}}\cdot 2S_x^{\mathrm{zp}} \tag{F.2.21a}$$

$$S_F^{\mathrm{ba}} = n_{\mathrm{ba}}\cdot m^2|\chi(\Omega_{\mathrm{m}})|^{-2}\cdot 2S_x^{\mathrm{zp}} = 4\hbar n_{\mathrm{ba}}\Omega_{\mathrm{m}}\Gamma_{\mathrm{m}}m \tag{F.2.21b}$$

as, respectively, the shot-noise limited imprecision of the homodyne measurement, Eq. (F.2.19), (referred from the photocurrent to the mechanical position) and its associated stochastic back-action, arising from radiation pressure shot noise, Eq. (F.2.8).

This product places a limit on the apparent motion of the oscillator. Namely, in the absence of feedback, Eq. (F.1.15) gives

$$\frac{S_y(\Omega_\mathrm{m})}{2S_x^\mathrm{imp}} = n_\mathrm{th} + n_\mathrm{ba} + n_\mathrm{imp} + \frac{1}{2} \geq n_\mathrm{th} + 1 \geq 1. \tag{F.2.22}$$

The limiting case in Eq. (F.2.22) occurs for $n_\mathrm{th} = 0$ and $n_\mathrm{ba} = n_\mathrm{imp} = \frac{1}{4}$. This corresponds to an oscillator in contact with a zero-temperature ambient thermal bath, measured with an imprecision of $S_x^\mathrm{zp}/2$, and exhibiting, due to stochastic back-action, a physical displacement of $S_x^\mathrm{zp}/2$ on top of its zero-point displacement, of magnitude S_x^zp.

A more general treatment [184] reveals the RHS of Eq. (F.2.20) and the RHS of Eq. (F.2.22) to coincide with the Heisenberg uncertainty principle and the standard quantum limit for a weak continuous (linear) position measurement, respectively.

F.3 Experimental details

F.3.1 Cryogenic Operation

The sample is embedded in a ^{3}He buffer gas cryostat (Oxford Instruments HelioxTL). As detailed in Riviere *et. al.* [124], laser light is coupled to the microdisk by means of a straight tapered optical fiber affixed to the cryostat probe head. To position the microdisk relative to the optical fiber, the sample chip is mounted on a 2-axis Attocube nanopositioner (ANPx50/LT). An important practical consequence of the near-field coupling architecture is that it enables us to place the tapered fiber in physical contact with the microdisk without influencing the quality factor of the nanobeam. We operate in this "contact mode" in order to suppress fluctuations in the coupling strength κ_{ex} due low frequency cryostat vibrations, as well as drift due to temperature change. As shown in Supplementary Figure F.6, changing the position of the contact point allows access to a wide range of coupling strengths, including nearly ideal [39] critical coupling.

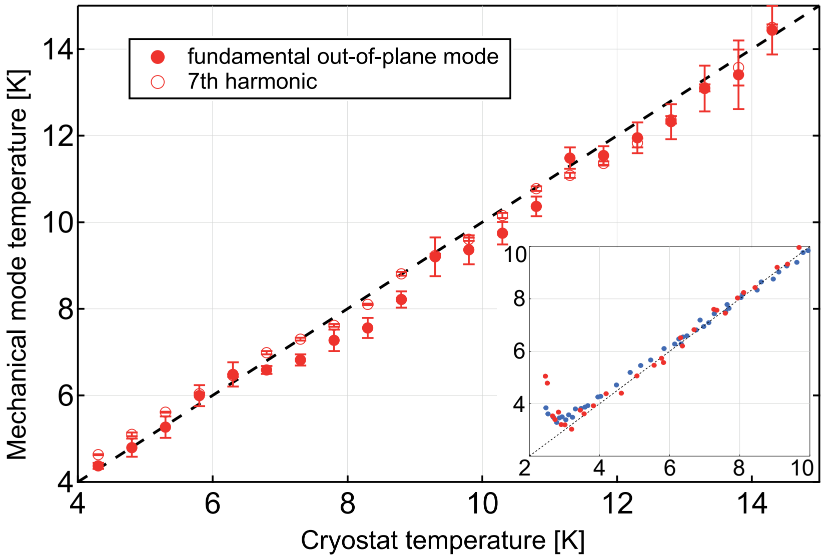

Supplementary Figure F.2 – Mode temperature vs. cryostat temperature.

We regulate the pressure and temperature of our cryostat in order to address different experimental challenges. Measurements which require independent knowledge of the sample temperature (e.g. optomechanical coupling, Sec. F.3.3) are performed using a large buffer gas pressure of ~ 100 mbar in order to ensure good thermalization with the sample holder, whose temperature is monitored using a calibrated Cernox sensor. Measurements requiring high mechanical quality factor are conducted with the buffer gas evacuated to a pressure of $< 10^{-3}$ mbar. We have verified that the sample remains thermalized with the sample holder at temperatures as low as 4 K (fig. F.2), by monitoring the thermomechanical noise of multiple beam modes using a weak sensor field (Supplementary Figure F.2). Below 4 K, a dramatic rise in temperature is observed for all modes (inset to fig. F.2). This temperature rise scales linearly with optical power, and suggests an increase in susceptibility to absorption heating. We conjecture that this effect is due to a rapid drop in thermal conductivity consistent with the universal behavior of amorphous glass (in this case Si_3N_4) at temperatures below ~ 10K [206]. To avoid this strong effect, we operate in temperature ranging from 4-5 K for all of the reported experiments.

F.3.2 Experimental setup

A schematic of the experiment setup is shown in fig. F.3. At its heart is the cryogenic, taper-coupled microdisk (Sec. F.3.1). The taper is spliced into a ~ 9 meter, single mode optical fiber (780HP), penetrating the cryostat probe through a pair of teflon vacuum feedthroughs. Optical fields coupled to the fiber are supplied by two intensity-stabilized (Thorlabs NE LCC3112H) external cavity diode lasers (ECDL, New Focus Velocity 6312 and 6316) operating at $\lambda \approx 775$ nm and 850 nm: the 'sensor' and 'feedback' laser, respectively. Each laser is phase modulated using a broadband EOM (PM, New Focus 4002). Phase modulation at 61(42) MHz is used to generate a PDH error signal with which to stabilize the sensor(feedback) laser frequency to the sensor(feedback) cavity mode. For the sensor field, a second phase modulation tone at $\Omega_{\mathrm{cal}}/2\pi = 40$ MHz is used to calibrate the homodyne measurement (Sec. F.3.3). Directly before(after) the signal fiber, the sensor and feedback fields are combined(split) using a dichroic mirror (DM). The sensor(feedback) PDH error signal is derived from a weak pickoff of the reflected(transmitted) cavity field.

The homodyne detector is formed by incorporating the cryogenic signal fiber into one arm of a carefully length-matched Mach-Zehnder interferometer. The local oscillator (LO) arm of the interferometer is derived from the sensor field using a beamsplitter located after the broadband EOM. Cancelling the signal generated by common-mode phase modulation on a single port of the balanced photodetector (FEMTO HCA-S) enables us to match the length of the signal and LO arm to within 1 mm, practically eliminating contamination of the measure-

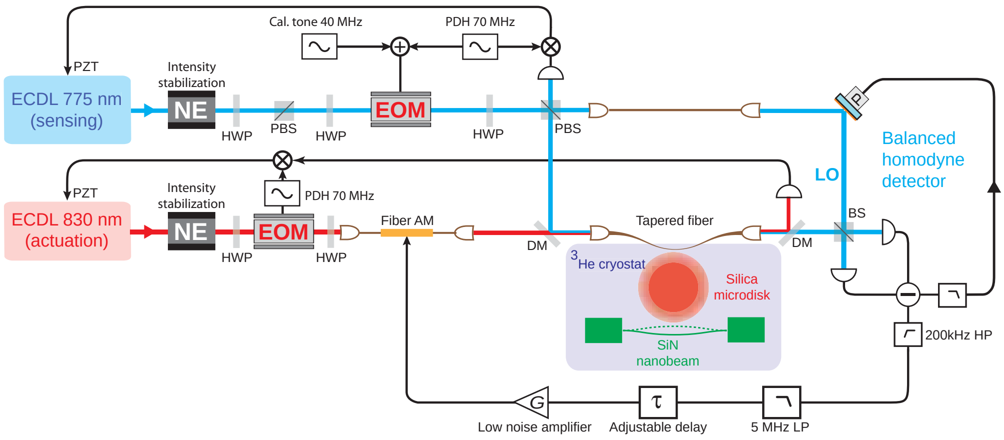

Supplementary Figure F.3 – Schematic of experimental setup.

ment by laser phase noise. Subsequent power balancing of the two detection ports achieves a common-mode rejection of residual amplitude modulation — mainly arising due to optical fiber etalons — by ~ 30 dB. The balanced photodetector, based on a matched pair of Si PIN photodiodes, features a low gain, DC-coupled transimpedance amplifier and a high gain ($5 \cdot 10^4$ V/A) AC-coupled transimpedance amplifer with a low NEP of ~ 10 pW/$\sqrt{\text{Hz}}$ at 5 MHz. We use a LO power of 4 mW to achieve a shot noise to detector noise ratio of $\gtrsim 6$ dB at Fourier frequencies near $\Omega_\text{m}/2\pi = 4.32$ MHz. The DC photosignal is used to stabilize the path length of the interferometer by feedback to a piezo-actuated mirror in the LO path.

For characterization of measurement imprecision, the AC homodyne photosignal is sent directly to the spectrum analyzer (SA, Tektronix RSA5106A). For feedback cooling, the photosignal is split on a 20 dB directional coupler (Minicircuits ZFDC-20-3+). The weak port is sent to the SA. The strong port is directed to a low $V_\pi (\approx 5$ V) fiber intensity modulator (EOSPACE) in the feedback beam path. For the signal(feedback) power used in the reported cooling experiment, 5.5(0.1) μW, it was necessary to further amplify the photosignal in order to achieve the largest reported damping rates. A low noise voltage amplifier (Minicircuits ZFL-500LN) was thus placed after the directional coupler, followed by a voltage-controlled RF attenuator (Minicircuits ZX73-2500-S+), used to tune the feedback gain. In order to suppress feedback to higher-order beam modes, the photosignal was also passed through a 5 MHz low-pass filter (Minicircuits BLP-5+). The remaining electronic path length was manually fine tuned, by minimizing the feedback spring effect, to achieve a total feedback delay of $3\pi/2\Omega_\text{m} \approx 175$ ns.

F.3.3 Calibration of optomechanical coupling rate g_0

We determine the zero-point optomechanical coupling rate g_0 of our system by calibrating the transduction factor $G_{V\omega}$ connecting thermomechanical cavity frequency noise, $S_\omega(\Omega) \approx 8g_0^2 n_\text{th}/\Gamma_\text{m} \cdot |\chi_\text{m}(\Omega)/\chi_\text{m}(\Omega_\text{m})|^2$ with the measured homodyne photocurrent noise, $S_V(\Omega) = |G_{V\omega}(\Omega)|^2 S_\omega(\Omega)$ (here photocurrent has been referred to the voltage V measured at the output of the photodetector transimpedance amplifier). Following the method detailed in [66], we take advantage of the fact that the cavity transduces laser frequency fluctuations and cavity

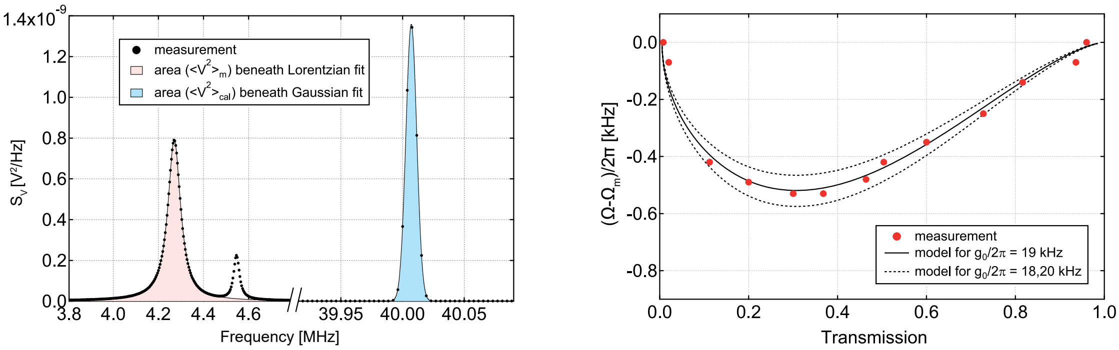

Supplementary Figure F.4 – Calibration of g_0. Left: thermal noise calibration of g_0 by using known RF frequency modulation. Right: Optical spring shift from a red-detuned sweep of the probe laser.

frequency fluctuations in the same way. To calibrate $G_{V\omega}$, we phase-modulate the sensor field at frequency Ω_{cal} with a known modulation depth β; this produces a reference tone of magnitude $S_V^{\mathrm{cal}}(\Omega) = \frac{1}{2}\Omega_{\mathrm{cal}}^2\beta^2\delta(\Omega-\Omega_{\mathrm{cal}})|G_{V\omega}(\Omega)|^2$. Comparing the integrated area beneath the reference tone, $\langle V^2\rangle_{\mathrm{cal}} = \frac{1}{2}\Omega_{\mathrm{cal}}^2\beta^2|G_{V\omega}(\Omega_{\mathrm{cal}})|^2$, and the thermomechanical noise peak, $\langle V^2\rangle_{\mathrm{m}} = 2g_0^2 n_{\mathrm{th}}|G_{V\omega}(\Omega_{\mathrm{m}})|^2$, gives,

$$g_0 = \frac{\beta\Omega_{\mathrm{cal}}}{2}\sqrt{\frac{1}{n_{\mathrm{th}}}\frac{\langle V^2\rangle_{\mathrm{m}}}{\langle V^2\rangle_{\mathrm{cal}}}}\left|\frac{G_{V\omega}(\Omega_{\mathrm{cal}})}{G_{V\omega}(\Omega_{\mathrm{m}})}\right|. \tag{F.3.1}$$

An example of a g_0 measurement is shown in fig. F.4. For this measurement, a buffer gas pressure of ~100 mbar was used to ensure good thermalization of the sample to probe head at $T \approx 3.3$ K ($n_{\mathrm{th}} \approx 1.6\cdot 10^4$). The resulting mechanical gas damping rate, $\Gamma_{\mathrm{m}} \approx 2\pi\cdot 64$ kHz, also allows us to ignore dynamic back-action effects for the moderate sensor power used, $P_{\mathrm{in}}^+ \approx 1$ μW. From separately determined $\beta \approx 0.057$ (inferred from a heterodyne beat measurement), $\Omega_{\mathrm{cal}} = 2\pi\cdot 40$ MHz (the value of $\Omega_{\mathrm{cal}} \gg \Omega_{\mathrm{m}}$ was chosen in order to reduce residual amplitude modulation), and $|G_{V\omega}(\Omega_c)|/|G_{V\omega}(\Omega_{\mathrm{m}})| \approx 0.98$, we infer $g_0 \approx 2\pi\cdot 21$ kHz.

As an independent measure of g_0, we red-detune the sensor field and compare the resulting shift of the mechanical frequency to a standard model for radiation pressure dynamical back-action Eq. (F.2.11). For this measurement, the mechanical damping rate was reduced by evacuating the buffer gas pressure to $< 10^{-3}$ mbar (Sec. F.3.4). In fig. F.4, the observed spring shift $\Delta\Omega_{\mathrm{ba}}$ is plotted versus cavity transmission for an input power of $P_{\mathrm{in}}^+ \approx 1\,\mu$W and a measured cavity linewidth of $\kappa \approx 2\pi\cdot 1070$ MHz. Incorporating the effect of measured cavity mode splitting (Sec. F.3.5) into the model, the measured spring shift is consistent with $g_0 \approx 2\pi\cdot 19$ kHz. The seperately determined values of 19 kHz and 21 kHz (Supplementary Figure F.4) are used to set error bars on estimates of C_0 and n_{imp} in the reported experiments (Supplementary Table 1).

F.3.4 Mechanical damping rate

To determine the intrinsic mechanical damping rate, Γ_{m}, it is necessary to minimize extraneous sources of physical and apparent damping; these include gas pressure, radiation pressure and bolomentric back-action, and slow thermal drift of the mechanical frequency. To mitigate the former, we conduct experiments with the buffer gas in our cryostat evacuated to a level $< 10^{-3}$ mbar. We verify that the oscillator still thermalizes with the sample holder to a temperature as low as 4 K (fig. F.5). To mitigate back-action and drift, we extract Γ_{m} from an impulse-response measurement conducted with a weak probe (feedback) beam power of < 50 nW.

The step-response measurement is conducted as follows: the mechanical oscillator is driven with radiation pressure by intensity modulating the feedback field at a frequency $\Omega_{\mathrm{d}} \approx \Omega_{\mathrm{m}}$. An RF switch is then used to rapidly shutter off the modulation. The subsequent exponential (ringdown) decay of the mechanical energy, with e-folding time $\tau = 2\pi/\Gamma_m$, is observed by demodulating the homodyne photocurrent at Ω_d with a demondulation bandwidth of $B \gg \Gamma_m$. An average of 100 such ringdowns in shown in the inset of fig. F.5. To record Γ_m vs temperature in this figure, it was necessary to track the frequency of the oscillator over a (temperature-induced) drift range of ~ 10 kHz. This was accomplished by incorporating the modulation and demodulations signal into a phase-locked-loop, using a digital lock-in amplifier (Zurich Instruments UHFLI).

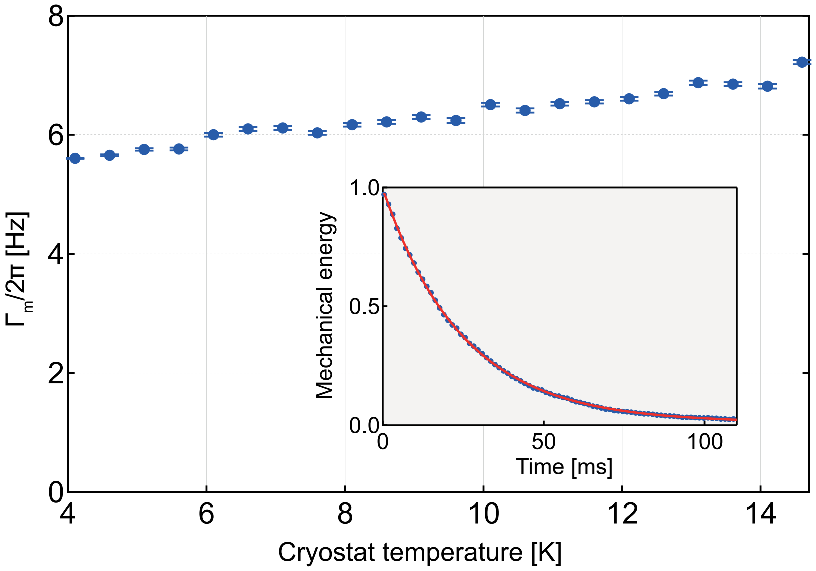

Supplementary Figure F.5 – Mechanical damping rate versus temperature. See Section F.3.4. Inset: ringdown example data (blue) and fit (red).

F.3.5 Mode splitting of probe cavity

To accurately estimate intracavity photon number, n_c, measurement imprecision, n_{imp}, and stochastic measurement back-action, n_{ba}, it is necessary to account for cross-coupling between optical cavity modes. In a whispering gallery microresonator, Rayleigh scattering from surface defects leads to coupling of otherwise degenerate clockwise (CW) and counter-clockwise (CCW) propagating modes [203] at a rate γ (Eq. (F.2.1a)). Since only the clock-wise mode (by convention) is driven by the field from the optical taper, this leads to an effective reduction of photon collection efficiency by a factor $(1+\gamma^2/\kappa^2)^2$ (Eq. (F.2.5)). At $\Delta = 0$, coherence between the CW and CCW fields leads to a further decrease in homodyne readout sensitivity by a factor $(1+\gamma^2/\kappa^2)^2/(1-\gamma^2/\kappa^2)^2$ (Eq. (F.2.19)) and the simplified form for n_{ba} given in Eq. (F.2.13).

As a confirmation of the coupled-mode model, we have characterized the steady state cavity transmission (Eq. (F.2.6)) as a function of external coupling strength, κ_{ex} (accessed by changing the taper's contact point on the microdisk's surface). As shown in Supplementary Figure F.6, the relationship of resonant transmission and total decay rate $\kappa = \kappa_0 + \kappa_{ex}$ shows good consistency with the model for an intrinsic decay rate of $\kappa_0 = 2\pi \cdot 440$ MHz and mode splitting $\gamma = 2\pi \cdot 360$ MHz. These values are used to analyze data presented in Figures 1-3 of the main text.

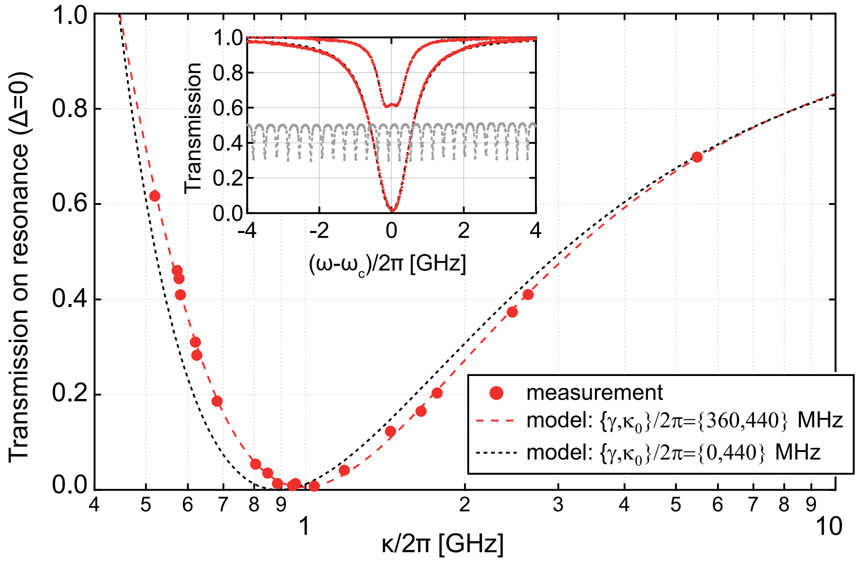

Supplementary Figure F.6 – Taper coupling ideality probed by cavity transmission. Inset: examples of cavity transmission (red) calibrated by using a pre-calibrated "comb" from a fiber loop cavity (gray).

F.4 Summary of experimental values and systematic uncertainty

Values used to determine experimental data points and their uncertainty in Figures 2-3 of the main text are summarized in Supplementary Table 1. We restrict our attention to sources of systematic uncertainty, as these were found to dominate over statistical uncertainty (e.g. for least-squares fitting of thermomechanical spectra). Uncertainties in $\{n_{\mathrm{imp}}, n_{\mathrm{tot}}\}$ (vertical axis in Figure 2 of main text) are primarily due to uncertainty in the value the cryostat temperature. Uncertainties in $\{n_{\mathrm{eff}}, n_{\mathrm{fb}}\}$ (vertical axis in Figure 3 of main text) are primarily due to uncertainty in both the cryostat temperature and the magnitude of extraneous back-action heating. Horizontal error bars in Figure 2 of the main text are primarily due to uncertainty in magnitude of the vacuum optomechanical coupling rate.

We highlight two sources of systematic uncertainty in the mechanical mode temperature: (1) discrepancy between the cryostat Cernox sensor reading and the temperature at the location of the sample, and (2) heating due to extraneous back-action. With regards to (1): two independently calibrated sensors placed in different locations on the sample holder read values $T = 4.1$ K and 4.6 K. We take this to be the systematic uncertainty. With regards to (2): Extraneous back-action heating is recorded versus optical power in Figure 2 of the main text. A similar measurement was made prior to the cooling experiment shown in Figure 3 of the main text. In the latter case, we observed approximately 0.4 K of measurement back-action heating for the $P_{\mathrm{in}}^{+} \approx 5.5\,\mu$W sensor power used. This is a factor of ~2 smaller than shown in Figure 2. The discrepancy is partly attributable to the use of a larger optical linewidth, $\kappa \approx 2\pi \cdot 1.85$ GHz, in the feedback experiment. As a conservative estimate, we assume a back-action heating of $(0.4, 1)$ K for Figure 3.

An estimate for the systematic uncertainty in Γ_m is made by taking the extreme values $2\pi \cdot (5.6, 5.8)$ Hz in the range $T = (4.1, 4.6)$ K in Supplementary Figure F.5. We note that in Figure 2 of the main text, extraneous back-action leads to a rise in effective bath temperature by as much as ~ 12 K, corresponding to $\Gamma_\mathrm{m} \approx 2\pi \cdot 6.6$ Hz. As we do not have a model for the influence of such localized heating on Γ_m, we have chosen to omit this possible source of uncertainty from the treatment in the main text.

Introduced in Sec. F.1	
x, p	position and momentum operator of the mechanical oscillator
$x_{\mathrm{zp}}, p_{\mathrm{zp}}$	$\sqrt{\text{variance}}$ of the position and momentum in the ground state
y	position estimate (apparent position inferred from measurement)
x_{imp}	imprecision of position estimate
$\Omega_{\mathrm{m}}, \Gamma_{\mathrm{m}}$	resonant frequency and damping rate of the oscillator
m	effective mass of the (extended) elastic oscillator mode
χ_{m}	intrinsic susceptibility of the oscillator position to an external force
T	temperature of the ambient thermal environment
F_{th}	Langevin force associated with the ambient thermal environment
$F_{\mathrm{ba}}, F_{\mathrm{ba,th}}$	Measurement back-action force, Langevin force associated with measurement noise
$F_{\mathrm{fb}}, F_{\mathrm{fb,th}}$	Feedback force, Langevin force associated with feedback noise
$\chi_{\mathrm{fb}}, \chi_{\mathrm{ba}}$	susceptibility of the linear feedback network, and back-action
$\chi_{\mathrm{eff}}, \Gamma_{\mathrm{eff}}$	effective susceptibility and damping rate of the oscillator in the presence of feedback and/or back-action
$n_{\mathrm{th}}, n_{\mathrm{ba}}, n_{\mathrm{fb}}$	effective thermal occupancy of the ambient thermal bath, measurement ('back-action') noise reservoir, and feedback noise reservoir.
n_{imp}	position imprecision referred to an effective thermal occupation
$n_{\mathrm{m}}, n_{\mathrm{m,min}}$	mean phonon occupancy of the oscillator in the presence of feedback, minimal possible occupation
$g_{\mathrm{fb}}, g_{\mathrm{fb,opt}}$	feedback gain, optimal value of feedback gain
Γ_{th}	thermal decoherence rate ($= n_{\mathrm{th}}\Gamma_{\mathrm{m}}$)
Introduced in Sec. F.2	
$\omega_{\mathrm{c}}, \omega_\ell, \lambda$	cavity resonance frequency, carrier frequency of optical input, wavelength of optical carrier ($\lambda = 2\pi c/\omega_\ell$, where c is the speed of light)
Δ_0, Δ	bare and renormalized laser-cavity detuning ($\Delta_0 = \omega_\ell - \omega_c$)
$\kappa_0, \kappa_{\mathrm{ex}}, \kappa$	intrinsic, coupling-induced, and total cavity decay rates ($\kappa = \kappa_0 + \kappa_{ex}$)
η_{c}	cavity coupling efficiency ($= \kappa_{\mathrm{ex}}/\kappa$)
γ	cavity mode splitting
$a_\pm, c$	intracavity field operator for the measurement (a) and feedback (c) optical mode, in a frame rotating at ω_ℓ; $+(-)$ refers to field propagating in (counter) the direction of injected power
$n_\pm$	steady state intracavity photon numbers
$s_{\mathrm{in}}^\pm$	field operators for modeling for the injected traveling wave, in a frame rotating at ω_ℓ
$\delta s_{\mathrm{in}}^\pm, \delta s_{\mathrm{vac}}^\pm$	white noise operators modeling the vaccuum fluctuations coupled in via the travelling wave inputs ('in'), and the intrinsic decay channels of the cavity ('vac')
$\chi_a^{(\gamma)}$	susceptibility of the optical field to cavity input noises, in the presence of splitting γ
g_0	vacuum optomechanical coupling rate
u	normalized mechanical position operator ($= x/x_{\mathrm{zp}}$)
$\delta f_{\mathrm{th}}, \xi_{\mathrm{th}}$	normalized thermal force and associated white noise operator
$f_{\mathrm{ba}}, \delta f_{\mathrm{ba}}$	dynamical and stochastic components of the normalized radiation pressure force from the measurement mode
f_{fb}	normalized radiation pressure feedback force
$\Omega_{\mathrm{ba}}, \Gamma_{\mathrm{ba}}$	mechanical frequency and damping rate renormalized by dynamic back-action
C_0	single-photon cooperativity ($= 4g_0^2/\kappa\Gamma_{\mathrm{m}}$)
Introduced in Sec. F.3	
G	optomechanical coupling expressed as a cavity frequency pull parameter ($= \partial\omega_c/\partial x = g_0/x_{\mathrm{zp}}$)

Supplementary Table F.1 – Glossary of important variables

Bibliography

[1] W. Commons, "Comet hale–bopp (c/1995 o1)," (1997), file: Comet Hale-Bopp 1995O1.jpg.

[2] W. Commons, "Ligo measurement of gravitational waves." (2016), file:LIGO measurement of gravitational waves.svg.png.

[3] LIGO Scientific Collaboration and Virgo Collaboration, Physical Review Letters **116**, 061102 (2016).

[4] N. Wiener, Acta Mathematica **55**, 117 (1930).

[5] P. R. Saulson, Phys. Rev. D **42**, 2437 (1990).

[6] H. A. Haus, *Waves and Fields in Optoelectronics* (Prentice-Hall, Inc., 1984).

[7] C. Gardiner and M. Collett, Phys. Rev. A **31**, 3761 (1985).

[8] A. Schliesser, R. Rivière, G. Anetsberger, O. Arcizet, and T. J. Kippenberg, Nature Physics **4**, 415 (2008).

[9] D. E. Chang, C. A. Regal, S. B. Papp, D. J. Wilson, J. Ye, O. Painter, H. J. Kimble, and P. Zoller, Proceedings of the National Academy of Sciences **107**, 1005 (2009).

[10] A. Schliesser, P. Del'Haye, N. Nooshi, K. J. Vahala, and T. J. Kippenberg, Physical Review Letters **97** (2006), 10.1103/physrevlett.97.243905.

[11] K. Ekinci and M. Roukes, Rev. Sci. Instru. **76**, 061101 (2005).

[12] A. N. Cleland and M. L. Roukes, Nature **392**, 160 (1998).

[13] H. Mamin and D. Rugar, App. Phys. Lett. **79**, 3358 (2001).

[14] K. Jensen, K. Kim, and A. Zettl, Nature Nano. **3**, 533 (2008).

[15] K. C. Schwab and M. L. Roukes, Physics Today **58**, 36 (2005).

[16] M. D. LaHaye, Science **304**, 74 (2004).

[17] N. Flowers-Jacobs, D. Schmidt, and K. Lehnert, Phys. Rev. Lett. **98**, 096804 (2007).

[18] C. A. Regal, J. D. Teufel, and K. W. Lehnert, Nat. Phys. **4**, 555 (2008).

[19] J. D. Teufel, D. Li, M. S. Allman, K. Cicak, A. J. Sirois, J. D. Whittaker, and R. W. Simmonds, Nature **471**, 204 (2011).

[20] T. J. Kippenberg and K. J. Vahala, Science **321**, 1172 (2008).

[21] M. Aspelmeyer, T. J. Kippenberg, and F. Marquardt, Rev. Mod. Phys. **86**, 1391 (2014).

[22] C. M. Caves, Phys. Rev. Lett. **45**, 75 (1980).

[23] J. Chan, T. P. M. Alegre, A. H. Safavi-Naeini, J. T. Hill, A. Krause, S. Groeblacher, M. Aspelmeyer, and O. Painter, Nature **478**, 89 (2011).

[24] E. Verhagen, S. Deléglise, S. Weis, A. Schliesser, and T. J. Kippenberg, Nature **482**, 63 (2012).

[25] Teufel, J. D. et. al., Nature **475**, 359 (2011).

[26] I. Wilson-Rae, N. Nooshi, W. Zwerger, and T. J. Kippenberg, Phys. Rev. Lett. **99**, 093901 (2007).

[27] V. B. Braginsky, V. B. Braginsky, and F. Y. Khalili, *Quantum measurement* (Cambridge University Press, 1995).

[28] D. J. Wilson, V. Sudhir, N. Piro, R. Schilling, A. Ghadimi, and T. J. Kippenberg, Nature **524**, 325 (2015).

[29] A. G. Krause, T. D. Blasius, and O. Painter, arXiv preprint arXiv:1506.01249 (2015).

[30] T. P. Purdy, R. W. Peterson, and C. A. Regal, Science **339**, 801 (2013).

[31] J. D. Teufel, F. Lecocq, and R. W. Simmonds, Phys. Rev. Lett. **116**, 013602 (2016).

[32] J.-M. Courty, A. Heidmann, and M. Pinard, Eur. Phys. J. D **17**, 399â€“408 (2001).

[33] A. Szorkovszky, A. C. Doherty, G. I. Harris, and W. P. Bowen, Phys. Rev. Lett. **107**, 213603 (2011).

[34] D. Kleckner and D. Bouwmeester, Nature **444**, 75 (2006).

[35] J. D. Thompson, B. M. Zwickl, A. M. Jayich, F. Marquardt, S. M. Girvin, and J. G. E. Harris, Nature **452**, 72 (2008).

[36] A. Schliesser, G. Anetsberger, R. RiviÃ¨re, O. Arcizet, and T. J. Kippenberg, New J. Phys. **10**, 095015 (2008).

[37] M. Eichenfield, J. Chan, R. M. Camacho, K. J. Vahala, and O. Painter, Nature **462**, 78 (2009).

[38] D. Van Thourhout and J. Roels, Nat. Phot. **4**, 211 (2010).

[39] S. Spillane, T. Kippenberg, O. Painter, and K. Vahala, Phys. Rev. Lett. **91**, 043902 (2003).

[40] G. Anetsberger, O. Arcizet, Q. P. Unterreithmeier, R. RiviÃ¨re, A. Schliesser, E. M. Weig, J. P. Kotthaus, and T. J. Kippenberg, Nat. Phys. **5**, 909 (2009).

[41] C. Doolin, P. Kim, B. Hauer, A. MacDonald, and J. Davis, New J. Phys. **16**, 035001 (2014).

[42] R. M. Cole, G. A. Brawley, V. P. Adiga, R. De Alba, J. M. Parpia, B. Ilic, H. G. Craighead, and W. P. Bowen, Phys. Rev. App. **3**, 024004 (2015).

[43] L. Neuhaus, E. van Brackel, E. Gavartin, P. Verlot, and T. Kippenberg, in *CLEO: Science and Innovations* (Optical Society of America, 2012) pp. CW3M–2.

[44] E. Gavartin, P. Verlot, and T. J. Kippenberg, Nat. Nano. **7**, 509 (2012).

[45] G. Anetsberger, E. Gavartin, O. Arcizet, Q. P. Unterreithmeier, E. M. Weig, M. L. Gorodetsky, J. P. Kotthaus, and T. J. Kippenberg, Phys. Rev. A **82** (2010).

[46] V. Sudhir, D. Wilson, R. Schilling, H. Schütz, S. Fedorov, A. Ghadimi, A. Nunnenkamp, and T. Kippenberg, Physical Review X **7**, 011001 (2017).

[47] S. S. Verbridge, J. M. Parpia, R. B. Reichenbach, L. M. Bellan, and H. G. Craighead, J. Appl. Phys. **99**, 124304 (2006).

[48] J. Rieger, A. Isacsson, M. J. Seitner, J. P. Kotthaus, and E. M. Weig, Nature Communications **5** (2014), 10.1038/ncomms4345.

[49] S. Schmid, K. D. Jensen, K. H. Nielsen, and A. Boisen, Phys. Rev. B **84**, 165307 (2011).

[50] G. I. González and P. R. Saulson, The Journal of the Acoustical Society of America **96**, 207 (1994).

[51] Q. P. Unterreithmeier, T. Faust, and J. P. Kotthaus, Phys. Rev. Lett. **105**, 027205 (2010).

[52] L. G. Villanueva and S. Schmid, Phys. Rev. Lett. **113**, 227201 (2014).

[53] S. S. Verbridge, R. Ilic, H. Craighead, and J. M. Parpia, App. Phys. Lett. **93**, 013101 (2008).

[54] A. Ghadimi, S. Fedorov, N. Engelsen, M. Bereyhi, R. Schilling, H. Schütz, D. J. Wilson, and T. J. Kippenberg, "Phononic crystal nanostrings with ultra-high quality factors," .

[55] J. D. Teufel, T. Donner, M. A. Castellanos-Beltran, J. W. Harlow, and K. W. Lehnert, Nat. Nano. **4**, 820 (2009).

[56] B. M. Zwickl, W. E. Shanks, A. M. Jayich, C. Yang, A. C. Bleszynski Jayich, J. D. Thompson, and J. G. E. Harris, Appl. Phys. Lett. **92**, 103125 (2008).

[57] D. K. Armani, T. J. Kippenberg, S. M. Spillane, and K. J. Vahala, Nature **421**, 925 (2003).

[58] I. S. Grudinin, V. S. Ilchenko, and L. Maleki, Phys. Rev. A **74**, 063806 (2006).

[59] A. A. Savchenkov, A. B. Matsko, V. S. Ilchenko, and L. Maleki, Opt. Express **15**, 6768 (2007).

[60] H. Lee, T. Chen, J. Li, K. Y. Yang, S. Jeon, O. Painter, and K. J. Vahala, Nat. Phot. **6**, 369 (2012).

[61] M. Oxborrow, in *Lasers and Applications in Science and Engineering* (International Society for Optics and Photonics, 2007) pp. 64520J–64520J.

[62] M. Borselli, T. Johnson, and O. Painter, Opt. Express **13**, 1515 (2005).

[63] T. Kippenberg, J. Kalkman, A. Polman, and K. Vahala, Phys. Rev. A **74** (2006).

[64] M. L. Povinelli, M. Loncar, M. Ibanescu, E. J. Smythe, S. G. Johnson, F. Capasso, and J. D. Joannopoulos, Opt. Lett. **30**, 3042 (2005).

[65] G. Anetsberger, *Novel cavity optomechanical systems at the micro-and nanoscale and quantum measurements of nanomechanical oscillators*, Ph.D. thesis, lmu (2010).

[66] M. L. Gorodetsky, A. Schliesser, G. Anetsberger, S. Deleglise, and T. J. Kippenberg, Opt. Exp. **18**, 23236 (2010).

[67] W. Zhang, M. Martin, C. Benko, J. Hall, J. Ye, C. Hagemann, T. Legero, U. Sterr, F. Riehle, G. Cole, *et al.*, Opt. Lett. **39**, 1980 (2014).

[68] C. H. Metzger and K. Karrai, Nature **432**, 1002 (2004).

[69] D. Wilson, C. Regal, S. Papp, and H. Kimble, Phys. Rev. Lett. **103**, 207204 (2009).

[70] O. Arcizet, R. Rivière, A. Schliesser, G. Anetsberger, and T. J. Kippenberg, Phys. Rev. A **80**, 021803 (2009).

[71] R. O. Pohl, X. Liu, and E. Thompson, Rev. Mod. Phys. **74**, 991 (2002).

[72] Q. P. Unterreithmeier, E. M. Weig, and J. P. Kotthaus, Nature **458**, 1001 (2009).

[73] P.-L. Yu, T. Purdy, and C. Regal, Phys. Rev. Lett. **108**, 083603 (2012).

[74] T. Bagci, A. Simonsen, S. Schmid, L. G. Villanueva, E. Zeuthen, J. Appel, J. M. Taylor, A. Sørensen, K. Usami, A. Schliesser, *et al.*, Nature **507**, 81 (2014).

[75] S. Schmid, T. Bagci, E. Zeuthen, J. M. Taylor, P. K. Herring, M. C. Cassidy, C. M. Marcus, L. G. Villanueva, B. Amato, A. Boisen, *et al.*, J. App. Phys. **115**, 054513 (2014).

[76] O. Arcizet, V. Jacques, A. Siria, P. Poncharal, P. Vincent, and S. Seidelin, Nat. Phys. **7**, 879 (2011).

[77] K. Hammerer, M. Aspelmeyer, E. S. Polzik, and P. Zoller, Phys. Rev. Lett. **102**, 020501 (2009).

[78] A. Jöckel, A. Faber, T. Kampschulte, M. Korppi, M. T. Rakher, and P. Treutlein, Nature Nano. (2014).

[79] E. Vetsch, D. Reitz, G. Sagué, R. Schmidt, S. Dawkins, and A. Rauschenbeutel, Phys. Rev. Lett. **104**, 203603 (2010).

[80] S. Gröblacher, A. Trubarov, N. Prigge, G. D. Cole, M. Aspelmeyer, and J. Eisert, Nat. Comm. **6** (2015).

[81] M. Metcalfe, Applied Physics Reviews **1**, 031105 (2014).

[82] A. G. Krause, M. Winger, T. D. Blasius, Q. Lin, and O. Painter, Nat. Phot. **6**, 768 (2012).

[83] J. Czochralski, Chem. **92**, 219 (1918), cited By 1.

[84] W. Commons, "Beginn des silizium floatingzone-prozess," (2005), file: Si-crystal floatingzone.jpg.

[85] H. Theuerer, "Method of processing semiconductive materials," (1962), uS Patent 3,060,123.

[86] K. R. Williams, K. Gupta, and M. Wasilik, Journal of Microelectromechanical Systems **12**, 761 (2003).

[87] T. Ito, T. Nakamura, and H. Ishikawa, IEEE Transactions on Electron Devices **29**, 498 (1982).

[88] T. Ghani, M. Armstrong, C. Auth, M. Bost, P. Charvat, G. Glass, T. Hoffmann, K. Johnson, C. Kenyon, J. Klaus, B. McIntyre, K. Mistry, A. Murthy, J. Sandford, M. Silberstein, S. Sivakumar, P. Smith, K. Zawadzki, S. Thompson, and M. Bohr, in *IEEE International Electron Devices Meeting 2003* (2003) pp. 11.6.1–11.6.3.

[89] W. Kern and R. S. Rosler, Journal of Vacuum Science and Technology **14**, 1082 (1977), https://doi.org/10.1116/1.569340 .

[90] C. Morosanu and E. Segal, Thin Solid Films **91**, 251 (1982).

[91] P. Temple-Boyer, C. Rossi, E. Saint-Etienne, and E. Scheid, Journal of Vacuum Science & Technology A: Vacuum, Surfaces, and Films **16**, 2003 (1998), https://doi.org/10.1116/1.581302 .

[92] A. Noskov, E. Gorokhov, G. Sokolova, E. Trukhanov, and S. Stenin, Thin Solid Films **162**, 129 (1988).

[93] R. T. Howe and R. S. Muller, IEEE Transactions on Electron Devices **33**, 499 (1986).

[94] K. Pister, M. Judy, S. Burgett, and R. Fearing, Sensors and Actuators A: Physical **33**, 249 (1992).

[95] C. Keller and M. Ferrari, in *Proc. Solid-State Sensor and Actuator Workshop* (1994) pp. 12–16.

[96] J. W. Judy, Smart Materials and Structures **10**, 1115 (2001).

[97] K. Ota, K. Sugihara, H. Sayama, T. Uchida, H. Oda, T. Eimori, H. Morimoto, and Y. Inoue, in *Digest. International Electron Devices Meeting,* (2002) pp. 27–30.

[98] J. P. Colinge, M. H. Gao, A. Romano-Rodriguez, H. Maes, and C. Claeys, in *International Technical Digest on Electron Devices* (1990) pp. 595–598.

[99] D. Maier-Schneider, A. Köprülülü, S. B. Holm, and E. Obermeier, Journal of Micromechanics and Microengineering **6**, 436 (1996).

[100] *Stress and Microstructure in Phosphorus Doped Polycrystalline Silicon*, Vol. 276 (Cambridge University Press, 1992).

[101] D. Maier-Schneider, J. Maibach, E. Obermeier, and D. Schneider, Journal of Micromechanics and Microengineering **5**, 121 (1995).

[102] B. E. Deal and A. S. Grove, Journal of Applied Physics **36**, 3770 (1965), https://doi.org/10.1063/1.1713945 .

[103] D. S. A. S. b. G. n. D. Laermer, Franz (Stuttgart, “Method of anisotropically etching silicon,” (1996).

[104] R. Haken, I. Baker, and J. Beynon, Thin Solid Films **18**, S3 (1973).

[105] T. Kippenberg, S. Spillane, D. Armani, and K. Vahala, Applied Physics Letters **83**, 797 (2003), cited By 101.

[106] F. Ramiro-Manzano, N. Prtljaga, L. Pavesi, G. Pucker, and M. Ghulinyan, Optics Express **20**, 22934 (2012), cited By 20.

[107] M. Ghulinyan, M. Bernard, R. Bartali, and G. Pucker, Applied Surface Science **359**, 679 (2015).

[108] K. Williams and R. Muller, Journal of Microelectromechanical Systems **5**, 256 (1996), cited By 398.

[109] A. Dillon, A. Ott, J. Way, and S. George, Surface Science **322**, 230 (1995), cited By 330.

[110] M. D. Groner, F. H. Fabreguette, J. W. Elam, and S. M. George, Chemistry of Materials **16**, 639 (2004), http://dx.doi.org/10.1021/cm0304546 .

[111] H. H and W. J, “Process for polishing semiconductor materials,” (1965), uS Patent 3,170,273.

[112] L. Blake and E. Mendel, Solid State Technology **13**, 42 (1970).

[113] M. Chow, J. Cronin, W. Guthrie, C. Kaanta, B. Luther, W. Patrick, K. Perry, and C. Standley, "Method for producing coplanar multi-level metal/insulator films on a substrate and for forming patterned conductive lines simultaneously with stud vias," (1988), uS Patent 4,789,648.

[114] A. Brand, A. Haranahalli, N. Hsieh, Y. Lin, G. Sery, N. Stenton, B. Woo, S. Ahmed, M. Bohr, S. Thompson, *et al.*, Intel Technology Journal Q **3**, 1998 (1998).

[115] J. H. Smith, S. Montague, J. J. Sniegowski, J. R. Murray, and P. J. McWhorter, in *Proceedings of International Electron Devices Meeting* (1995) pp. 609–612.

[116] L. M. Cook, Journal of non-crystalline solids **120**, 152 (1990).

[117] P. B. Zantye, A. Kumar, and A. Sikder, Materials Science and Engineering: R: Reports **45**, 89 (2004).

[118] J. K. W. Yang and K. K. Berggren, Journal of Vacuum Science & Technology B: Microelectronics and Nanometer Structures Processing, Measurement, and Phenomena **25**, 2025 (2007), http://avs.scitation.org/doi/pdf/10.1116/1.2801881 .

[119] D. L. Olynick, B. Cord, A. Schipotinin, D. F. Ogletree, and P. J. Schuck, Journal of Vacuum Science & Technology B, Nanotechnology and Microelectronics: Materials, Processing, Measurement, and Phenomena **28**, 581 (2010), https://doi.org/10.1116/1.3425632 .

[120] H. Namatsu, Y. Takahashi, K. Yamazaki, T. Yamaguchi, M. Nagase, and K. Kurihara, Journal of Vacuum Science & Technology B: Microelectronics and Nanometer Structures Processing, Measurement, and Phenomena **16**, 69 (1998), http://avs.scitation.org/doi/pdf/10.1116/1.589837 .

[121] T. H. P. Chang, Journal of Vacuum Science and Technology **12**, 1271 (1975), https://doi.org/10.1116/1.568515 .

[122] G. Owen and P. Rissman, Journal of Applied Physics **54**, 3573 (1983), https://doi.org/10.1063/1.332426 .

[123] W. Henschel, Y. M. Georgiev, and H. Kurz, Journal of Vacuum Science & Technology B: Microelectronics and Nanometer Structures Processing, Measurement, and Phenomena **21**, 2018 (2003), http://avs.scitation.org/doi/pdf/10.1116/1.1603284 .

[124] R. Riviere, O. Arcizet, A. Schliesser, and T. J. Kippenberg, Rev. Sci. Instrum. **84**, 043108 (2013).

[125] V. Sudhir, R. Schilling, S. A. Fedorov, H. Schütz, D. J. Wilson, and T. J. Kippenberg, Physical Review X **7**, 031055 (2017).

[126] V. Braginsky and A. Manukin, Sov. Phys. JETP **25**, 653 (1967).

[127] C. M. Caves, M. Zimmermann, K. S. Thorne, and R. W. Drever, Rev. Mod. Phys. **52**, 341 (1980).

[128] M. Jaekel and S. Reynaud, Europhys. Lett. **13**, 301 (1990).

[129] C. Fabre, M. Pinard, S. Bourzeix, A. Heidmann, E. Giacobino, and S. Reynaud, Phys. Rev. A **49**, 1337 (1994).

[130] S. Mancini and P. Tombesi, Phys. Rev. A **49**, 4055 (1994).

[131] S. P. Vyatchanin and E. A. Zubova, Phys. Lett. A **201**, 269 (1995).

[132] A. Buonanno and Y. Chen, Phys. Rev. D **64**, 042006 (2001).

[133] H. J. Kimble, Y. Levin, A. B. Matsko, K. S. Thorne, and S. P. Vyatchanin, Phys. Rev. D **65**, 022002 (2001).

[134] Y. Chen, S. L. Danilishin, F. Y. Khalili, and H. Müller-Ebhardt, General Relativity and Gravitation **43**, 671 (2011).

[135] J. Aasi *et al.*, Nature Phot. **7**, 613 (2013).

[136] H. Vahlbruch, M. Mehmet, K. Danzmann, and R. Schnabel, Phys. Rev. Lett. **117**, 110801 (2016).

[137] M. Aspelmeyer, T. J. Kippenberg, and F. Marquardt, Rev. Mod. Phys. **86**, 1391 (2014).

[138] D. J. Wilson, V. Sudhir, N. Piro, R. Schilling, A. Ghadimi, and T. J. Kippenberg, Nature **524**, 325 (2015).

[139] D. W. C. Brooks, T. Botter, S. Schreppler, T. P. Purdy, N. Brahms, and D. M. Stamper-Kurn, Nature **488**, 476 (2012).

[140] A. H. Safavi-Naeini, S. Gröblacher, J. T. Hill, J. Chan, M. Aspelmeyer, and O. Painter, Nature **500**, 185 (2013).

[141] T. P. Purdy, P. Yu, R. W. Peterson, N. S. Kampel, and C. A. Regal, Physical Review X **3**, 031012 (2013).

[142] W. H. P. Nielsen, Y. Tsaturyan, C. B. Møller, E. S. Polzik, and A. Schliesser, Proc. Natl. Acad. Sci. **114**, 62 (2017).

[143] F. Y. Khalili, H. Miao, H. Yang, A. H. Safavi-Naeini, O. Painter, and Y. Chen, Phys. Rev. A **86**, 033840 (2012).

[144] A. Weinstein, C. Lei, E. Wollman, J. Suh, A. Metelmann, A. Clerk, and K. Schwab, Phys. Rev. X **4**, 041003 (2014).

[145] T. P. Purdy, P.-L. Yu, N. S. Kampel, R. W. Peterson, K. Cicak, R. W. Simmonds, and C. A. Regal, Phys. Rev. A **92**, 031802 (2015).

[146] M. Underwood, D. Mason, D. Lee, H. Xu, L. Jiang, A. B. Shkarin, K. Børkje, S. M. Girvin, and J. G. E. Harris, Phys. Rev. A **92**, 061801 (2015).

[147] M. Evans *et al.*, Phys. Rev. Lett. **114**, 161102 (2015).

[148] P. Verlot, A. Tavernarakis, T. Briant, P.-F. Cohadon, and A. Heidmann, Phys. Rev. Lett. **104**, 133602 (2010).

[149] K. Borkje, A. Nunnenkamp, B. Zwickl, C. Yang, J. Harris, and S. Girvin, Phys. Rev. A **82**, 13818 (2010).

[150] T. P. Purdy, K. E. Grutter, K. Srinivasan, and J. M. Taylor, arXiv:1605.05664 (2016).

[151] V. B. Braginsky, M. L. Gorodetsky, F. Y. Khalili, and K. S. Thorne, Phys. Rev. D **61**, 044002 (2000).

[152] T. Corbitt, Y. Chen, F. Khalili, D. Ottaway, S. Vyatchanin, S. Whitcomb, and N. Mavalvala, Phys. Rev. A **73**, 023801 (2006).

[153] R. Schilling, H. Schütz, A. Ghadimi, V. Sudhir, D. Wilson, and T. Kippenberg, Phys. Rev. Applied **5**, 054019 (2016).

[154] L. Buchmann, S. Schreppler, J. Kohler, N. Spethmann, and D. Stamper-Kurn, Phys. Rev. Lett. **117**, 030801 (2016).

[155] J. B. Clark, F. Lecocq, R. W. Simmonds, J. Aumentado, and J. D. Teufel, Nature Physics **12**, 683 (2016).

[156] T. Caniard, P. Verlot, T. Briant, P.-F. Cohadon, and A. Heidmann, Physical Review Letters **99** (2007), 10.1103/physrevlett.99.110801.

[157] F. Marino, F. Cataliotti, A. Farsi, M. de Cumis, and F. Marin, Physical Review Letters **104**, 073601 (2010).

[158] P. Cohadon, A. Heidmann, and M. Pinard, Phys. Rev. Lett. **83**, 3174 (1999).

[159] S. Fedorov, V. Sudhir, R. Schilling, H. Schütz, D. Wilson, and T. Kippenberg, Physics Letters A (2017), 10.1016/j.physleta.2017.05.046.

[160] V. Giovannetti, S. Lloyd, and L. Maccone, Science **306**, 1330 (2004).

[161] J. Suh, A. J. Weinstein, C. U. Lei, E. E. Wollman, S. K. Steinke, P. Meystre, A. A. Clerk, and K. C. Schwab, Science **344**, 1262 (2014).

[162] F. Lecocq, J. Clark, R. Simmonds, J. Aumentado, and J. Teufel, Physical Review X **5**, 041037 (2015).

[163] N. Kampel, R. Peterson, R. Fischer, P.-L. Yu, K. Cicak, R. Simmonds, K. Lehnert, and C. Regal, Phys. Rev. X **7**, 021008 (2017).

[164] B. Abbott, R. Abbott, R. Adhikari, P. Ajith, B. Allen, G. Allen, R. Amin, S. Anderson, W. Anderson, M. Arain, *et al.*, New Journal of Physics **11**, 073032 (2009).

[165] P. Bushev, D. Rotter, A. Wilson, F. Dubin, C. Becher, J. Eschner, R. Blatt, V. Steixner, P. Rabl, and P. Zoller, Physical review letters **96**, 043003 (2006).

[166] B. d'Urso, B. Odom, and G. Gabrielse, Physical review letters **90**, 043001 (2003).

[167] H. M. Wiseman and G. J. Milburn, *Quantum measurement and control* (Cambridge university press, 2009).

[168] C. Sayrin, I. Dotsenko, X. Zhou, B. Peaudecerf, T. Rybarczyk, S. Gleyzes, P. Rouchon, M. Mirrahimi, H. Amini, M. Brune, *et al.*, Nature **477**, 73 (2011).

[169] R. Vijay, C. Macklin, D. Slichter, S. Weber, K. Murch, R. Naik, A. N. Korotkov, and I. Siddiqi, Nature **490**, 77 (2012).

[170] M. Hatridge, S. Shankar, M. Mirrahimi, F. Schackert, K. Geerlings, T. Brecht, K. Sliwa, B. Abdo, L. Frunzio, S. M. Girvin, *et al.*, Science **339**, 178 (2013).

[171] A. A. Clerk, M. H. Devoret, S. M. Girvin, F. Marquardt, and R. J. Schoelkopf, Reviews of Modern Physics **82**, 1155 (2010).

[172] S. Mancini, D. Vitali, and P. Tombesi, Physical Review Letters **80**, 688 (1998).

[173] H. Wiseman, Physical Review A **51**, 2459 (1995).

[174] T. Westphal, D. Friedrich, H. Kaufer, K. Yamamoto, S. Gossler, H. Mueller-Ebhardt, S. L. Danilishin, F. Y. Khalili, K. Danzmann, and R. Schnabel, Physical Review A **85**, 063806 (2012).

[175] K. W. Murch, K. L. Moore, S. Gupta, and D. M. Stamper-Kurn, Nature Physics **4**, 561 (2008).

[176] J. D. Teufel, T. Donner, D. Li, J. W. Harlow, M. S. Allman, K. Cicak, A. J. Sirois, J. D. Whittaker, K. W. Lehnert, and R. W. Simmonds, Nature **475**, 359 (2011).

[177] M. Poggio, C. Degen, H. Mamin, and D. Rugar, Physical Review Letters **99**, 017201 (2007).

[178] T. Li, S. Kheifets, and M. G. Raizen, Nature Physics **7**, 527 (2011).

[179] C. Genes, D. Vitali, P. Tombesi, S. Gigan, and M. Aspelmeyer, Physical Review A **77**, 033804 (2008).

[180] K. Jacobs, H. I. Nurdin, F. W. Strauch, and M. James, Physical Review A **91**, 043812 (2015).

[181] Y. Tsaturyan, A. Barg, E. S. Polzik, and A. Schliesser, Nature Nanotechnology (2017), 10.1038/nnano.2017.101.

[182] T. Buehler, D. Reilly, R. Starrett, A. D. Greentree, A. Hamilton, A. Dzurak, and R. Clark, Applied Physics Letters **86**, 143117 (2005).

[183] R. De Alba, F. Massel, I. R. Storch, T. Abhilash, A. Hui, P. L. McEuen, H. G. Craighead, and J. M. Parpia, Nature nanotechnology **11**, 741 (2016).

[184] A. A. Clerk, M. H. Devoret, S. M. Girvin, F. Marquardt, and R. J. Schoelkopf, Rev. Mod. Phys. **82**, 1155 (2010).

[185] L. B. Mercer, J. Lightwave Tech. **9**, 485 (1991).

[186] V. B. Braginsky, M. L. Gorodetsky, and S. P. Vyatchanin, Phys. Lett. A **264**, 1 (1999).

[187] V. B. Braginsky, M. L. Gorodetsky, and S. P. Vyatchanin, Phys. Lett. A **271**, 303 (2000).

[188] G. Lindblad, Rep. Math. Phys. **10**, 393 (1976).

[189] S. Gnutzmann and F. Haake, Z. Phys. B **101**, 263 (1996).

[190] F. Haake and R. Reibold, Phys. Rev. A **32**, 2462 (1985).

[191] K. Jacobs, I. Tittonen, H. Wiseman, and S. Schiller, Phys. Rev. A **60**, 538 (1999).

[192] V. Giovannetti and D. Vitali, Phys. Rev. A **63**, 023812 (2001).

[193] N. Wiener, *Extrapolation, Interpolation and Smoothing of Stationary Time Series* (MIT Technology Press, 1949).

[194] M. Athans, IEEE Transactions on Automatic Control **16**, 529 (1971).

[195] T. Kailath, *Linear Systems* (Prentice-Hall, 1980).

[196] M. James, H. Nurdin, and I. Petersen, IEEE Transactions on Automatic Control **53**, 1787 (2008).

[197] H. I. Nurdin, M. R. James, and I. R. Petersen, Automatica **45**, 1837 (2009).

[198] Y. Makhlin, G. Schön, and A. Shnirman, Rev. Mod. Phys. **73**, 357 (2001).

[199] C. W. Gardiner and P. Zoller, *Quantum Noise* (Springer, 2004).

[200] M. Lax, Phys. Rev. **129**, 2342 (1963).

[201] E. Gavartin, P. Verlot, and T. J. Kippenberg, Nature Comm. **4**, 2860 (2013).

[202] K. Y. Fong, M. Poot, X. Han, and H. X. Tang, Phys. Rev. A **90**, 023825 (2014).

[203] T. Kippenberg, S. Spillane, and K. Vahala, Opt. Lett. **27**, 1669 (2002).

[204] M. Aspelmeyer, T. J. Kippenberg, and F. Marquardt, Rev. Mod. Phys. **86**, 1391 (2014).

[205] H. J. Carmichael, J. Opt. Soc. Am. B **4**, 1516 (1987).

[206] R. O. Pohl, X. Liu, and E. Thompson, Rev. Mod. Phys. **74**, 991 (2002).

Ryan D. Schilling

CONTACT INFORMATION

30 Avenue de Tivoli
1007 Lausanne, VD
Switzerland
+41 78 891 2261
ryan.schilling@epfl.ch
schillingis@gmail.com

EDUCATION

Swiss Federal Institute of Technology (EPFL), Lausanne, Switzerland

Ph.D., Electrical Engineering (expected January 2018)

- Dissertation: "Quantum Optomechanics at Room Temperature"
- Advisor: Prof. Tobias J. Kippenberg
- Courses: nonlinear optics, quantum optics, machine learning
- Teaching: general physics I-IV, digital systems design with VHDL

Research: Led the development of a new class of optomechanical sensor where the state transfer between light and mechanics is of the same order as the mechanical decoherence rate (at ambient and cryogenic temperatures). This allowed for the observation of non-classical correlations of light in both temperature regimes [3,5]. This advance was facilitated by integrating a high-stress Si_3N_4 nanobeam in the near field of a SiO_2 optical whispering gallery mode resonator. Chemical mechanical planarization was utilized to achieve separations between these micron-scale elements as small as 20 nm. Careful process design allowed for state-of-the-art performance of the optical and mechanical resonators, while achieving strong evanescent coupling [6].

University of Toronto, Toronto, Canada

M.S., Electrical and Computer Engineering (January 2013)

- Dissertation: "Self-Referencing and Sensitivity Optimization in Photonic Crystal Slabs for Biosensing Applications"
- Advisor: Prof. Ofer Levi
- Courses: computational EM, photonic devices, nanofabrication technology

Research: Developed a photonic crystal-based microfluidic refractive index sensor for the purpose of label-free biosensing. A novel self-referencing scheme was proposed and demonstrated for the purpose of minimizing environmental noise, such as temperature fluctuations. A photonic crystal design that allows the evanescent field to be shifted asymmetrically from the substrate into the sensing fluid was also proposed and demonstrated. These results were presented at several international conferences, including CLEO and Photonics West.

University of British Columbia, Vancouver, Canada
Degree with distinction (Dean's honor list all eligible terms)

B.S., Electrical and Computer Engineering (June 2010)

Thesis project: Design and development of a wrist-worn continuous ECG and SpO_2 monitor that streams to a repository via a bluetooth smartphone connection. Received offer from supervising professor to further develop project.
Extracurricular research:

- Fabrication and electrical characterization of nanofibers for use in gas sensing (supervisor: Prof. K. Cheung, 2010)

- Registration of computed tomography and ultrasound kidney meshes using principle component analysis (supervisor: Prof. S. Salcudean, 2009)

Technical Skills

Laboratory
- Precision interferometric measurements utilizing fiber and free-space optics
- Design and construction of high vacuum systems with nanomechanical stages, electronics, optics

Cleanroom
- Chemical-mechanical planarization for vertical integration of optical, mechanical, and electronic systems
- Wet-etch techniques for realizing chip-integrated high finesse optical cavities
- Electron-beam lift-off processes for integrating capacitive elements in optomechanical systems
- Thin film deposition (LPCVD, PECVD, ALD, metal evaporation/lift-off)
- Film characterization (ellipsometry, SEM, AFM, FTIR)
- Etching (RIE, ICP, IBE, various wet-etches, chemical-mechanical planarization)

Programming
- C++, MATLAB, Java, HDL

Awards

2011 NSERC (Natural Sciences and Engineering Research Council) CREATE Graduate Scholarship

2010 NSERC CREATE Graduate Scholarship

2010 NSERC Undergraduate Research Award

2009 NSERC Undergraduate Research Award

Publications

[1] A.H. Ghadimi, S.A. Fedorov, N.J. Engelsen, M.J. Bereyhi, R. Schilling, D.J. Wilson, T.J. Kippenberg. "Strain Engineering for Ultra-coherent Nanomechanical Oscillators," *arXiv:1711.06247* (2017).

[2] C. Javerzac-Galy, A. Kumar, R. Schilling, N. Piro, S. Khorasani, M. Barbone, I. Goykhman, J.B. Khurgin, A.C. Ferrari, T.J. Kippenberg. "Excitonic Emission of Monolayer Semiconductors Near-field Coupled to High-Q Microresonators," *arXiv:1710.04294* (2017).

[3] V. Sudhir, R. Schilling, S.A. Fedorov, H. Schtz, D.J. Wilson, and T.J. Kippenberg. "Quantum Correlations of Light from a Room-Temperature Mechanical Oscillator," *Phys. Rev. X*, **7** 031055 (2017).

[4] S.A. Fedorov, V. Sudhir, R. Schilling, H. Schütz, D.J. Wilson, T.J. Kippenberg. "Evidence for Structural Damping in a High-stress Silicon Nitride Nanobeam and its Implications for Quantum Optomechanics," *Phys. Lett. A*, 24528 (2017).

[5] V. Sudhir, D.J. Wilson, R. Schilling, H. Schütz, S.A. Fedorov, A.H. Ghadimi, A. Nunnenkamp, and T.J. Kippenberg. "Appearance and Disappearance of Quantum Correlations in Measurement-based Feedback Control of a Mechanical Oscillator," *Phys. Rev. X*, **7** 011001 (2017).

[6] R. Schilling, H. Schütz, A. Ghadimi, V. Sudhir, D.J. Wilson, and T.J. Kippenberg. "Near-Field Integration of a SiN Nanobeam and a SiO_2 Microcavity for Heisenberg-Limited Displacement Sensing," *Phys. Rev. App.* **5**, 054019 (2016).

[7] H. Okamoto, R. Schilling, H. Schütz, V. Sudhir, D.J. Wilson, H. Yamaguchi, and T.J. Kippenberg. “A strongly Coupled Λ-type Micromechanical System,” *App. Phys. Lett.* **5**, 054019 (2016).

[8] D.J. Wilson, V. Sudhir, N. Piro, R. Schilling, A. Ghadimi, and T.J. Kippenberg. “Measurement-based Control of a Mechanical Oscillator at its Thermal Decoherence Rate,” *Nature* **524**, 325 (2015).

[9] C. Nicolaou, W.T. Lau, R. Gad, H. Akhavan, R. Schilling, and O. Levi. “Enhanced Detection Limit by Dark Mode Perturbation in 2D Photonic Crystal Slab Refractive Index Sensors,” *Optics Express* **25**, pp. 31698-31712 (2013).

Reference Contacts

Prof. Tobias J. Kippenberg
(Ph.D. advisor)
Laboratory of Photonics and Quantum Measurement
École Polytechnique Fédérale de Lausanne
PH D3 355, Station 3
Lausanne, VD 1015
Switzerland
+41 21 693 4428
tobias.kippenberg@epfl.ch

Prof. Ofer Levi
(M.S. advisor)
Biophotonics Group
Rosebrugh Building
164 College Street
M5S 3E2 Toronto
Canada
+1 416 946 5373
ofer.levi@utoronto.ca

Dr. Dalziel Wilson
(Research colleague and mentor at EPFL)
Laboratory of Photonics and Quantum Measurement
École Polytechnique Fédérale de Lausanne
PH D3 365, Station 3
Lausanne, VD 1015
Switzerland
+41 76 664 6567
dalziel.wilson@gmail.com